Methods of Nonlinear Femtosecond Spectroscopy in the Visible and Ultraviolet Regime and their Application to Coupled Multichromophore Systems

Dissertation zur Erlangung des
naturwissenschaftlichen Doktorgrades
der Julius-Maximilians-Universität
Würzburg

vorgelegt von
Ulrike Selig-Parthey
aus Eggenfelden

Würzburg 2012

Methods of Nonlinear Femtosecond Spectroscopy in the Visible and Ultraviolet Regime and their Application to Coupled Multichromophore Systems

Dissertation zur Erlangung des
naturwissenschaftlichen Doktorgrades
der Julius-Maximilians-Universität
Würzburg

vorgelegt von
Ulrike Selig-Parthey
aus Eggenfelden

Würzburg 2012

Eingereicht bei der Fakultät für Chemie und Pharmazie
am _______________

Gutachter der schriftlichen Arbeit
1. Gutachter: Prof. Dr. T. Brixner
2. Gutachter: Prof. Dr. B. Engels

Prüfer des öffentlichen Promotionskolloquiums
1. Prüfer: Prof. Dr. T. Brixner
2. Prüfer: Prof. Dr. B. Engels
3. Prüfer: Prof. Dr. F. Würthner
Tag des Promotionskolloquiums: 14.12.2012
Doktorurkunde ausgehändigt am: _______________

To my parents.

Contents

Zusammenfassung

Zeitaufgelöste spektroskopische Untersuchungen zu Energietransferprozessen zwischen Molekülen in Lösung bilden die Grundlage nicht nur für unser Verständnis elementarer natürlicher Vorgänge wie der Photosynthese, sondern auch für gerichtete Synthesen zur Optimierung organischer opto-elektronischer Bauteile.

Die kohärente zweidimensionale (2D) Spektroskopie eröffnet hier neue Möglichkeiten, da sie – durch Aufdeckung der Korrelation zwischen Absorptions- und Emissionsfrequenz – die konventionelle transiente Absorption (TA) um die Offenbarung der Ursache erweitert.

Im Rahmen dieser Arbeit wurden zwei optische Aufbauten entworfen und umgesetzt, die die Aufnahme von elektronischen 2D Spektren im sichtbaren und im bis dahin unerschlossenen ultravioletten Spektralbereich ermöglichen. Beide Designs beruhen auf dem Prinzip der ausschließlich paarweisen Strahlführung, wodurch die Modulation des Signals auf die Differenz zwischen Übergangsfrequenz des Systems und Laserfrequenz reduziert wird. Damit verringern sich – wie theoretisch und experimentell gezeigt – die Anforderungen sowohl an die mechanische Stabilität der Laborumgebung als auch an die Genauigkeit der verwendeten Verzögerungsbühnen erheblich, von Bruchteilen der Oszillationsperiode des anregenden Lichts auf Bruchteile der Laserpulsdauer.

Sowohl die 2D Spektroskopie als auch die transiente Absorption sowie unterschiedliche theoretische Ansätze und Simulationsmodelle wurden in den weiteren Teilen dieser Arbeit auf gekoppelte Multichromophor-Systeme unterschiedlicher Komplexität angewandt.

Im einfachsten dieser Systeme, einem Perylen-basierten Heterodimer, einer Kooperation mit Prof. Dr. Frank Würthner und Prof. Dr. Bernd Engels an der Universität Würzburg, konnte durch globale Analyse von sechs verschiedenen TA-Messungen ein ultraschneller Energietransfer im 100 fs Bereich zweifelsfrei identifiziert werden. Ein Vergleich mit Vorhersagen aus der Förster-Theorie legt einen Zusammenbruch dieser auf punktförmigen Übergangsdipolen beruhenden Theorie bei den vorliegenden Interchromophor-Abständen nahe. Darüber hinaus wurde für die Piko- bis Nanosekunden-Zeitskalen ein Schema vorgestellt, das Konformationsänderungen sowie einen Ladungstransfer beinhaltet und das die beobachtete Dynamik wie auch die gemessenen Fluoreszenz-Quantenausbeuten konsistent beschreibt.

In einer weiteren Kooperation wurden in Zusammenarbeit mit der Gruppe von Prof. Dr. Gregory Scholes (University of Toronto, Kanada) Fluoren-Carbazol-Makromoleküle untersucht, die in der Gruppe von Prof. Dr. Paul Burn (University of Queensland, Australien) synthetisiert worden waren. In diesen sogenannten Dendrimeren konnte durch die Kombination von 2D Spektroskopie und Femtosekunden-Anisotropie-Zerfalls-Experimenten eine anfängliche Delokalisierung der Wellenfunktion des angeregten Zustands abgeleitet werden, die mit der zweiten Generation saturiert. Die Umgebungsunordnung in Raumtemperatur-Lösung führt hier zu einer ultraschnellen Lokalisierung innerhalb

der Zeitauflösung des Experiments, gefolgt von inkohärenten Energietransfer-Prozessen.

In tubularen Zink Chlorin Aggregaten schließlich, semisynthetischen Analoga zu den Lichtsammelantennen natürlicher Chlorosome, die ebenfalls von Prof. Dr. Frank Würthner's Gruppe bereitgestellt wurden, ist die Kopplung zwischen den einzelnen Molekülen so stark, dass kohärent gekoppelte Segmente selbst bei Raumtemperatur Bestand haben. Die Ausdehnung dieser kohärenten Domänen, die Exzitonen-Delokalisierungslänge, konnte aus der Intensitätsabhängigkeit des transienten Absorptionssignals auf 5-20 Monomere bestimmt werden. 2D Spektren zeigten dabei den effizienten Energietransfer zwischen benachbarten Domänen im Aggregat, also einen ultraschnellen Exzitonen-Diffusionsprozess.

Summary

Time-resolved spectroscopic studies of energy transfer between molecules in solution form a basis for both, our understanding of fundamental natural processes like photosynthesis as well as directed synthetic approaches to optimize organic opto-electronic devices. Here, coherent two-dimensional (2D) spectroscopy opens up new possibilities, as it reveals the correlation between absorption and emission frequency and hence the full cause-and-effect chain.

In this thesis two optical setups were developed and implemented, permitting the recording of electronic 2D spectra in the visible and in the hitherto unexplored ultraviolet spectral range. Both designs rely on the exclusive manipulation of beam pairs, which reduces the signal modulation to the difference between the transition frequency of the system and the laser frequency. Thus – as has been shown experimentally and theoretically – the timing precision as well as mechanical stability requirements are greatly reduced, from fractions of the oscillation period of the exciting light wave to fractions of the pulse duration.

Two-dimensional spectroscopy and femtosecond transient absorption (TA) as well as different theoretical approaches and simulation models were then applied to coupled multichromophore systems of increasing complexity.

Perylene bisimide–perylene monoimide dyads were investigated in cooperation with Prof. Dr. Frank Würthner and Prof. Dr. Bernd Engels at the University of Würzburg. In these simplest systems studied, global analysis of six different TA experiments unequivocally revealed an ultrafast interchromophoric energy transfer in the 100 fs range. Comparison between the obtained transfer rates and the predictions of Förster theory suggest a breakdown of this point-transition-dipole-based picture at the donor-acceptor distances realized in our compounds. Furthermore, a model including conformational changes and an interchromophoric charge transfer has been derived to consistently describe the observed pico- to nanosecond dynamics and fluorescence quantum yields.

A second collaboration with Prof. Dr. Gregory Scholes (University of Toronto, Canada) and Prof. Dr. Paul Burn (University of Queensland, Australia) addressed the photophysics of a series of fluorene-carbazole dendrimers. Here, a combination of 2D-UV spectroscopy and femtosecond ansiotropy decay experiments revealed the initial delocalization of the excited state wave function that saturates with the second generation. In room temperature solution, disorder-induced localization takes place on the time scales comparable to our instrument response, i.e. ~ 100 fs, followed by energy transfer via incoherent hopping processes.

Lastly, in tubular zinc chlorin aggregates, semi-synthetic analogues of natural light-harvesting antennae that had again been synthesized in the group of Prof. Dr. Frank Würthner, the interchromophoric coupling is so strong that coherently coupled domains prevail even at room temperature. From an analysis of intensity-dependent TA measurements the dimensions of these domains, the exciton delocalization length, could be determined to span 5-20 monomers. In addition, 2D spectra uncovered efficient energy transfer between neighboring domains, i.e. ultrafast exciton diffusion.

1 Motivation

We have built our industrialized world upon the possibility to convert one energy form into another. Thomas Newcomen's invention of the first commercially successful steam engine in 1712 [1], that was later improved by James Watt resulting in his well-known patent in 1769, was a historical turning point as it allowed the conversion of heat into mechanical energy. Roughly at the same time [2], research on electricity and magnetism intensified – names like Volta, Ampere, Ohm, Maxwell, Faraday, Siemens, and many others should ring a bell – which led to the development of an electric generator. Enabling the transformation of mechanical (or chemical in the case of a battery) energy into movement of electric charges and vice versa, the emerging field of electrical engineering represents the second pilar of modern life.

Jumping a few centuries forward, a series of subsequent inventions revolutionized our standard of living as well as role perception in society: The mobility of individuals and traded goods has increased to priorly unthinkable levels and the predominance of the physically superior has drastically reduced. This came at a cost of a global primary energy demand of 0.5 zettajoules (5×10^{20} Joules) in 2011, over 80% of which is satisfied from fossil sources [3].

With the dawning realization that the carbon cycle time scales that govern production of fossil fuels from organic matter via geochemical processes are incompatible with time scales of civilization, i.e. the insight that our fossil fuel resources are effectively limited, came the idea to skip the lengthy steps of the carbon cycle and use solar energy directly, e.g. in the form of solar cells.

Here, the most vital energy conversion process, natural photosynthesis can teach engineers and researchers, in particular those working on organic solar cells [4], a lesson when it comes to efficiency. In photosynthetic organisms, a network of light-harvesting pigments absorbs photons and transfers this excitation energy to the photochemical reaction centers that convert it into a stable electrochemical potential with an overall near-unity quantum yield of 0.95 [5]. On a microscopic level, the efficiency of this energy conversion is largely determined by the efficiency of the energy transfer processes, which for a given pair of interacting pigments – or chromophores as we will call the functional molecular subunits involved in the absorption and emission of light throughout this thesis – depends on the type of interaction between them and the strength of their coupling compared to perturbations induced by the surrounding.

A detailed investigation of the mechanisms underlying natural and artificial light-harvesting efficiencies is crucial for a directed optimization of device performance, not only in solar cells. Numerous applications of organic functional materials such as light emitting diodes, transistors, organic lasers or optical memories, could benefit and utilize these findings in systematic and concerted synthetic approaches.

To complement our current understanding of energy transfer on the molecular level we have to advance existing experimental methods on the one hand and share the results obtained from application of these methods on the other. After a brief review on the theoretical basics of energy transfer and time-resolved spectroscopy in Chapter 2, both aspects will be covered: Two different experimental setups for coherent electronic two-dimensional spectroscopy, a femtosecond technique that is immediately sensitive to interchromophoric couplings, will be introduced in Chapter 3. Both rely on the concept of pairwise beam manipulation which greatly reduces the required timing precision and mechanical stability. The presented implementation for excitation at visible wavelengths uses only conventional optics and is hence a robust, simple and cost-efficient alternative to existing designs. An all-reflective layout, realized for the 250-400 nm spectral range, on the other hand is a high-end solution that specifically suits the needs of excitation conditions that require precise dispersion control.

The second part of this thesis deals with the photophysics of organic multichromophore complexes in room temperature solution on femto- to nanosecond timescales. Interchromophoric distances in our supramolecular architectures will be comparable to the size of the individual molecules. Hence, energy transfer is mediated by Coulombic forces associated with their transition dipoles, rather than radiative mechanisms that involve the emission of one photon from a donor and its subsequent absorption by an acceptor molecule. The linear absorption of all systems studied shows evidence of excitonic coupling, i.e. coherent interaction between the constituing chromophores that leads to delocalization of the excited state wave functions. Yet we will see that disorder induced dephasing quickly destroys this coherence resulting in incoherent energy migration.

Starting out with only two coupled chromophores in a perylene bisimide–perylene monoimide dyad in Chapter 3, we will be able to reproduce the linear absorption spectrum qualitatively within dipole approximation and quantitatively with *ab initio* calculations. Energy transfer times retrieved from transient absorption data will then question the validity of commonly applied Förster theory at the short distances realized in our compounds. Besides we will develop a model including an intramolecular charge transfer channel to consistently describe the dimer dynamics on the pico- to nanosecond time scales.

Turning to dendrimeric structures in Chapter 4 will drastically increase complexity, such that the identification of effective chromophores in these conjugated systems will be a first challenge. From anisotropy decays and two-dimensional spectra we will deduce significant initial coupling followed by an ultrafast localization process in these compounds and suggest an intramolecular charge transfer as the origin of the redshifted emission in higher generation dendrimers.

In the last system studied, zinc chlorin aggregates that mimic natural photosynthetic light-harvesting antennae (Chapter 5), complexity will effectively be reduced, even though they comprise by far the largest number of chromophores: The comparably defined transition dipole orientation realized in their tubular geometry concentrates oscillator strength in few electronic transitions. Here, we will retrieve an estimate for the delocalization length of the excited state wave functions from transient absorption data and reveal ultrafast energy transfer processes between neighboring aggregate segments.

Finally, Chapter 6 will summarize the presented results and give a short outlook on future experiments.

2 Theoretical Background

While this chapter aims at providing a theoretical basis for the experiments described in the following chapters, it can by no means comprehensively review the full quantum mechanics, laser pulse and even time-resolved spectroscopy fundamentals required for a detailed understanding of the presented results. It should hence rather be considered a subjectively accentuated overview to refresh a biased reader's memory and maybe complement it with some aspects that I personally would have liked to know four years ago.

We will begin this chapter with a short review on the derivation of the fundamental quantity in light matter interaction, the transition dipole moment, before we turn to the energy transfer properties of molecular ensembles that arise from the Coulombic coupling between the transition dipoles of the individual chromophores. Two limiting cases can be distinguished: In supramolecular arrangements with short inter-chromophore distances this coupling will be so strong that the picture of individual excited molecules is no longer appropriate and a description based on collective excitations delocalized over several molecules, so-called excitons, will be introduced. We will see that excitonic interactions are associated with changes in the linear absorption, allowing in principle the deduction of coupling strength and relative spatial position from this experimentally easily accessible quantity. For larger distances, on the other hand, the couplings become smaller than the energetic disorder induced by the surrounding bath (the solvent) and the intermolecular interaction is no longer evident from the linear spectra. Yet the transition dipole coupling leads to inter-molecular energy transfer and we are in the classical regime of incoherent Förster transfer.

In the experiments described in the following chapters we will - as ever so often - have to deal with the exciting yet complicated intermediate regime, where fluctuations in the bath lead to an extremely fast localization of an initially delocalized exciton.

Section 2.5 is devoted to one of our most powerful working horses, the Fourier Transform: We will briefly recall its definition and some important properties before discussing the discrete Fourier Transform in more detail. The latter is of fundamental importance for data evaluation in multidimensional spectroscopies, and a simulation study addressing distortions originating from experimental deficiencies will help us to understand the phase stability discussion in Chapter 3.

After introducing the concept of heterodyne detection as a means to fully recover an unknown signal field in amplitude and phase (Section 2.6), we are all set for the subsequent theoretical description of spectroscopy. Here, perturbation theory will be applied to establish a connection between the light-induced polarization, the density matrix of the quantum mechanical system studied and the excitation field.

2.1 Transition Dipole Moments

Light as an electromagnetic wave interacts with the microscopic charge distribution $\varrho_m(\vec{r}, t)$ of matter, which in classical electrodynamics is described by Maxwell's equations. A transition to quantum mechanics can be made by formulating the classical system Hamiltonian and substituting the quantum mechanical operators for the momentum. Approximating our molecular system, which for now will be a single molecule, as a discrete ensemble of charges q_i with masses m_i at spatial positions $\vec{r_i}$ the non-relativistic Hamiltonian of the interaction process has the general form [6]

$$\mathcal{H} = \sum_i \frac{1}{2m_i} \left(\vec{p_i} + q_i \vec{A}(\vec{r}, t)\right)^2 - q_i \phi(\vec{r}, t) \tag{2.1}$$

Here, $\phi(\vec{r}, t)$ and $\vec{A}(\vec{r}, t)$ are the potential and vector potential, respectively, associated with the electromagnetic field via

$$\vec{E}(\vec{r}, t) = -\frac{\partial \vec{A}(\vec{r}, t)}{\partial t} - \nabla \phi(\vec{r}, t) \tag{2.2}$$

$$\vec{B}(\vec{r}, t) = \nabla \times \vec{A}(\vec{r}, t). \tag{2.3}$$

Neglecting terms that are quadratic in $\vec{A}(\vec{r}, t)$, i.e. for field strengths small enough not to significantly disturb the intramolecular binding potential, and wavelengths larger than the molecular dimensions, i.e. $\mathrm{e}^{i\vec{k}\vec{r}} \approx 1$, this bulky Hamiltonian can be approximated by the much simpler expression

$$\mathcal{H} = -\vec{\mu}\, \vec{E}(\vec{r}, t) \tag{2.4}$$

corresponding to treating the molecule as a simple dipole represented by the dipole operator $\vec{\mu}$

$$\vec{\mu} = \sum_i q_i \, \vec{r}_i. \tag{2.5}$$

The diagonal matrix elements of $\vec{\mu}$, μ_{ii}, reflect the permanent dipole moment of our molecular system in state i, whereas the off-diagonal elements μ_{if} determine the probability of a light induced transition from an initial molecular state i to a final state f. More precisely, the square of the off-diagonal matrix element μ_{if} weighted with the transition frequency, also known as the oscillator strength f, determines the strength of this transition. The so-called transition dipole moments μ_{if} are of course the quantities of interest for a spectroscopic experiment. In contrast to the stationary permanent dipoles, they oscillate in time with the transition frequency ω_{if}, i.e. while the axis of μ_{if} can be calculated for a given molecular geometry, its orientation along this axis is time-dependent. Note that even for systems with no permanent dipoles, the transition dipoles can still be non-zero.

2.2 Dipole-Dipole Interactions

While dipole-dipole interactions play a decisive role in the association of non-covalently linked neutral species via van-der-Waals forces, here, we will be especially interested in the angular and distance dependence of the interaction energy of two *transition* dipoles. From our basic electrodynamics lecture [7] we recall that the potential of an arbitrary charge density distribution can be approximated by a so-called multipole expansion, and that for uncharged matter the first non-vanishing term of this expansion is the one corresponding to a dipole. The potential $\Phi(\vec{r})$ of a dipole $\vec{\mu}$ located at $\vec{r'}$

$$\Phi(\vec{r}) = \frac{1}{4\pi\epsilon_0} \frac{1}{|\vec{r}-\vec{r'}|^2} \frac{\vec{\mu}\cdot(\vec{r}-\vec{r'})}{|\vec{r}-\vec{r'}|} \tag{2.6}$$

is associated with a dipole field $\vec{E}_\mu(\vec{r})$

$$\vec{E}_\mu(\vec{r}) = -\nabla\Phi(\vec{r}) = -\frac{1}{4\pi\epsilon_0} \frac{1}{|\vec{r}-\vec{r'}|^3} \left(\vec{\mu} - \frac{3\left(\vec{\mu}\cdot(\vec{r}-\vec{r'})\right)(\vec{r}-\vec{r'})}{|\vec{r}-\vec{r'}|^2} \right). \tag{2.7}$$

A second transition dipole $\vec{\mu}_2$ at $\vec{r}_2$ placed in the proximity of $\vec{\mu}_1$ will now experience the field of $\vec{\mu}_1$ leading to an interaction energy V (often referred to as dipole-dipole coupling)

$$V = -\vec{\mu}_2 \cdot \vec{E}_\mu(\vec{r}_2) = \frac{1}{4\pi\epsilon_0} \frac{1}{|\vec{r}_2-\vec{r}_1|^3} \left(\vec{\mu}_1\cdot\vec{\mu}_2 - \frac{3\left(\vec{\mu}_1\cdot(\vec{r}_2-\vec{r}_1)\right)\vec{\mu}_2\cdot(\vec{r}_2-\vec{r}_1)}{|\vec{r}_2-\vec{r}_1|^2} \right). \tag{2.8}$$

Introducing the center-to-center distance vector $\vec{R}_{12} = \vec{r}_2 - \vec{r}_1$ as well as the angles between the two dipoles and this vector θ_i and the inter-dipole angle α (cf. figure 2.1 (a)) and using the identity $\theta_2 = \theta_1 - \alpha$, V can be rewritten as

$$V = \frac{1}{4\pi\epsilon_0} \left(\frac{\mu_1\mu_2\cos\alpha}{R_{12}^3} - \frac{3\mu_1\mu_2\cos\theta_1\cos(\theta_1+\alpha)}{R_{12}^3} \right) \tag{2.9}$$

The resulting interaction energy is plotted in figure 2.1 (b) as a function of θ_1 and α for a fixed distance R_{12}. We immediately verify from equation (2.9), that the V spans a range $V_{min} = -\frac{2}{4\pi\epsilon_0}\frac{\mu_1\mu_2}{R_{12}^3} \leq V \leq +\frac{2}{4\pi\epsilon_0}\frac{\mu_1\mu_2}{R_{12}^3} = V_{max}$, with the lowest energy corresponding to the energetically favorable in-line arrangement of two parallel dipoles ($\theta_1 = \alpha = 0$) and V_{max} resulting from their antiparallel alignment ($\theta = 0, \alpha = \pi$). For vanishing coupling, $V = 0$, two limiting cases can be distinguished: $V = 0$ for perpendicular dipoles only as long as additionally one of them is also perpendicular to R_{12}, and $V = 0$ for parallel dipoles ($\alpha = 0$) that incline the magic angle $\theta_1 = 54.7°$ with their center to center distance. Transition dipole arrangements with $\theta_1 > 54.7°$ are referred to as H-type, while arrangements with $\theta_1 < 54.7°$ are called J-type. Note that for equal interchromophore distances the coupling strength $|V|$ in ideal H ($\theta = 90°$) is smaller than in prefect J dimers ($\theta = 0°$). We will in the next section deduce the differences in the optical properties of J and H aggregates. However, from a look at the limiting cases, i.e. the situations corresponding to the corners of the 2D graph in figure 2.1 (b),

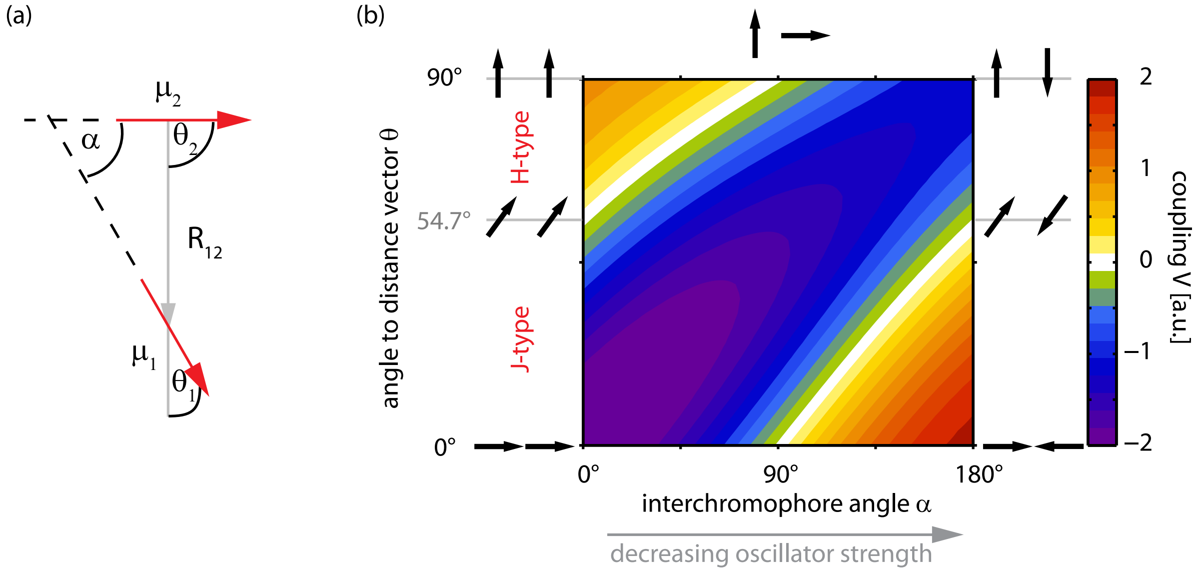

Figure 2.1: Definition of angles (a), and interaction energy V as a function of the interchromophore angle α and angle to center-to-center distance vector θ (b). See text for further explanations.

we can already predict some of the main features: For the J-type arrangement, the net transition dipole will be largest for the situation corresponding to the lowest energy (lower left corner) while it vanishes for $V = V_{max}$ (lower right corner). In contrast, in the ideal H-type case, a light wave couples most efficiently to the energetically least favorable arrangement (upper left corner) while the net transition dipole moment of the antiparallel arrangement (upper right corner) is zero.

2.3 Excitons

Having found the transition dipole of the single molecule as the quantity that dominates interaction between light and matter, we are now interested in the influence of intermolecular interactions associated with the individual transition dipoles on the excited states of our ensemble. The concept described in the following is known as exciton-theory and its origin is nowadays mainly accredited to Kasha [8–10], who indeed in the 1960ies merged the results of others and his own studies on the excited state properties of molecular dimers and aggregates into a theoretical framework that serves as a starting point of today's more elaborate calculations. The latter include, e.g. the incorporation of vibrational degrees of freedom, more sophisticated geometries and the effects of disorder (see e.g. [11–13] and references cited therein). After introduction of the basic Hamiltonian and a few general considerations on the properties of excitonic states we will use an idealized linear aggregate to point out the characteristic features of excitonically coupled ensembles, i.e. the correlation between the shift in the absorption spectrum and the orientation of molecular transition dipoles and the presence of a superradiant state.

The Hamiltonian for any ensemble consisting of N interacting molecules with interaction energy V can be written as

$$H = \sum_{i=1}^{N} \left(H_i + \frac{1}{2} \sum_{j=1, j \neq i}^{N} V_{ij} \right) \tag{2.10}$$

or alternatively in matrix form

$$H = \begin{pmatrix} H_0 & v_{01} & v_{02} & \dots & v_{0N} \\ v_{10} & H_1 & v_{12} & \dots & v_{1N} \\ v_{20} & v_{21} & H_2 & \dots & v_{2N} \\ \vdots & \vdots & \vdots & \ddots & v_{0N} \\ H_0 & v_{01} & v_{02} & \dots & H_N \end{pmatrix} \tag{2.11}$$

with the Hamiltonian of the isolated molecule i, H_i, and the coupling between a pair of molecules i and j, $v_{ij} = v_{ji} = \frac{1}{2}V_{ij}$. From our basic quantum mechanics lecture we remember that to solve the stationary Schrödinger equation we must find the eigensystem of this Hamiltonian: The eigenvalues of H correspond to the energies while the eigenvectors of H yield the eigenstates for our coupled system in site representation.[1]

Our focus on the collective excited state properties legitimates the common assumption in exciton theory that the ground state of the coupled system, $|0\rangle$, (corresponding to the situation where none of the molecules are excited) can be approximated by a product of the individual ground states of all molecules. Note, however, that within this assumption the molecules have no reason to stick together in the first place.

While numerical diagonalization of H can efficiently be achieved for not too complicated systems, analytical solutions of the Schrödinger equation can only be found for some idealized cases. Before we turn to some of these special cases we can already make several predictions regarding the eigenstates of the coupled system [14]: First of all, there are 2^N eigenstates in N independent two-level molecules, therefore we also expect 2^N eigenstates in the coupled system. Secondly, as H conserves the number of excitations, we expect the eigenstates to reflect the situations where 1, 2, 3...N molecules are excited. More precisely, there must be a manifold of $\frac{N!}{m!(N-m)!}$ states corresponding to the situation where our ensemble shares m excitations, because there are $\frac{N!}{m!(N-m)!}$ different realizations of m molecules excited in the uncoupled system. These manifolds are commonly referred to as m-exciton bands. Within dipole approximation, i.e. when the effective size of the coupled system is much smaller than the optical wavelength, radiative transitions are only possible between neighboring exciton bands, $\Delta m = \pm 1$. Therefore in the discussion of third-order optical techniques, corresponding to a net interaction with two photons, only the one-exciton and two-exciton bands must be considered besides the ground state. Furthermore, we can also predict the approximate energy of the mth exciton bands as $E \sim m\hbar\omega_0$, which for the physically relevant case when the interchromophore-coupling is much smaller than the electronic transition energy of the

---

[1] Site representation means that the i-th component of the eigenvector corresponds to the amplitude of the wave function at site i, i.e. the contribution of molecule i to the delocalized state.

monomer $V \ll \hbar\omega_0$ will also be a good estimate for the energy of the dipole allowed transitions in the coupled system.

Regarding the analytic solutions, we will first look at the smallest coupled system possible, the dimer: As the experiments presented in Chapter 4 were performed on a heterodimer, we will explicitly consider two *different* monomers with transition energies e_1 and e_2, with corresponding transition dipole moments μ_1 and μ_2, and interaction energy V. The results we obtain of course include the extensively studied case of a homodimer in the limit $e_1 = e_2 = e$ and $\mu_1 = \mu_2 = \mu$. The eigenenergies for the singly excited states of the coupled system E_1 and E_2 are easily found to be (see e.g. [15])

$$E_{1/2} = E_{\pm} = \frac{1}{2}\left(e_1 + e_2 \pm \sqrt{\Delta e^2 + |V|^2}\right) \tag{2.12}$$

where we have introduced the energy difference $\Delta e = e_2 - e_1$. The corresponding one-exciton eigenstates can be written as linear combinations of the product states $|1\rangle = |\phi_1^*\phi_2\rangle$ in which only molecule 1 and $|2\rangle = |\phi_1\phi_2^*\rangle$ in which only molecule 2 is excited

$$\Psi_+ = \cos\theta\,|1\rangle - \sin\theta\,|2\rangle, \tag{2.13}$$

$$\Psi_- = \sin\theta\,|1\rangle + \cos\theta\,|2\rangle. \tag{2.14}$$

The mixing angle θ, $\theta = \frac{1}{2}\arctan\left(\frac{V}{\Delta e}\right)$, varies between $\theta = \pm\frac{\pi}{4}$ for the perfect homodimer ($\Delta e = 0, V = \pm|V|$) corresponding to a full delocalization of the one-exciton states over both monomers, and $\theta = 0$ for $V \ll \Delta e$, i.e. in the limit of couplings smaller than the energy difference the one-exciton states maintain largely the character of the uncoupled situations $|1\rangle$ and $|2\rangle$.

The transition dipole moments between ground state and one-exciton states, $\vec{M}_{\pm} = \langle 0\,|\vec{\mu}|\,\Psi_{\pm}\rangle$ read

$$\vec{M}_+ = \cos\theta\,\vec{\mu}_1 - \sin\theta\,\vec{\mu}_2 \tag{2.15}$$

$$\vec{M}_- = \sin\theta\,\vec{\mu}_1 + \cos\theta\,\vec{\mu}_2. \tag{2.16}$$

This is the mathematical proof of the intuitive picture we developed in the previous section for the possibility to couple an electromagnetic wave to two interacting transition dipoles: For two identical in-line dipoles ($V < 0$, $\theta = -\frac{\pi}{4}$) the transition to the lower lying exciton state $\vec{M}_-$ carries all the oscillator strength, while the upper exciton state is dark, leading to a red-shifted absorption. The opposite holds for the ideal H-type arrangement.

For a heterodimer ($\Delta e \neq 0$), while the tendencies are the same, the dark state is no longer completely dark even if the transition dipole vectors are identical.

Turning now to larger coupled systems let us consider the unrealistic yet highly instructive case of a perfect linear aggregate, an equidistant chain of N identical two-level molecules with electronic transition energy ϵ_0 and parallel transition dipole moments μ (cf. figure 2.3 (a)). Besides, we will restrict ourselves to nearest neighbor interactions only, which given the $\frac{1}{R^3}$-dependence of dipole-dipole-coupling is not severe. For such a system all eigenstates can be found analytically [16] and the one-exciton states Ψ_k^1

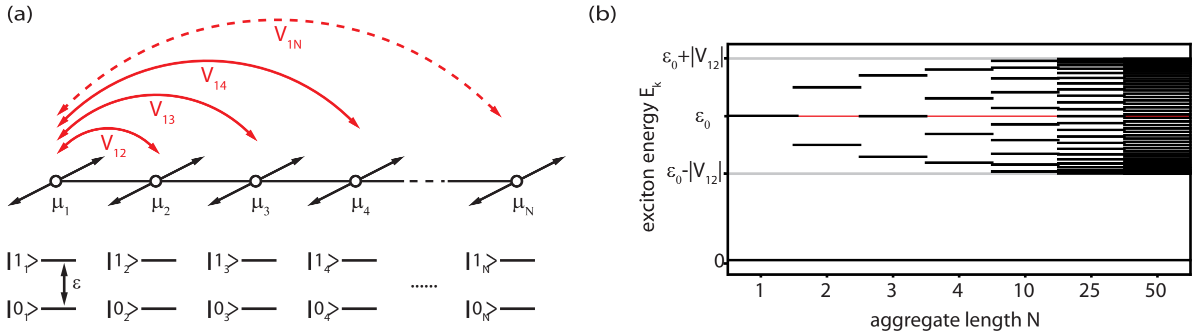

Figure 2.2: Idealized linear aggregate of N interacting parallel transition dipoles (a). Exciton energies E_k^1 of the one-exciton band for different aggregate length N in the limit of nearest neighbor coupling (b).

can be written as linear combinations of the states $|n\rangle$ in which all molecules except molecule n are in the ground state [17]

$$\Psi_k^1 = \sqrt{\frac{2}{N+1}} \sum_{n=1}^{N} \sin\left(\frac{n\pi k}{N+1}\right) |n\rangle \quad k = 1 \ldots N. \tag{2.17}$$

The corresponding one-exciton energies E_k read

$$E_k^1 = \omega_0 + V \cos\left(\frac{\pi k}{N+1}\right). \tag{2.18}$$

From this formula we immediately recognize that the one-exciton band spans an energy range corresponding to twice the interaction energy $\Delta E^1 = 2V$ in the limit of large N and $\Delta E^1 = V$ in the case of a dimer for which the limitation to nearest neighbor coupling is exact. This is illustrated in figure 2.2 (b). Notably, due to the $\cos(1/N)$-dependence, 95% of the maximum band splitting are already reached for $N = 9$ (99% for $N = 21$). Furthermore, the cosine dispersion relation leads to a bunching of states at the upper and lower band edge.

The transition dipole moments to the one-exciton band M_{0k}^1 follow

$$M_{0k}^1 = \begin{cases} \cot\left(\frac{\pi k}{2N+1}\right) & k \text{ odd} \\ 0 & k \text{ even} \end{cases} \tag{2.19}$$

i.e. the transition to the one-exciton state with $k = 1$ dominates the absorption of the linear chain, with $f_{0k=1}^1$ approaching 81% of the total oscillator strength in the limit of large N. This superradiance, the concentration of nearly all ensemble oscillator strength into a single collective transition, that is frequently observed in molecular aggregates, originates from the in-phase oscillation of the individual transition dipoles for $k = 1$. For even k and larger odd k as can be easily verified from a look at the wave functions, the dipoles add up destructively. For periodic boundary conditions, i.e. when closing the chain to a large ring by identification of the N's molecule with the nearest neighbor of the first site, the $k = 1$-state even collects 100% of the oscillator strength, leaving all other transitions dark [18].

Depending on the sign of the interaction energy V the state associated with $k = 1$ is located at different ends of the one-exciton band: For $V < 0$, i.e. a J aggregate, $k = 1$ corresponds to the lower band edge leading to a bathochromic shift of magnitude V with respect to the monomeric transition at ω_0 in the linear absorption spectrum. In contrast, for H aggregates, $V > 0$, a hypsochromic shift will be observed.

Notably, while the observation of a spectral shift upon increasing the molecular concentration, is a profound indicator of aggregation and allows to deduce the coupling strength (if ground state interaction is neglected or a good estimate is at hand), it provides limited information on the chain length: As stated above the $\cos(1/N)$-dependence of the spectral shift implies saturation at $N \sim 10$ monomeric units. Here, for J aggregates, a comparison of aggregate and monomer radiative lifetimes τ can provide additional information [18]: Since the radiative decay time is inversely proportional to the oscillator strength f,

$$\frac{1}{\tau} \propto f \propto M^2, \tag{2.20}$$

and a single transition collects almost all of the oscillator strength

$$f_{\mathrm{agg}} \sim N f_{\mathrm{mono}}, \tag{2.21}$$

the aggregate excited state will decay N times faster than the monomer

$$\tau_{\mathrm{agg}} \sim \frac{\tau_{\mathrm{mono}}}{N}. \tag{2.22}$$

It is beyond the scope of this thesis to discuss the details of multi-exciton bands. Yet it is important to note that two-exciton states, that will appear as excited state absorptions in our transient absorption data, are *not* direct products of one-exciton states. This is an immediate consequence of the Pauli exclusion principle, that leads to infinite effective on-site repulsion [17], appearing as a blueshift in the one-to-two-exciton band transitions in our data. The interested reader is referred to references [14,16], where eigenenergies and eigenstates of multi-exciton bands as well as intraband transition energies are explicitly calculated. Pretty much all other Spano-papers are also worth reading.

For more realistic systems, we have to take into account the influence of the surrounding solvent molecules, that will affect the monomeric transition energies as well as the relative orientation of the transition dipoles. Diagonal disorder, i.e. different transition energies for the individual monomers, lead to localization of the wave functions, which can be understood form the above results for the heterodimer. Similarly, off-diagonal disorder (in the couplings) leads to localization as it effectively strengthens some of the interactions and weakens others. Taking into account that the homogeneous spectral line width of a transition is a measure of the disorder a chromophore is exposed to, we can identify the ratio of interchromophoric coupling and homogeneous line width as the decisive quantity governing delocalization-localization transitions.

The aggregate features discussed above remain valid in the presence of disorder if one introduces an effective length of the aggregate, the delocalization length N_{deloc} [17].

Within segments of length $N \leq N_{\text{deloc}}$ of the original aggregate, the ratio of disorder and interchromophoric coupling is sufficiently small, and these segments can be regarded as coherence domains. Once one of the domains is excited the energy can be incoherently transfered to neighboring units, a process known as exciton migration or exciton diffusion. When multiple excitons are generated on a single aggregate, they can meet and interact, often annihilate. The resulting dynamics can be used to deduce effective diffusion constants and lengths, quantities highly relevant for light-harvesting applications [19].

An extension of this theory to tubular and helical tubular aggregates studying the particular features arising from the chirality of such system can be found e.g. in [20–22].

2.4 Förster Energy Transfer

To develop an intuitive understanding of Förster energy transfer and establish a connection to experimentally accessible quantities, it is helpful to follow the line of thought of Förster's original publications [23–26]: Let us start out with a system comprised of identical molecules in solution and try to come up with a proper description of the time-dependent excitation probability $\rho_D(t)$ of molecule D in the presence of energy transfer (ET) to and from other molecules in the ensemble. In contrast to the trivial *sequential* photon emission-and-reabsorption process we will here regard ET and excited state decay as *parallel* processes

$$\begin{aligned} \frac{d\rho_D(t)}{dt} &= -\frac{1}{\tau_D}\rho_D(t) + \sum_A \left(k_{AD}\rho_A(t) - k_{DA}\rho_D(t)\right) && (2.23)\\ &= -\frac{1}{\tau_D}\rho_D(t) + \sum_A k_{AD}\left(\rho_A(t) - \rho_D(t)\right). && (2.24) \end{aligned}$$

The first term on the right hand side of equation (2.23) accounts for the intrinsic decay of excited state D, i.e. τ_D is the excited state lifetime determined by radiative (τ_r) and non-radiative (τ_{nr}) deactivation mechanisms in the absence of ET to other chromophores

$$\frac{1}{\tau_D} = \frac{1}{\tau_r} + \frac{1}{\tau_{nr}}. \tag{2.25}$$

The second and third term describe energy transfer from molecule A to D with rate constant k_{AD} and vice versa, $k_{DA} = k_{AD}$. Theodor Förster's accomplishment lies in the thorough quantum mechanical derivation of the rates k_{DA}, that we will now briefly review. For the transfer rate from an electronically excited molecule D in the vibrational state ν'_D corresponding to vibrational energy e'_D to molecule A initially in the electronic ground state with vibrational energy e_A yielding ground state molecule D with e_D and excited state molecule A with e'_A he finds

$$k_{DA} = \frac{2\pi}{\hbar} \int\limits_{E=0}^{\infty} \int\limits_{e_A=0}^{\infty} \int\limits_{e'_D=0}^{\infty} g'(e'_D)g(e_A)\left|u_{DA}(e'_D, e_A; E_0 - E + e'_D, E - E_0 + e_A)\right|^2 de'_D de_A dE. \tag{2.26}$$

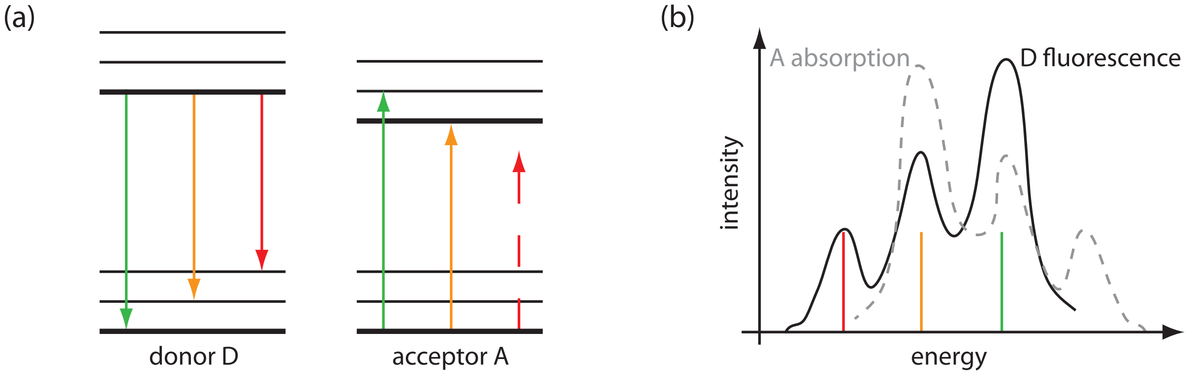

Figure 2.3: Illustration of Förster energy transfer. Resonant transitions of donor and acceptor are depicted in the same colors (a). Note that, even though the overlap of donor emission and acceptor extinction determines the efficiency of the process for a given orientational factor κ and distance R_{DA} (b), it is not mediated via photons.

Here, $g'(e'_D)$ and $g(e_A)$ are distribution functions, normalized to 1 on an energy scale, describing the occupation of vibrational energies in the excited and ground state, respectively, u_{DA} is the matrix element of the interaction mediating the transfer, and E_0 is the electronic transition energy. Note that all integration variables are continuous because we are dealing with molecules in solution. For interchromophore distances larger than a chemical bond length the energy u_{DA} is given by the Coulomb interaction between the charge density distributions of molecules D and A, which for intermolecular distances larger than the molecular dimensions can be approximated by two interacting transition dipoles $\vec{\mu}_D$ and $\vec{\mu}_A$ spatially separated by $\vec{R}_{DA} = \vec{R}_D - \vec{R}_A$

$$u_{DA}(e'_D, e_A; e_D, e'_A) = \frac{\vec{\mu}_D(e_D, e'_D) \cdot \vec{\mu}_A(e_A, e'_A)}{n^2 R_{DA}^3} - \frac{3\left(\vec{\mu}_D(e_D, e'_D) \cdot \vec{R}_{DA}\right)\left(\vec{\mu}_A(e_A, e'_A) \cdot \vec{R}_{DA}\right)}{n^2 R_{DA}^5}. \tag{2.27}$$

$$\vec{\mu}_i(e_i, e'_i) = -e \int \phi_i^*(e_i, \vec{r}_i)\vec{r}_i\phi'_i(e'_i, \vec{r}_i)\,\mathrm{d}\vec{r}_i \tag{2.28}$$

To calculate the transition dipoles in Förster theory the eigenstates ϕ_i of molecule i depend only on the set of electronic coordinates $\vec{r}_i$. Nuclear degrees of freedom are assumed stationary during the electronic transition, i.e. the Born-Oppenheimer approximation is applied.

With these approximations we have now deduced an expression for the energy transfer rate $k_{DA} := k_{ET}$ from donor D to acceptor A that is essentially an energy-integral over transition dipoles, weighted with their relative orientation and distance. This means we have now paved the way for a connection to experimentally accessible quantities, namely the fluorescence spectrum of the donor D, $\overline{I}_\lambda^D$, *normalized to unit area*, and the absorption spectrum, more precisely the extinction coefficient $\epsilon_A(\lambda)$, of the acceptor

A [27]:

$$k_{ET} = \frac{k_D}{R_{DA}^6} \left[\frac{9 \ln 10}{128\,\pi^5 N_A} \frac{\Phi_D}{n^4} \left(\frac{\vec{\mu}_D \cdot \vec{\mu}_A - 3(\vec{\mu}_D \cdot \vec{R})(\vec{\mu}_A \cdot \vec{R})}{\mu_D \mu_A} \right)^2 \int \overline{I}_\lambda^D \epsilon_A(\lambda) \lambda^4 \, \mathrm{d}\lambda \right] \tag{2.29}$$

$$\int \overline{I}_\lambda^D \, \mathrm{d}\lambda = 1 \tag{2.30}$$

Here, Φ_D is the fluorescence quantum yield of D and k_D is its excited state decay rate, both in the absence of ET. N_A is Avogadro's constant and n is the refractive index of the surrounding medium that shields the dipole fields. We note the R^6-distance dependence of the transfer rate that we can from the derivation of equation (2.29) trace back to squaring the R^3-dependence of the dipole-dipole interaction. Recalling that $k_r = \Phi_D k_D$ we recognize a maybe counterintuitive dependence of the transfer rate k_{ET} on the radiative rate constant k_r: The shorter the radiative lifetime, the higher k_{ET}. However, a short radiative lifetime correlates with a large oscillator strength of the donor and therefore efficient dipole-dipole coupling.

Defining an orientational factor κ

$$\kappa = \left(\frac{\vec{\mu}_D \cdot \vec{\mu}_A - 3(\vec{\mu}_D \cdot \vec{R})(\vec{\mu}_A \cdot \vec{R})}{\mu_D \mu_A} \right) \tag{2.31}$$

with $\vec{R}$ a unit vector along the center to center distance of donor and acceptor and the overlap-integral J

$$J = \int \overline{I}_\lambda^D \epsilon_A(\lambda) \lambda^4 \, \mathrm{d}\lambda \tag{2.32}$$

we can introduce a characteristic quantity for a given Förster pair D and A, their so-called Förster radius[2] R_0

$$R_0^6 = \frac{9 \ln 10}{128\,\pi^5 N_A} \frac{\Phi_D}{n^4} \kappa^2 J \tag{2.33}$$

and recast equation (2.29) in a far simpler form:

$$k_{ET} = k_D \left(\frac{R_0}{R_{\mathrm{DA}}} \right)^6 . \tag{2.34}$$

Obviously, when donor and acceptor are separated by a distance $R_{\mathrm{DA}} = R_0$, the ET rate equals the excited state decay rate of the donor, i.e. the transfer efficiency Φ_{ET}

$$\Phi_{ET} = \frac{k_{ET}}{k_D + k_{ET}} \tag{2.35}$$

---

[2] various forms of this equation exist in publications and textbooks, many of them with misleading or even wrong prefactors. Even in some of Förster's original publications the prefactors are incorrect [27].

reaches 50%.

While Förster theory has been extremely successful in the description of energy transfer and is commonly applied to derive intermolecular distances in particular in biochemical applications [28], its validity is limited in many current investigations of comparably strongly coupled multichromophore systems [27, 29, 30].

Different aspects of its limitations, all directly or indirectly linked to the intermolecular distance, become evident already from looking at the energy transfer rate equation (2.29):

Firstly, the fluorescence spectrum of the donor molecule is used in the calculation of the overlap integral. Hence standard Förster theory can only be applied when the energy transfer occurs slower than vibrational relaxation because an equilibrated excited state is assumed. Secondly, donor and acceptor are considered transition point dipoles, an approximation that clearly breaks down when intermolecular distances approach the size of the individual molecules. In such cases, transition charge densities rather than point dipoles have to be considered in the calculation of the intermolecular coupling. In donor-acceptor dyads that are covalently bound, through-bond contributions to the interaction have to be taken into account. Moreover, it has been found that even optically dark states, that are not captured at all in the dipole approximation, can efficiently mediate energy transfer e.g. in carotenoids [31]. A similar effect is observed when the donor and acceptor molecules are coherently coupled aggregates and their distances are sufficiently small compared to intra-aggregate dimensions. Generalized Förster theory (GFT) has been developed to deal with interacting supramolecular structures. Last but not least, the solvent influence can exceed the simplified screening effect of an isotropic dielectricum that is implied in its sole contribution as homogeneous refractive index in equation (2.29): When R_{DA} is small, the baths surrounding D and A may no longer be uncorrelated and a detailed analysis of the donor, acceptor and solvent modes is needed to correctly predict the energy transfer rates.

2.5 The Fourier Transform

The Fourier transform (FT) is a linear integral transform that connects reciprocal spaces such as the position and momentum, or time and frequency domain [32]. We define the Fourier Transform from time to frequency domain of a function $f(t)$ as

$$F(\omega) = \mathrm{FT}\{f(t)\} = \frac{1}{\sqrt{2\pi}} \int_{-\infty}^{\infty} f(t) e^{+i\omega t} dt \tag{2.36}$$

and the inverse Fourier Transform, FT^{-1}, as

$$f(t) = \mathrm{FT}^{-1}\{F(\omega)\} = \frac{1}{\sqrt{2\pi}} \int_{-\infty}^{\infty} F(\omega) e^{-i\omega t} d\omega \tag{2.37}$$

Please note that other definitions exist and are commonly used. The above formulas agree e.g. with the Wolfram *Mathematica* 8.0 standard settings, but FT and FT^{-1} are reversed in LabView. While other definitions of the prefactors do not affect the results discussed in this thesis, differences in the Fourier Kernel definition have to be taken into account in the phase definitions e.g. of electric fields (the sign of the phase will change).

For a full understanding of multidimensional spectroscopy, as we will see in sections 2.6 and 2.7, the Fourier Transform is of fundamental importance. We will therefore dedicate the next section to a summary of the basic properties of a FT, which will help us to predict common properties of all 2D spectra. As profound knowledge on the discrete Fourier transform is called for when planning and evaluating a 2D experiment we will discuss it in more detail subsequently. This section closes with a theoretical treatment of the influences that experimental deficiencies, in particular random fluctuations in the time domain have on the reconstructed spectrum.

2.5.1 Properties of the Fourier Transform

For the above Fourier pair $f(t) \Longleftrightarrow F(\omega)$ the following important relations hold:

Time and frequency scaling

$$f(at) \Longleftrightarrow \frac{1}{a} F\left(\frac{\omega}{a}\right) \tag{2.38}$$

Shifts

$$f(t-t_0) \Longleftrightarrow F(\omega) e^{i\omega t_0} \tag{2.39}$$

$$F(\omega-\omega_0) \Longleftrightarrow f(t) e^{-i\omega_0 t} \tag{2.40}$$

Symmetries

$$f(t) \in \mathbb{R} \Longleftrightarrow F(\omega) = F^*(-\omega) \tag{2.41}$$

2.5.2 The Discrete Fourier Transform

So far we have treated the Fourier Transform as a continuous integral transform. However, from an experiment, we will always get a finite number of data points. Those can e.g. arise from sampling of the wavelength axis with the finite number of pixels of the CCD camera in a spectrometer, or the finite number of delay points we used for scanning the coherence time in our 2D experiments. Finding proper data intervals and ranges is then in principle up to the experimenter. We will now introduce the sampling theorem, a very general theorem from information theory, that will then help us to identify appropriate scanning intervals and ranges [32].

The Sampling Theorem

Let us start out with a continuous time-domain signal $y(t)$, that we sample at equidistant points in time with a periodic sampling function $p(t)$, with sampling period T_s. The discrete signal values we get from this procedure can then be written as

$$y_s(t) = y(t)p(t). \tag{2.42}$$

We further assume that the samples are taken instantaneously, such that $p(t)$ can be approximated by a train of δ-functions

$$p(t) = \sum_{k=-\infty}^{\infty} \delta(t - kT_s). \tag{2.43}$$

We define the sampling frequency $f_s = 1/T_s$ to be sufficiently high, when the original signal $y(t)$ can be fully represented by the set of samples $y_s(kT_s)$. This is equivalent to saying that the spectrum of the sampled signal, $Y_s(f)$, has to contain all the information present in $\mathrm{FT}\{y(t)\}$. Here we have introduced the frequency f that relates to the angular frequency ω as $\omega = 2\pi f$. Since $p(t)$ is periodic, it can be represented by a Fourier series

$$p(t) = \sum_{n=-\infty}^{\infty} C_n \mathrm{exp}(i2\pi n f_s t) \tag{2.44}$$

with Fourier coefficients C_n,

$$C_n = 1/T_s \int_{-T_s/2}^{T_s/2} p(t)\mathrm{exp}(-i2\pi n f_s t)dt = \frac{1}{T_s} = f_s \ \forall n, \tag{2.45}$$

such that we can write the Fourier Transform of the sampled signal, $Y_s(f)$, as

$$\begin{align} Y_s(f) &= \int_{-\infty}^{\infty} y(t)p(t)\mathrm{exp}(-i2\pi f t)dt \tag{2.46} \\ &= \sum_{n=-\infty}^{\infty} f_s \int_{-\infty}^{\infty} y(t)\mathrm{exp}(i2\pi n f_s t)\mathrm{exp}(-i2\pi f t)dt \tag{2.47} \\ &= \sum_{n=-\infty}^{\infty} f_s \int_{-\infty}^{\infty} y(t)\,\mathrm{exp}(-i2\pi(f - n f_s)t)dt. \tag{2.48} \end{align}$$

Comparison of (2.48) with the Fourier Transform of the continuous signal, $Y(f)$,

$$Y(f) = \int_{-\infty}^{\infty} y(t)\mathrm{exp}(-i2\pi f t)dt \tag{2.49}$$

shows, that sampling $y(t)$ with a train of δ-functions reproduces the spectrum $Y(f)$ around DC ($n = 0$) and at all harmonics of the sampling frequency f_s (cf. figure 2.4 (a)).

Knowing this, we can now define a criterion for the minimum sampling frequency f_s that allows for correct reconstruction of a spectrum $Y(f)$ with maximum frequency f_H:

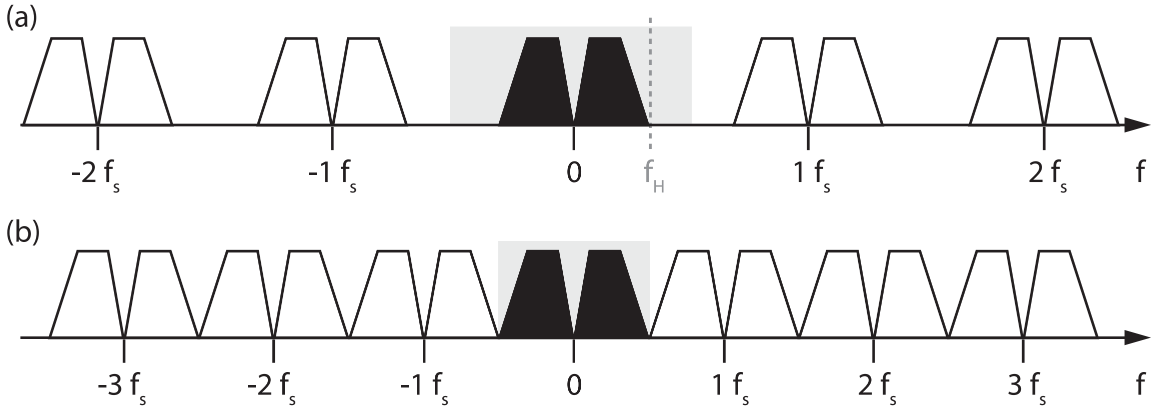

Figure 2.4: (a) Equidistant sampling of a time-domain signal results in reproduction of the original spectrum (filled graph) around DC (f=0) and all harmonics of the sampling frequency $\pm n f_s$. (b) Nyquist sampling with $f_s = f_N = 2f_H$. The frequency range that will be covered in a discrete Fourier Transform is shaded in gray.

To exclude artifacts the spectrum centered around DC ($f = 0$) must not overlap with the neighboring spectra centered around $\pm f_s$, which is fulfilled only if

$$f_s > 2f_H = f_N. \tag{2.50}$$

Equation (2.50) is often referred to as the Nyquist-Shannon-criterion and $f_N = 2f_H$ is called the Nyquist frequency (cf. figure 2.4 (b)).

For the above considerations we have only included our finite temporal resolution which led to constraints for the minimum sampling frequency for a spectrum of maximum frequency f_H. Next, we will also take into account the finite total number of points M that we get from an experiment. We define the discrete Fourier Transform $Y = \{Y_0, Y_1, \ldots Y_{M-1}\}$ of a time domain array $y = \{y_0, y_1, \ldots, y_{M-1}\}$ as

$$Y_k = \frac{1}{\sqrt{N}} \sum_{m=0}^{M-1} y_m e^{i2\pi km/M} \qquad \text{for } k = 0, \ldots, M-1. \tag{2.51}$$

Obviously, the $k = 0$ element corresponds to the DC-term, i.e. a simple sum over all elements in y, and the resolution in the frequency domain is given by

$$\Delta f = \frac{f_s}{M} = \frac{1}{T_s M}. \tag{2.52}$$

As the total time interval covered in data acquisition, $T_s M$, determines the frequency resolution Δf_s, a frequency resolution of $\Delta f_s = 1/t_d$ suffices to reveal all possible spectral features for a signal of limited duration t_d. In practice, so-called zero-padding is often applied to signals of limited duration, i.e. zero amplitude values are added to the signal array y which increases the frequency resolution. Zero-padding the array length to a power of 2 is beneficial for the computation time, because it allows the use of Fast-Fourier Transform (FFT) algorithms. Furthermore, zero-padding is often used for cosmetic reasons, as an increased frequency resolution smooths the data and leads to a "prettier" data presentation, e.g. in contour graphs. One should, however, always be aware that zero-padding means adding the information that the signal is zero outside the measurement window, which - strictly speaking- you cannot know unless you measured it (in which case you wouldn't have to zero-pad...).

The full frequency axes associated with the discrete FT span

$$\left\{0, \Delta f, 2\Delta f, \ldots, \left(\frac{M}{2}-1\right)\Delta f, \frac{M}{2}\Delta f, -\left(\frac{M}{2}-1\right)\Delta f, \ldots, -2\Delta f, -\Delta f\right\} \tag{2.53}$$

for M even and

$$\left\{0, \Delta f, 2\Delta f, \ldots, \left(\frac{M}{2}-1\right)\Delta f, \frac{M}{2}\Delta f, -\frac{M}{2}\Delta f, -\left(\frac{M}{2}-1\right)\Delta f, \ldots, -2\Delta f, -\Delta f\right\} \tag{2.54}$$

for M odd, i.e. the maximum absolute frequency value in the resulting spectrum is $\frac{M}{2}\Delta f = f_s/2$. Furthermore it is noteworthy, that if the $t = 0$ data point is not the first element of the data array y the Fourier transform Y will possess an additional linear phase that accounts for the time zero shift in y. In other words when e.g. Fourier transforming along the τ-scan covering $[-\tau_{max}, \tau_{max}]$ in a 2D- experiment proper rotation of the data array before the FT or subtraction of a linear phase $\omega\tau_{max}$ afterwards is required. In analogy to equation (2.51) we define the inverse Fourier transform from the frequency to the time domain as

$$y_m = \frac{1}{\sqrt{M}} \sum_{k=0}^{M-1} Y_k \mathrm{e}^{-\mathrm{i}2\pi km/M} \qquad \text{for } m = 0, \ldots, M-1. \tag{2.55}$$

Undersampling

For signals with limited bandwidth $B = f_H - f_L$, i.e. signals that cover only a limited spectral range $f_L \leq f \leq f_H$, sampling at certain frequencies lower than f_N still allows for the full spectrum to be recovered. This follows immediately from the fact that in this case $n_{max} = \lfloor \frac{f_H}{B} \rfloor$ non-overlapping copies of our original spectrum fit into the frequency interval $[0, f_H]$. All we are left to do with now is to identify the appropriate sampling frequency ranges $[f_{s,min}(n), f_{s,max}(n)]$ for a given $n \leq n_{max}$.

To deduce these ranges it is helpful to look at the example depicted in figure 2.5 (a)-(c). The same time domain signal corresponding to triangular spectrum of limited bandwidth $B = f_H - f_L = 1$ and maximum frequency $f_H = 4.5$ is assumed for these three graphs. Panels (a)-(c) correspond to different sampling frequencies f_s and the subset of the frequency axis reconstructed from a discrete FT for each value of f_s is shaded in gray in each case. Spectra corresponding to positive (solid) and negative (dashed) multiples of the sampling frequency f_s are depicted in the same color. Figure 2.5 (a) shows the Nyquist-sampled situation, i.e. $f_s = f_N = 2f_H$. As $n_{max} = \lfloor \frac{4.5}{1} \rfloor = 4$ we can fit four non-overlapping copies in the frequency interval $[0, f_H]$ in our example. This can be achieved by applying sampling frequencies that obey

$$\frac{2f_H}{n} \leq f_s \leq \frac{2f_L}{n-1} \tag{2.56}$$

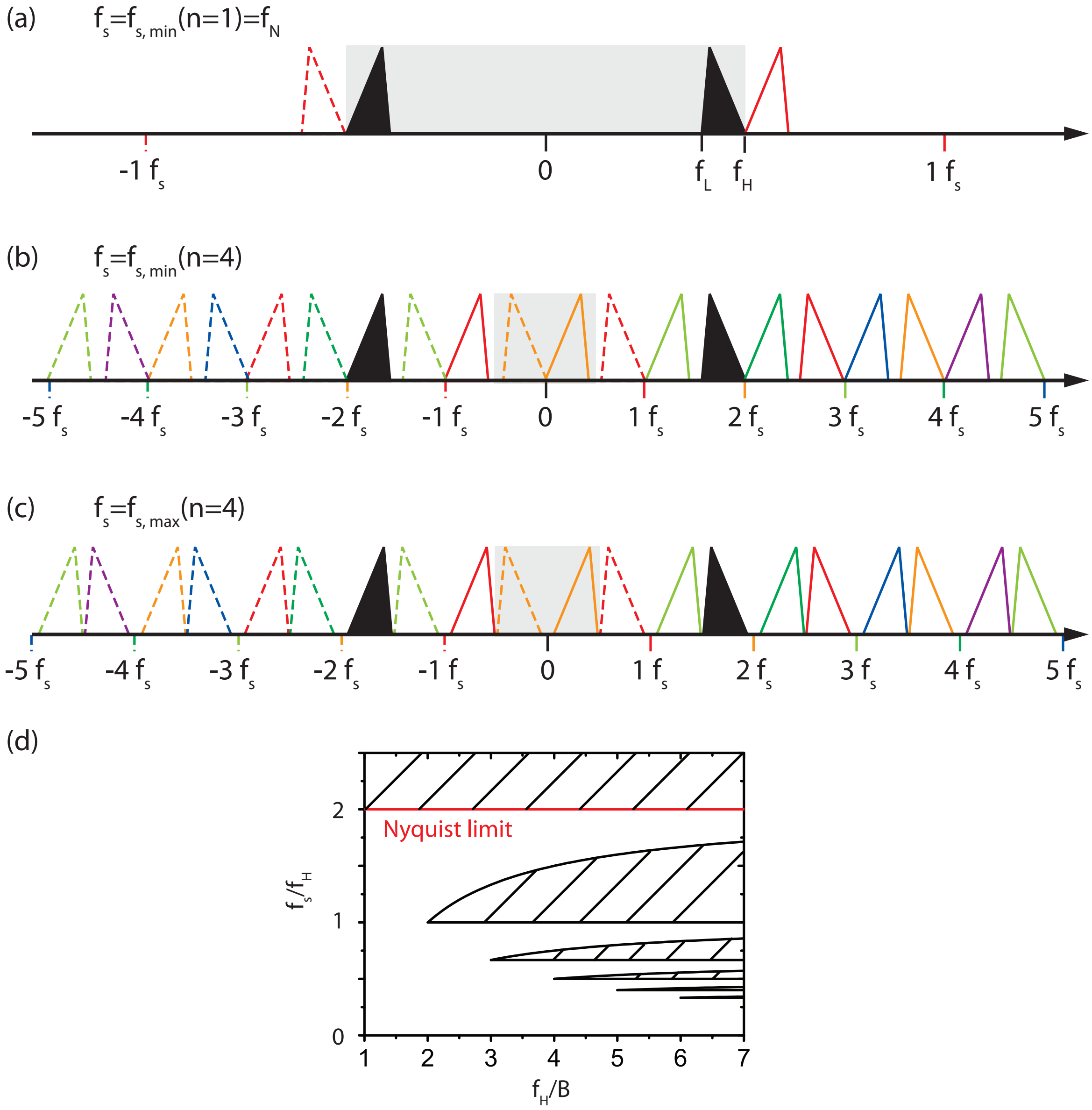

Figure 2.5: (a)-(c)Illustration of undersampling. Individual panels correspond to different sampling frequencies of $f_s = f_N$(a), $f_s = f_{s,\mathrm{min}}(n = 4)$(b) and $f_s = f_{s,\mathrm{max}}(n = 4)$ (c), and the spectral range recovered from a discrete FT is shaded in gray. Spectra corresponding to positive (solid) and negative (dashed) multiples of the sampling frequency f_s are drawn in the same color. The frequency range covered in the discrete FT is shaded in gray. See text for further explanations. (d) Allowed sampling frequencies (dashed areas) in units of the maximum frequency f_H as a function of the ratio of maximum frequency and spectral bandwidth, $\frac{f_H}{B}$.

as illustrated in 2.5 (b) for the case $f_s = \frac{2f_H}{n} = f_{s,\mathrm{min}}(n=4) = \frac{2\times4.5}{4} = 2.25$ and 2.5 (c) for the case$f_s = \frac{2f_L}{n-1} = f_{s,\mathrm{max}}(n=4) = \frac{2\times3.5}{3} = 2.\overline{3}$. The condition for the lower frequency bound can be derived from comparison of the DC-spectrum (black) and the spectrum corresponding to $nf_s = 4f_s$ (dark green) in figure 2.5 (b):

$$f_H \leq nf_s - f_H \Longleftrightarrow \frac{2f_H}{n} \leq f_s. \tag{2.57}$$

Similarly, the DC and the $(n-1)f_s = 3f_s$ spectrum (light green) of fig.2.5 (c) yield

$$(n-1)f_s - f_L < f_L \Longleftrightarrow f_s \leq \frac{2f_L}{n-1} \tag{2.58}$$

for the upper frequency limit for a given n. While the shape of the spectrum is maintained as long as frequencies fulfilling equation (2.56) are chosen, the frequency axis has to be adjusted to cover the appropriate range. A convenient way to do this is explained in section 3.3.2. Finally, figure 2.5 (d) shows the allowed sampling frequencies (dashed areas) in units of the maximum frequency f_H as a function of the ratio of maximum frequency and spectral bandwidth, $\frac{f_H}{B}$.

Influence of Experimental Deficiencies

When it comes to experimental data, the aforementioned conclusions can only be considered the “noise-free” limit, and it is important to familiarize oneself with the limitations that imperfections of the experiment impose on the significance of the acquired data. Two types of error sources have to be distinguished when recording a signal $y_s(t)$: fluctuations in the amplitude, i.e. in the y_s-direction, and inaccuracies in the time axis t. While the former – if random – will average out for a large enough number of data points N to reveal the actual $y_s(t)$, the latter – even if random – will lead to a systematic deviation from $y_s(t)$ even for $N \to \infty$ except for the very special case of a linear time-dependence of $y_s(t)$.

The distortion in the spectral domain as a result of random mis-timings $t \to t + \Delta t_i$ during sampling the time-domain signal depends on the quality of the timing noise, i.e. the probability distribution $\mathrm{P}(\Delta t_i)$. Here, we will only have a closer look at the special case of Gaussian timing noise, i.e.

$$P(\Delta t_i) = \frac{1}{\sqrt{2\pi}\sigma} \mathrm{e}^{-\frac{1}{2}\left(\frac{\Delta t_i}{\sigma_t}\right)^2} \tag{2.59}$$

with standard deviation σ_t. In this case, it can be mathematically shown that in the limit of large N the reconstructed absolute value of the spectrum $|Y(f,\sigma_t)|$ follows

$$\frac{|Y(f,\sigma_t)|}{|Y(f,\sigma_t = 0)|} = \mathrm{e}^{-\frac{1}{2}(\sigma_t 2\pi f)^2}, \tag{2.60}$$

i.e. the spectral amplitude decrease originating from Gaussian timing fluctuations with standard deviation σ_t can again be described by a Gaussian, and $\sigma_t f = \frac{\sigma_t}{T}$ is the quantity determining the quality of the reconstruction. To illustrate this the results of a numerical

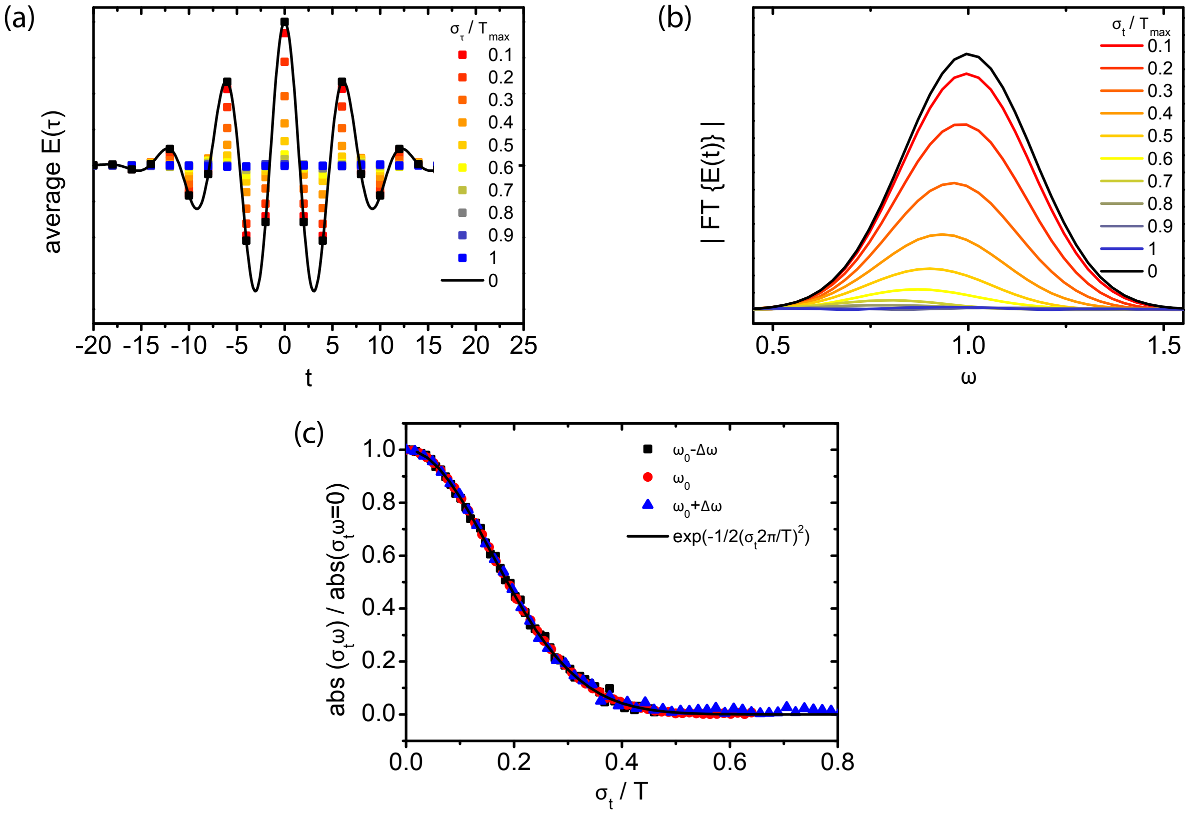

Figure 2.6: Influence of timing noise on the reconstructed spectrum. Average time domain field (a) and corresponding spectrum (b) for different values of $\frac{\sigma_t}{T}$ obtained from averaging 2000 realizations. The decrease in the reconstructed amplitude can be described by a Gaussian $\mathrm{e}^{-\frac{1}{2}(\sigma_t 2\pi f)^2}$ (c).

simulation are shown in figure 2.6. Here, the Gaussian time domain field of a $\tau_p = 10$ fs transform limited laser pulse

$$y(t) = E(t) = \mathrm{e}^{-\frac{2\ln 2 t^2}{\tau_p^2}} \cos(\omega_0 t) \tag{2.61}$$

with center frequency $\omega_0 = 1\ \frac{\mathrm{rad}}{\mathrm{fs}}$ has been sampled in 2 fs steps for -100 fs$\leq t \leq 100$ fs, and this time axis was subject to random fluctuations according to equation (2.59) for different values of σ_t. As equation (2.60) holds only in the limit of large N, 2000 realizations have been averaged for each value of σ_t. From figure 2.6 we see that with decreasing timing precision (increasing σ_t), the oscillations in the time domain signal are averaged out (cf. figure 2.6 (a)), resulting in a decrease of reconstructed spectral intensity (cf. figure 2.6 (b)). For any fixed value of σ_t, the effect is larger on the high frequency side, where the oscillation periods T are shorter. As one would intuitively expect, for each frequency ω, the reconstructed spectral intensity is virtually zero when $\frac{\sigma_t}{T} \geq 0.5$ (cf. figure 2.6 (c)), i.e. when the timing accuracy is smaller than half the corresponding oscillation period such that the time domain signal averages to zero in the limit of large N.

2.6 Heterodyne Detection via Spectral Interference

To characterize the weak signal field in $\chi^{(3)}$-experiments such as 2D spectroscopy, a highly sensitive detection technique is required. A common method of choice is spectral interferometry [33]. In this heterodyne detection scheme the signal field E_s, $E_s(\omega) = A_s(\omega)\mathrm{e}^{i\omega t_s}$, is superimposed with a completely known, time-delayed reference field E_r, $E_r(\omega) = A_r(\omega)\mathrm{e}^{i\omega t_r}$, and the interference of both laser pulses in the spectral domain is recorded with a spectrometer. The detected intensity $I_{\mathrm{SI}}(\omega)$ reads

$$\begin{aligned} I_{\mathrm{SI}}(\omega) &= |E_s(\omega) + E_r(\omega)|^2 && (2.62)\\ &= E_s(\omega)E_s^*(\omega) + E_r(\omega)E_r^*(\omega) + E_s(\omega)E_r(\omega)^* + E_r(\omega)E_s^*(\omega) && (2.63)\\ &= I_s(\omega) + I_r(\omega) + A_s(\omega)A_r(\omega)^*\mathrm{e}^{\mathrm{i}\omega(t_s-t_r)} + A_r(\omega)A_s(\omega)^*\mathrm{e}^{-\mathrm{i}\omega(t_s-t_r)} && (2.64) \end{aligned}$$

where we have used $I_i(\omega) = E_i(\omega)E_i(\omega)^*$. To isolate the complex signal field $A_s(\omega)$ from the above expression, we will now first Fourier transform equation (2.62), apply an appropriate filter in the time-domain, and transform the filtered-expression back. The (inverse) Fourier transform of (2.62), consists of three summands

$$\begin{aligned} \mathrm{FT}^{-1}\{I_{\mathrm{SI}}(\omega)\} &= \mathrm{FT}^{-1}\{I_s(\omega) + I_r(\omega)\}+ \\ &+ \mathrm{FT}^{-1}\{A_s(\omega)A_r(\omega)^*\mathrm{e}^{\mathrm{i}\omega(t_s-t_r)}\} + \mathrm{FT}^{-1}\{A_r(\omega)A_s(\omega)^*\mathrm{e}^{-\mathrm{i}\omega(t_s-t_r)}\}. \end{aligned} \tag{2.65}$$

The first summand is non-oscillatory and therefore corresponds to a peak at $t = 0$. Remembering the Fourier transform of the delta function

$$\delta(t - t_0) = \frac{1}{\sqrt{2\pi}} \int_{-\infty}^{+\infty} \mathrm{e}^{-\mathrm{i}\omega(t-t_0)} d\omega = \mathrm{FT}^{-1}\{\mathrm{e}^{\mathrm{i}\omega t_0}\} \tag{2.66}$$

we can immediately see that the second and third summand, that contain the signal information we are interested in, peak at $t = t_s - t_r$ and $t = -(t_s - t_r)$, respectively, in the time domain. This means for a temporal separation $|t_s - t_r|$ larger than the temporal width of the individual peaks we can separate these three contributions. If we now assume that $t_r > t_s$ (which was the case for all 2D measurements presented in the following chapters) and cut out the peak at $t < 0$ with a rectangular filter, transforming the filtered part back to the spectral domain yields

$$A_s(\omega)A_r(\omega)^*\mathrm{e}^{\mathrm{i}\omega(t_s-t_r)}. \tag{2.67}$$

Rewriting the complex amplitudes $A_i(\omega) = \tilde{A}_i(\omega)\mathrm{e}^{\mathrm{i}\phi_i(\omega)}$ as a product of the real valued amplitude $\tilde{A}_i(\omega)$ and a dispersive phase term $\mathrm{e}^{\mathrm{i}\phi_i(\omega)}$ we get

$$\tilde{A}_s(\omega)\tilde{A}_r(\omega)\mathrm{e}^{\mathrm{i}\omega(t_s-t_r)}\mathrm{e}^{\mathrm{i}(\phi_s(\omega)-\phi_r(\omega))}. \tag{2.68}$$

Dividing the absolute value of expression (2.68) by the square root of the known reference intensity $\tilde{A}_r(\omega) = \sqrt{I_r(\omega)}$, and adding the known full reference phase $\Phi_r = \omega t_r + \phi_r(\omega)$ to its phase we retrieve the signal amplitude $\tilde{A}_s(\omega)$ and phase $\Phi_s = \omega t_s + \phi_s(\omega)$ relative to an arbitrary time zero.

2.7 Theoretical Description of Spectroscopy Experiments

In many spectroscopic techniques light, i.e. an external electromagnetic field, polarizes matter and the light field emitted from the sample as a result of the induced polarization $P(\vec{r},t)$ is detected. Hence, to understand a spectroscopy experiment we have to establish the connection between the microscopic properties and dynamics of a quantum mechanical system and this light-induced polarization $P(\vec{r},t)$.

To this end, we will first recall the relationship between electric fields and polarization in matter, before introducing a quantum mechanical description of $P(\vec{r},t)$ based on the density operator. In a perturbation theory approach, we will expand the density operator in powers of the electric field resulting in the response function formalism. In a short illustration of the simplest case, the linear response function, we will encounter the concept of lineshape functions as an intuitive way and powerful means to include interaction with the surrounding bath. Afterwards, we will turn to time-resolved experiments, i.e. the third-order polarization. Here, we will see that by systematically varying a sequence of three excitation pulses 2D spectroscopy measures the complete third-order response function, while the information content of transient absorption with its two pulses is limited.

2.7.1 Nonlinear Polarization

When a laser pulse interacts with matter its electric field causes a polarization of the material that can be split into linear and non linear contributions [34]

$$P = P^{(1)} + P_{\mathrm{NL}} = P^{(1)} + P^{(2)} + P^{(3)} + \dots \quad . \tag{2.69}$$

Maxwell's equations require that – in the case of transverse electric fields ($\nabla E = 0$)– this polarization is in turn associated with an electric (signal) field via

$$\nabla^2 E(\vec{r},t) - \frac{1}{c^2}\frac{\partial^2}{\partial t^2}E(\vec{r},t) = \frac{4\pi}{c^2}\frac{\partial^2}{\partial t^2}P(\vec{r},t) \tag{2.70}$$

that contains information on the material properties and makes them accessible to the observer. All quantities of spectroscopic interest, electronic and nuclear degrees of freedom as well as their relaxation dynamics manifest themselves in the polarization and its time dependence and transfer to the signal field. As we are dealing with a quantum mechanical system, the relevant observable is, however, the expectation value of this polarization,

$$\langle P(\vec{r},t)\rangle = \mathrm{Tr}\left[V\rho(t)\right], \tag{2.71}$$

i.e. the trace over the interaction operator V and the density matrix $\rho(t)$.

2.7.2 The Response Function Formalism

To mathematically describe a spectroscopy experiment, i.e. to calculate the polarization, we have to know the dynamics of the density matrix of our quantum mechanical system that results from the interaction with an external electric field. In other words, we have to solve the Liouville-van Neumann equation [34]

$$\dot{\rho} = -\frac{\mathrm{i}}{\hbar}\left[H,\rho\right] = -\frac{\mathrm{i}}{\hbar}\left[H_0,\rho\right] - \frac{\mathrm{i}}{\hbar}\left[H_{\mathrm{int}}(t),\rho\right] \tag{2.72}$$

the mixed-state equivalent to the Schrödinger equation, for a Hamiltonian H that contains an external field $E(\vec{r},t)$

$$H = H_0 + H_{\mathrm{int}}(t) = H_0 - E(\vec{r},t)V. \tag{2.73}$$

To solve equation (2.72) it is helpful to switch to Liouville space notation. Liouville space is isomorphic to Hilbert space yet treats the density matrix as a vector, which greatly simplifies the following discussion. Equation (2.72) then reads

$$\dot{\rho} = -\frac{\mathrm{i}}{\hbar}\mathbf{L}\rho - \mathbf{L}_{\mathrm{int}}(t)\rho \tag{2.74}$$

Next, we expand $\rho(t)$ in powers of the electric field, i.e. in the number of interactions with this field

$$\rho(t) = \rho^{(0)}(t) + \rho^{(1)}(t) + \rho^{(2)}(t) + \dots \quad . \tag{2.75}$$

The n-th order term of the formal solution of equation (2.74) can be written as [34]

$$\begin{aligned}\rho^{(n)}(t) = \left(-\frac{\mathrm{i}}{\hbar}\right)^n \int\limits_{t_0}^{t} \mathrm{d}\tau_n \int\limits_{t_0}^{\tau_n} \mathrm{d}\tau_{n-1} \dots \int\limits_{t_0}^{\tau_2} \mathrm{d}\tau_1 \\ \times\mathbf{G}(t-\tau_n)\mathbf{L}_{\mathrm{int}}(\tau_n)\mathbf{G}(\tau_n-\tau_{n-1})\mathbf{L}_{\mathrm{int}}(\tau_{n_1})\cdots\mathbf{G}(\tau_2-\tau_1)\mathbf{L}_{\mathrm{int}}(\tau_1)\mathbf{G}(\tau_1-t_0)\rho(t_0)\end{aligned} \tag{2.76}$$

Here, we have introduced the interaction times τ_i, $t \geq \tau_n \geq \tau_{n-1} \cdots \geq \tau_1 \geq t_0$, as well as the Green's function of the quantum mechanical system in the absence of an external field in Liouville space $\mathbf{G}(t)$,

$$\mathbf{G}(t) \equiv \theta(t)\mathrm{e}^{-\frac{\mathrm{i}}{\hbar}\mathbf{L}t}. \tag{2.77}$$

To interpret equation (2.76) we will read it from right to left, starting out with a system in thermal equilibrium $\rho(t_0)$ at $t = t_0$ (cf. figure 2.7). Up to the first interaction time τ_1 the system evolves according to $\mathbf{G}(\tau_1 - t_0)$. For a system like ours that is initially already in thermal equilibrium nothing changes of course,

$$\mathbf{G}(\tau_1 - t_0)\rho(t_0) = \rho(t_0). \tag{2.78}$$

At $t = \tau_1$, $\mathbf{L}_{\mathrm{int}}(\boldsymbol{\tau_1})$ perturbs the system, i.e. the first interaction takes place. Subsequently, the dynamics of the density operator is again governed by the Liouville Operator of the unperturbed system $\mathbf{L}$ until the next interaction $\mathbf{L}_{\mathrm{int}}(\tau_2)$. This sequence proceeds until the n-th interaction, followed by free evolution of the unperturbed system until t. To include the dependence on the external electric field explicitly, we now use

$$\mathbf{L}_{\mathrm{int}}(\tau_2) = -E(t)\mathbf{V} \tag{2.79}$$

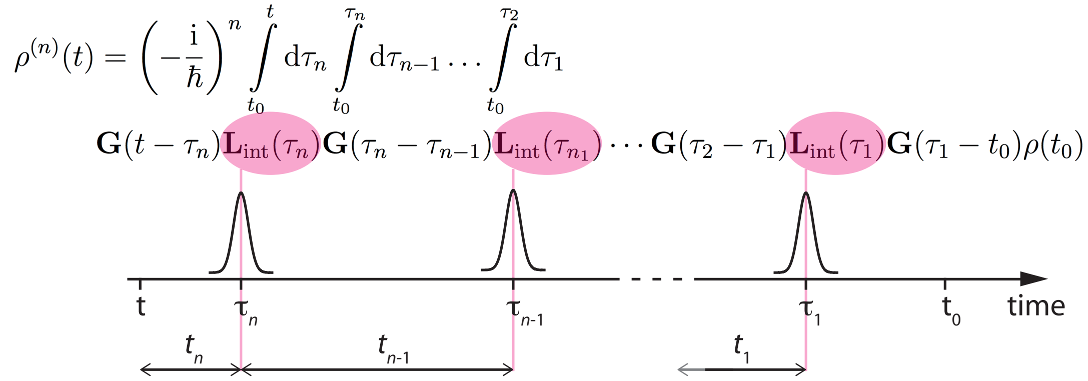

$$\rho^{(n)}(t) = \left(-\frac{\mathrm{i}}{\hbar}\right)^n \int\limits_{t_0}^{t} \mathrm{d}\tau_n \int\limits_{t_0}^{\tau_n} \mathrm{d}\tau_{n-1} \ldots \int\limits_{t_0}^{\tau_2} \mathrm{d}\tau_1$$

$$\mathbf{G}(t-\tau_n)\mathbf{L}_{\mathrm{int}}(\tau_n)\mathbf{G}(\tau_n-\tau_{n-1})\mathbf{L}_{\mathrm{int}}(\tau_{n_1})\cdots\mathbf{G}(\tau_2-\tau_1)\mathbf{L}_{\mathrm{int}}(\tau_1)\mathbf{G}(\tau_1-t_0)\rho(t_0)$$

Figure 2.7: Illustration of equation (2.76) and definition of time variables.

where $\mathbf{V}$ is the time-independent interaction operator in Liouville space. Besides, we will change our time variables from the interaction time τ_j to intervals t_j

$$t_1 \equiv \tau_2 - \tau_1, t_2 \equiv \tau_3 - \tau_2, \ldots t_n \equiv t - \tau_n \tag{2.80}$$

between the individual interactions, and make the transition $t_0 \to -\infty$. This yields

$$\begin{aligned} \rho^n(t) = \left(\frac{\mathrm{i}}{\hbar}\right)^n \int\limits_0^\infty \mathrm{d}t_n \int\limits_0^\infty \mathrm{d}t_{n-1} \ldots \int\limits_0^\infty \mathrm{d}t_1\, \mathbf{G}(t_n)\mathbf{V}\mathbf{G}(t_{n-1})\mathbf{V}\ldots\mathbf{G}(t_1)\mathbf{V}\rho(-\infty) \\ \times E(\vec{r}, t-t_n)E(\vec{r}, t-t_n-t_{n-1})\cdots E(\vec{r}, t-t_n-t_{n-1}\cdots-t_1) \end{aligned} \tag{2.81}$$

Switching to the interaction picture, $\mathbf{V}$ becomes time-dependent

$$\mathbf{V}(t) \equiv \mathrm{e}^{\frac{\mathrm{i}}{\hbar}\mathbf{L}t}\mathbf{V}\mathrm{e}^{-\frac{\mathrm{i}}{\hbar}\mathbf{L}t} \tag{2.82}$$

and the density operator term in n-th order of the electric field reads

$$\begin{aligned} \rho^{(n)}(t) = \left(\frac{\mathrm{i}}{\hbar}\right)^n \int\limits_0^\infty \mathrm{d}t_n \int\limits_0^\infty \mathrm{d}t_{n-1} \ldots \int\limits_0^\infty \mathrm{d}t_1 \\ \times \mathbf{G}(t_n + t_{n-1} + \cdots + t_1)\mathbf{V}(t_{n-1} + \cdots + t_1)\ldots\mathbf{V}(t_1)\mathbf{V}(0)\rho(-\infty) \\ \times E(\vec{r}, t-t_n)E(\vec{r}, t-t_n-t_{n-1})\ldots E(\vec{r}, t-t_n-t_{n-1}-\cdots-t_1) \end{aligned} \tag{2.83}$$

Coming back to our original aim, calculating the expectation value of the polarization,

$$\langle P(\vec{r}, t)\rangle = \mathrm{Tr}\{V\rho(t)\} = \langle\langle V \mid \rho\rangle\rangle, \tag{2.84}$$

we can now use the above results to write the nth-order polarization

$$\begin{aligned} P^{(n)}(\vec{r}, t) =& \langle\langle V \mid \rho^{(n)}\rangle\rangle = \int\limits_0^\infty \mathrm{d}t_n \int\limits_0^\infty \mathrm{d}t_{n-1} \ldots \int\limits_0^\infty \mathrm{d}t_1 S^{(n)}(t_n, t_{n-1}, \ldots, t_1) \\ & \times E(\vec{r}, t-t_n)E(\vec{r}, t-t_n-t_{n-1})\ldots E(\vec{r}, t-t_n-t_{n-1}-\cdots-t_1). \end{aligned} \tag{2.85}$$

Here, we have introduced the n-th order response function $S^n(t_n, t_{n-1}, \ldots, t_1)$

$$S^{(n)}(t_n, t_{n-1}, \ldots, t_1) \equiv \left(\frac{\mathrm{i}}{\hbar}\right)^n \langle\langle V \,| G(t_n) \mathbf{V} \mathbf{G}(t_{n-1}) \mathbf{V} \ldots \mathbf{G}(t_1) \mathbf{V} |\, \rho(-\infty) \rangle\rangle \tag{2.86}$$

Notably, it contains the complete microscopic information about our quantum mechanical system as it includes the full time evolution of the density operator for given interaction conditions. From equation (2.85) we recognize the priceless advantage of the response function formalism: It lies in the separation of the quantum mechanically treated system dynamics ($S^{(n)}$) and the classically treated external electric field. Notably, the time-domain response function $S(t_n, \ldots, t_1)$ is a real quantity because both, the polarization $P(t)$ as well as the external electric field $E(t)$ are observables and hence $\in \mathbb{R}$.

To get from equation 2.86 back to a Hilbert space representation of the n-th order response function, we use the operator identity $\mathbf{V}A = [V, A] = VA - AV$ as well as the cyclic invariance of the trace operation and derive [34]

$$\begin{aligned} S^{(n)} = {} & \left(\frac{\mathrm{i}}{\hbar}\right)^n \theta(t_n) \ldots \theta(t_1) \\ & \times \mathrm{Tr}\{V(t_1 + \cdots + t_n)[V(t_1 + \cdots + t_{n-1}, [V(t_1 + \cdots + t_{n-1}), [\ldots, [V(t_1), [V(0), \rho_0]]]]]])\}. \end{aligned} \tag{2.87}$$

2.7.3 Linear Response and Lineshape Functions

Before we turn to a more detailed description of the third order polarization and time-resolved experiments we will have a closer look at the linear response function $S^{(1)}$.

Introducing the so-called Liouville pathway $J(t_1)$

$$J(t_1) = \mathrm{Tr}[V(t_1)V(0)\rho(-\infty)] \tag{2.88}$$

we can write the linear response as

$$S^{(1)}(t_1) = \frac{\mathrm{i}}{\hbar}\theta(t_1)(J(t_1) - J^*(t_1)). \tag{2.89}$$

For an isolated electronic two-level system with transition dipole moment μ, i.e.

$$V = \begin{pmatrix} 0 & \mu \\ \mu & 0 \end{pmatrix} \tag{2.90}$$

we can easily calculate the linear response from its time-dependent interaction operator $V(t)$

$$V(t) = U_0^\dagger(t) V U_0(t) \tag{2.91}$$

with the time evolution operator $U_0(t)$

$$U_0(t) = \begin{pmatrix} \mathrm{e}^{-\frac{\mathrm{i}}{\hbar}H_g t} & 0 \\ 0 & \mathrm{e}^{-\frac{\mathrm{i}}{\hbar}H_e t} \end{pmatrix}. \tag{2.92}$$

We retrieve

$$J(t) = |\mu|^2 \, \mathrm{e}^{-\mathrm{i}\omega_{eg} t_1} \tag{2.93}$$

and

$$S^{(1)}(t_1) = -\frac{1}{\hbar} |\mu|^2 \sin(\omega_{eg} t), \tag{2.94}$$

respectively, where we have introduced the transition frequency $\omega_{eg}{=}\frac{1}{\hbar}(E_e - E_g)$. Little to our surprise the response function oscillates at the transition frequency of our two-level system. This is nothing but the time-domain manifestation of the fact that the system's linear absorption, more precisely its linear susceptibility, the Fourier Transform of $S^{(1)}(t)$, comprises two δ-peaks at $\pm\omega_{eg}$. The concept of negative frequencies may seem awkward, yet it is an immediate consequence of $S^{(1)}(t) \in \mathbb{R}$.

For more realistic systems we have to take into account nuclear degrees of freedom in our Hamiltonian and calculating the trace in equation (2.88) becomes much more involved. Thorough treatment [34] yields an additional term in the Lioville pathway $J(t)$ that contains the so-called lineshape function $g(t)$:

$$J(t) = |\mu|^2 \, \mathrm{e}^{-\mathrm{i}\omega_{eg} t} \mathrm{e}^{-g(t)}. \tag{2.95}$$

The lineshape function $g(t)$ is in fact an integral over the frequency-frequency correlation function $C(t)$

$$C(t) = \langle \delta\omega(t) \delta\omega(0) \rangle \tag{2.96}$$

$$g(t) = \int_0^t \mathrm{d}\tau \int_0^\tau \mathrm{d}t' C(t') \tag{2.97}$$

For the limiting case of a purely inhomogeneously broadened system, i.e. when we have an ensemble of molecules with a *static* distribution of transition frequencies, C(t) is constant. Consequently, $g(t) \propto t^2$ and we have a Gaussian damping of our oscillatory response function leading to a Gaussian absorption line profile in the Fourier Transform of $S^{(1)}$, which explains the nomenclature. In contrast, in a purely homogeneously broadened system the transition frequency changes over time, e.g. as a result of changes in the charge distribution in the local environment of the chromophore, and e.g. $g(t) = \Gamma t - \mathrm{i}\lambda t$, in which case the absorption line shape will be a Lorentzian.

2.7.4 Time-Resolved Experiments – $\mathbf{P^{(3)}(\tilde{r}, t)}$ and $\mathbf{S^{(3)}(t_3, t_2, t_1)}$

With $P^{(2)}(\vec{r}, t)$ (as well as all higher even orders of $P(\vec{r}, t)$) vanishing in isotropic media for symmetry reasons [34], the lowest order polarization relevant for our time-resolved, i.e. multi-pulse experiments is $P^{(3)}(\vec{r}, t)$:

$$\begin{aligned} P^{(3)}(\vec{r}, t) = & \int_0^\infty \mathrm{d}t_3 \int_0^\infty \mathrm{d}t_2 \ldots \int_0^\infty \mathrm{d}t_1 S^{(3)}(t_3, t_2, t_1) \\ & \times E(\vec{r}, t - t_3) E(\vec{r}, t - t_3 - t_2) E(\vec{r}, t - t_3 - t_2 - t_1). \end{aligned} \tag{2.98}$$

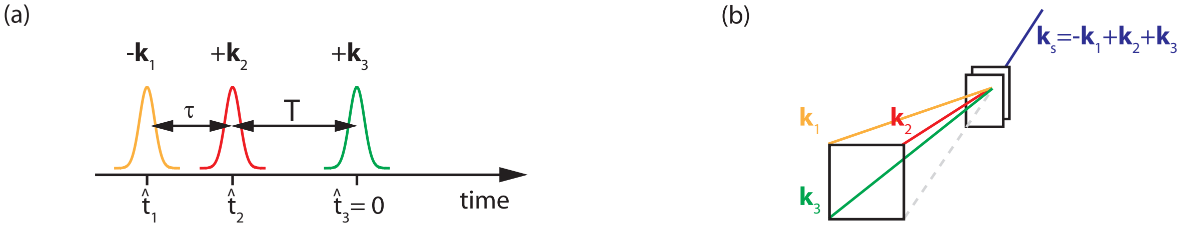

Figure 2.8: (a) Definition of time variables. (b) Box geometry.

The basic idea of a 2D experiment is the following: Via a systematic variation of the interaction times $t - t_3$, $t - t_3 - t_2$, and $t - t_3 - t_2 - t_1$ we can capture the entire time dependence of $P^{(3)}$, thus obtaining the complete microscopic information about the system that is inclosed in $\rho^{(3)}$. Full resolution of the system dynamics corresponding to a measurement of the neat third-order response function is of course only possible for δ-function excitation pulses. In reality, we are dealing with laser pulses of finite duration and the timings under experimental control are only the pulse arrival times, i.e. we can only restrict the interaction times to the pulse envelopes.

The excitation field for a 2D experiment is comprised of a sequence of three ideally identical pulses [35] with complex amplitudes $A(t) = \tilde{A}(t)\mathrm{e}^{-\mathrm{i}\phi(t)}$ centered at ,$\hat{t}_1$, $\hat{t}_2$, and, $\hat{t}_3$ in time, and with center frequency ω_0

$$E(t) = A(t-\hat{t}_1)\mathrm{e}^{-\mathrm{i}\omega_0(t-\hat{t}_1)+\mathrm{i}\vec{k}_1\vec{r}} + A(t-\hat{t}_2)\mathrm{e}^{-\mathrm{i}\omega_0(t-\hat{t}_2)+\mathrm{i}\vec{k}_2\vec{r}} + A(t-\hat{t}_3)\mathrm{e}^{-\mathrm{i}\omega_0(t-\hat{t}_3)+\mathrm{i}\vec{k}_3\vec{r}} + \mathrm{c.c.}. \tag{2.99}$$

For the following derivation we choose the arrival time of the third pulse as our time zero, $\hat{t}_3 = 0$. Further we introduce the time interval $\tau = \hat{t}_2 - \hat{t}_1$, the so-called coherence time, and the population time T as the difference between the second and third pulse, $T = -\hat{t}_2$ for the pulse order shown in figure 2.8 (a). Substituting equation (2.99) in equation (2.98) yields $6 \times 6 \times 6 = 216$ terms as each field in the multiplication $E(\vec{r}, t-t_3)E(\vec{r}, t-t_3-t_2)E(\vec{r}, t-t_3-t_2-t_1)$ comprises 6 summands. Each term consists of three amplitude function $A(t)$ or $A^*(t)$ and the respective phase factors that determine its direction $\vec{k}$, and frequency ω. So far, the polarization still contains contributions that arise from multiple interaction with the same pulse. For these contributions the interaction times are not under experimental control, i.e. they will shadow the 2D signal that we are actually looking for. One way to experimentally isolate those contributions to the polarization that arise from exactly one interaction with each of the three excitation pulses is to use a box geometry arrangement of the excitation beams [35] and detect the signal field emitted in the phasematching direction $\vec{k}_s = -\vec{k}_1 + \vec{k}_2 + \vec{k}_3$ (figure 2.8 (b)). This corresponds to selecting 6 out of the 216 terms contributing to the polarization. All six terms share a common phase factor

$$\mathrm{e}^{-\mathrm{i}\omega_0(t+\hat{t}_1-\hat{t}_2-\hat{t}_3)} = \mathrm{e}^{-\mathrm{i}\omega_0 t+\mathrm{i}\omega_0\tau} \tag{2.100}$$

that is independent of the integration variables t_i. In addition, each term contains one of the following phase factors

$$\mathrm{e}^{-\mathrm{i}\omega_0(t_1-t_3)} \tag{2.101}$$

$$\mathrm{e}^{\mathrm{i}\omega_0(t_1+t_3)} \tag{2.102}$$

$$\mathrm{e}^{\mathrm{i}\omega_0(t_3+2t_2+t_1)}, \tag{2.103}$$

and we will group them accordingly. Finally, we will apply the rotating wave approximation and consider only slowly oscillating terms in the calculation of $P^{(3)}$. This yields [35, 36]

$$\begin{aligned} P^{(3)}(\tau,T,t) = {} & \mathrm{e}^{-\mathrm{i}\omega_0 t+\mathrm{i}\omega_0\tau} \int_0^\infty \mathrm{d}t_3 \int_0^\infty \mathrm{d}t_2 \ldots \int_0^\infty \mathrm{d}t_1 \\ \times\{ & S^{(3)}_{\text{R, RWA}}(t_3,t_2,t_1)\mathrm{e}^{\mathrm{i}\omega_0(t_3-t_1)} \big[A^*(t-\hat{t}_1-t_3-t_2-t_1)A(t-\hat{t}_2-t_3-t_2)A(t-\hat{t}_3-t_3) \\ & \qquad +A^*(t-\hat{t}_1-t_3-t_2-t_1)A(t-\hat{t}_3-t_3-t_2)A(t-\hat{t}_2-t_3)\big] \\ + & S^{(3)}_{\text{NR, RWA}}(t_3,t_2,t_1)\mathrm{e}^{\mathrm{i}\omega_0(t_3+t_1)} \big[A(t-\hat{t}_2-t_3-t_2-t_1)A*(t-\hat{t}_1-t_3-t_2)A(t-\hat{t}_2-t_3) \\ & \qquad +A^*(t-\hat{t}_1-t_3-t_2-t_1)A(t-\hat{t}_3-t_3-t_2)A(t-\hat{t}_2-t_3)\big] \\ + & S^{(3)}_{\text{DC, RWA}}(t_3,t_2,t_1)\mathrm{e}^{\mathrm{i}\omega_0(t_1+2t_2+t_3)} \big[A(t-\hat{t}_2-t_3-t_2-t_1)A(t-\hat{t}_3-t_3-t_2)A(t-\hat{t}_1-t_3) \\ & \qquad +A(t-\hat{t}_3-t_3-t_2-t_1)A(t-\hat{t}_2-t_3-t_2)A^*(t-\hat{t}_1-t_3)\big]\} \end{aligned} \tag{2.104}$$

Here, we have defined response functions $S_{i,\text{RWA}}$ that correspond to sums over rephasing (R), non-rephasing (NR), and double-coherence (DC) Liouville pathways. Rephasing Liouville pathways share a common phase factor $\mathrm{e}^{-\mathrm{i}\omega_{eg}(t_1-t_3)}$, i.e. the phase acquired during t_1 is the complex conjugate of the phase acquired during t_3. As this requires a first interaction with negative $\vec{k}$, rephasing terms contribute only for $\tau > 0$. Rephasing contributions lead to the emission of a photon echo, i.e. $P^{(3)}_{\text{R}}(t)$ peaks τ femtoseconds after the third interaction. In contrast, in non-rephasing pathways (common phase factor $\mathrm{e}^{-\mathrm{i}\omega_{eg}(t_1+t_3)}$) the first interaction occurs with positive $\vec{k}$ such that they contribute only for $\tau < 0$ and a free-induction decay is observed. For double-coherence pathways, as the name implies, the system remains in a coherence during the population time, which is only possible in $N > 2$-level systems. Besides, their signal is limited to $\tau \sim T \sim 0$ in a 2D experiment, as the first two interactions must occur with positive $\vec{k}$ to reach the higher lying coherence.

The different Liouville pathways contributing to $P^{(3)}(\tau,T,t)$ in two-dimensional spectroscopy, commonly labeled $R_1 - R_4$, are illustrated in figure 2.9 in a pictorial density matrix representation along with the corresponding excitation pulse sequences. In a two-level system, pathways in which the system is in the excited state population after the second interaction, i.e. during T, lead to stimulated emission SE, while the ground state bleach (GSB) signal originates from molecules that spend T in the ground state. Note that, in our 2D spectra these signals will appear as positive contributions, while for the TA-data we have adapted the convention of negative GSB and SE. In $N \geq 3$-level systems, oppositely signed excited state absorptions (ESA) occur given the excitation spectrum covers the energy gap ω_{ef}.

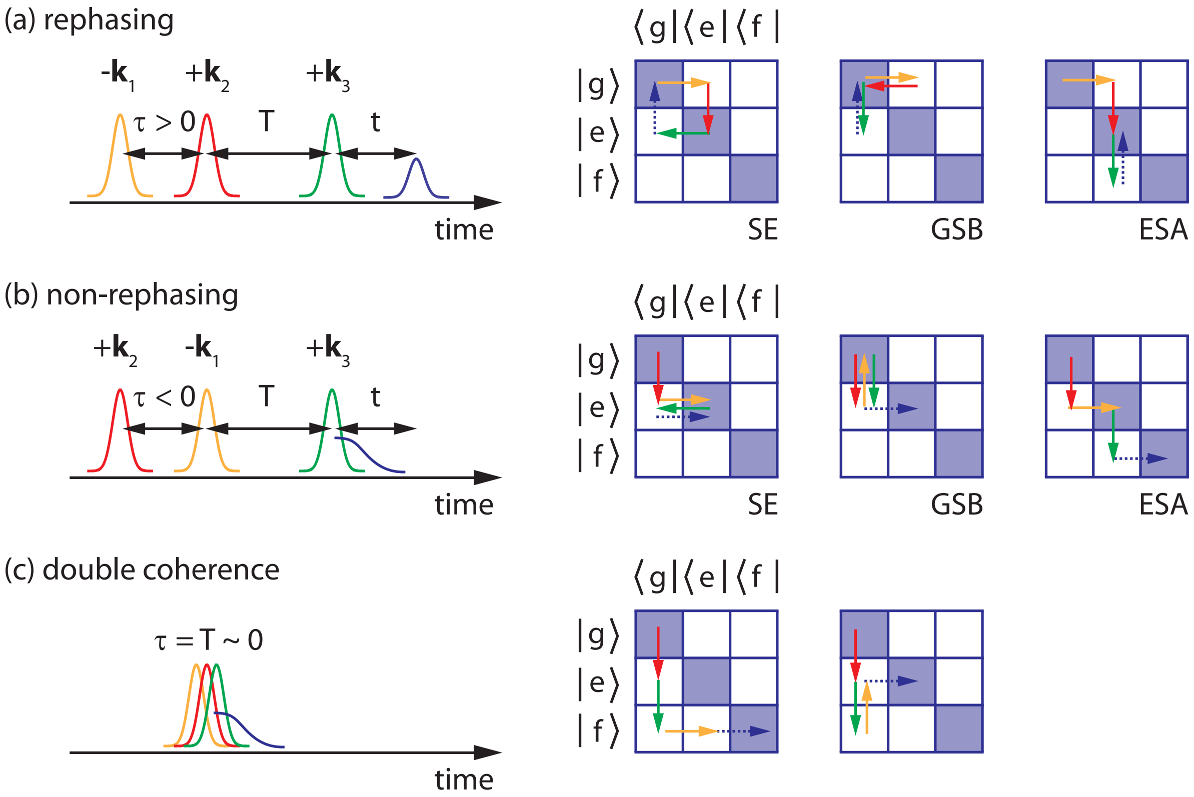

Figure 2.9: Rephasing (a), non-rephasing (b), and double-coherence (c) Liouville pathways in a pictorial density matrix representation. The corresponding pulse time-orderings are shown on the left. Individual pathways correspond to stimulated emission (SE), ground state bleach (GSB) and excited state absorption (ESA) contributions in transient absorption (TA) nomenclature as indicated.

2.7.5 From $\mathrm{P}^{(3)}(\tilde{\mathrm{r}}, \mathrm{t})$ to a 2D Spectrum

To obtain a theoretical two-dimensional spectrum $S_{2\mathrm{D}}(\omega_\tau, T, \omega_t)$ with its two intuitive frequency axes we can simply apply a two-dimensional Fourier Transform along the time axes t and τ to $\mathrm{i}P^{(3)}(\tau, T, t)$ for a fixed population time T [35]. In the experiment, however, we detect the emitted signal field rather than the polarization employing the spectral-interference-based method introduced in section 2.6. In addition, we are measuring $E_s(\tau, T, \omega_t)$ rather than $E_s(\tau, T, t)$ because we are using a spectrometer to detect the signal field for each combination of the interpulse delays. The relationship between field and polarization then reads

$$E_s(\tau, T, \omega_t) \propto \frac{\mathrm{i}\omega_t}{n(\omega_t)} P^{(3)}(\tau, T, \omega_t). \tag{2.105}$$

and we only have to perform the remaining Fourier Transform along the τ-axis

$$S_{\mathrm{2D}}(\omega_\tau, T, \omega_t) = \int_{-\infty}^{\infty} \mathrm{d}\tau \; \mathrm{i}P^{(3)}(\tau, T, \omega_t)\mathrm{e}^{\mathrm{i}\omega_\tau \tau} \tag{2.106}$$

$$= \int_{-\infty}^{\infty} \mathrm{d}\tau \; E_s(\tau, T, \omega_t)\frac{n(\omega_t)}{\omega_t}\mathrm{e}^{\mathrm{i}\omega_\tau \tau}. \tag{2.107}$$

A two-dimensional spectrum is a complex quantity, $S_{\mathrm{2D}}(\omega_\tau, T, \omega_t) \in \mathbb{C}$, and with the definition given above its real part comprises the absorptive features while its imaginary part contains the dispersive system properties (the two-dimensional equivalent of a refractive index). While the 2D spectrum in principle covers negative and positive frequency axis in both dimensions, each frequency quadrant already contains the full information, because $E_s(\tau, T, t) \in \mathbb{R}$ and hence $S_{\mathrm{2D}}(\omega_\tau, T, \omega_t) = S^*_{\mathrm{2D}}(-\omega_\tau, T, \omega_t) = S^*_{\mathrm{2D}}(\omega_\tau, T, -\omega_t)$

2.7.6 Transient Absorption

So far, we have discussed multidimensional spectroscopy in great detail without even mentioning its older and weaker brother, transient absorption (TA). The simple reason lies in the fact, that the TA signal is nothing but the projection of the real part of a two-dimensional spectrum onto the probe frequency axis, ω_t [35, 36], i.e.

$$S_{\mathrm{TA}}(T, \omega_t) = \int \mathrm{d}\omega_\tau \; \mathrm{Re}\left[S_{\mathrm{2D}}(\omega_\tau, T, \omega_t)\right]. \tag{2.108}$$

Or – to put it the other way around – two-dimensional spectroscopy is a transient absorption experiment, that additionally spectrally resolves the excitation (or pump) frequency axis (ω_τ). To establish the connection between TA signals and molecular dynamics, we equally must consider $P^{(3)}(\tau, T, t)$. Merely, the first two interactions now occur within the same pulse (the pump), and the third interaction with the probe. Hence $\vec{k}_s = -\vec{k}_{pu} + \vec{k}_{pu} + \vec{k}_{pr}$ and the signal automatically co-propagates with the probe beam, which is why nobody worries about phase matching in TA. Furthermore, the signal is intrinsically heterodyned with the probe pulse, whose spectrum in the absence of the pump is separately measured and accounted for during data evaluation.

The fact that the probe triggers the signal emission and is used to detect it at the same time results in an unambiguous measurement of the absolute signal phase. This information along with the projection-slice-theorem (2.108) can then be used to determine the absolute phase of a two-dimensional spectrum acquired in box geometry with a time delayed local oscillator [36]. In this so-called phasing process the real part of the projection of the 2D spectrum onto the ω_t-axis multiplied with an adjustable phase factor $\mathrm{e}^{\mathrm{i}\Phi_c + \mathrm{i}(\omega_t - \omega_0)t_c}$ [35]

$$A_{\mathrm{2D}}(T, \omega_t) = \mathrm{Re}\left[\frac{\omega_t}{n(\omega_t)} \int \mathrm{d}\omega_\tau \; S_{\mathrm{2D}}(\omega_\tau, T, \omega_t)\mathrm{e}^{\mathrm{i}\Phi_c + \mathrm{i}(\omega_t - \omega_0)t_c}\right] \tag{2.109}$$

is overlapped with the spectrally resolved pump-probe signal

$$A_{\mathrm{pp}}(T,\omega_t)=\left(\frac{I^{\mathrm{pr}}_{\mathrm{pu}}(\omega_t)}{I^{\mathrm{ref}}_{\mathrm{pu}}(\omega_t)}-\frac{I^{\mathrm{pr}}_{0}(\omega_t)}{I^{\mathrm{ref}}_{0}(\omega_t)}\right)\frac{I^{\mathrm{ref}}_{\mathrm{pu}}(\omega_t)+I^{\mathrm{ref}}_{0}(\omega_t)}{2\sqrt{I^{\mathrm{pr}}_{0}(\omega_t)}}. \tag{2.110}$$

Here, I_{pr} is the probe intensity and I_{ref} is the intensity of a reference beam that does not interact with the sample and is simultaneously measured to reduce the experimental noise. Intensities measured in the absence of a pump beam carry a subscript 0, while those with with the pump present are labeled I^{i}_{pu}.

Note that for the transient absorption experiments presented in the following chapters, the data shown, $S_{\mathrm{pp}}(T)$, is not $A_{\mathrm{pp}}(T)$. Rather, to stick with the conventions of TA, the change in optical density that has been induced by the pump pulse, ΔOD, is plotted. For a TA measurement employing a separate reference beam,

$$S_{\mathrm{pp}}(T)=-\left(\log_{10}\left(\frac{I^{\mathrm{pr}}_{\mathrm{pu}}}{I^{\mathrm{ref}}_{pu}}\right)-\log_{10}\left(\frac{I^{\mathrm{pr}}_{0}}{I^{\mathrm{ref}}_{0}}\right)\right)=\Delta\mathrm{OD}. \tag{2.111}$$

We were, however, using a shot-to-shot TA setup that leaves an additional reference beam obsolete. Thus, in our case, the probe intensity measured with and without pump were combined as

$$\Delta\mathrm{OD}=-\log_{10}\left(\frac{I^{\mathrm{pr}}_{\mathrm{pu}}}{I^{\mathrm{pr}}_{0}}\right) \tag{2.112}$$

2.7.7 Anisotropy

So far we have not explicitly thought about the transition dipole moments and electric fields as vectorial quantities. It is however quite clear that even in an isotropic sample, a linearly polarized laser pulse, e.g. the pump in a TA experiment, will always only excite a subensemble of molecules with a non-vanishing $\vec{\mu}$-component in its polarization direction [37]. The TA-signal that we detect with a probe pulse that is linearly polarized along a different axis will then be proportional to the intersection between the pumped and probed subensembles, and hence depend on the angle β between pump and probe polarization.

For waiting times $T > 0$ the initially excited subensemble will be subject to rotational diffusion, i.e. its transition dipole moment orientations will approach an isotropic distribution again with time-constants characteristic for the solute-solvent system studied. The rotational reorientation will in general lead to a change in overlap with the probe polarization vector and thus provoke a signal change even for systems with infinite excited state lifetimes. In other words, our signal also depends on the angle α between the transition dipole moment that has initially been excited and the transition dipole moment that we probe.

To ensure that our TA-signal only reflects population changes we can impose the condition that our signal must not depend on the relative orientation of these two transition dipole moments. This leads to $\beta = 54.7°$, the so-called magic angle, that has to be employed between pump and probe polarization directions.

On the other hand, the above discussion implies that with a proper choice of relative polarizations of pump and probe pulses, we should be able to detect the depolarization dynamics of molecular systems, which is done in anisotropy decay experiments.

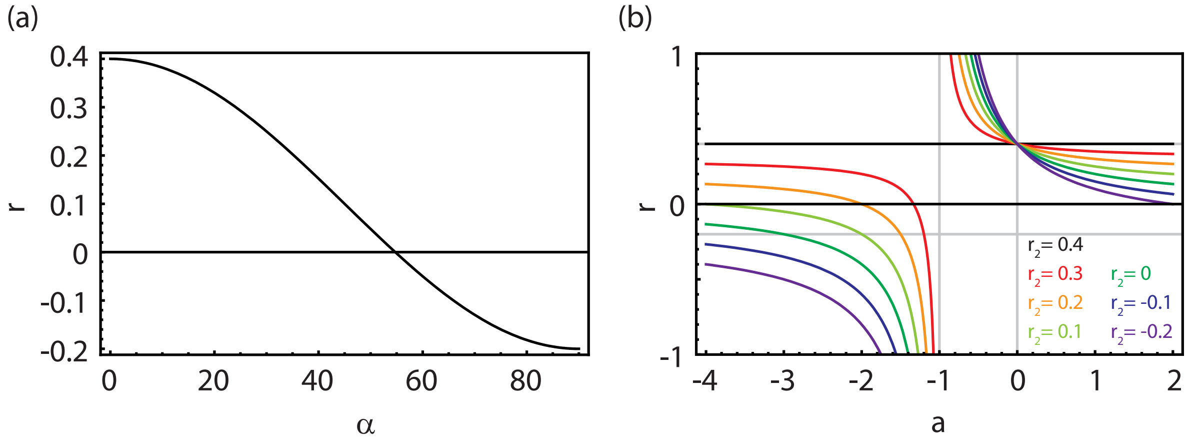

Figure 2.10: (a) Anisotropy r as a function of the angle between transition dipoles α.(b) Total anisotropy $r = \frac{1}{1+a}r_1 + \frac{a}{1+a}r_2$ for a signal $S_{\text{MA}} = a_1 + a_2$ with relative amplitudes $a_2/a_1 = a$ of the two contributions in the case $r_1 = 0.4$.

Anisotropy Definitions

We define the anisotropy $r(t)$ as the difference of the TA-signal with parallel ($\beta = 0°$) and perpendicular ($\beta = 90°$) probe polarizations, $S_{\|}$ and $S_{\perp}$, respectively, divided by the total signal

$$r(t) = \frac{S_{\|} - S_{\perp}}{S_{\|} + 2S_{\perp}}. \tag{2.113}$$

One peculiar property of anisotropy data is, that r shows an instantaneous onset and yields finite values comparably long before the time zero $T = 0$ of the experiment. This can be understood if we remember that the signal we measure is the convolution of a Gaussian and the dynamics of the system: As the Gaussian never drops to zero, r will yield finite (and meaningful) values as soon as the signal amplitude is above noise limit. The relation between $r(t)$ and the angle $\alpha(t)$ between the initially excited and the probed transition dipole is found to be

$$r(t) = \frac{1}{10}(1 + 3\cos(2\alpha(t))) \tag{2.114}$$

or

$$\alpha(t) = \arccos(\sqrt{\frac{1 + 5r(t)}{3}}). \tag{2.115}$$

As possible angles range from $\alpha = 0°$ to $\alpha = 90°$, r is restricted to $-1/5 \leq r \leq 2/5$ (cf. figure 2.10 (a)). In particular, for an ensemble of two-level systems the TA is a combination of bleach and stimulated emission and the initial angle between pumped and probed transition dipole is 0°, corresponding to $r(t = 0) = 2/5 = 0.4$. As the molecules rotate the anisotropy will decay to $r = 0$.

Furthermore the α-independent magic angle signal S_{MA} can be calculated from these two independent measurements via

$$S_{\mathrm{MA}} = \frac{S_{\parallel} + 2S_{\perp}}{3}. \tag{2.116}$$

Other useful relations are

$$S_{\mathrm{MA}} = \frac{S_{\parallel}}{2r+1} \tag{2.117}$$

and

$$S_{\mathrm{MA}} = \frac{S_{\perp}}{1-r}. \tag{2.118}$$

Anisotropy of Multilevel Systems

In general, the magic angle TA-signal S_{MA} at a specific probe wavelength will be a (incoherent) sum over different contributions a_i,

$$S_{\mathrm{MA}} = \sum_i a_i, \tag{2.119}$$

where the a_i can be bleaches, stimulated emissions ($a_i < 0$ for both) and excited state absorptions ($a_i > 0$) corresponding to different μ_i, with different angles α_i relative to the initially pumped transition dipole moment and corresponding individual anisotropies r_i

$$r_i = \frac{S_{\parallel,i} - S_{\perp,i}}{S_{\parallel,i} + 2S_{\perp,i}}. \tag{2.120}$$

The total anisotropy r, can then, e.g. be calculated from the total parallel signal $S_{\parallel}$

$$S_{\parallel} = \sum_i S_{\parallel,i} \tag{2.121}$$

and S_{MA} yielding a weighted average

$$r = \frac{\sum_i r_i a_i}{\sum_i a_i}. \tag{2.122}$$

A couple of important conclusions regarding the possible values for r in a multilevel system can be drawn from this formula

- Trivially, if all r_i are identical, $r = r_i$, and if $a_j \gg a_i \; \forall i \neq j$ the anisotropy r_j of transition j will dominate the measured anisotropy.
- If no ESAs contribute to the signal, i.e. $a_i < 0 \; \forall i$, and $-0.2 \leq r_i \leq 0.4 \; \forall i$, -0.2 and 0.4 remain the upper and lower bounds for r.
- On the other hand if ESAs contribute to the signal, i.e. some $a_i > 0$, then $-\infty < r < +\infty$.

These findings are illustrated in figure 2.10 (b) for the case of two contributions with relative amplitude $a = \frac{a_2}{a_1}$ and $r_1 = 0.4$. $a > 0$ corresponds to the situation where both contributions have the same sign, while for $a < 0$ they have different signs. The total anisotropy r has a pole at $a = 1$, where the denominator approaches zero. For $0 < a < 1$ and $\angle(\mu_{GSB}, \mu_{ESA}) \neq 0$ the total anisotropy becomes larger than 0.4.

Information Content of Anisotropy Data

When the excited state lifetime of the molecular system studied is at least comparable to its rotational diffusion time, rotational diffusion time constants can be extracted from $r(t)$. While for arbitrarily shaped molecules rotations along different molecular axes with distinct moments of inertia have to be taken into account [37], it is sufficient for our purposes to consider a spherical particle of radius r. In this case the anisotropy decay introduced by rotational diffusion follows [37]

$$r(t) \propto \mathrm{e}^{-6D_s t} \tag{2.123}$$

with the diffusion coefficient D_s. Under stick boundary conditions, the diffusion coefficient is related to the temperature T, the volume of the particle $V = \frac{4}{3}\pi r^3$, and the viscosity of the surrounding medium η via the Debye-Stokes-Einstein expression

$$D_s = \frac{kT}{6V\eta}, \tag{2.124}$$

where k is Boltzmann's constant.

More importantly for our applications, anisotropy is an efficient probe for energy transfer as long as it occurs significantly faster than rotational diffusion. In an isotropic molecular sample that is excited with a linearly polarized pump pulse, incoherent intermolecular energy transfer will cause a randomization of excited transition dipole orientations. In fact, long before the advent of time-resolved spectroscopies, the depolarization of fluorescence in highly concentrated molecular solutions was one of the observations pointing at the presence of such transfer processes. In the absence of excited state absorptions, i.e. in emission-based anisotropy measurements or for weakly interacting two-level systems the limiting value of r reached after energy transfer has ceased, can even provide information on the geometry of coupled multichromophore systems: For spherical symmetry, complete randomization corresponds to $r = 0$, while for $N > 2$ non-parallel transition dipoles in a plane, a finite polarization remains and $r = 0.1$.

Noteworthily, in coherently coupled two-level systems, the anisotropy is no longer limited to $r < 0.4$, such that the r-values observed at early times, can actually measure delocalization and electronic dephasing [38–40].

3 Experimental Realization of Two-Dimensional Spectroscopy

Having established the theoretical background of time-resolved spectroscopies in the last chapter we will now turn to the experimental implementation.

We will begin this chapter with a short overview of the laser system and optical setups used in this thesis before reviewing prior experimental realizations of electronic 2D spectroscopy. A comparison of (partially) collinear and box-type beam geometry will motivate our decision for a fully noncollinear optical layout, before we discuss different means that have been employed to ensure phase stability. As a result of this discussion we will see that the concept of pairwise beam manipulation that both of our setups rely on and that had originally been introduced in the group of Miller for a diffractive optics based setup, can be generalized and drastically reduces the required timing precision.

After a short description of our setup for broadband two-dimensional spectroscopy in the visible that uses only conventional optics, we will discuss the prearrangements and data acquisition scheme as well as the data analysis procedure in detail. Experimental 2D traces of a laser dye acquired with on purpose fluctuations in the coherence time will confirm that pulse duration time scales rather than the carrier frequency govern the accuracy of the retrieved spectra.

An all reflective box geometry setup that specifically suits the low-dispersion needs of UV wavelengths will be introduced in section 3.4 and retrieved stability values comparable to the best values reported in the VIS but realized at much shorter wavelengths will be presented.

3.1 Laser System and Transient Absorption Setup

A schematic overview of the optical setups used in this thesis is depicted in figure 3.1. The light source for all experiments described in this and the subsequent chapters was a commercial Spitfire Pro regenerative amplifier (Spectra Physics) providing 120 fs pulses centered at 800 nm with a pulse energy of 4 mJ at a repetition rate of 1 kHz.

1 mJ of the Spitfire output is used to pump a noncollinear optical parametric amplifier (NOPA) yielding pulses as short as 15 fs in the visible spectral range, i.e. between 500 nm and 750 nm (TOPAS white, Light Conversion). Corresponding pulse energies of 10-70 μJ typically have to be attenuated by several orders of magnitude for 2D VIS experiments, where ~nJ-pulses are employed. The NOPA is equipped with an optional internal frequency doubling unit that provides 1-7 μJ pulses in the ultraviolet ($250 - 375$ nm) spectral range.

Besides serving the respective 2D setups that will be discussed in detail in sections 3.3

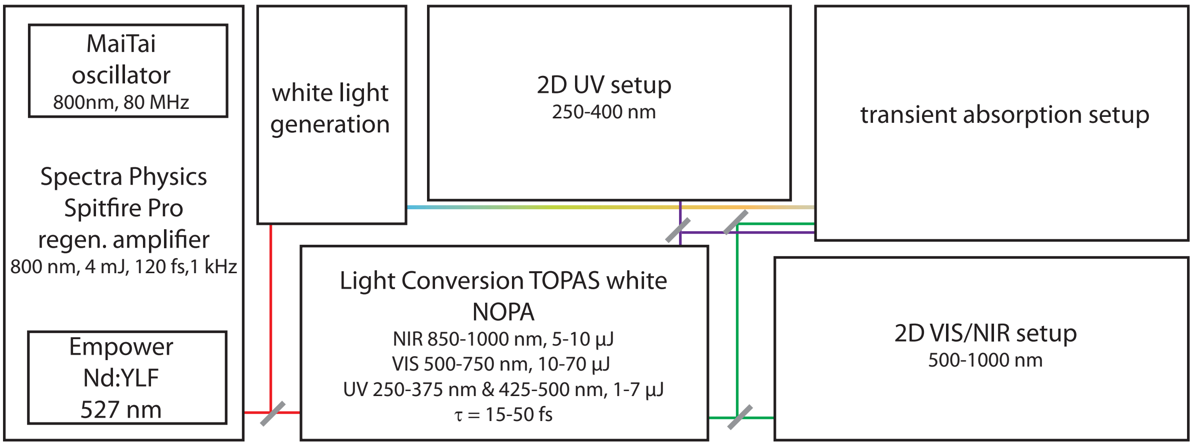

Figure 3.1: Schematic overview of the optical setups used in this thesis.

and 3.4, the visible as well as the UV output of the noncollinear OPA can be coupled into a transient absorption setup, described in detail in [41]. For new molecular samples it is highly advisable to gather their population dynamics in a transient absorption (TA) experiment first, to identify relevant timescales and excitation wavelengths. The TA setup can be switched between a degenerate pump-probe mode in which a small fraction of the TOPAS beam is split off by a pair of thin glass wedges and used as a probe, and a continuum version, that uses a VIS or UV white light continuum probe. In both cases the camera (PIXIS 2K, Roper Scientific) of a PI Acton SpectraPro 2500i spectrometer is synchronized with the Pockels cell of the Spitfire amplifier and a Chopper wheel in the pump beam operating at 500 Hz, which allows for a shot-to-shot readout of the probe intensity. A 60 cm Newport delay stage supports pump probe delays T of up to $\sim$ 4 ns, and $f = 50$ cm and $f = 25$ cm spherical Aluminum mirrors are used to focus the pump and probe beam, respectively, into the sample. Unless stated otherwise the presented TA data have been acquired under magic-angle conditions, realized by inserting an appropriate $\frac{\lambda}{2}$ plate into one of the beams.

3.2 Previous Experimental Realizations of Two-Dimensional Spectroscopy

Coherent multidimensional spectroscopy [36,42,43] was introduced to the optical regime in the late nineteen nineties and beginning of the twenty first century and can thus still be considered a comparably young field. After the pioneering experimental realizations for electronic excitations at near infrared wavelength in the group of Jonas [44] and for vibrational excitation in the MIR in the groups of Hochstrasser [45], Hamm [46] and Tokmakoff [47], two-dimensional spectroscopy in the visible spectral range was independently developed and demonstrated in the groups of Miller [48] and Fleming [49]. In the following years electronic 2D spectroscopy has successfully been applied to a variety of systems including monomeric molecules [35, 50], multichromophoric molecular assemblies such as natural light harvesting systems [51–54], artificial aggregates of defined geometry [55] and disordered conjugated polymers [56] as well as metal [57] and semiconductor [58–62] nanostructures.

The success of these early experiments has inspired multiple variations of the original technique to increase the information content of electronic 2D spectra and address specific physical problems: To study energy transfer between electronic states that are widely separated in energy two-color 2D spectroscopy [63] has been developed and its extension to two-dimensional spectroscopy with a continuum probe [64] in principle allows for simultaneous coverage of the NUV-to NIR spectral range in the ω_t-dimension. In the latter case, probe-chirp correction can be applied during data analysis to remove signal distortions that result from the non-flat spectral phase of a white light continuum [65]. So-called cross-peak specific 2D spectroscopy [66] uses polarized pulse sequences to suppress signals arising from the strong diagonal peak contributions and promotes the off-diagonal features associated with the interchromophoric couplings. Correlations between doubly excited electronic states and the constituent singly excited states can be investigated with double-quantum coherence experiments [59, 67, 68], i.e. 2D experiments where the first two interactions are with positive wave vectors, such that the system is pumped into a higher-lying coherence rather than a population with the second pulse. Besides, experiments based on incoherent detection such as fluorescence [69] or emitted photo-electrons have been carried out [57]. The latter seems particularly noteworthy as the corresponding technique, two-dimensional nanoscopy, overcomes the optical diffraction limit such that the determination of the nonlinear optical response with 50 nm spatial resolution could be shown [57].

3.2.1 Box Geometry versus (Partially) Collinear Schemes

We have seen in chapter 2.7.4 that to measure the complete third order response function of a given molecular system we have to excite our sample with a sequence of three pulses and systematically vary the time-delays between them. The first experimental challenge lies in the isolation of the signal field that originates from exactly one interaction with each of these three pulses from other signal contributions. For finite angles between all three excitation beams the phase matching direction $\vec{k}_s = -\vec{k}_1 + \vec{k}_2 + \vec{k}_3$ differs from the propagation directions $\vec{k}_1$, $\vec{k}_2$, and $\vec{k}_3$ allowing for spatial separation of the signal field, i.e. background-free detection. A so-called box geometry arrangement as depicted in figure 3.2 (right) has proven particularly useful as in this case the signal automatically co-propagates with the time-delayed detection beam, the local oscillator, as long as the wavelengths of all employed pulses are sufficiently similar.

Fully collinear [70] or partially collinear [64, 71] pump-probe geometry setups (figure 3.2, bottom left) on the other hand can be realized with pulseshapers. In both cases, additional measurements with different relative phases of the excitation pulses have to be carried out to isolate the 2D signal from conventional pump probe signals that arise e.g. from two interactions with one of the two pump pulses [72]. While measurements under precise magic angle conditions allow for detection of pure population and coherence dynamics even in systems that rapidly depolarize and spectrally broad probe pulses are easily realized in this partially collinear scheme, this comes at the cost

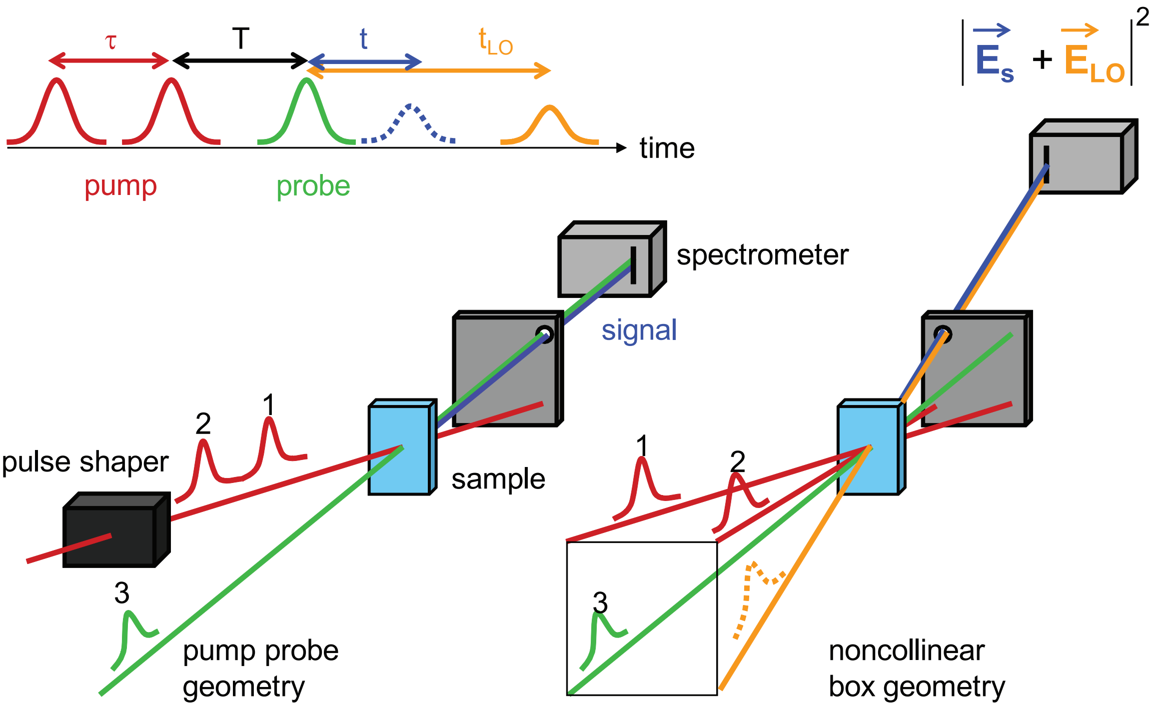

Figure 3.2: Pulse-sequence(top), partially collinear pulseshaper-based (left) and box geometry (right) layouts for 2D spectroscopy.

of measuring only absorptive 2D spectra. A combination of Fourier Transforms and causality enforcement can then mathematically generate an imaginary part of the 2D spectrum [63]. Yet this corresponds to a Kramers-Kronig transformation over a limited frequency range and therefore provides no new information on the molecular system. In contrast, the measurement of real and imaginary parts of the third order signal in box geometry setups with heterodyne detection reveals both, the absorptive and the true dispersive susceptibility in the investigated spectral range. Furthermore, rephasing and non-rephasing Liouville pathways can be recorded separately in fully non-collinear 2D implementations: Different time orderings of the three interactions, $-\vec{k}_1 + \vec{k}_2 + \vec{k}_3$ for rephasing and $\vec{k}_2 - \vec{k}_1 + \vec{k}_3$ for non-rephasing signals, are easily achieved via positive and negative coherence times, respectively. In pump-probe geometry, causality enforcement again has to be applied to separate these two signals [63], that can provide additional information on vibronic modulation of electronic line shapes [73] and coherence dynamics in coupled multichromophoric systems [74].

Besides, as the electric field of the probe pulse triggers the signal emission and at the same time acts as local oscillator, there is no independent reference pulse whose intensity can be adjusted to optimally boost the signal which limits the sensitivity of the method.

The combination of all these considerations let us choose a noncollinear layout for our experiments.

3.2.2 Phase Stability in Two-Dimensional Spectroscopy

If we recall that in 2D spectroscopy we are aiming at resolving the pump frequency dependence, i.e. we are trying to detect a signal modulation with $\omega_{eg} \sim \omega_0$ as a function of the coherence time τ, we immediately see the most challenging experimental requirement: It lies in timing control on the order of fractions of the oscillation period $T_0 = \frac{2\pi}{\omega_0}$. This timing control has two aspects: The minimum step sizes $\delta\tau$ of the means that are being used to introduce the coherence time, e.g. delay stages, must be smaller than half the minimum oscillation period of the signal $\delta\tau < \frac{T_{min}}{2}$ if one wants to avoid undersampling and, more importantly, the relative phase stability of the laser pulses that generate and measure the third order signal. This latter condition translates to variations in the optical path lengths as a result of vibrations or thermal drifts of reflective optical elements or even air currents that must be much smaller than the excitation wavelength $\lambda_0 = \frac{2\pi c}{\omega_0}$.

In the perturbative response function formalism (chapter 2.7.4) we have decomposed the fast oscillating third order polarization $P^{(3)}$ into a system independent phase factor $\mathrm{e}^{-\mathrm{i}\omega_0 t + \mathrm{i}\omega_0(-\hat{t}_1+\hat{t}_2+\hat{t}_3)}$ that oscillates fast at the central frequency of the employed laser pulses ω_0, and a threefold convolution integral. The latter contains a sum over products of system specific Liouville pathways and the pulse envelopes of the three excitation pulses. It is important to note two things at this point: Firstly, in the integral kernels only the slowly varying pulse envelopes explicitly depend on the pulse arrival times, that are affected by environmental perturbations in the experiment. And secondly, as we are integrating over the interaction times t_i that are limited to the pulse duration via convolution with the envelopes only terms that oscillate slowly as a function of t_i will yield significant contributions to the polarization (rotating wave approximation). Therefore, if we manage to balance the system independent phase factor $\mathrm{e}^{-\mathrm{i}\omega_0 t + \mathrm{i}\omega_0(-\hat{t}_1+\hat{t}_2+\hat{t}_3)}$ in our 2D experiment, our stability requirements will greatly reduce. This is illustrated for the case of a first order polarization $P^{(1)}_{\mathrm{RWA}}(t)$ that results from excitation of a quantum mechanical system of transition frequency ω_{eg} with a Gaussian laser pulse spectrally centered at ω_0 in figure 3.3. $P^{(1)}(t)$ already contains all of the elements discussed above for $P^{(3)}(t)$, but can be represented much clearer. $P^{(1)}_{\mathrm{RWA}}(t)$ has been calculated as a convolution of the first order response $S^{(1)}(t)$

$$S^{(1)}(t) = \frac{\mathrm{i}}{\hbar}\,\theta(t)\left(\mathrm{e}^{-\mathrm{i}\omega_{eg}t}\mathrm{e}^{-\Delta t^2} + \mathrm{c.c.}\right) \tag{3.1}$$

of a homogeneously broadened system with line shape function $g(t) = \Delta t^2$, and a Gaussian excitation pulse $E(t)$

$$E(t) = \mathrm{e}^{-\frac{(t-\hat{t}_1)^2}{\tau_p^2}}\,\mathrm{e}^{-\mathrm{i}\omega_0(t-\hat{t}_1)} + \mathrm{c.c.} \tag{3.2}$$

where we have explicitly introduced the pulse arrival time $\hat{t}_1$ to stress the analogy to

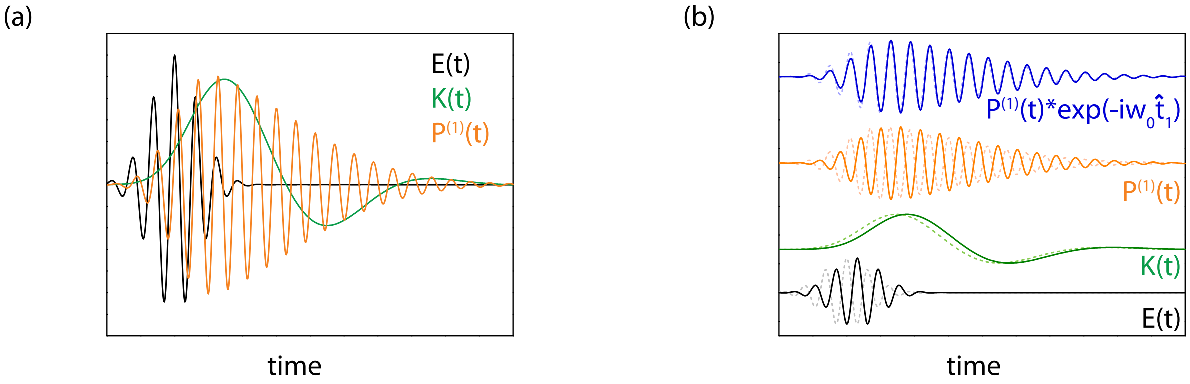

Figure 3.3: Influence of stabilizing the absolute phase on the polarization $P^{(1)}_{\mathrm{RWA}}(t)$. (a) Gaussian excitation field $E(t)$(black), slowly varying integral $K(t)$ (green), and polarization $P^{(1)}_{\mathrm{RWA}}(t)$ (orange). (b) Comparison of $E(t)$, $K(t)$, and $P^{(1)}_{\mathrm{RWA}}(t)$ for $\hat{t}_1 = 0$ (dotted) and $\hat{t}_1 = \frac{\pi}{\omega_0}$ (straight). For the blue curve, only the arrival time dependence of $K(t)$ was evaluated as would be the case when balancing the phase factor $\mathrm{e}^{\mathrm{i}\omega_0\hat{t}_1}$ with an identical phase shift of a hypothetical reference pulse.

$P^{(3)}_{\mathrm{RWA}}$, i.e.

$$P^{(1)}_{\mathrm{RWA}}(t) = \int_0^\infty \mathrm{d}t_1\; S^{(1)}(t_1)E(t-t_1) \tag{3.3}$$

$$= \frac{\mathrm{i}}{\hbar}\mathrm{e}^{-\mathrm{i}\omega_0 t}\mathrm{e}^{\mathrm{i}\omega_0\hat{t}_1}\int_0^\infty \mathrm{d}t_1\; \mathrm{e}^{-\mathrm{i}(\omega_{eg}-\omega_0)t_1}\mathrm{e}^{-\Delta t_1^2}\mathrm{e}^{-\frac{(t-\hat{t}_1^2)}{\tau_p^2}} + \mathrm{c.c.} \tag{3.4}$$

Figure 3.3 shows the Gaussian excitation field (black), the integral K(t) (green),

$$K(t) = \frac{\mathrm{i}}{\hbar}\int_0^\infty \mathrm{d}t_1\; \mathrm{e}^{-\mathrm{i}(\omega_{eg}-\omega_0)t_1}\mathrm{e}^{-\Delta t_1^2}\mathrm{e}^{-\frac{(t-\hat{t}_1^2)}{\tau_p^2}} + \mathrm{c.c.}, \tag{3.5}$$

that oscillates at the difference frequency $\Delta\omega = \omega_{eg} - \omega_0$ and is damped due to the line shape function. The polarization $P^{(1)}_{\mathrm{RWA}}(t)$ (orange) oscillates at the system's transition frequency, ω_{eg}, as a result of the combination of the system independent phase factor $\mathrm{e}^{-\mathrm{i}\omega_0 t}\mathrm{e}^{\mathrm{i}\omega_0\hat{t}_1}$ and the slowly varying phase of the integral. The absolute phase of the polarization follows the excitation with a phase shift of $\pi/2$ due to the factor i in the response function. Consequently, if we employ a phase sensitive detection scheme, a shift in the arrival time of only $\Delta\hat{t}_1 = \frac{\pi}{\omega_0}$ already leads to complete information loss (cf. figure 3.3(b), orange). In contrast, if we manage to keep the absolute phase that is being detected constant upon a shift in the arrival time $\hat{t}_1$, e.g. by shifting the phase of a hypothetical reference pulse by the same amount, the deviation in the detected signal field will be much smaller (blue curve in figure 3.3: It is now governed by the arrival time sensitivity of K(t) (green curve in figure 3.3 (b)), i.e. the system dynamics relative to the laser frequency ω_0.

Having identified and illustrated a possible mechanism to decrease the signal sensitivity to the pulse arrival time(s) in the simpler linear case we can now return to the more involved third order response function. In $P^{(3)}$, the arrival times $\hat{t}_i$ of all three pulses determine the absolute signal phase, as can be seen from the phase factor $\mathrm{e}^{\mathrm{i}\omega_0(-\hat{t}_1+\hat{t}_2+\hat{t}_3)}$ that reflects the phase matching condition $\vec{k}_s = -\vec{k}_1 + \vec{k}_2 + \vec{k}_3$ in the signs of the $\hat{t}_i$. To detect the signal we are heterodyning it with a fourth pulse, the local oscillator, such that the experimentally measured absolute phase, $\phi_{SI,0}$, is the phase relative to the local oscillator $\phi_{SI,0} = \mathrm{i}\omega_0(-\hat{t}_1 + \hat{t}_2 + \hat{t}_3 - \hat{t}_{\mathrm{LO}})$.

Note that, even though transient absorption can formally be described with the same formula for $P^{(3)}(\hat{t}_1, \hat{t}_2, \hat{t}_3, t)$, relative phases do not influence the measured signal, because the first two interactions occur with the same (the pump) pulse, i.e. $\hat{t}_1 = \hat{t}_2 = \hat{t}_{pump}$ and the intrinsic heterodyning with the probe ensures phase stability in the detection mechanism, $\hat{t}_3 = \hat{t}_{\mathrm{LO}}$. The time difference between pump and probe, the population time T in a 2D experiment, is far less critical, because the system is - as the name implies- in a population and thus the signal does not oscillate at the transition frequency as a function of this time delay.

For 2D spectroscopy in pump probe geometry the pulseshaper-generated pump double-pulses travel the same optical path which along with the probe-heterodyned detection makes these setups intrinsically phase-stable. For an analysis of timing precisions and stability of pulse shaper pulse pairs see e.g. [75]. In box geometry implementations, to avoid artifacts in the recorded 2D traces in particular at visible or even shorter wavelengths, phase stabilizing mechanisms are called for. Active stabilization via a feedback loop and continuous readjustment of path length has been demonstrated in the groups of Cundiff [76] and Hamm [77]. While this effectively keeps the pulse phases constant, additional interferometers, reference lasers, and electronics make such setups complex and expensive. Trivially, yet efficiently, passive phase stability is achieved when all four beams are steered via the same reflective optical elements, such that vibrations of this element affect the arrival times of all pulses equally. The box geometry setups of Brixner et al. [35] and Nemeth et al. [68], that use diffractive optics to generate four phase-stable beams are therefore intrinsically phase-stable. The introduction and variation of time delays between the pulses of course requires means to address individual pulses which in their case has been realized via moveable glass wedge pairs in the individual beams. As these are transmissive elements the influence of vibrations on the optical path are negligible. While a very high timing precision can be reached with these wedge pairs, a delay dependent chirp is introduced. This becomes significant when spectrally broad pulses in the visible or ultraviolet are being used.

A closer look at the detected signal phase $\phi_{SI,0} = \mathrm{i}\omega_0(-\hat{t}_1 + \hat{t}_2 + \hat{t}_3 - \hat{t}_{\mathrm{LO}})$ opens up a different approach to the phase stability issue: Obviously, $\phi_{SI,0}$ will not change upon variations in the pulse arrival times $\Delta\hat{t}_i$ as long as we manipulate the pulses in pairs that enter the phase expression with opposite signs, i.e. as long as the following conditions hold

$$\Delta\hat{t}_1 = \Delta\hat{t}_2 \quad \text{and} \quad \Delta\hat{t}_3 = \Delta\hat{t}_4 \quad \text{or} \tag{3.6}$$

$$\Delta\hat{t}_1 = \Delta\hat{t}_3 \quad \text{and} \quad \Delta\hat{t}_2 = \Delta\hat{t}_4. \tag{3.7}$$

Translating this into boundary conditions for the design of our experimental setup, $\phi_{SI,0}$ will remain constant if we let beams 1 and 2 as well as 3 and 4, or alternatively beams 1 and 3 as well as 2 and 4 travel over the same reflective optical elements.

Such a pairwise beam manipulation (PBM) results in stability values that are comparable to glass-wedge/DO-implementations even at UV wavelength as we will see in the next sections. It has, however, one significant advantage over those layouts: As an immediate consequence of steering pulses only in pairs, the detected spectral interference signal exhibits no fast oscillations as a function of the coherence time, but is modulated only on time scales $\Delta\omega = \omega_{eg} - \omega_0$ (and possibly contributions from a complex line shape $g(t)$), i.e. it follows the green curve rather than the orange curve of our linear example in figure 3.3. Similar to 2D experiments with pulse shapers, where the relative phase of the two pump pulses can be adjusted to yield a slowly varying signal [72], the rotating frame is thus inherent in a PBM experiment, yet allowing for the full benefits of a noncollinear beam geometry. This – in addition to significantly lowering the mechanical stability requirements of the setup – reduces the required timing precision from fractions of the oscillation period $T = \frac{2\pi}{\omega_0}$ to time scales comparable to the pulse duration [72], i.e. typically by an order of magnitude. As the price of delay stages scales with their precision, setups based on pair-wise beam manipulation open up an intrinsically phase-stable, cost-efficient alternative.

The concept of pairwise beam manipulation has earlier been applied in the group of Miller [48] who still attributed the stability of his setup to the diffractive optical element that had been used to create the four beams. In the next sections we will present two optical setups that fully exploit the potential of this powerful consideration: A design for the visible spectral range, that in principle works for all wavelength regimes and uses only conventional optics and a fully reflective implementation that specifically suits the low-dispersion needs of two-dimensional spectroscopy in the ultraviolet.

3.3 Inherently phase-stable 2D spectroscopy in the visible

Our setup for broadband two-dimensional spectroscopy in the visible spectral range is depicted in figure 3.4. It has been published in [78]: The incoming beam of a noncollinear OPA is split by a first beam splitter (BS1) with conventional metallic coating. The transmitted beam (dashed line) propagates in the drawing plane, and the reflected beam (solid line) is redirected via mirror M1 into a parallel and vertically displaced plane. Both beams hit a second conventional metallic beam splitter (BS2), now creating four beams that are used as excitation pulses (1, 2, and 3) and as a local oscillator (4) in standard noncollinear box geometry after focusing with a spherical mirror (f = 25 cm) via a folding mirror (FM) into the sample. To ensure that all pulses pass the same amount of

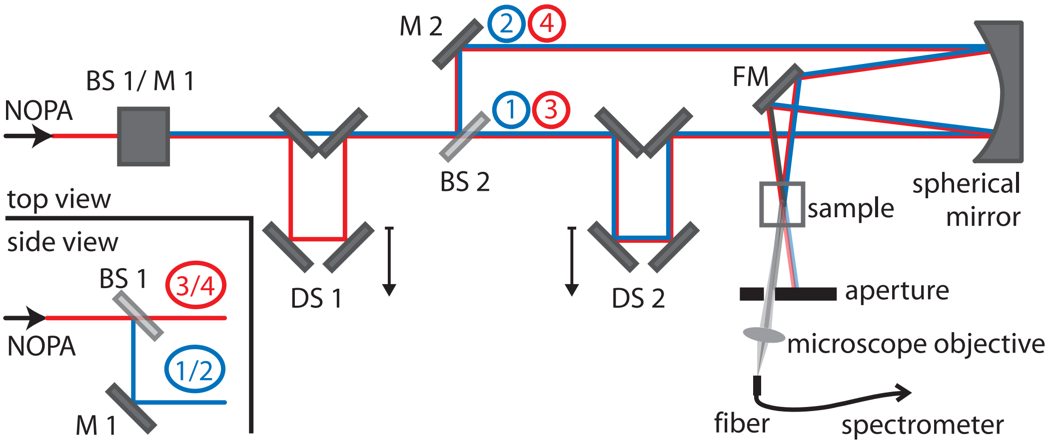

Figure 3.4: 2D VIS setup. See text for further explanation.

material, glass plates of the same thickness as the beamsplitters are introduced into the paths of the beams that are being reflected by BS1 and BS2, respectively. They have been omitted for clarity.

Time delays are provided by two 200 nm travel-range piezo stages (PX200CAP, Piezosystem Jena) that can delay pulse pair 3/4 versus 1/2 (DS1) as well as pair 1/3 versus 2/4 (DS2). To allow for larger population times of up to 300 ps, the piezo at DS1 is mounted onto a delay stage with 50 mm travel range (M-UTM50CC, Newport). In this way, all required delays can be provided as will be discussed in the next paragraph.

After the sample, the heterodyne signal is passed through an aperture. It is then either collected with a microscope objective, and coupled into a single mode fiber or travels free-space to a CCD array spectrometer (Acton SpectraPro 2500i with PIXIS 2K). An additional attenuator in beam 4 (not shown) is used to adjust the local-oscillator intensity and introduces a time delay of $\sim 1-2$ ps between LO and pulse 3. Scattering terms can be removed via automated beam shutters that have been installed on the lid of the setup enclosing box to minimize heat impact.

The characteristic property of this setup, the pairwise beam manipulation, calls for a specific scanning scheme in our 2D experiments, where for each population time T we want to vary the coherence time τ from $-|\tau_{max}|$ to $+|\tau_{max}|$ while keeping the time difference between the second and the third pulse constant. This is illustrated in figure 3.5: The additional glass in the local oscillator beam path delays it by $t_{34}(0)$ with respect to the other pulses (a). A population time $T > 0$ is realized by moving the Newport stage at DS 1 (b). For a negative coherence time τ beam 1 and 3 are delayed with respect to 2 and 4 with the piezo at DS 2, resulting also in a shorter time difference between the local oscillator and the third pulse (c). A positive coherence time requires both piezo actuators to move: The one at DS 2 introduces a time delay τ between pulses 1 and 2, but inevitably decreases the population time T at the same time (e). This is corrected for by delaying pulse pair 3/4 with respect to 1/2 by τ with the second piezo at DS 1 (f). The time delays $t_{i4}(\tau, T)$ between the three excitation pulses and the local oscillator can be written as

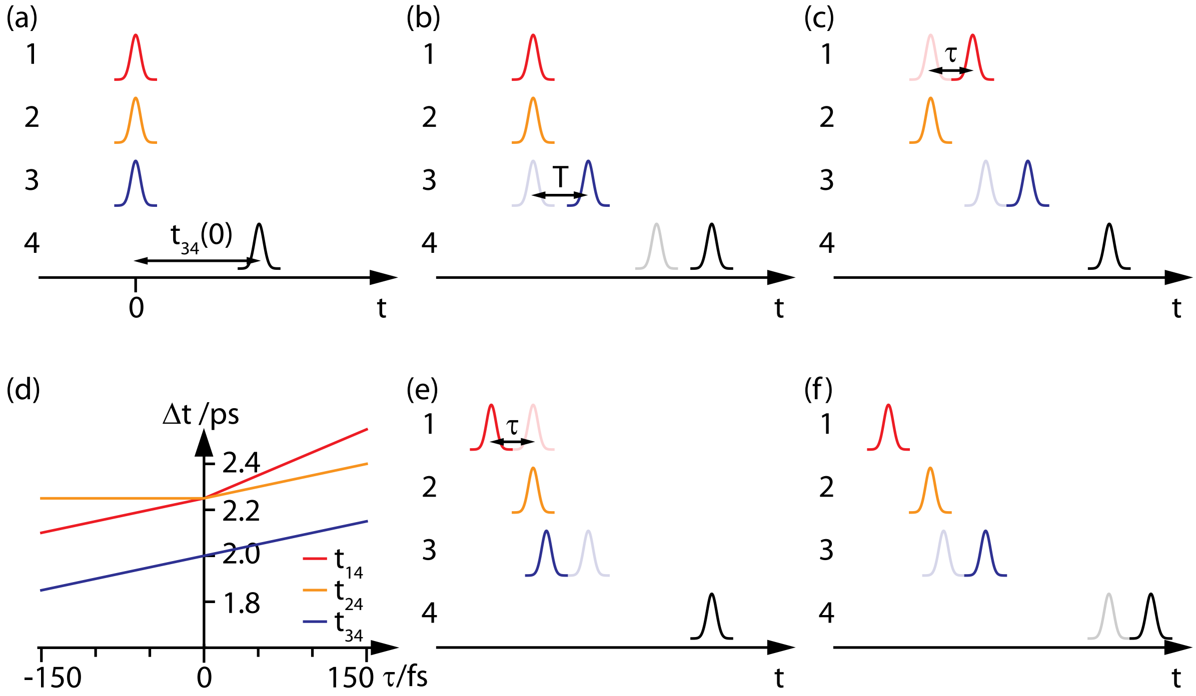

Figure 3.5: (a)-(c), (e), (f) Pairwise beam manipulation requires a specific scanning scheme for 2D spectroscopy (see text for further explanations), (d) Time differences $t_{x4} = t_4 - t_x$ for all three excitation pulses during a τ-scan for $T = 250$ fs and $t_{34}(0) = 2$ ps.

$$t_{14}(\tau, T) = \begin{cases} t_{34}(0) + \tau + T, & \text{if } \tau < 0 \\ t_{34}(0) + 2\tau + T, & \text{if } \tau > 0 \end{cases} \tag{3.8}$$

$$t_{24}(\tau, T) = \begin{cases} t_{34}(0) + T, & \text{if } \tau < 0 \\ t_{34}(0) + \tau + T, & \text{if } \tau > 0 \end{cases} \tag{3.9}$$

$$t_{34}(\tau, T) = t_{34}(0) + \tau \tag{3.10}$$

(see also figure 3.5 (d)). The τ and T dependence of t_{i4} implies that if scattering terms must be removed to reduce signal distortions resulting from coherently scattered light of the excitation pulses [35], these have to be recorded for each coherence time individually. Yet, as only those scattering contributions that have a similar time difference to the local oscillator as the emitted signal field (triggered by the arrival of pulse 3) will survive the Fourier Windowing algorithm, only $I_{34} = |E_3 + E_4|^2$ has to be recorded for population times larger than the width of the Fourier Window.

3.3.1 Data Acquisition

After the light source, a noncollinear OPA, has been tuned to the desired excitation wavelength and spectral width, the beam is coupled into the 2D setup. Spatial overlap of all beams at the sample position is confirmed with either a CCD camera or a pinhole. Typically, when the incoming beam has been aligned to the two apertures in the setup, no further adjustments have to be made. However, when major realignments in the NOPA beam path before the 2D setup have been made, it may be necessary to adjust the collimation of the incoming beam to ensure that the focus of the single beams coincides with their spatial overlap.

To facilitate switching between the 2D experiment and the pump probe experiment for phasing, the reference beam for the pump probe measurement, typically the transmitted portion of a backside polished Ag-mirror, should be coupled into the spectrometer already at this point.

To characterize the excitation pulses FROG-measurements [79] are then carried out, and the pulse compression is iteratively adjusted to yield the shortest possible pulse. For the experiments performed at visible wavelengths, a 10 μm BBO crystal has been placed at the sample position and the cooperative SHG signal of beams 1 and 2 was recorded with an Ocean Optics fiber spectrometer as a function of the interpulse delay that is controlled via the piezo at DS2. A commercial software package has been used to retrieve the pulse duration from the experimental FROG traces.

Afterwards, a single mode fiber is placed at the sample position and the temporal overlap between all three excitation pulses is determined from their spectral interference patterns. Here, the arrival time of pulse 2 that cannot be varied defines the experimental time zero. For details on the procedure see [80]. With all three excitation pulses at temporal overlap a spectral interference spectrum of the local oscillator and beam 3 is recorded along with the spectra of the single pulses. The spectral phase of the local oscillator relative to the excitation pulses, i.e. its delay but also its higher order phase terms, will later be extracted from this SI spectrum for data analysis.

Hereafter the sample is inserted into the setup, and the local oscillator is coupled into the spectrometer. (For delicate samples and if mirrors have been removed from the beam path to the spectrometer, a pre-alignment of the LO to the spectrometer without the sample in place and before determination of the time zero may be beneficial, depending on the alignment skills of the experimenter). At $T = \tau = 0$ (and with all beams unblocked!), the z-position of the sample is then varied until modulations appear on the LO spectrum. When the modulation depth – or the peak height of the $\Delta \sim t_{34}(0)$-peak in the Fourier Transform – has been maximized, the Newport stage at DS1 is moved to a negative population time (~ -1 ps $< T < -300$ fs) to minimize scattering influences: For causality reasons, all persisting modulation must be due to scattered light. These contributions are then minimized by moving the sample cell perpendicular to the beams. As the scattered light of the excitation beams can destructively interfere it is helpful to block the individual beams every now and then in the minimization process. The steps of signal maximum and scattering minimization should be repeated until the optimum is found. Having found the optimum, the actual measurement routine can be started, i.e. for each population time T the coherence time τ is continuously varied from negative to positive values in an appropriate step size, and the spectral interference of local oscillator and third order signal field I_{SI} as well as scattering terms I_{124} and I_{34}, and typically also the local oscillator spectrum I_{LO} are recorded at each point.

After 2D data for all desired population times has been acquired, pump probe measurements for the phasing procedure described in section 2.7.6 have to be performed. Typically, pulse 3 serves as the probe and is coupled into the spectrometer, while pulse

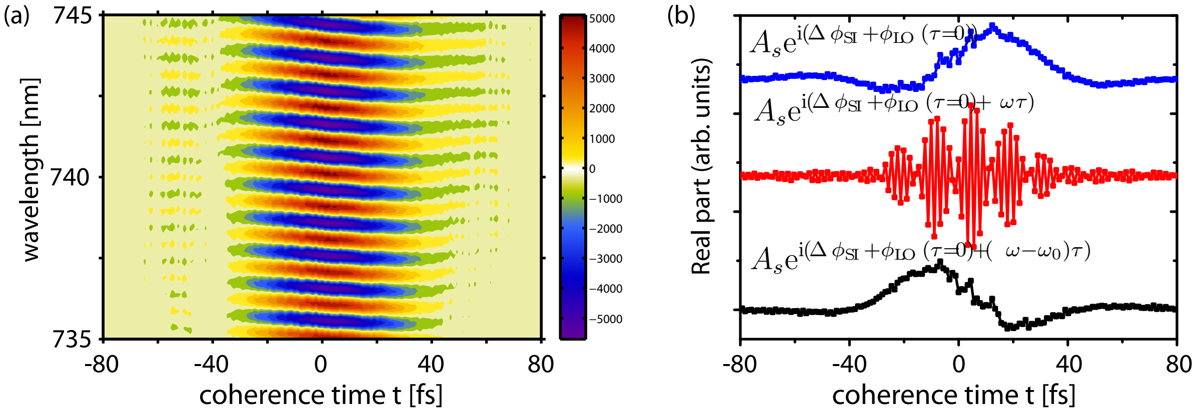

Figure 3.6: Oscillatory term of the SI data, equation(3.12) (a). Example of the signal phase retrieval (b), see text for further explanation.

1 or pulse 2 or - more frequently - both are used as pump.

3.3.2 Data Analysis

In a first step of data analysis of a data set acquired for a certain population time T, the scattering terms are removed from the raw data yielding a scattering corrected spectral interference pattern $I_{\mathrm{SI}}^{\mathrm{sc}}(\omega_t,\tau)$

$$I_{\mathrm{SI}}^{\mathrm{sc}}(\omega_t,\tau) = I_{\mathrm{SI}}(\omega_t,\tau) - I_{124}(\omega_t,\tau) - I_{34}(\omega_t,\tau) + I_{\mathrm{LO}}(\omega_t,\tau). \tag{3.11}$$

To retrieve the signal amplitude $A_s(\omega_t,\tau)$ and its phase relative to the local oscillator a Fourier windowing algorithm described in detail in section 2.6 is applied to $I_{\mathrm{SI}}^{\mathrm{sc}}(\omega_t,\tau)$ for each measured coherence time. During this procedure the varying time-delay between pulse 3 and the local oscillator as a result of the pairwise beam manipulation has to be included in the placement of the Fourier windows as well as in the calculation of the signal phase: To account for $\Delta t_{34}(\tau)$ (cf. equation (3.8)) in the Fourier window position, their centers are shifted linearly with τ. While this may have minor influence for the typically employed ≥ 600 fs-wide rectangular Fourier windows, in situations where one wants to use smaller windows to reduce the influence of scattering of beams 1 and 2 for larger population times, it becomes significant.

Having applied the windows in the time domain and Fourier transformed back to ω_t, we are left with the oscillatory term of the original SI signal, i.e.

$$\tilde{A}_s(\omega_t,\tau)\tilde{A}_{\mathrm{LO}}(\omega_t)\mathrm{e}^{\mathrm{i}\omega_t(t_s-t_{\mathrm{LO}}(\tau))}\mathrm{e}^{\mathrm{i}(\phi_s(\omega_t,\tau)-\phi_{\mathrm{LO}}(\omega_t))} \tag{3.12}$$

an example of which is depicted in figure 3.6 (a). The corresponding experiment on the laser dya HITCI dissolved in ethanol is described in section 3.3.3. Note that, as a result of the pairwise beam manipulation, this signal exhibits no fast oscillations in the τ-dimension. Dividing expression (3.12) by $\tilde{A}_{\mathrm{LO}}(\omega - t) = \sqrt{I_{\mathrm{LO}}(\omega_t)}$ we recover the signal amplitude.

To extract the phase of the signal field relative to the third pulse, our time-zero, we first apply the same Fourier windowing technique to the SI-spectrum of beam 3 and the local oscillator recorded for $\tau = 0$, where 3 now acts as the reference. This yields the phase of the local oscillator relative to the third pulse at $\tau = 0$

$$\Phi_{\mathrm{LO}} = \omega_t \left(t_{\mathrm{LO}}(\tau = 0) - t_3\right) + \left(\phi_{\mathrm{LO}}(\omega_t) - \phi_3(\omega_t)\right). \tag{3.13}$$

Adding this expression to the phase recovered from the spectral interference (equation (3.12))

$$\Phi_{\mathrm{SI}} + \Phi_{\mathrm{LO}} = \omega_t(t_s - t_3 - \omega_t\tau) + \phi_s(\omega_t) - \phi_3(\omega_t), \tag{3.14}$$

removes the oscillations in the ω_t-dimension. Yet – as a result of the pairwise scanning which causes the residual linear phase $-\omega_t\tau$ that balances the fast signal oscillation – the signal is still only slowly varying as a function of τ. To illustrate this, the real part of $A_s e^{i(\Delta\phi_{\mathrm{SI}}+\phi_{\mathrm{LO}}(\tau=0))}$ for $\lambda_t = 740$ nm is depicted in figure 3.6 (b)(blue). If desired, the signal oscillation at the transition frequency of the molecular system can be recovered by adding a linear phase term $\omega_t\tau$, which yields the red curve in figure 3.6 (b). Here, the observed beating pattern results from contributions of different transition frequencies to the nonlinear response and/or the slightly double-peaked laser spectrum. This signal field that contains the full signal phase relative to the third pulse can then be used for the final Fourier Transform along τ (equation (2.107)) that will generate the two-dimensional spectrum. Typically, we do, however, add a linear phase term $(\omega_t - \omega_0)\tau$ to expression (3.14), and shift the frequency axis ω_τ accordingly, which shifts the spectrum into the correct frequency range even for undersampled data sets.

Finally, the real and imaginary parts of 2D spectra retrieved from different measurements for the same population time can be averaged after verifying that no systematic phase drift occurred in the course of the experiments. To determine the absolute phase of the averaged spectrum, the projection of its real part is then overlapped with the pump probe data as described in section 2.7.6. In the case of systematic phase drifts over long measurement times, phasing the spectra individually before averaging may still yield valuable results.

3.3.3 Proof of Reduced Timing Precision Requirement

The phase stability of our VIS setup over several hours has been proven in a demonstration experiment on the laser dye Nile Blue [78], and short term stability values of $\frac{\lambda}{92}$ have been found. A detailed discussion can be found in [81]. Here, we will focus on the implications of pairwise beam manipulation for the necessary timing precision in the experiment.

To verify that pairwise beam manipulation greatly reduces the timing precision required to obtain a distortion-free 2D spectrum, we carried out a series of 2D measurements where we deliberately misplaced the piezo actuators and compared the resulting spectra to those recorded without misplacements. For these experiments we chose HITCI, a laser dye, dissolved in ethanol (OD ~ 0.3 in 200 μm path length) as a molecular sample and used 30 fs pulses spectrally centered at 730 nm for excitation. The linear absorption spectrum of HITCI in ethanol is shown in figure 3.7 (a), along with the excitation spectrum used. Pulse energies at the sample were 1-2 nJ per pulse in a 160 μm diameter spot ($\frac{1}{e^2}$ intensity level).

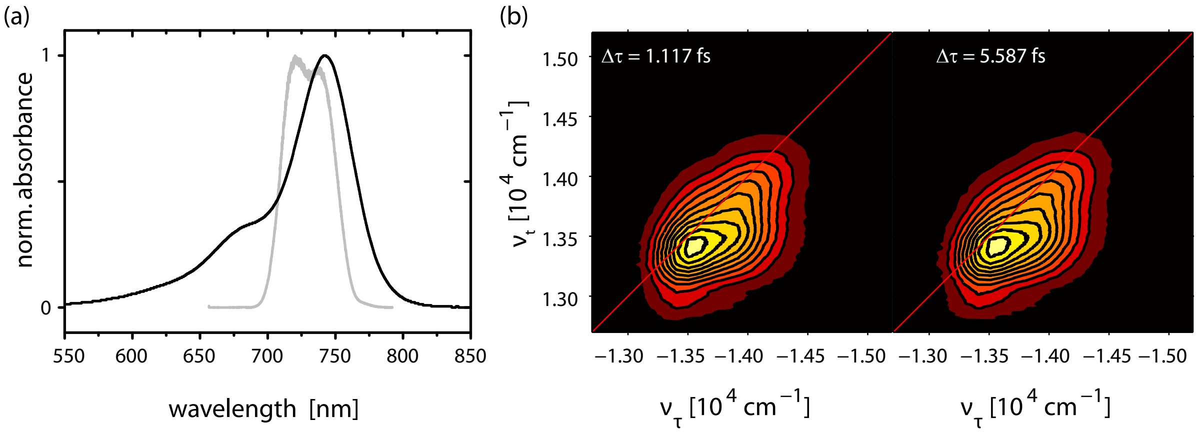

Figure 3.7: (a) Normalized linear absorbance of the laser dye HITCI in ethanol (black) and laser intensity (gray). (b) Comparison of absolute values of the 2D spectra obtained from sampling with $\Delta\tau_0 = 1.117$ fs (left) and $\Delta\tau_0 = 5.587$ fs (right). Five spectra have been averaged for the right graph in order to obtain comparable signal to noise ratios.

On purpose misplacements of the piezo positions $x_{i\sigma}$ were introduced as random Gaussian offsets to the positions x_{i0} of an unperturbed coherence time scan, i.e.

$$x_{i\sigma} = x_{i0} + \Delta x_{i\sigma} \quad \text{with} \quad P(\Delta x_{i\sigma}) = \frac{1}{\sqrt{2\pi\sigma}} \mathrm{e}^{-\frac{1}{2}\left(\frac{\Delta x_{i\sigma}}{\sigma}\right)^2}. \tag{3.15}$$

For a population time of $T = 200$ fs the coherence time was varied between $\tau_0 = \pm 162.023$ fs in steps of $\Delta\tau_0 = 5.587$ fs, and five different misplaced realizations were recorded for each value of σ. Sampling with $\Delta\tau_0 = 5.587$ fs yields virtually identical spectra to sampling at $\Delta\tau_0 = 1.117$ fs, the Nyquist step size imposed by the transition frequencies of the molecule studied, as can be seen from the absolute values of the 2D spectra obtained for the two cases for $\sigma = 0$ (figure 3.7(b)). Here, the real and imaginary parts of five spectra measured with the larger step size have been averaged to obtain a comparable signal to noise ratio in both cases.

As a matter of fact, these $\sigma = 0$ fs measurements are of course subject to the intrinsic positioning inaccuracy of the piezo actuators, specified as < 15 nm (or 0.1 fs) by the manufacturer. Nevertheless, we will refer to them as $\sigma = 0$ fs to indicate that there has been no *intentional* misplacement.

In addition to these $\sigma = 0$ measurements two-dimensional spectra were recorded for standard deviations σ of $\sigma = 75$ nm, $\sigma = 150$ nm, $\sigma = 375$ nm , $\sigma = 500$ nm, $\sigma = 750$ nm as well as $\sigma = 1125$ nm, that relate to the oscillation period of the employed laser pulses $T_0 = \frac{\lambda_0}{c} = 2.435$ fs $\sim T_{eg}$ as $\frac{\sigma}{T_0} = 0.2$, $\frac{\sigma}{T_0} = 0.4$, $\frac{\sigma}{T_0} = 1.0$, $\frac{\sigma}{T_0} = 1.4$, $\frac{\sigma}{T_0} = 2.0$, and $\frac{\sigma}{T_0} = 3.1$, respectively.

The absolute values of the 2D spectra obtained for different values of the misplacement σ are compiled in figure 3.8 (a): All data sets have been normalized to the maximum absolute value of the 2D spectrum depicted in the first row, that results from averaging over the real and imaginary parts of the five individual 2D spectra depicted in rows 2-5, to emphasize the effect of the misplacements on the reconstructed lineshape. In

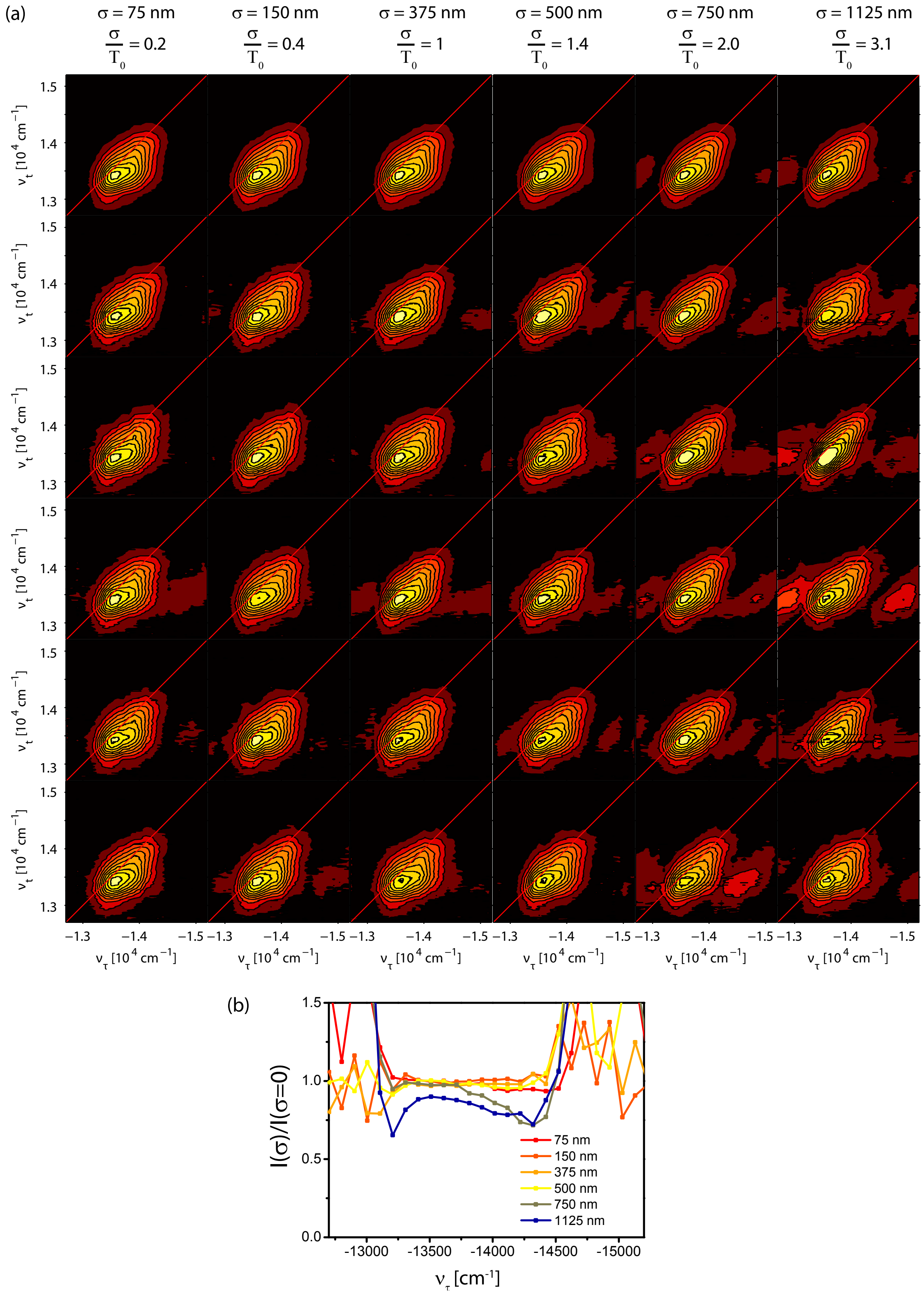

Figure 3.8: Two-dimensional spectra obtained with deliberate misplacements in τ (a): Different columns correspond to different standard deviations as indicated on the top. Averaging over the real and imaginary parts of rows 2-5 within each column yields the top row. Within each column, spectra are normalized to the maximum of the averaged spectrum. Frequency dependence of the amplitude deviation, $I(\sigma,\nu_\tau)/I(\sigma=0,\nu_\tau)$ (b).

the individual realizations we recognize that the fluctuations in the piezo positions, i.e. in the time-domain, result in signal amplitude outside the spectral range of the unperturbed 2D spectrum. For $\sigma \leq 500$ nm, however, these distortions are limited to the 5% contour line in magnitude, and the shape of the averaged 2D spectrum remains virtually unchanged. To quantify the excitation frequency dependent amplitude loss associated with the reduced timing precision, the absolute value of the averaged 2D spectra has been integrated over the detection frequency ν_t yielding

$$I(\sigma, \nu_\tau) = \int \mathrm{d}\nu_t \, |S_{2D}(\sigma, \nu_t, \nu_\tau)| \, . \tag{3.16}$$

The ratio $I(\sigma, \nu_\tau)/I(\sigma = 0, \nu_\tau)$ is depicted in figure 3.8(b) for the different values of sigma. Here, to minimize effects arising from spectral drifts of the laser or changes of the sample OD, different reference data sets $I(\sigma = 0, \nu_\tau)$ derived from averaging over in total four $\sigma = 0$-spectra measured before and after the five spectra for each σ have been used. From figure 3.8(b) we see that not only the line shape but also the magnitude of the signal remains virtually unchanged for $\sigma \leq 500$ nm, i.e. $I(\sigma, \nu_\tau)/I(\sigma = 0, \nu_\tau) \geq 0.95$. For larger misplacements we observe a decrease in the integrated reconstructed amplitude down to 75% for $\sigma = 1125$ nm. This amplitude decrease is significantly more severe on the high frequency side as one would expect given the shorter corresponding oscillation periods T.

While it is hardly reasonable to define a minimum required timing precision for all 2D experiments, because this will always depend on the particular features one wishes to resolve, we can compare the above results to the requirements of other experimental layouts: Setups that manipulate the arrival times of the individual excitation pulses, such as e.g. [35] and [68], will not be able to reconstruct any signal amplitude when the random fluctuations of their positioning means reach half the oscillation period of the system transition frequency, i.e. $\frac{\sigma_t}{T} = 0.5$ as we have learned in section 2.5.2. This compares to amplitude distortions smaller than 5% even at $\frac{\sigma_t}{T} = 1$ in the presented HITCI-measurements, which in conventional setups can only be achieved with a timing precision of $\frac{\sigma_t}{T} = 0.05$ as calculated from

$$\mathrm{e}^{-\frac{1}{2}(\frac{2\pi\sigma_t}{T})^2} = 0.95. \tag{3.17}$$

This experimentally proves that the required timing precision and mechanical stability in setup designs that rely on pairwise beam manipulation is more than an order of magnitude lower than in setups that steer individual beams.

3.4 Fully Non-Collinear Two-Dimensional Spectroscopy in the Ultraviolet

With the success of electronic two-dimensional spectroscopy in the visible spectral range, its extension to ultraviolet is a logical step: Excitation at shorter wavelengths gives access to smaller molecules, that can be treated at a higher level of theory. Thus 2D-UV spectroscopy could be used as a probe of ab initio electronic structure calculations. On the other hand, these small molecules are often embedded in highly complex molecular superstructures, e.g. in biomolecules. Here, theoretical two-dimensional spectra of the DNA double helix [82] predict that 2D UV spectroscopy could eventually help to clarify the efficient deactivation pathways that make the genetic code so remarkably photostable. The group of Shaul Mukamel extensively studied the coupling between aromatic aminoacids in proteins and found, that 2D UV spectra are sensitive to the structure and growth kinetics af potentially neurotoxic amyloid fibrils [83–86].

While theoretically proposed 2D UV spectra of the protein back bone, i.e. around 200 nm, seem beyond the possibilities of frequency-doubled noncollinear OPAs setups in the near future, even in the 250-400 nm spectral range where ultrashort light sources become more and more available [87,88] two-dimensional spectroscopy is highly challenging. Some of these challenges are not 2D-specific, but affect also other (time-resolved) spectroscopies in the UV [89]: First, the signal from a UV chromophore will often be much lower than in the visible, because transition dipoles e.g. of aromatic amino acids such as Tryptophan, Tyrosine, and Phenylalanine are several orders of magnitude smaller than those of visible chromophores. The possibilities to compensate these smaller extinction coefficients with a higher molecule concentration or longer optical path lengths are limited by unwanted aggregation and propagation effects in long samples.

Moreover, detection of these smaller signals is complicated by a significant increase in scattering contributions from the pump pulses that interfere with the signal: Rayleigh scattering increases with the fourth power of frequency, resulting in an 80 times higher scattering intensity at 267 compared to 800 nm.

Furthermore, with a shorter wavelength, one approaches the electronic resonances of literally all materials, even optical glasses and crystals. Hence, dispersion effects are significant as becomes evident from the following example: After propagation through 2 mm of fused silica, an initially transform limited pulse of 20 fs duration centered at 800 nm is only negligibly stretched to 22 fs. In contrast, the same amount of glass will almost triple the duration of an initially 20 fs pulse centered at 266 nm to 58 fs. Consequently, transmissive optics should be avoided to maintain maximum time resolution. Even the dispersion of air can no longer be neglected, calling for short beam paths in the experiment. As has recently been shown theoretically and experimentally, a small linear chirp on the excitation pulses already causes a mixing of real and imaginary parts of the third-order polarization [90]. The resulting deformations in the 2D spectra can erroneously be interpreted as spectral broadening or cross peaks, which emphasizes the need for precise dispersion control. In addition, nonresonant contributions during temporal pulse overlap increase drastically as one- and two-photon resonances are approached [91] and interfere with the resonant signal emitted by the chromophore. Though often neglected, nonresonant contributions in FWM have been observed in the visible [92], and heterodyne detection was applied to identify and subtract them. In the UV, careful analysis has to be carried out to obtain the purely resonant short-time dynamics.

On top of all these issues that pertain to all time-resolved and even linear spectroscopies in the ultraviolet domain, phase stability has to be accomplished for a 2D UV experiment. After the detailed discussion in section 3.2.2 we now know, that this will be roughly twice as hard in the UV where excitation frequencies double compared to measurements in the visible.

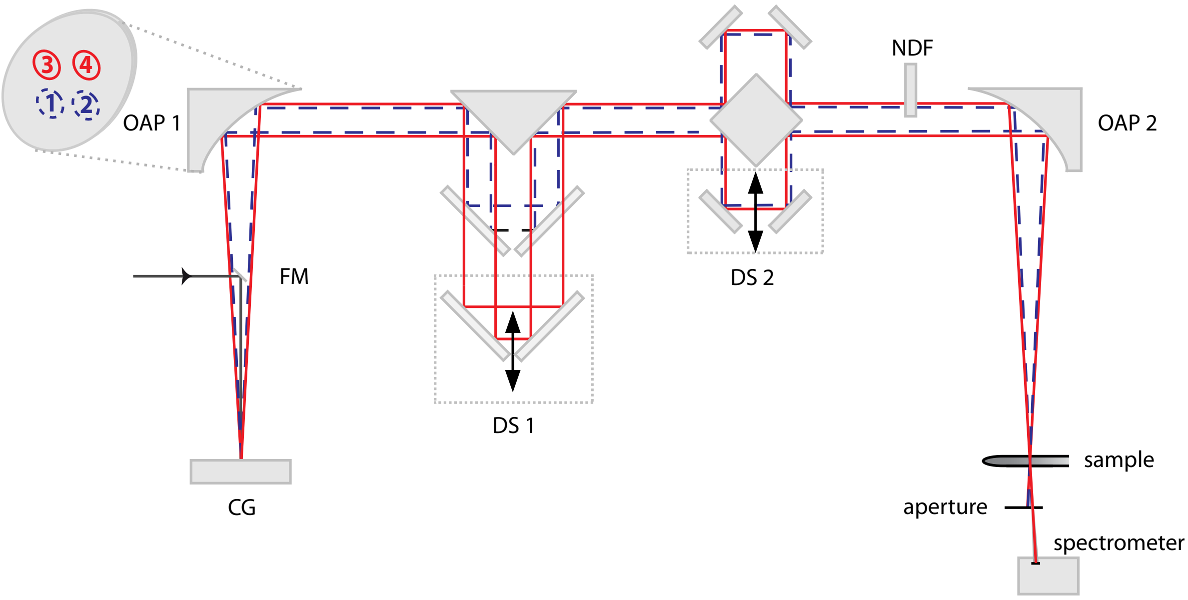

Figure 3.9: All-reflective setup for fully non-collinear 2D spectroscopy in the UV.

In fact, by the time we developed and published our 2D UV-setup the shortest wavelength employed in noncollinear 2D experiments was 400 nm [93], and 266 nm excitation had only recently been shown with a setup employing an acousto-optic modulator pulse shaper [94]. Since then, 2D UV photon echo studies of the monomeric DNA bases Adenine [95, 96], Uracil [95] and Thymine [97] have been reported, and ultrabroadband incoherent two-dimensional spectroscopy was demonstrated [98].

3.4.1 Setup

To optimally suit the needs of fully noncollinear multidimensional spectroscopy in the ultraviolet, we combined the concept of pairwise beam manipulation with an all-reflective optical layout [89].

In this setup (figure 3.9) the incoming UV-beam is focused with a $f = 50$ cm spherical aluminium (Al) mirror onto an Al-coated crossed grating ($g = 6.25\,\mu$m), a custom-made item by Carl Zeiss MicroImaging. Its first diffraction orders are recollimated with an off-axis parabolic mirror ($f = 15$ cm, OAP 1), and all except the four beams used for excitation and heterodyne detection are blocked by a mask (not shown). These four beams then pass a first delay stage (DS 1) composed of an Al-coated 90° prism and a vertically split rooftop mirror. The upper half of the latter can be displaced with respect to the lower half with a piezo actuator (PX 200CAP, Piezosystem Jena) mounted on a motorized stage (MFA-CC, Newport). Thus, a well-defined time delay of up to ~ 150 ps can be introduced between beams 3 and 4 with respect to 1 and 2. To adjust the coherence time, i.e. delay beam pair 1 and 3 with respect to 2 and 4, a second delay stage (DS 2) is used: It consists of a combination of an Al-coated glass cube and two opposing rooftop mirrors, one of which is mounted on a second piezo actuator and supports a maximum delay of ≥ 1 ps, i.e. a coherence time range of $\tau \geq \pm 500$ fs.

To delay the local oscillator by ~ 2 ps with respect to the three excitation pulses and attenuate its intensity it passes a 1-mm-thick variable neutral density filter wheel (NDF). All four beams are focused into the sample by a second off-axis parabolic mirror (OAP 2, $f = 15$ cm) to a common 250 μm spot ($\frac{1}{e^2}$ intensity level). After the sample beams 1-3 are blocked by an aperture, while the interference of LO and third-order signal field is detected with the same spectrometer used for the 2D VIS-experiments, i.e. an Acton Spectra Pro 2500i with PIXIS 2K CCD camera. Again, the excitation beams can be blocked individually via automated shutters to record and subtract scattering terms (not shown).

With the parameters given here, this setup is optimized for applications between 250 and 375 nm. Its concept could, however, be transferred to other wavelength regimes. The small footprint of the arrangement (20 cm × 30 cm) minimizes the UV beam path in air and contributes to the setup stability. The transverse beam separation within the interferometer is below 1.5 cm.

3.4.2 Demonstration Experiment and Phase Stability Proof

To prove the feasibility of fully noncollinear two-dimensional spectroscopy in the ultraviolet spectral range, we chose para-terphenyl (pTP) dissolved in ethanol as our molecular sample. As the name implies pTP is a linear molecule consisting of three covalently linked phenyl-rings (cf. inset of figure 3.10 (a)). The antagonistic interplay of conjugation over neighboring phenyl rings and *ortho*-hydrogen repulsion leads to a finite torsional angle between the phenyl ring planes in solution [99]. PTP's first electronic transition is associated with a strong ($\epsilon > 3 \times 10^4$ lmol^{-1}cm^{-1}), broad, and featureless peak centered at 280 nm in ethanol. Upon photoexcitation the molecule planarizes and the librational motion of neighboring phenyl rings has to be taken into account to explain its strongly modulated fluorescence that significantly deviates from simple mirror image symmetry [100].

The pTP molecule had been investigated before by homodyne four-wave-mixing techniques [101, 102], and we chose a similar excitation wavelength of $\lambda = 287$ nm for our experiments. Pulse energies at the sample position were 3-5 nJ/pulse and from the transient grating signal of a 100 μm fused silica plate we retrieved a pulse duration of 50 fs corresponding to 1.1 times their transform limit.

PTP (Sigma-Aldrich) and ethanol (Uvasol, Merck) were used as received. The mixture was heated slightly to 25°C, sonicated for several hours, and filtered to remove scattering particles. During the experiments the pTP-solution with an optical density of 0.45 at the excitation wavelength was cycled through a 200 μm fused silica flow cell with a micro-angular gear pump.

To ensure the 2D signal we detect originates from the pTP chromophore and not the solvent, we first recorded transient grating data of pTP in solution and neat solvent, i.e. we scanned the population time for $\tau = 0$ fs and heterodyned the emitted signal field with the local oscillator. Integrating the signal intensity retrieved from the data analysis procedure described in section 3.3.2 over the wavelength axis yields the data displayed in figure 3.10 (b) and (d). In the data of the pTP solution we immediately recognize a a dominant peak at time zero that has to be attributed largely to nonresonant

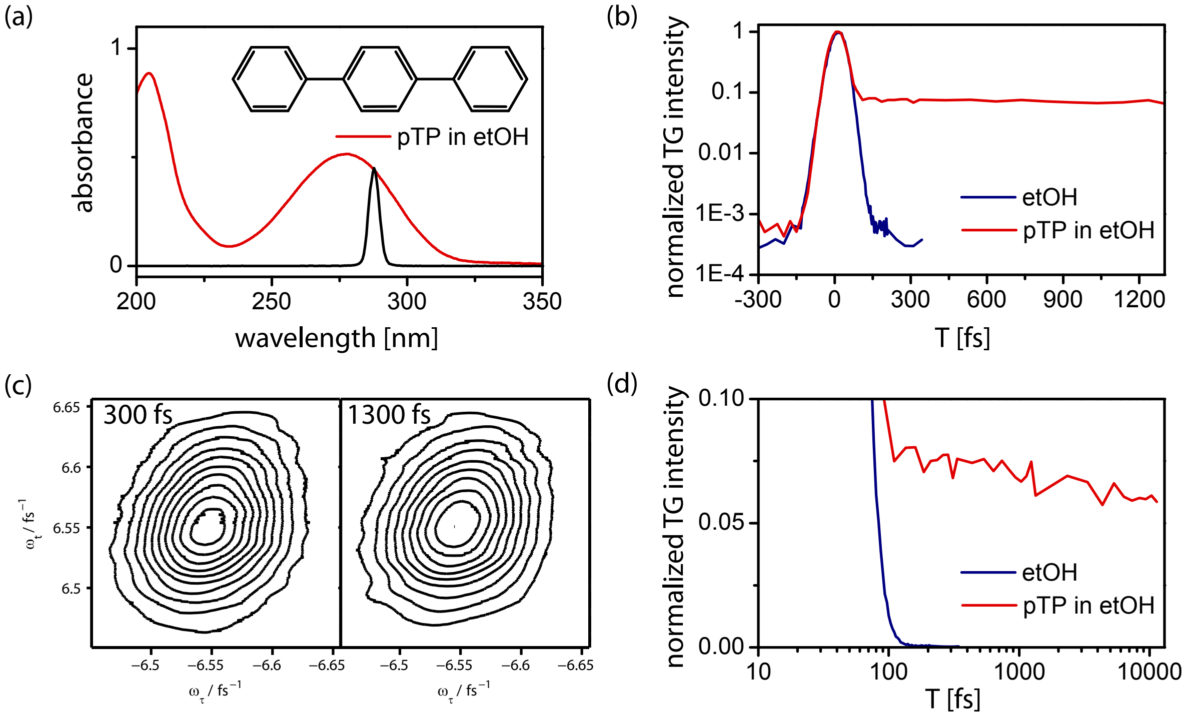

Figure 3.10: (a) Linear absorbance of pTP in ethanol (200 μm path, red) and laser spectrum (black) as well as molecular structure of pTP . (b) and (d) Normalized transient grating intensity of neat ethanol (blue) and pTP dissolved in ethanol (red). (c) absorptive 2D spectra of PTP in ethanol for $T = 300$ fs and $T = 1300$ fs. Contour lines from 10% to 90% of the maximum of the $T = 300$ fs data are drawn in steps of 10%

contributions from the cuvette glass windows and the solvent. At $T > 100$ fs, when these signals have ceased because the excitation pulses no longer overlap temporally, the pTP signal exhibits a decay constant in the low ps regime. This latter finding agrees with the $\sim$ 6 ps time constant that has been reported in and assigned to spectral diffusion due to ground state hole relaxation.

In the absorptive two-dimensional spectra of pTP recorded for $T = 300$ fs and 1300 fs this decay is reflected in a 7% decrease in overall amplitude. As a result of the narrow laser bandwidth compared to the broad pTP absorption, virtually no shape changes are found between the two population times. Yet our primary aim, to prove the feasibility of 2D UV, has been accomplished.

To quantify the phase stability of the setup, we performed two long term measurements: In a first experiment we recorded the spectral interference of the LO and the third order signal field of the pTP solution for $\tau = 0$ fs $T = 500$ fs with an integration time of 2 s over 5 hours. For each data point the signal phase was reconstructed following the procedure described earlier and the deviation with the respect to the phase of the first acquired data point is shown in figure 3.11. An initial phase drift to $\sim -\frac{\pi}{10}$ is observed and attributed to equilibration processes in the setup after sample insertion. These data exhibit a standard deviation of 0.096 rad over 5 hours corresponding to a stability of $< \frac{\lambda}{65}$, i.e. a mechanical stability of 4.4 nm in a setup that does not rely on

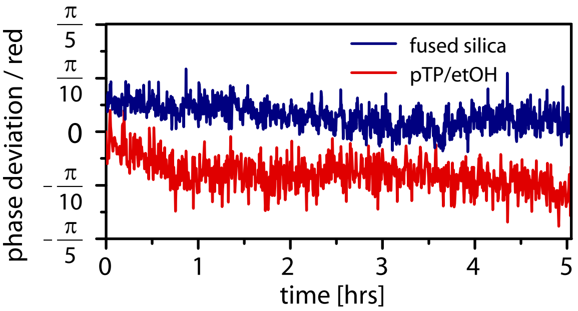

Figure 3.11: Phase stability data retrieved from pTP in ethanol (red) and fused silica (blue)

	Prokhorenko et al. [103]	our setup
short term stability	$\frac{560\text{ nm}}{125}$	$\frac{287\text{ nm}}{130}$
long term stability	$\frac{560\text{ nm}}{90}$	$\frac{287\text{ nm}}{90}$

Table 3.1: Comparison of the best stability values reported in the VIS and our best values

pairwise beam manipulation. As 2D spectra can be phased individually to pump probe data, the more relevant quantity is, however, the stability over a single coherence time scan, which for the 2D spectra displayed in figure 3.10 was 50 minutes. Evaluating the same data set over these shorter time intervals we find typical stability values of $\frac{\lambda}{79}$, and variations as low as $\frac{\lambda}{88}$ can be achieved. In addition to the phase stability, these data also demonstrate the reproducibility of the delay positioning is clearly sufficient for a 2D experiment: Every 18 minutes both delay stage were moved to $\tau = 10$ fs, $T = -6.2$ ps for one point and then back to $\tau = 0$ fs $T = 500$ fs. The random phase values reconstructed for negative population times have been omitted from figure 3.11 for clarity.

To exclude the possibility of fast phase fluctuations averaging out over the 2 s integration time and to facilitate comparison with literature stability values, we then repeated the above experiment with the $\tau = T = 0$ fs signal of a 1 mm fused silica glass substrate and 0.3 s integration time. The resulting phase deviation is shown in blue in figure 3.11, offset by $\frac{\pi}{20}$. In this case, the phase stability value over 5 hours is $\frac{\lambda}{85}$, and typically $\frac{\lambda}{109}$ over 50 minutes, where $\frac{\lambda}{130}$ was the best value realized . Again, both delay stages have been moved over the same distances every 12 minutes. The higher stability values of the fused silica compared to the pTP experiment can be traced back to a better ratio of signal to coherently scattered light. Notably, the stability values we determined for our UV setup are comparable to the best values that have been reported in the visible [103], but have been realized at much shorter wavelength (cf. table 3.1).

3.5 Conclusion

In the scope of this thesis two setups for multidimensional spectroscopy, one for visible excitation $\lambda > 500$ nm and one for ultraviolet wavelengths (250 nm - 400 nm), have been developed. In both layouts the concept of pairwise beam manipulation (PBM) is realized: When steering the four beams of a 2D experiment only in pairs that enter the measured phase with opposite sign, the detected signal modulation is goverend by the difference between system and laser frequency $\Delta\omega = \omega_{eg} - \omega_0$, rather than the much faster oscillation of the transition frequency ω_{eg}. In other words, the rotating frame is inherent in a PBM scanning scheme. Hence, the full benefits of a noncollinear beam geometry

– higher sensitivity, separation of non-rephasing and rephasing Liouville pathways as well as measurement of absorptive and dispersive 2D spectra – can be retrieved under timing precision and mechanical stability requirements that are significantly reduced to fractions of the pulse duration.

This has been theoretically derived for the more illustrative case of a linear polarization, experimentally demonstrated in measurements were mis-timings were deliberately introduced, and led to phase stabilities measured at ultraviolet wavelengths that are comparable to the best values reported for the visible.

Both presented designs can in principle be transferred to other wavelength regimes. The VIS implementation based on only conventional optics represents a robust, simple and cost-efficient alternative for noncollinear two-dimensional spectroscopy that will be particularly beneficial for less dispersion sensitive applications in the VIS, NIR and IR spectral range. The all-reflective layout on the other hand is a high-end solution that specifically suits the needs of 2D-UV, but should be considered also for other excitation conditions that require precise dispersion control.

4 Energy Redistribution in a Coupled PBI-Bichromophore

We will start out our studies on energy transfer in coupled multichromophore systems with the simplest system possible, the dimer.

The presented project has been a cooperation within the framework of the Graduiertenkolleg 1221 "Steuerung elektronischer Eigenschaften von Aggregaten π-konjugierter Moleküle". The investigated compounds have been synthesized in the group of Prof. Dr. Frank Würthner and *ab initio* calculations have been performed in the group of Prof. Dr. Bernd Engels, both members of the Chemistry Department at the University of Würzburg.

The building block of our model dimers will be a perylene bisimide (PBI) unit, a substance class that has gained much attention in the last decades because PBIs uniquely combine high extinction coefficients tunable across the visible spectral range with remarkable photo- and thermal stability [104]. Besides, its electron deficiency makes it one of the best n-type organic semiconductors known to date [105] motivating extensive research efforts associated with potential applications in organic optoelectronics.

We will begin this chapter with a short introduction to the properties of this remarkable chromophore, followed by a discussion of the structures and linear spectral properties of the specific substances we will be dealing with. To provide a basis for a thorough discussion on the energy transfer in a real dimer, two vastly different theoretical methods will be applied and their ability to reproduce the linear spetra will be compared: The transition-point-dipole approximation and a high-end ab initio electronic structure calculation performed in the group of Professor Bernd Engels. Even though we will find strong evidence for excitonic coupling in the linear absorption spectra, we will close our theoretical treatment with the calculation of transfer rates in the framework of Förster theory, the common incoherent standard in the description of intermolecular energy transfer.

In the subsequent experimental section transient absorption (TA) data acquired for two different pump-wavelengths will be presented along with two-dimensional spectra measured with the box-geometry setup introduced in section 3.3. Thorough analysis of global fits to the TA data sets will allow us to disentangle ultrafast rates for the inter-chromophore energy transfer from the similarly fast processes of solvation and vibrational relaxation. To consistently describe the observed dynamics on the ~ 100 ps to nanoseconds time scales, a model including conformational dynamics and intermolecular charge transfer will be developed. Finally, the findings will be summarized and an outlook on future work will be given.

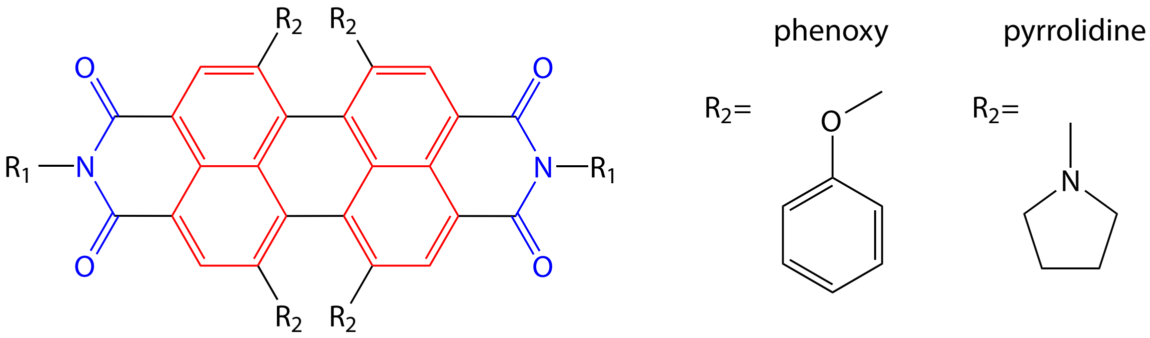

Figure 4.1: The perylene bisimide chromophore consists of two naphthalene half units (red), each of which is attached to an imide unit (blue). Substituents at the imide nitrogen, R_1, mainly control the solubility, while substituents at the bay positions, R_2, affect solubility and spectra.

4.1 The Perylene Bisimide Chromophore

Perylene bisimide (figure 4.1) belongs to the family of rylene dyes and consists in its simplest form of two naphthalene half units (the perylene core) each of which is attached to an imide unit [104, 106].

The extended π-system of such a two-dimensional chromophore leads to strong long-wavelength absorption paired with a very high photostability compared to a linear (1D) counterpart, where many more conjugated double-bonds are needed to shift electronic transitions to the visible spectral range [107]. The electron deficiency of the PBI disfavors photooxidation, a major destruction mechanism, and further contributes to the stability [104].

Furthermore, attractive π-π interaction between PBI chromophores enables self-organized aggregation into supramolecular structures. However, extended π-systems are difficult to solubilize, and synthetic solutions to overcome this drawback are called for. As the HOMO and the LUMO exhibit nodes at the imide nitrogens, solubilizing substituents added at the imide positions are only weakly coupled to the actual chromophore [108] and leave its low-energy electronic transitions, i.e. absorption and fluorescence properties, almost unchanged, as long as they are fixed in an orthogonal conformation. On the other hand, substituents at the carbocyclic scaffold, the so-called bay area, affect both the solubility of the system and its spectra and are frequently used to tune the absorption and emission of PBIs from the visible to the near-infrared region.

The bay-unsubstituted PBI [104] exhibits the highest S_0-S_1 transition energy ($\lambda_{\text{abs}} = 526$ nm in chloroform). Its spectrum shows a characteristic pronounced vibronic progression and its near quantitative orange fluorescence ($\Phi_F = 1$, $\lambda_{\text{em}} = 533$ nm in chloroform) is offset by a small Stokes-shift only. Bay-substitution with phenoxy-groups bathochromically shifts the absorption (to $\lambda_{\text{abs}} = 573$ nm in chloroform for four-fold substitution), an additional blue-shifted absorption peak attributed to S_0-S_2-absorption appears, and the vibronic progression is less pronounced. These phenoxy groups introduce a sterical strain in the bay area that leads to a propeller-like twisting of the two naphthalene half units with torsional angles $\Theta \sim 30°$ and different conformations [109–111] corresponding to extended or folded phenoxy substituents [111] exist. These red PBIs show a moderate solvatochromism. With the addition of strongly electron-donating groups such as pyrrolidine a redshift up to $\lambda_{\text{abs}} = 686$ nm in chloroform can be achieved, accompanied by a NIR emission ($\lambda_{\text{em}} = 721$ nm in chloroform) and a large Stokes-shift caused by the charge transfer (CT) character of the transition. The CT leads to a non-radiative deactivation of the excited state via charge recombination that competes with fluorescence and significantly reduces the quantum yield to $\Phi_F = 0.35$ in chloroform. These green PBIs are often reported to be the least stable in solution [112].

For all these chromophores, the transition dipole moment of the first electronic transition is aligned along the long axis of the PBI core [113].

While applications of perylene-bisimides include optical recording media, organic photo- and semiconductors, and solar cells [114], studies of immediate relevance for our experiments are time-resolved investigations of perylene-based poly($2 \leq N \leq 10$)-chromophoric assemblies in solution. Besides systems composed of the same (=homo) [115–120, 120–122] or different (=hetero) [112, 123, 124] PBIs, combinations of PBIs and other chromophores [111, 125–135], among them e.g. structurally related rylene chromophores such as terrylene [126] and perylene monoimides [124], pyrenes [127, 128, 136] and porphyrins [132, 134, 137, 138] have been synthesized into arrangements ranging from J-type [115–117, 122, 123] or H-type dimers [115, 119, 121, 139], to zigzag-arrays [112], molecular squares [128] and dendrimers [111, 125–127].

The focus of these studies – inspired by possible applications of PBIs as light harvesting antennas and/or electron acceptors – lies of course on the efficiency of intermolecular energy transfer as well as charge transfer to the electron-deficient PBI unit and their often complex competitive interplay.

Typically, energy transfer within such systems is discussed as a Förster process, i.e. an incoherent process arising from the coupling of the transition dipoles of the chromophores, and at least satisfactory agreement is found. However, for small intermolecular distances higher rates than predicted by Förster theory have been reported [138, 140].

For a structurally related perylene monoimide-terrylene bisimide (PMI-TBI) dyad bridged via a pentaphenylne spacer, single molecule spectroscopy combined with extensive theoretical modeling of the electronic interaction beyond Förster theory showed an $\sim$ 3-fold increase in electronic interaction originating from bridge contributions to the donor excited state [141]. The influence of molecular orbitals of a bridging spacer on electronic coupling, in particular their beneficial role for interchromophore charge transfer in a J-type PBI-bridge-PBI homo-dyad had earlier been addressed in [116]. Another notable exception from the Förster treatment are the time-resolved single-molecule studies carried out in the group of van Hulst [142, 143], that addressed the effect of static disorder and the role of vibrational modes in coherently coupled PBI complexes.

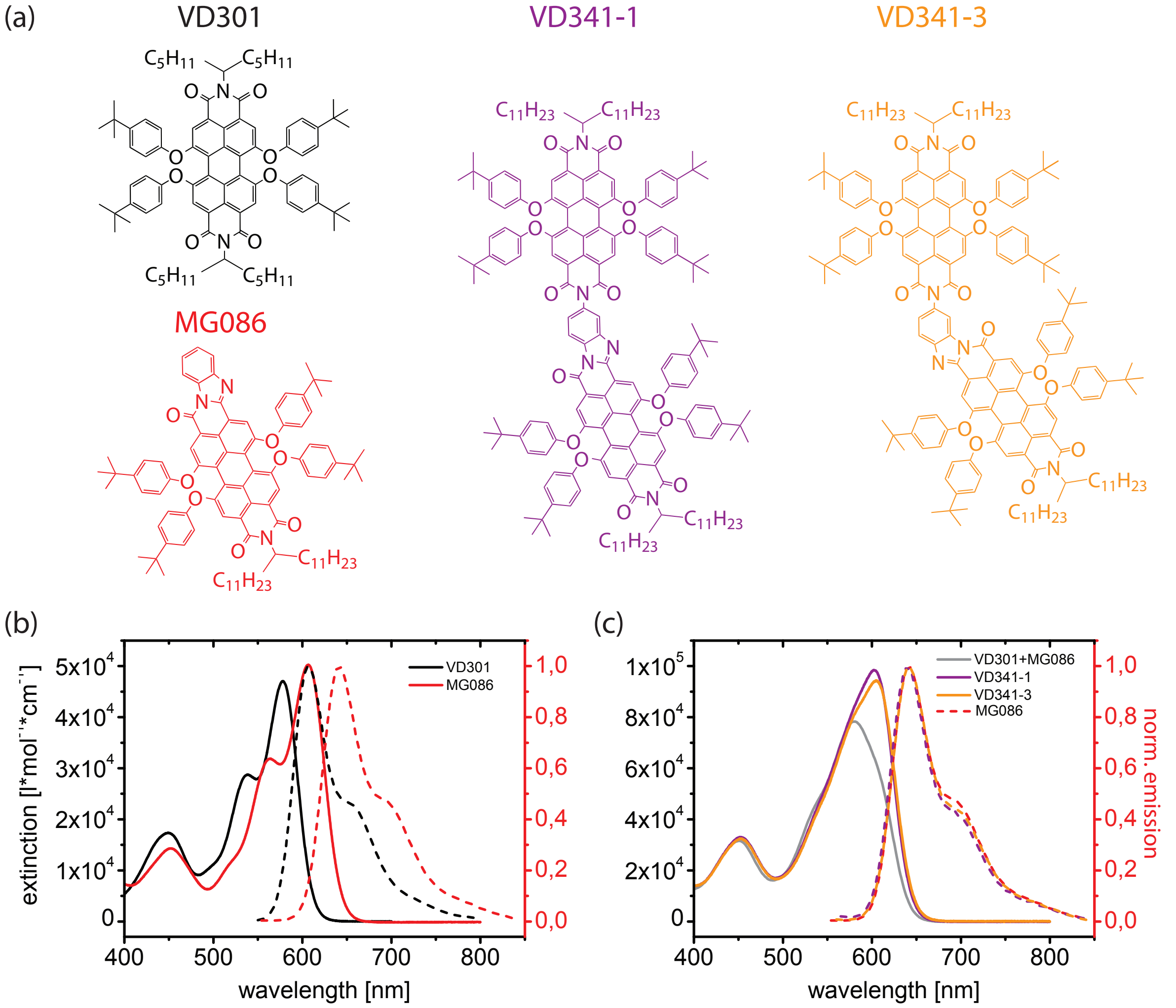

Figure 4.2: Structure (a), absorption (b and c, straight lines) and fluorescence (b and c, dashed) spectra in CH_2Cl_2 of the investigated compounds. See text for further explanations.

4.2 Structure and Linear Spectral Properties of the Investigated Compounds

The two bichromophores studied in the experiments described below are structural isomers of a tetraphenoxy perylene bisimide-tetraphenoxy imidazole-perylene monoimide synthetically fixed to a J-type arrangement with defined interchromophore angles. Their structures are shown in figure 4.2 (a) along with the structures of two monomeric reference compounds. All these substances were synthesized in the group of Professor Frank Würthner at the Department of Organic Chemistry, University of Würzburg. For the sake of simplicity, we will in the following adopt the compound-labelling that has been established in the Würthner group, i.e. the monomers will be referred to as VD301 and MG086, and the bichromophores as VD341-1 and VD341-3, respectively (cf. figure 4.2 (a)).

Even though the two reference chromophores are covalently linked in VD341-1 and

Table 4.1: Spectral properties and fluorecence quantum yield Φ_f in CH_2Cl_2

	λ_{abs}	ν_{abs}	λ_{em}	Φ_{f}
MG086	607 nm	16474 cm^{-1}	642 nm	0.83 ± 0.02
VD301	578 nm	17301 cm^{-1}	607 nm	0.94 ± 0.01
VD341-1	602 nm	16611 cm^{-1}	640 nm	0.29 ± 0.02
VD341-3	605 nm	16529 cm^{-1}	642 nm	0.43 ± 0.03

VD341-3, the node at the imide nitrogen in both the HOMO and LUMO of PBIs impedes conjugation over the linking phenyl ring. Geometry optimization (MOPAC, PM6 Hamiltonian, full structures) of the ground state in vacuum predicts dihedral angles of 62° and 43° for VD341-1 and VD341-3, respectively, for the torsion around the relevant C-N-single bond.

As the exclusion of dispersion interactions in this semi-empirical method is one of its many shortcomings, more elaborate computational methods were applied to the similar systems depicted in the insets of figure 4.5 (a) and (b) to study the role of this torsional motion in the first electronic transitions. To reduce the computational cost the imide substituents as well as the phenyl rings of the phenoxy groups of our original bichromophores have been replaced by methyl moieties. Volker Settels (Prof. Dr. Bernd Engels' group) performed calculations including Grimme's empirical dispersion correction for the ground state energies (BLYP-D level) and time-dependent Hartree-Fock methods (TD-HF) for the calculation of excited state energies, where the resulting excitation energies where then added to the BLYP-D ground state energies as dispersion is not accounted for in TD-HF (for details see TD-HF-D calculations described in reference [144]). The resulting potential energy curves as a function of the torsional angle ϕ (figure 4.5 (a) and (b), upper panels) exhibit a broad minimum in the ground as well as in the excited states corresponding to insignificant coupling of this mode to the radiative transitions. Furthermore, this torsion has negligible effect on the relative orientation of the S_0-S_1 transition dipoles of the monomers, because these are aligned along the long axis of the perylene core, i.e. the rotation axis for this motion. This allows us to treat these systems as (hetero-)dimers rather than a single extended chromophore, and study the energy transfer dynamics resulting from the Coulombic interaction of the two composing monomers assuming a fixed inter-transition-dipole angle of $\alpha_{VD341-1} = 158°$ and $\alpha_{VD341-3} = 140°$, respectively.

In the linear absorption spectrum of the phenoxy-PBI monomer VD301 in CH_2Cl_2 (figure 4.2 (b), black curve), we recognize the broad vibronic progression and the additional S_0-S_2 peak of a red PBI described in the previous section. Its fluorescence spectrum (black dashed line in figure 4.2 (b)) is redshifted by ~ 30 nm and beautifully mirrors the shape of the absorption. The same holds for the second reference substance, MG086, that is redshifted with respect to VD301 as a result of the replacement of one imide group by an imidazole (red curves in figure 4.2 (b)).

The absorption spectra of the bichromophores VD341-1 and VD341-3 (figure 4.2 (c)) look very similar, broad and unstructured/featureless, with the compound with the

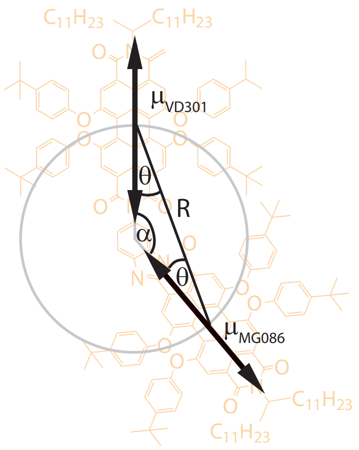

Figure 4.3: point-dipole model

	MG086	VD301	VD341-1	VD341-3
μ [D]	7.7	7.3	11.5	11.4
R [Å]	-	-	16.7	15.7
α [°]	-	-	158	140
θ [°]	-	-	11	20
V [cm^{-1}]	-	-	59	68
R_0 [nm]	-	-	8.0	7.9
τ_{FT}	-	-	450 fs	340 fs

Table 4.2: Parameters for calculation of dipole-dipole coupling, retrieved coupling strength V, Förster radius R_0 and Förster transfer time τ_{FT}

larger interchromophore angle, VD341-1, peaking at slightly bluer wavelengths (λ_{abs} = 602 nm vs. λ_{abs} = 605 nm) and exhibiting a slightly larger maximum extinction coefficient. Interestingly, both spectra differ significantly from the sum over the monomeric absorption spectra (gray curve), that one would expect for two uncoupled transition dipoles: The dimeric extinction is higher and red-shifted with respect to the simple sum in both cases. The normalized fluorescence spectra on the other hand, look virtually identical to the fluorescence spectrum of MG086, the reference compound with the lower S_0-S_1 transition energy, independent of the excitation wavelength (data not shown). This suggests that in both bichromophores the emissive state is the locally excited MG086 chromophore. The fluorescence quantum yield is significantly reduced in both dimers to $\Phi_{f,\mathrm{VD341\text{-}1}} = 0.29$ and $\Phi_{f,\mathrm{VD341\text{-}3}} = 0.43$ compared to the highly fluorescent monomers ($\Phi_{f,\mathrm{VD301}} = 0.94$ and $\Phi_{f,\mathrm{MG086}} = 0.83$) indicating the presence of a nonradiative decay channel in the bichromophores. The linear spectral properties including the fluorescence quantum yields are summarized in table 4.1.

4.3 Theoretical Predictions: Point-Dipoles vs. TD-HF-D

To gain deeper insights to the mechanisms underlying the shape of the linear spectra, we will now first approximate the bichromophores as the two transition dipoles μ_i of the reference compounds, separated by a distance R, inclining an inter-transition dipole angle α, and an equal angle θ between $\vec{\mu}$ and the distance vector $\vec{R}$ for both chromophores (figure 4.3). Comparison with the *ab initio* calculations performed by Volker Settels that more accurately reproduce the experimental linear absorption will then point out the limitations of the point-dipole approximation regarding a quantitative description.

As discussed in section 2.2 dipole–dipole coupling of the two transition dipoles should result in two delocalized excitonic excited states, with transition energies shifted by the

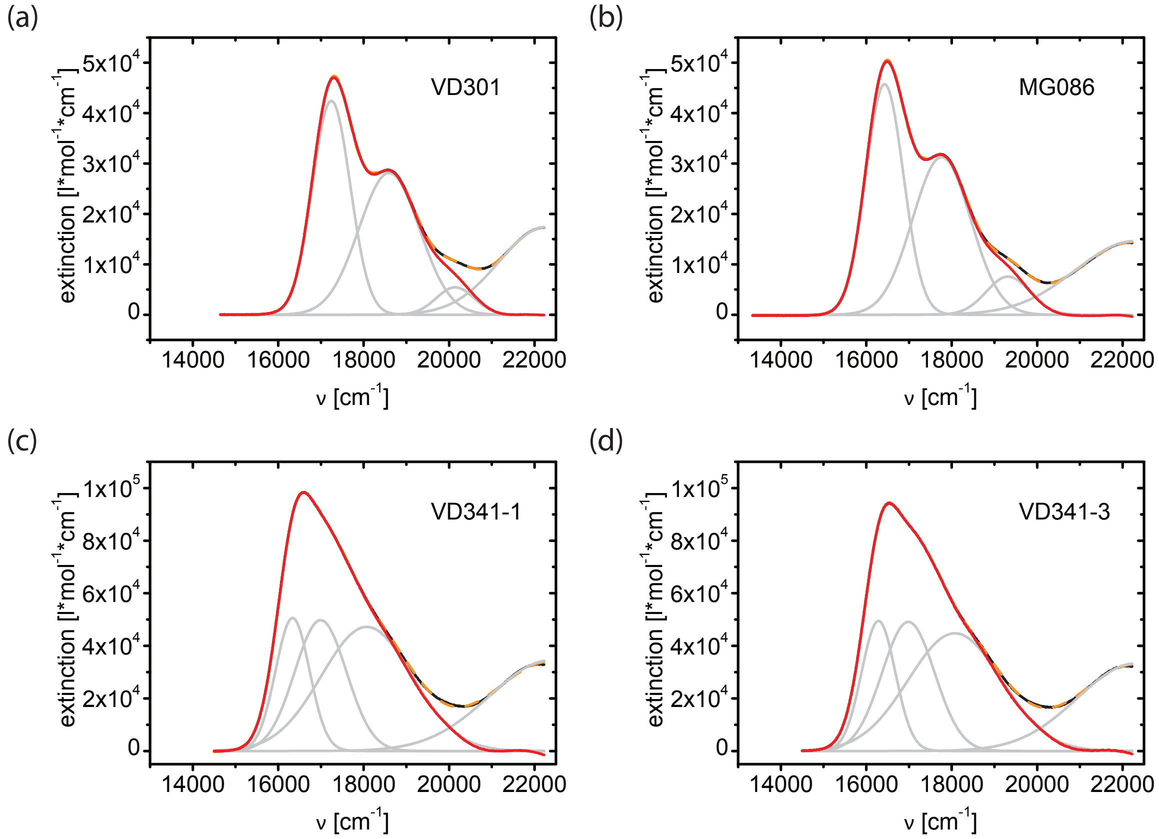

Figure 4.4: Retrieval of the transition dipole moments μ. Original spectrum (black), four gaussian fit (orange dashed), four gaussians (gray) and original extinction minus S_0-S_2 peak used for integration (red)

interaction energy V

$$V = \frac{1}{n^2}\frac{\mu_{MG086}\mu_{VD301}}{R^3}(\cos\alpha + 3(\cos\theta)^2) \tag{4.1}$$

relative to the transitions of the individual chromophores. To account for solvent screening of the dipole field a factor $1/n^2$ has been introduced, where n is the refractive index of the solvent. The magnitude of the transition dipoles of the individual substances can be calculated from an integral over the extinction coefficient $\epsilon(\overline{\nu})$ [110][1]:

$$\mu_i = \left(\frac{3hc\epsilon_0 \ln 10}{2\pi^2 N_A}\int \frac{\epsilon_i(\overline{\nu})}{\overline{\nu}}\,\mathrm{d}\overline{\nu}\right)^{1/2} \tag{4.2}$$

Here, h and N_A are Planck's and Avogadro's constant, respectively, c is the speed of light, ϵ_0 is the vacuum permittivity and the integral runs over the spectral range of the transition of interest. To minimize S_0-S_2-contamination in the calculation of μ all extinction curves $\epsilon(\overline{\nu})$ were individually fitted to a sum of four Gaussians, and the Gaussian

---

[1] Note that in this reference a factor of 10^{-3} has erroneously been introduced, presumably to account for the apparent mismatch of dm^{-3} and cm in the common units of the extinction coefficient, $\mathrm{M}^{-1}\mathrm{cm}^{-1}$. The values reported for the dipole moments are, however, correct.

corresponding to the S_0-S_2-transition was then subtracted from $\epsilon(\overline{\nu})$ before integration (cf. figure 4.4). The resulting transition dipoles are $\mu_{MG086} = 7.7$ D, $\mu_{VD301} = 7.3$ D, $\mu_{VD341-1} = 11.5$ D, and $\mu_{VD341-3} = 11.4$ D. Note that for the bichromophores the integral ran over both excitonic states as these are inseparable in the absorption spectra. The values retrieved for the monomeric transition dipoles are in the range expected from literature PBI and PMI values [110, 141] and conservation of oscillator strength is approximately fulfilled given $(7.7^2 + 7.3^2)\mathrm{D}^2 = 113\ \mathrm{D}^2 \approx 11.4^2\ \mathrm{D}^2 = 130\ \mathrm{D}^2$.

From the geometry optimization of the ground state in vacuum we get inter-chromophore center-to-center distances of $R_{VD341-1} = 16.7$ Å and $R_{VD341-3} = 15.7$ Å. Assuming the geometrical model depicted in figure 4.3, the angle between the transition dipoles and R, θ, is connected to the interchromophore angle α, $\theta = (\pi - \alpha)/2$. Substituting all these values along with the refractive index of DCM, $n = 1.42$ and the angles $\alpha_{VD341-1} = 158°$ and $\alpha_{VD341-3} = 140°$ into equation (4.1) results in couplings $V_{VD341-1} = 59\ \mathrm{cm}^{-1}$ and $V_{VD341-3} = 68\ \mathrm{cm}^{-1}$. The energetically more favorable alignment of the transition dipoles in VD341-1 is outweighed by the smaller interchromophore distance in VD341-3, leading to a larger coupling in the latter case. Both interaction energies are small compared to the energy difference between the monomeric reference compounds of $\Delta e = 827\ \mathrm{cm}^{-1}$ and small compared to all spectral linewidths ($> 1000\ \mathrm{cm}^{-1}$, cf. figure 4.4) at room temperature, i.e. point-dipole approximation predicts a weakly coupled system.

These findings at hand, we now expect the two excitonic states emerging from the transition point dipole coupling to largely maintain the character of the monomeric references MG086 and VD301 in terms of localization and transition energies. More precisely, for the predicted coupling strengths of $V \sim 70\ \mathrm{cm}^{-1}$ and an energy gap of $\Delta e = 827\ \mathrm{cm}^{-1}$, an amplitude ratio $\frac{\mathrm{MG086}}{\mathrm{VD301}} = \frac{\cos\theta}{\sin\theta}$ with the mixing angle θ, $\theta = \frac{1}{2}\arctan\frac{V}{\Delta e}$, of only $\cos\theta : \sin\theta = 24 : 1$ is expected for the excitonic states (cf. section 2.3). Consequently, in point-dipole approximation the linear absorption spectra of the dimers should closely resemble the sum over the two monomers (grey curve in figure 4.2) in disagreement with the experimental findings.

Qualitatively, the point-dipole predictions agree with the findings of much more elaborate ab initio BLYP-D/TD-HF-D calculations of Volker Settels on the simplified systems: The energy splitting between the two first electronic transitions (green and yellow curve in figure 4.5 (a) and (b)) of $\Delta E = 1248\ \mathrm{cm}^{-1}$ for $\alpha \sim 158°$ and $\Delta E = 1363\ \mathrm{cm}^{-1}$ for $\alpha \sim 140°$ is slightly larger for the smaller interchromophore angle. However, if we assume that the energy difference Δe between the simplified monomers is comparable to the value for MG086 and VD301, i.e. $\Delta e \sim 827\ \mathrm{cm}^{-1}$, the interaction energies of the ab initio calculations are significantly larger than the values calculated for point dipoles. This finding is not surprising given the spatial proximity of our chromophores: At small distances the molecules do no longer "see" each other as point dipoles, but the actual charge distribution becomes relevant and a description in terms of interacting transition densities is necessary. Stronger coupling results in more delocalized excitonic states as can be seen from the molecular orbital composition of the lower excitonic transition in the VD341-1-like compound depicted in figure 4.5 (c): TD-HF-D optimization predicts the LUMO of VD341-1 to be almost exclusively localized on the MG086 part, and the LUMO+1 on the VD301 half. HOMO and HOMO-1 are exclusively localized at MG086

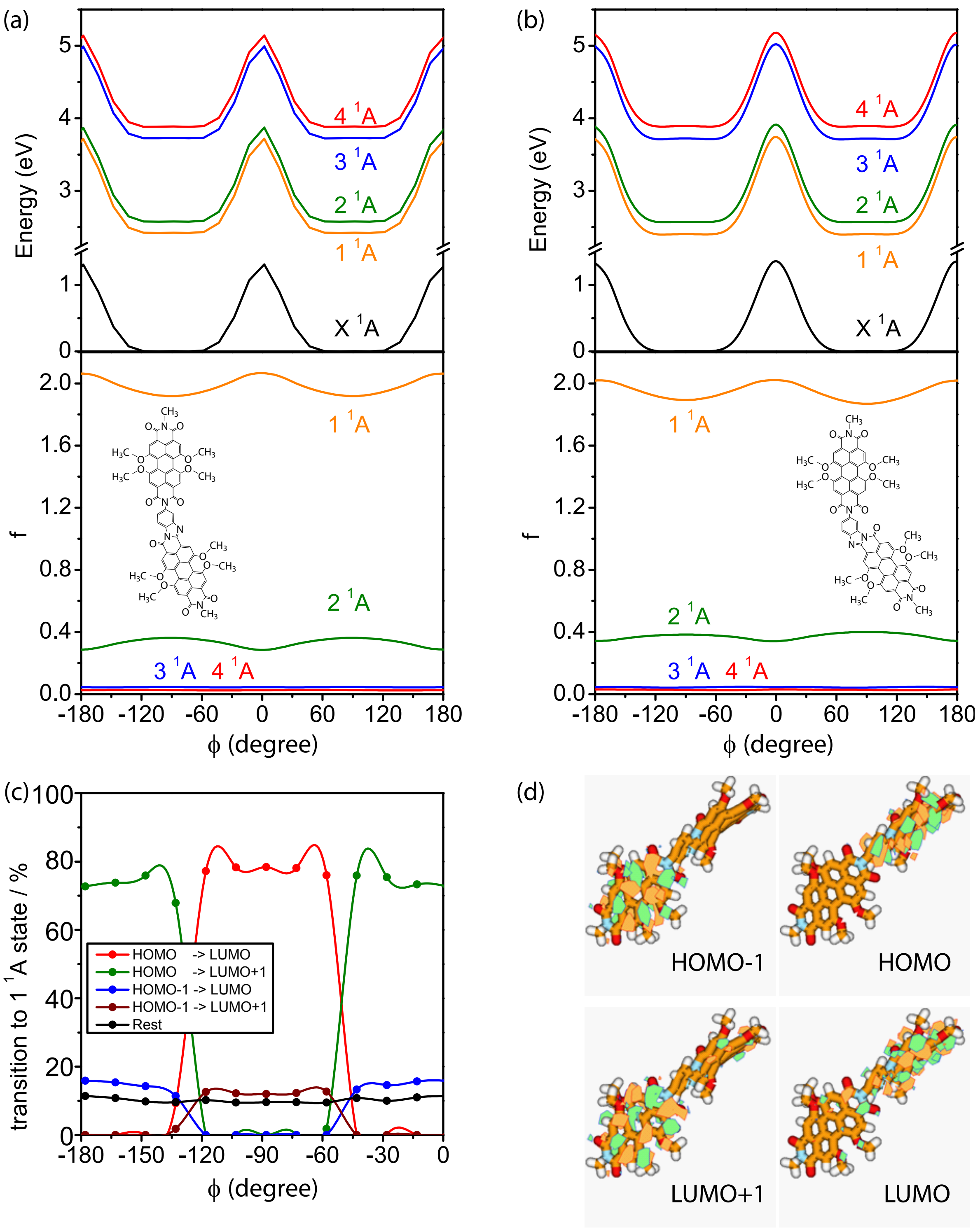

Figure 4.5: TD-HF-D results. Energy (upper panels) of the ground state (black) and electronically excited states and oscillator strength of the corresponding transitions (lower panel) for systems similar to VD341-1 (a) and VD 341-3 (b) as a function of the torsional angle ϕ. The MO composition for the transition to the 1^1 A state and the corresponding molecular orbitals are shown for the VD341-1-like structure in graphs (c) and (d), respectively.

and VD301, respectively, validating our earlier assumption of a decoupled ground state. The molecular orbital composition for the transition to the lower lying excitonic state of 80% HOMO to LUMO (both at MG086) and only <15% HOMO-1 to LUMO+1 (both at VD301) still shows a strong dominance of MG086 character for this state. Notably, to realize an amplitude ratio of $80 : 15 \sim 5 : 1$ for point dipoles with $\Delta e = 827$ cm^{-1}, an interaction energy of $V \sim 440$ cm^{-1} would be required.

The origin of the difference of the dimeric extinction coefficient compared to the simple sum over the reference compounds lies in the redistribution of oscillator strength rather than a large spectral shift of the excitonic levels: Even though the coupling strengths are smaller than the spectral line widths, the J-type arrangement of the transition dipoles increases the oscillator strength of the low-energy transition at the cost of the high energy electronic transition. Numerically fitting the dimer extinctions ϵ_{dimer} as a sum over the two reference extinctions neglecting spectral shifts, i.e.

$$\epsilon_{\text{dimer}} = a\,\epsilon_{\text{MG086}} + b\,\epsilon_{\text{VD301}}, \tag{4.3}$$

yields values of $a = 1.8$ and $b = 0.4$ for VD341-1 and $a = 1.8$ and $b = 0.3$ for VD341-3, respectively, in very good agreement with the oscillator strengths ratios of $\approx 1.8 : 0.4$ (cf. figure 4.5 (a) and (b) lower panel) for lower:upper excitonic level predicted by the ab initio calculations.

We will close this section with a Förster pair treatment of our bichromophores with VD301 acting as the energy donor and MG086 as the acceptor. Even though the strong deviation of the linear spectra from the simple sum over the two reference compounds suggests an excitonic interaction rather than pure Förster energy transfer, the transfer rates retrieved from this commonly applied theory will still serve as significant reference values. With an overlap integral of $J = 3.30 \times 10^{15}$ M^{-1}cm^{-1}nm^{4} from the linear spectra, the refractive index of dichloromethane $n = 1.42$, the fluorescence quantum yield of VD301 $\Phi_D = 0.94$, and orientational factors $\kappa^2_{\text{VD341-1}} = 3.857$ and $\kappa^2_{\text{VD341-3}} = 3.546$, respectively, the Förster radii R_0 of the bichromophoric systems (cf. equation (2.33))

$$R_0 = \left(\frac{9 \ln 10}{128\,\pi^5 N_A} \frac{\Phi_D}{n^4} \kappa^2 J \right)^{\frac{1}{6}} \tag{4.4}$$

are $R_{0,\text{VD341-1}} = 8.0$ nm and $R_{0,\text{VD341-3}} = 7.9$ nm, respectively. Förster energy transfer rates of $k_{\text{VD341-1}} = 2.2 \times 10^{12}$ s^{-1} and $k_{\text{VD341-3}} = 2.9 \times 10^{12}$ s^{-1} corresponding to $\tau_{\text{VD341-1}} = 450$ fs and $\tau_{\text{VD341-1}} = 340$ fs, respectively, are found using the excited state lifetime of the phenoxy-substituted PBI donor VD301 of 5.5 ns (in toluene) [145] and the interchromophoric distances from table 4.2. For both bichromophores, given $R_0/R > 4$, Förster theory predicts transfer efficiencies of unity.

4.4 Transient Absorption

To study the dynamics of these bichromohoric systems transient absorption measurements using a whitelight continuum covering the visible spectral range as a probe have been performed. In order to separate the interchromophoric energy transfer from other

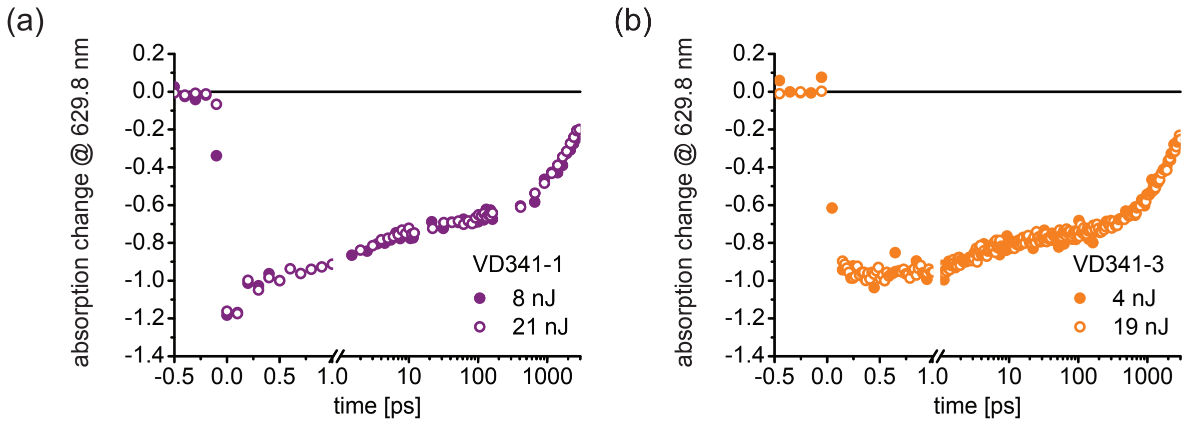

Figure 4.6: Dependence of the TA signal on the pump pulse energy. (a) For excitation at 630 nm transients of VD341-1 at 629.8 nm (normalized to 0.5 ps) are shown for pulse energies of 8 nJ (filled circles) and 21 nJ (open circles). (b) For excitation at 555 nm transients of VD341-3 at 629.8 nm (normalized to 0.4 ps) are shown for pulse energies of 4 nJ (filled circles) and 19 nJ (open circles). In both cases, the dynamics are identical for the employed pulse energies.

processes that occur on similarly fast time-scales, i.e. solvent reorganization and redistribution of vibrational energy, the dynamics following excitation at two different pump wavelengths, $\lambda_{\text{ex}} = 630$ nm ($\tau_{\text{ex}} = 55$ fs) and $\lambda_{\text{ex}} = 555$ nm ($\tau_{\text{ex}} = 60$ fs) were recorded. For excitation at 630 nm, the red edge of all absorption spectra, no Förster transfer is expected, whereas for 555 nm we should be able to excite the donor chromophore and study the subsequent transfer. Note that the excitonic coupling decreases the oscillator strength of the higher lying level. In addition, the reference chromophore MG086 (the energy acceptor in our Förster pair) was measured for both pump wavelengths for comparison.

All molecules were dissolved in dichloromethane (spectroscopic grade, Aldrich), and the concentration was adjusted to yield an optical density of $0.3 - 0.5$ at the pump wavelengths in a 500 μm-pathlength flow cell. Measurements were performed at room temperature. To reduce the influence of laser intensity fluctuations 5 to 40 transient maps were averaged for each compound and each pump wavelength. Pump pulse energies of $\approx$ 20 nJ for all measurements have been confirmed to fall into the linear regime (cf. figure 4.6).

4.4.1 Experimental Data

The transient maps of all six measurements are composed in figure 4.7 and share the following features: A dominant negative contribution corresponding to the ground state bleach (500-650 nm) and stimulated emission accompanied by an excited state absorption at shorter probe wavelength $\lambda_{\text{pr}} < 550$ nm. Full bleach recovery is not observed for any of the three substances within the accessible time window of 3 ns, but population relaxation to the ground state in the low ns regime can already be inferred from the signal decrease at long times. Interestingly, bleach recovery is faster than in MG086 for both dimers.

For all substances, an additional initial red shift of the signal is observed for excitation

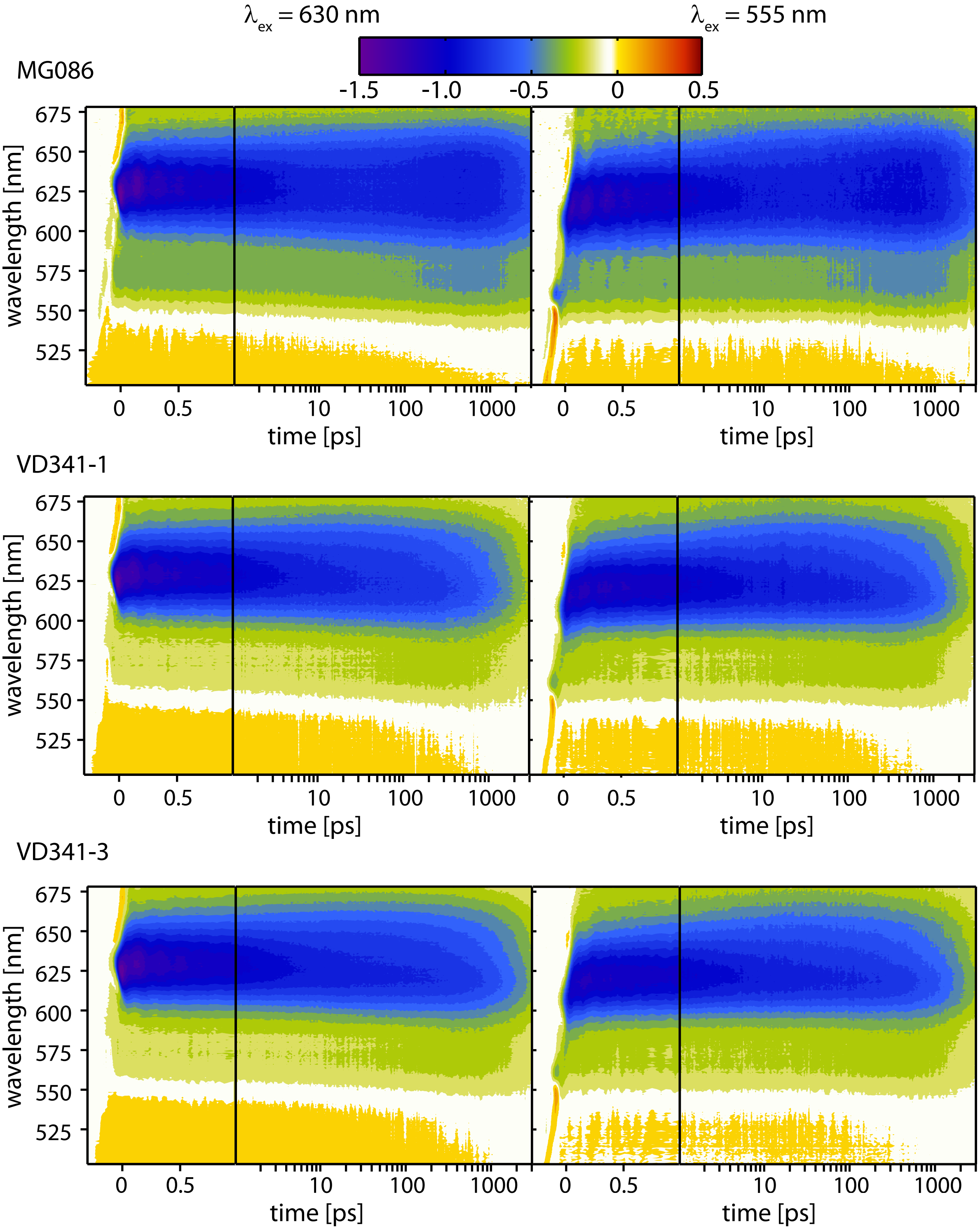

Figure 4.7: Transient maps for excitation at 630 nm (left) and 555 nm (right). Each data set has been normalized to the maximum bleach after 1 ps for better comparability.

at 555 nm indicating additional relaxation processes in all substances following the deposition of excess energy into the excited electronic state. The long time dynamics on the other hand show little dependence on the pump wavelength.

Damped oscillations in the signal amplitude with an oscillation period of $\sim$ 150 fs at early times can be found in all maps. The generation and relaxation of (ground or excited state) low-frequency vibrational wave packets in the chromophores is one reasonable explanation for such modulations, given the finite Huang-Rhys factors of several modes with $\nu < 400$ cm^{-1} already in the simpler perylene molecule [73]. However, the Raman spectrum of dichloromethane also includes low frequency modes and similar oscillations have been observed for other molecules dissolved in DCM in our group before, but vanished when switching to chloroform, suggesting that the solvent at least partially contributes to these signals.

4.4.2 Results of the Global Fitting Routine

To gain quantitative insights into the present energy redistribution mechanisms, each transient map was fitted globally with the open-source data analysis software GloTarAn [146]. In the fits for the bichromophore data sets the instrument response function and dispersion parameters to account for the probe chirp were fixed to the values obtained from fitting the corresponding MG086 data set of the respective excitation wavelength. All other parameters, i.e. spectral amplitudes and time constants were free.

Fast Dynamics - Vibrational Relaxation, Solvation and Inter-Chromophoric Energy Transfer

For excitation at the red edge of the absorption spectra (λ_{ex}=630 nm) a sum over four exponentials and a delta-function coherent artifact, both convolved with the instrument response function, suffice to fit the experimental data for all three substances. The retrieved time constants are compiled in table 4.3 and the corresponding decay-associated spectra are depicted in figure 4.8 (a) (upper panel) along with the linear absorption and fluorescence as well as the pump pulse spectrum. The short time dynamics of all three molecules can be separated into a 300-400 fs (τ_2) and a $\sim$ 4 ps (τ_3) component with decay associated spectra that show the characteristic modulation of a vibronic progression in agreement with femtosecond TA literature on PBI-based systems, e.g. [125,126,131,137, 145]. Both DAS are composed of a strong decaying stimulated emission contribution at the excitation wavelength and smaller amplitude excited state absorptions for probe wavelengths outside the region covered by the pump pulse spectrum. In the reference chromophore, MG086, we expect the early dynamics of the excited state to be dominated by solvent reorganization because the red edge of the absorption spectrum corresponds to the vibronic 0-0 transition in PBIs [147] and we are providing little vibrational excess energy. However, the relatively broad excitation spectrum ($\approx$ 1500 cm^{-1} bottom width) can very well populate excited vibrational levels in the ground state, and their relaxation will appear as a decaying excited state absorption in the TA data. As spectroscopic experiments are only senstive to changes in the energy gaps, a distinction between solvent reorganization, vibrational energy redistribution and relaxation can a priori not be made.

Table 4.3: Time constants retrieved from global fitting of TA data

	$\lambda_{\mathrm{ex}} = 630$ nm			$\lambda_{\mathrm{ex}} = 555$ nm				
					free		constrained	
	MG086	VD341-1	VD341-3	MG086	VD341-1	VD341-3	VD341-1	VD341-3
τ_1	-	-	-	-	130 fs	160 fs	70 fs	70 fs
τ_2	270 fs	400 fs	280 fs	360 fs	630 fs	1.2 ps	400 fs(c)	280 fs (c)
τ_3	3.7 ps	4.3 ps	4.0 ps	3.7 ps	5.9 ps	11 ps	4.3 ps(c)	4.0 ps(c)
τ_4	280 ps	160 ps	280 ps	330 ps	210 ps	340 ps	210 ps	340 ps
τ_5	6.8 ns	2.4 ns	3.0 ns	4.4 ns	2.2 ns	2.5 ns	2.2 ns	2.6 ns

Taking into account the rotational diffusion time constant of DCM of ~ 2 ps [148] gives no clear preference for the shorter or the longer time scale for solvent reorganization, such that we can only assign both time constants, τ_2 and τ_3, to a mixture of these processes.

The decay associated spectra retrieved for the dimers look virtually identical to MG086 and the corresponding time constants can equally be attributed to vibrational relaxation and solvent dynamics.

To fit the data sets acquired for excitation at 555 nm, a sum over four exponentials again suffices to reproduce the experimental MG086 dynamics and the two shortest time constants of $\tau_2 = 360$ fs and $\tau_3 = 3.7$ ps are very similar to the ones retrieved for $\lambda_{\mathrm{ex}} = 630$ nm. The DAS (figure 4.8 (a) bottom panel, left) corresponding to the shortest time constant, τ_2, shows again a stimulated emission contribution that in this case extends from the pump wavelength at 555 nm to ~ 625 nm and mimics the shape of the MG086 absorption. Following the same argumentation as above, we attribute these time constants to a mixture of solvation and vibrational relaxation. In contrast to the $\lambda_{\mathrm{ex}} = 630$ nm datasets, an additional decay component is needed to fit the dynamics following excitation at 555 nm for both bichromophores, VD341-1 and VD341-3, as can be seen most clearly in the transients 4.8(b). Global fitting with all time constants and amplitudes free yields $\tau_1 = 130$ fs for VD341-1 and $\tau_1 = 160$ fs for VD341-3 with decay associated spectra depicted as orange curves in the bottom panel of figure 4.8(a). For both dimers, these DAS consist of a disappearing (negative amplitude for $\lambda_{probe} \sim 560 - 615$ nm) and an appearing stimulated emission (positive amplitude for $\lambda_{probe} \sim 615 - 655$ nm), that we identify as the decaying stimulated emission of the dimer state mainly localized on VD301 that transfers its energy to the one located at MG086, leading to SE from the MG086 excited states. Note that both features are blue-shifted with respect to the equilibrium fluorescence spectra of the individual chromophores, because the energy transfer occurs before the excited state equilibrates. The free fitting routine leads to somewhat unphysical shifts in the time constants τ_2 and τ_3, especially in VD341-3. Therefore a second, constrained fit routine in which the time constants for solvation and solvent reorganization were fixed to the values obtained for $\lambda_{\mathrm{ex}} = 630$ nm of the respective bichromophore was also applied. This constrained fit resulted in identical time constants $\tau_1 = 70$ fs for both dimers with DAS depicted as orange curves in the middle panel of 4.8(a) that maintain the features described before, and almost indistinguishable transients. This also gives us a rough idea of the accuracy

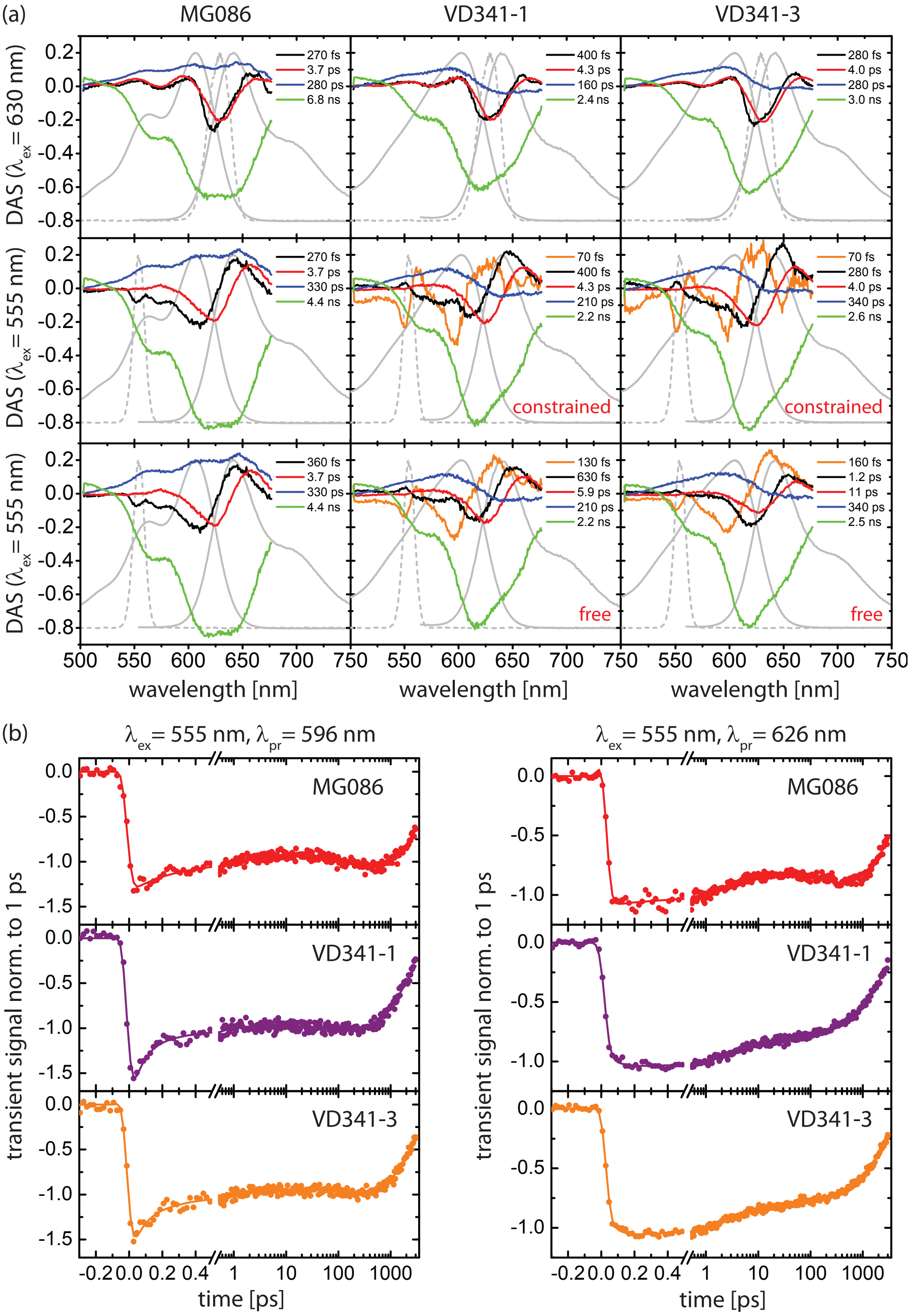

Figure 4.8: Decay associated spectra (DAS) for pump wavelengths of 630 nm (upper panel) and 555 nm (center and lower panel) retrieved from global fitting of transient absorption data for MG086 (left column), VD341-1 (center column), and VD341-3 (right column). The linear absorption and fluorescence (gray) of each molecule as well as the pump pulse spectrum (gray, dashed) are also shown.

of the energy transfer times, that we can – given the time resolution of 50-60 fs and the multitude of simultaneous processes – only confine to $\tau_1 \approx 70 - 160$ fs. Within our accuracy, the energy transfer times of both isomers, VD341-1 and VD341-3, should be considered equal.

Comparison of these times with the predictions of Förster theory ($\tau_{\text{VD341-1}} = 450$ fs and $\tau_{\text{VD341-3}} = 340$ fs) shows that energy transfer within our dimers is more than twice as fast as expected from this model based on interacting point dipoles. Remembering the failure of this approximation in the description of the linear spectra, these findings are not surprising. Again, a description in terms of interacting transition densities, taking into account the actual spatial extent of these quantities would be necessary for the small interchromophoric distances in our systems. Furthermore, the overlap integral of donor emission and acceptor absorption used in the calculation of Förster rates assumes an equilibrated excited state whereas vibrational relaxation, solvation and energy transfer are obviously simultaneous processes in our systems. The actual role of coherence within this process can not conclusively be discussed from the present data: While we can infer an excitonic (=coherent) interaction from the linear spectra, the decay associated spectra retrieved from global fitting routines are compatible with an incoherent process. Given typical electronic dephasing times of well below 100 fs in room temperature solutions [149] and the time resolution of our experiments (60 fs) we can only speculate that a disorder induced localization of the excitation on VD301 could be followed by incoherent energy transfer to the MG086 half. Likewise, some of the initially delocalized excitation energy would as a result of disorder localize on MG086.

Long Time Dynamics - Conformational Dynamics and the Origin for Fluorescence Quenching

Regarding the longest time constants, τ_5, that fall into the nanosecond regime we realize a decreased bleach recovery time in both dimers compared to the MG086 reference for both pump wavelengths (cf. table 4.3). This finding in combination with the fact that no offset is needed in the global fits excludes more efficient population of a long-lived triplet state as the origin of the decreased fluorescence quantum yields in the dimers. Instead a comparably fast competing non-radiative channel seems to contribute to the deactivation of the excited state.

Before we address the underlying mechanism for this deactivation, a more detailed look at the DAS corresponding to the nanosecond time constants is indicated: These long time constants describe the decay of the vibrationally equilibrated excited state and the associated spectra should therefore be composed of a bleach signal with a spectral shape that is identical to the absorption spectrum, a stimulated emission signal that looks like the fluorescence spectrum weighted with the fluorescence quantum yield and a factor of λ^4 to account for the difference between spontaneous and stimulated emission [150], and possibly excited state absorptions. Good qualitative agreement between the τ_5-DAS (green curves in figure 4.8(a)) and a sum over the linear absorption and fluorescence (grey curves) can be found in the case of MG086 for both pump wavelengths, while in both bichromophores this DAS deviates significantly from the linear absorption around $\lambda_{\text{pr}} = 575$ nm. Taking into account that the excited state absorptions of the equilibrated dimer excited states, the locally excited MG086 half, should be very similar to the monomeric MG086, we can attribute the bump in the DAS of the dimers around $\lambda_{\mathrm{pr}} = 575$ nm to the excitation of the second chromophore, VD301, in these compounds.

Turning now to the intermediate time constants of $\tau_4 = 140 - 330$ ps, we recognize significant differences in the DAS (blue curves in figure 4.8 (a)) when comparing the dimers to the monomer, pointing already at the role that the associated process(es) play(s) in the deactivation of the excited states.

For the monomeric reference MG086 and $\lambda_{\mathrm{ex}} = 630$ nm we find a $\tau_4 = 280$ ps component ($\tau_4 = 330$ ps for $\lambda_{\mathrm{ex}} = 555$ nm), that agrees with a time constant of 500 ps found in transient absorption studies on a four-fold phenoxy substituted PBI and attributed to conformational changes [145] given the lower viscosity of our solvent ($\eta_{DCM} = 0.39$ mPas at 30° vs $\eta_{\mathrm{toluene}} = 0.59$ mPas). The presence of different conformations differing in the orientations of the bay-substituents is frequently observed for rylene dyes in solution [109–111,126,127,151] with interconversion time scales ranging from ~ 100 ps up to nanoseconds depending on the length of the substituents as well as the solvent viscosity. We will in the following adapt the nomenclature of ref [145] and distinguish the limiting cases of extended and folded conformations: The species with all dihedral angles between the CO bond of the phenoxy and the corresponding peripheral carbon-carbon-bond of the perylene core $\pm 45°$ will be referred to as extended, whereas molecules with ≥ 1 twisting angle in the range of $90 - 135°$ will be called folded.

The positive amplitude of the MG086-DAS associated with τ_4 for both pump wavelengths (blue curve in figure 4.8 (a)) can in principle be either a decaying excited state absorption, or an increase in the bleach signal which would mean that the ground state molecules undergo a conformational change. In the latter case, as the long-time signal gets more negative, i.e. less probe light is being absorbed, the ground state molecules would have to convert into a species with smaller extinction coefficient. However, we can exclude ground state conformational dynamics as (the predominant) signal origin for the following reasons:

Consider two possible molecular conformations 1 and 2 that interconvert into each other with rate constants k_{12} (conversion of 1 into 2) and k_{21}, respectively. The kinetics of such a system are of course simple

$$\frac{dn_1}{dt} = -k_{12} n_1(t) + k_{21} n_2(t) \tag{4.5}$$

$$\frac{dn_2}{dt} = +k_{12} n_1(t) - k_{21} n_2(t) \tag{4.6}$$

and tell us that the equilibrium population of conformations, i.e. the population of conformation before interaction with our pump pulse, is given by the ratio of the rate constants

$$\left(\frac{n_1}{n_2}\right)_{\mathrm{eq}} = \frac{k_{21}}{k_{12}}. \tag{4.7}$$

If we now further assume that the two conformation possess different extinction coefficients ϵ_1 and ϵ_2, respectively, the optical density of the sample can be written as

$$\mathrm{OD} = (\epsilon_1 n_1 + \epsilon_2 n_2)\, d \tag{4.8}$$

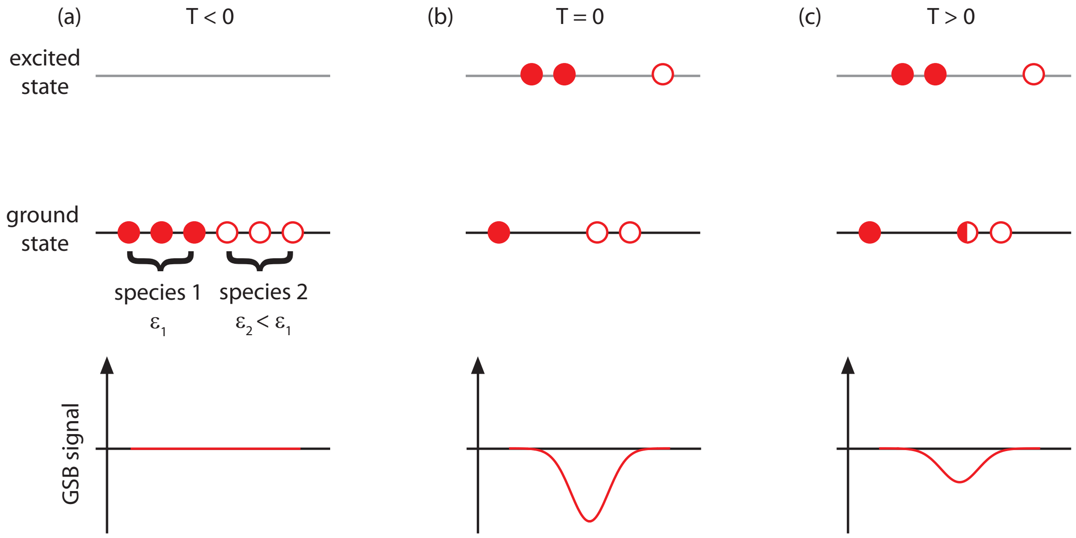

Figure 4.9: Illustration of bleach signals (bottom) expected for ground state conformational dynamics assuming $\frac{k_{21}}{k_{12}} = 1$. (a) Before interaction with the pump pulse, the ensemble is in thermal equilibrium. (b) As $\epsilon_1 > \epsilon_2$ is assumed, the pump preferentially excites species 1 (filled circles), leading to a net excess of species 2 in the ground state (GS). (c) As the ensemble is driven towards its conformational equilibrium again, the GS molecules must undergo a net conversion into the species with higher ϵ resulting in a bleach decrease.

where d is the sample pathlength.

As one pump photon is needed to promote one molecule from the ground to the excited state, the total number of absorbed pump photons (per volume) Δn_P can be written as

$$\Delta n_P = \Delta n_1 + \Delta n_2 \tag{4.9}$$

with Δn_i the change in ground state population of species i.

At the same time, the change in ground state population of species i is related to the number of absorbed photons, the extinction coefficients ϵ and the concentrations n via

$$\Delta n_i = \Delta n_P \frac{\epsilon_i n_i}{\epsilon_i n_i + \epsilon_j n_j}, \tag{4.10}$$

which we can rewrite using equation (4.7) as

$$\Delta n_i = \Delta n_P \frac{\epsilon_i \frac{k_{ji}}{k_{ij}}}{\epsilon_i \frac{k_{ji}}{k_{ij}} + \epsilon_j}. \tag{4.11}$$

Defining a common denominator D

$$D = \epsilon_1 \frac{k_{21}}{k_{12}} + \epsilon_2 \tag{4.12}$$

we find for the ground state concentrations n' immediately after interaction with the pump pulse

$$\frac{n'_1}{n'_2} = \frac{n_1 - \Delta n_1}{n_2 - \Delta n_2} = \frac{n_1 - D^{-1}\epsilon_1 \frac{k_{12}}{k_{21}} \Delta n_P}{n_2 - D^{-1}\epsilon_2 \Delta n_P} = \left(\frac{n_1}{n_2}\right)_{\text{eq}} \frac{n_2 - \frac{\epsilon_1}{D}\Delta n_P}{n_2 - \frac{\epsilon_2}{D}\Delta n_P} \tag{4.13}$$

Thus, if we assume – without loss of generality – $\epsilon_1 > \epsilon_2$, i.e. that molecules in conformation 1 have a higher extinction coefficient at our pump wavelength than species 2, then our pump pulse will preferentially excite n_1 driving the ground state population of conformations out of equilibrium to a new ground state population ratio after the pump pulse given by equation (4.13) (cf. figure 4.9 (a) and (b)).

Consequently, as the remaining ground state population drives towards its equilibrium again, a net excess of molecules in conformation 1 will build up compared to the situation immediately after interaction with the pump as illustrated in figure 4.9 (c). As we postulated $\epsilon_1 > \epsilon_2$, this corresponds to a net conversion into the species with larger extinction coefficient, a bleach decrease, which is incompatible with the sign of our DAS. Hence we can exclude ground state conformational changes as the primary origin of the observed signal in the ~ 300 ps range.

A further indication for the involvement of the excited state population lies in the non-zero signal amplitude at $\lambda > 630$ nm for MG086, i.e. in the fluorescence region. Given the spectral similarity of the two conformations postulated in ref [145], we would not expect significant signal amplitude outside the original bleach region for pure ground state dynamics as the signal origin.

Thus, we can assume that the DAS of the 280 ps-component in the region $\lambda < 630$ nm is a decaying excited state absorption of excited state population undergoing a conformational change. The DAS contribution at $\lambda > 630$ nm can than either be also ESA or an emerging stimulated emission. With the common assumption that the S_1-S_2 energy gap is smaller than the S_0-S_1 energy gap (i.e. a red-shifted ESA is expected) and taking into account that a conformational change associated with a decrease in S_1-S_2 absorption is not very likely to result in a higer transition dipole moment between S_1 and the ground state, a decaying ESA is the more likely explanation also for the positive amplitude for $\lambda > 630$ nm. Stretching the last argument a little more, the sub ensemble of the excited state population undergoing the conformational change most likely converts into a species with decreased S_0-S_1 oscillator strength, suggesting that the non-unity fluorescence quantum yields in phenoxy-substituted PBIs (or PMIs in our case) are related to conformational dynamics. A possible scenario would be folding of the phenoxy arms after photoexcitation of the predominantly open [110] ground state molecules, where the smaller distance between substituents and perylene core could facilitate (partial) intramolecular charge transfer. As the rearrangement of the phenoxy arms couples to the electronic transition, radiationless deactivation of the excited state via internal conversion associated with this movement, a variation of the lose-bolt effect [152], is also imaginable.

Regarding the bichromophores, the total number of possible conformations of the now eight phenoxy substituents is larger and additional interactions between the phenoxy arms of the two different chromophores are in principle imaginable. However, the fixed J-type arrangement and tilt around the interchromophoric C-N bond leads to rather large inter-phenoxy distances, such that only small deviations from the conformational dynamics of the MG086 monomer are expected. Therefore, the significant differences between the dimers and MG086 in the τ_4-DAS, the vanishingly small (for VD341-3) and even slightly negative (for VD341-1) amplitude in the fluorescence region, arise most likely from an additional process that occurs on timescales comparable to the conformational dynamics. An inter-chromophore charge transfer, as observed for similar systems [116, 117, 124], resulting in a dark CT state would explain the decreased amplitude for $\lambda > 630$ nm, as the positive amplitude associated with the conformational change would be counter-balanced by a disappearing stimulated emission. The faster time constants for VD341-1 compared to VD341-3 indicate a more efficient CT for the larger interchromophore angle in agreement with the lower fluorescence quantum yield.

A certain pump-wavelength dependence is observed for τ_4 and τ_5 in all compounds. This originates, however, most likely from different delay-dependent focusing of the pump beam for the two pump wavelengths, and the time constants should be considered identical within our error margins.

4.5 Coherent 2D Spectroscopy

With the original aim to shed further light on the interchromophoric energy transfer two-dimensional spectra of the monomeric reference MG086, and the dimer with the smaller interchromophore angle, VD341-3, were acquired with the box-geometry setup described in detail in section 3.3. Excitation pulses of 1 nJ energy at the sample position were centered at 592 nm with a spectral FWHM of 30 nm and 27 fs duration as determined from a SHG-FROG with a 10μm BBO, corresponding to 1.7× their transform limit. Sample solutions in DCM had an optical density of ≈ 0.3 at the excitation wavelength in a 500 μm path length flow cell (UTW, Starna). The time delay between the local oscillator and the third pulse, $t_{34}(\tau = 0)$, was $t_{34}(\tau = 0) = 1.8$ ps. τ-scans covered a range of $\tau = \pm 100.872$ fs for MG086 and $\tau = \pm 117.684$ fs for VD341-3, respectively, undersampled in steps of $\Delta\tau = 5.604$ fs. A 600 l/mm grating was used in the spectrograph and integration times were 0.7 s/spectrum. At each delay point scattering terms I_{34} (beams 1 and 2 blocked) and I_{124} (beams 3 blocked) as well as the local oscillator intensity were acquired and removed from the spectral interference before Fourier evaluation of the data. Both data sets were phased with the same parameters to spectrally-resolved pump probe data acquired in the same setup, however on a different day. For the resulting 2D spectra depicted in figure 4.10 (absolute value) and 4.11 (real and imaginary parts), 4 spectra were averaged for the MG086 data sets and ≥ 10 spectra were averaged in the case of VD341-3. The depicted wavenumber range corresponds to a wavelength range of $568 - 629$ nm.

In the real part of the 2D spectra of MG086 the maximum signal lies ~ 300 cm^{-1} below the diagonal already for $T = 0$ fs which can be explained with red-shifted stimulated emission contributions to thermally not populated vibrational levels in the electronic gound state. The initial elongation along the diagonal, i.e. the pump wavelength dependence of the signal reflecting the system memory, is lost within the first 100 fs and followed by an overall amplitude decrease. Such fast broadening dynamics are frequently found in electronic 2D spectra and assigned to the inertial solvent response [cite hybl and many other people]. The presence of a second negative peak at $-\omega_\tau = \omega_t \sim 17100$ cm^{-1} in the imaginary part indicates the presence of a second vibronic resonance. The nodal line between this feature and the main positive contribution in the imaginary part (black dashed line in the top panel of figure 4.11) levels off from an initial anti-diagonal ori-

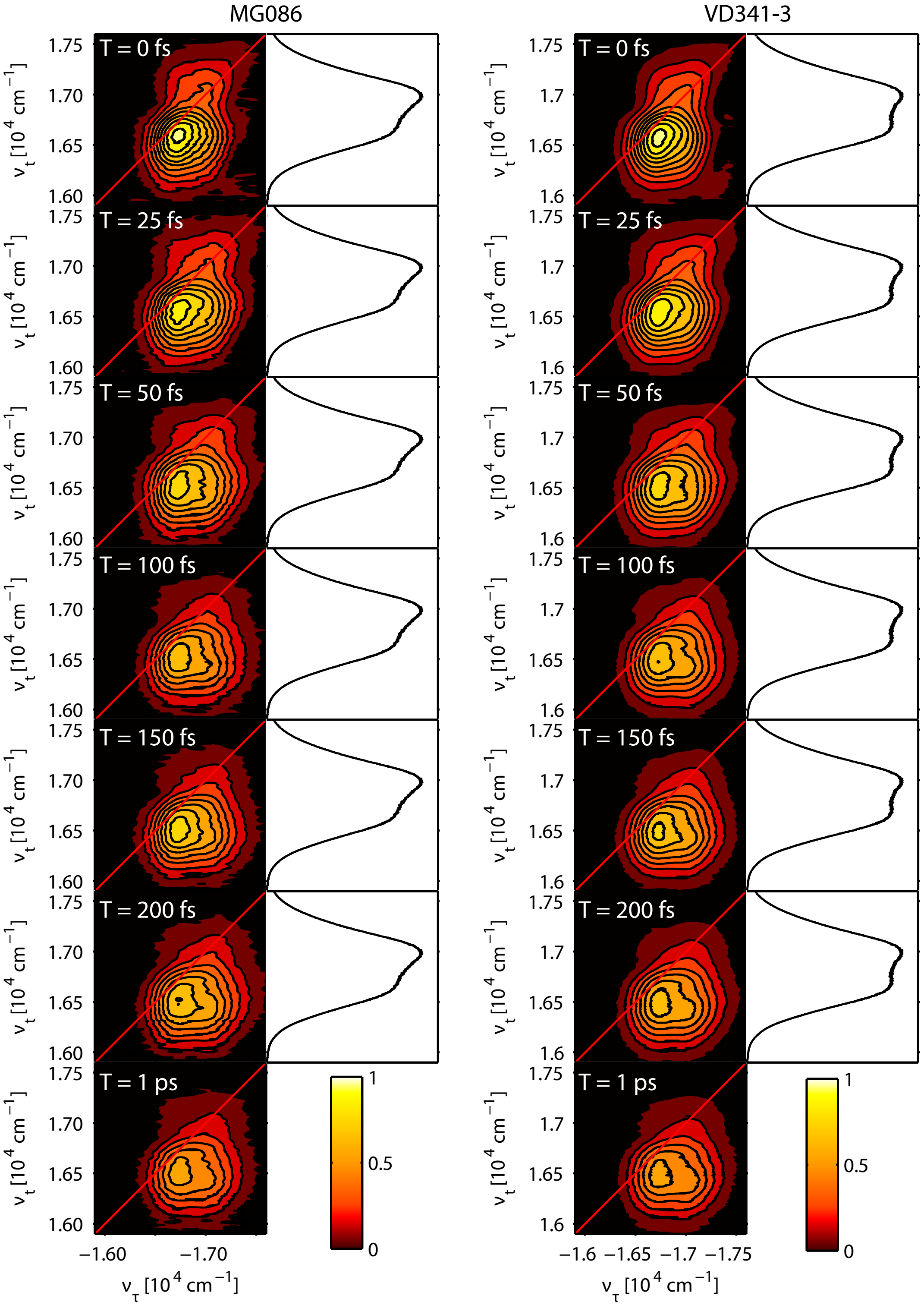

Figure 4.10: Absolute values of the 2D spectra of MG086 (left) and VD341-3 (right). Spectra have been normalized to the maximum value of the $T = 0$ fs spectrum and contour lines are drawn in steps of 10% starting at 5%. The intensity of the local oscillator measured after the sample and used for signal reconstruction is also shown.

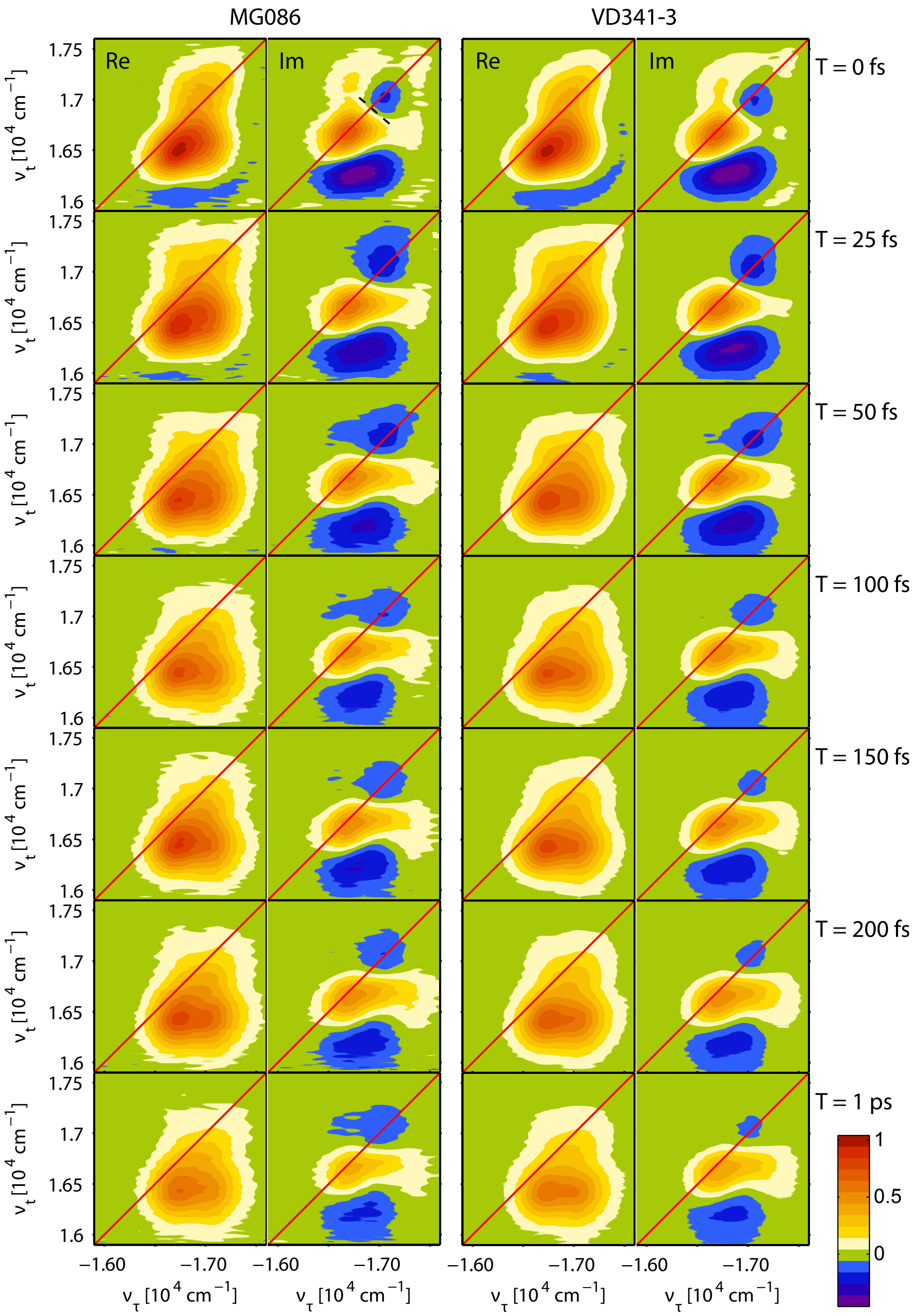

Figure 4.11: Real and imaginary parts of the 2D spectra of MG086 (left) and VD341-3 (right). Spectra have been normalized to the maximum value of the $T = 0$ fs spectrum and contour lines are drawn in steps of 10% from -45% to 95%.

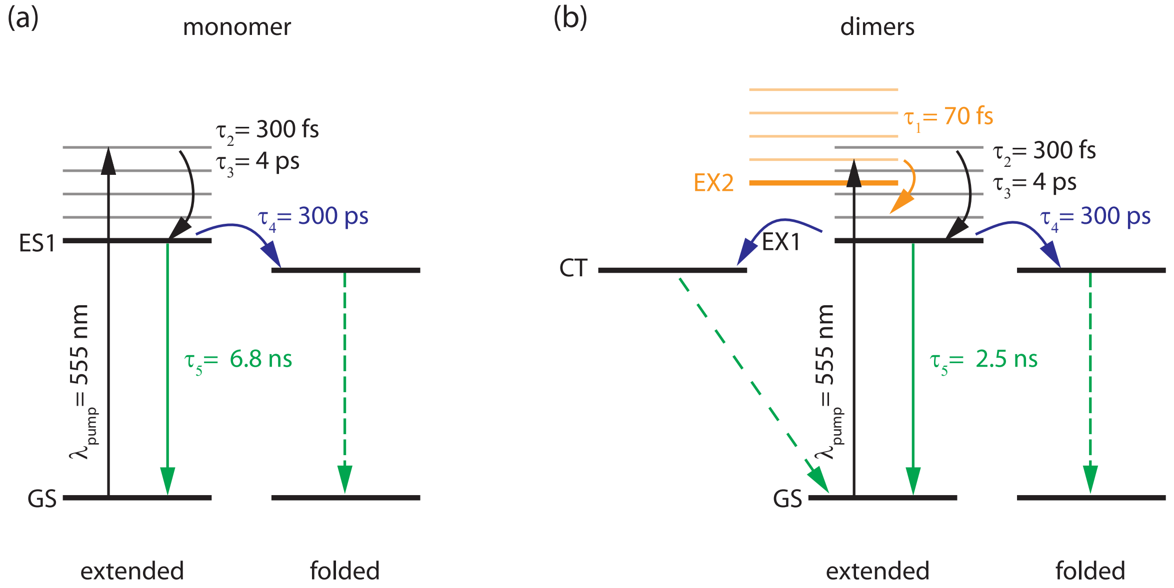

Figure 4.12: Simplified schemes for the population dynamics following excitation at 555 nm for the MG086 monomer (a) and the bichromophores (b). Straight arrows correspond to radiative transitions with dashed lines indicating reduced oscillator strength. Processes contributing to one time constant are depicted in the same color. The Stokes-shift, i.e. the energetic shift of the excited states associated with solvation, is not shown for clarity.

entation to more parallel to the x-axis on the timescale of the inertial solvent response. The nodal line of the lower feature on the other hand maintains a larger slope up to 1 ps. The 2D spectra of VD341-3 look virtually identical to their monomeric counterparts, except for a slightly different overall amplitude decay. Unfortunately, the 2D measurements contribute no further information on the energy transfer dynamics in the bichromophoric system. A major limitation for these 2D experiments was the narrow spectral width of the excitation pulses compared to the broad linewidth of the molecular systems and in particular the large spectral separation of the features associated with the energy transfer (cf. orange curves in figure 4.8): With the pulses employed in this study only the lower lying excitonic state could efficiently be populated and probed.

4.6 Summary

In summary, we have studied two hetero-bichromophoric systems consisting of PBI and PMI chromophores synthetically fixed to different interchromophore angles. The clear deviation of the bichromophoric linear absorption spectra from a sum over the extinction of the two composing monomers could be attributed to the redistribution of oscillator strength in a geometrically confined J-type-dimer arrangement. While a point dipole model approximating the transition dipole moments from integrals over the extinction coefficients and based on intermolecular distances retrieved from geometry optimizations with the semi-empirical PM6-Hamiltonian could only qualitatively explain the observed absorption, quantitative agreement with *ab initio* calculations performed in the group of Bernd Engels was found.

The dynamics retrieved for the dimers as well as a monomeric reference compound, MG086, from transient absorption measurements using a white light continuum probe and two different excitation wavelengths were analyzed with a global fitting routine and can consistently be described by the model depicted in figure 4.12: In MG086, photoexcitation is followed by solvation and vibrational relaxation dynamics with time constants of 300 fs and 4 ps (black arrow in figure 4.12 (a)). The phenoxy groups of a subensemble of the excited state population then undergo a conformational change on the 300 ps time scale (blue arrow) resulting in a species with decreased oscillator strength indicated by the dashed green line.

When exciting the dimers at 555 nm, i.e. in the blue part of their absorption spectrum, an additional ultrafast energy transfer process between the two chromophores could be resolved (orange arrow in figure 4.12 (b)). The corresponding transfer times of $\sim$ 70-160 fs fall into the order of magnitude predicted by Förster theory, but are shorter, pointing at the limitations of this widely used theory at the short distances realized in our compounds.

The strong differences in the spectra associated with the $\sim$ 300 ps decay times when comparing monomer and dimers suggest an additional deactivation channel of the excited state and inter-chromophore charge transfer in the dimers has been proposed.

While no dependence of the very fast energy transfer on the inter-chromophore angle could be observed, charge transfer is faster for the larger interchromophore angle, i.e. in VD341-1.

Future studies could focus on this inter-chromophore charge transfer, that we have so far only postulated as the most likely explanation for a nonradiative decay mechanism evident from the fluorescence quantum yields and the TA data. Extending the probe wavelengths further to the NIR in transient absorption experiments, where the spectral signature of the PBI-anion is expected [136], could prove our hypothesis and disentangle the time scales of charge transfer - including potential back electron transfer rates - from conformational dynamics.

5 Interchromophoric Interactions in Molecular Dendrimers

Molecular systems of increasing complexity, two series of carbazole dendrimers with fluorene cores and fluorene surface groups have been investigated in collaboration with Prof. Gregory Scholes (University of Toronto, Canada) and Prof. Paul Burn (University of Queensland, Australia). The results of this work are compiled in this chapter.

In such highly branched systems, an exponential increase in the number of chromophores with generation is accompanied by an increase in excited electronic state density. In addition we will have to drop one of the fundamental assumptions of the last chapter, the approximation of a decoupled ground state, as the covalent bonds in the dendrimers lead to conjugation over neighboring carbazoles and fluorenes. Both, the high number of almost degenerate excited states and significant interactions in the ground state hinder a straightforward modeling of these compounds with an excitonic Hamiltonian based on interacting point dipoles of the composing individual fluorene and carbazole chromophores.

After a short introduction to the general concept of a dendrimer and a short literature review we will therefore extensively discuss the molecular structures and linear spectra of the investigated compounds: Semi-empirical calculations along with comparison to literature results on related molecules will serve as a basis for the identification of effective chromophores, i.e. the relevant electronic transitions and their relative strength.

The experimental results of transient absorption measurements for different mutual orientation of the pump and probe polarization will then be combined to the conventional magic angle signal S_{MA} on the one hand and anisotropy decays, $r(t)$, on the other. From S_{MA}, that is sensitive to population relaxation and solvation, and the steady-state luminescence spectra we will deduce an intramolecular charge transfer as the possible origin of a pronounced broadened and redshifted emission in the higher generation dendrimers. In contrast, detailed analysis of the anisotropy r(t) that probes the relative orientation of transition dipoles will shed some light on initial exciton delocalization and subsequent ultrafast energy transfer dynamics. However, ambiguous experimental results will impede full resolution of the matter. In two-dimensional spectra of the fluorene-cored Fl-Gx series as well as in the anisotropy data of all compounds identical dynamics are observed for second and third generation dendrimers. Larger antidiagonal linewidth in these higher generations compared to the first generation, Fl-G1, point at a higher number of coupled transitions. Pump-frequency dependent decay constants in the $\sim$ 30 fs regime resolved in the Fl-G1 2D spectra will be traced back to ultrafast depolarization dynamics.

Finally, we will close this chapter with a conclusion of these preliminary results and a thorough discussion of possible continuative experiments, both steady state and time-resolved, that could be carried out to distinguish the different possibilities presented in the experimental section.

5.1 Molecular Dendrimers

Dendrimers are highly branched macromolecules with a precisely defined molecular structure consisting of a central core with so-called dendrons attached to it [153]. Each dendron in turn consists of branching units with the last branching unit at the periphery terminated by a surface group that controls the processing properties of the dendrimer. The degree of branching is known as the generation of the dendrimer (cf. figure 5.1).

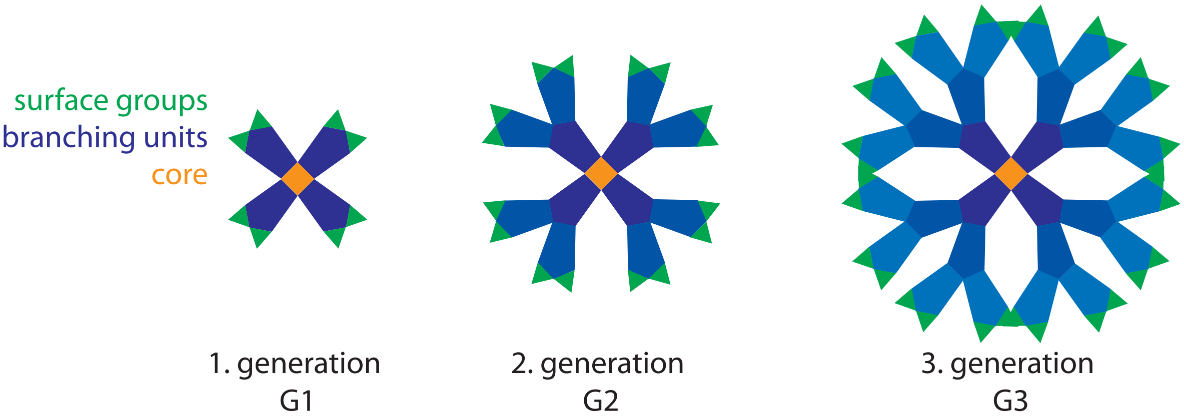

Figure 5.1: Schematic representation of a dendrimer with four dendrons. It consists of a central core (orange) with branching units (blue) attached to it. The outermost branching units of each generation are terminated by surface groups (green).

As the number of branches increases exponentially in these fractal compounds, whereas the available volume increases only with the third power of the distance to the core, the outer layers of a dendrimer exhibit a very high density. This imposes a severe sterical strain, results in a transition to globular shapes even for initially planar or extended systems and ultimately limits the growth of the dendrimers to a maximum viable generation number.

The comparably simple synthesis of such well-defined architectures paired with a very high density of customizable functional units opens a broad field of potential applications in areas ranging from medical biology to materials science [154–156]: Host-guest chemistry uses the shielded microenvironments, the intradendrimeric voids, while applications as anchor groups exploit the high number of surface units that can bind many more substituents than a tetrahedron or the benzene core [155]. In catalysis, dendrimers combine the advantages of homogeneous and heterogeneous catalysis, while their precisely known molecular structure allows for a detailed analysis of the catalytic events [156]. Strong intramolecular interactions as a result of the dense packing are the basis for applications as enhanced nonlinear optical materials [157], organic light emitting diodes and solar cells [158, 159]. Self-similar structures often exhibit the lowest excitation energy at the center making dendrimers asymmetric energy funnels, where the branches serve as light harvesting antennas that efficiently transfer the absorbed energy to the core [160].

Owing to their fractal character dendrimers form a popular playground for theoretical studies within an excitonic i.e. coherent picture [161–164], while experiments that are performed in condensed phases and typically at room temperature investigate the dephasing or dephased limit of energy transfer. To experimentally resolve the dynamics of these energy transfer processes, different methods of ultrafast spectroscopy are commonly applied: Besides conventional transient absorption [165–169] the emission-based technique of time-resolved fluorescence anisotropy [166, 169–174] has proven one of the most powerful tools, as it probes the changes in transition dipole moment orientation that are associated with exciton localization and migration. Many experimental investigations focus on incoherent hopping type energy transfer and find time constants between picoseconds and subnanoseconds depending on the kind of chromophores and the intradendrimeric distances in good agreement with Förster theory. In some cases of large dendrimers, where the exciton migrates over many chromophores before it reaches the core, exciton diffusion length have been deduced [175, 176]. Increasing efforts are being made – in particular in the group of Goodson [166, 167, 171, 172, 175] – towards experimentally resolving also the excitonic interactions in strongly coupled dendrimers that govern the first sub-100 fs. To this end, three-pulse photon echo experiments have been performed to complement the aforementioned techniques [166, 169].

5.2 Structures and Linear Spectral Properties of the Investigated Carbazole-Fluorene Dendrimers

The structures of the in total nine compounds studied are displayed in figure 5.2: Two different series of carbazole dendrimers, one with a fluorene core and another with a spirobifluorene core have been investigated along with the dendrons of each generation. All compounds are terminated with fluorene surface groups at the periphery. In the following the substances with fluorene core will be denoted as Fl-Gx (x=1-3), whereas the spirobifluorene ones will be referred to as SBF-Gx (x=1-3). As can be easily verified from figure 5.2 (a), the number of carbazole units N_C increases as $N_C^{Fl} = \sum_{g=1}^{G} 2^g$ with generation G in the Fl-dendrimers and $N_C^{SBF} = 2 \times \sum_{g=1}^{G} 2^g = 2N_C^{Fl}$ in the SBF-compounds. Similarly, as each outerlayer carbazole is bound to two fluorene chromophores the number of fluorene chromophores N_F follows $N_F^{Fl} = 2 \times 2^g + 1$ and $N_F^{SBF} = 2N_F^{Fl}$, respectively, where the second summand accounts for the (spirobi)fluorene core.

All substances have been synthesized by members of Prof. Dr. Paul Burn's research group at the University of Queensland, Australia, who also provided the linear spectra[1] depicted in figure 5.2 (b), as well as the extinction coefficients and fluorescence quantum yields compiled in table 5.1. The investigated compounds are structurally closely related to dendrimers published by the Burn's group in reference [177] that apart from the synthetic details deals with an intended application in the detection of nitroaromatic explosives such as TNT via fluorescence quenching.

---

[1] except the luminescence spectra of the G1 and G2 dendrons that were measured in Würzburg

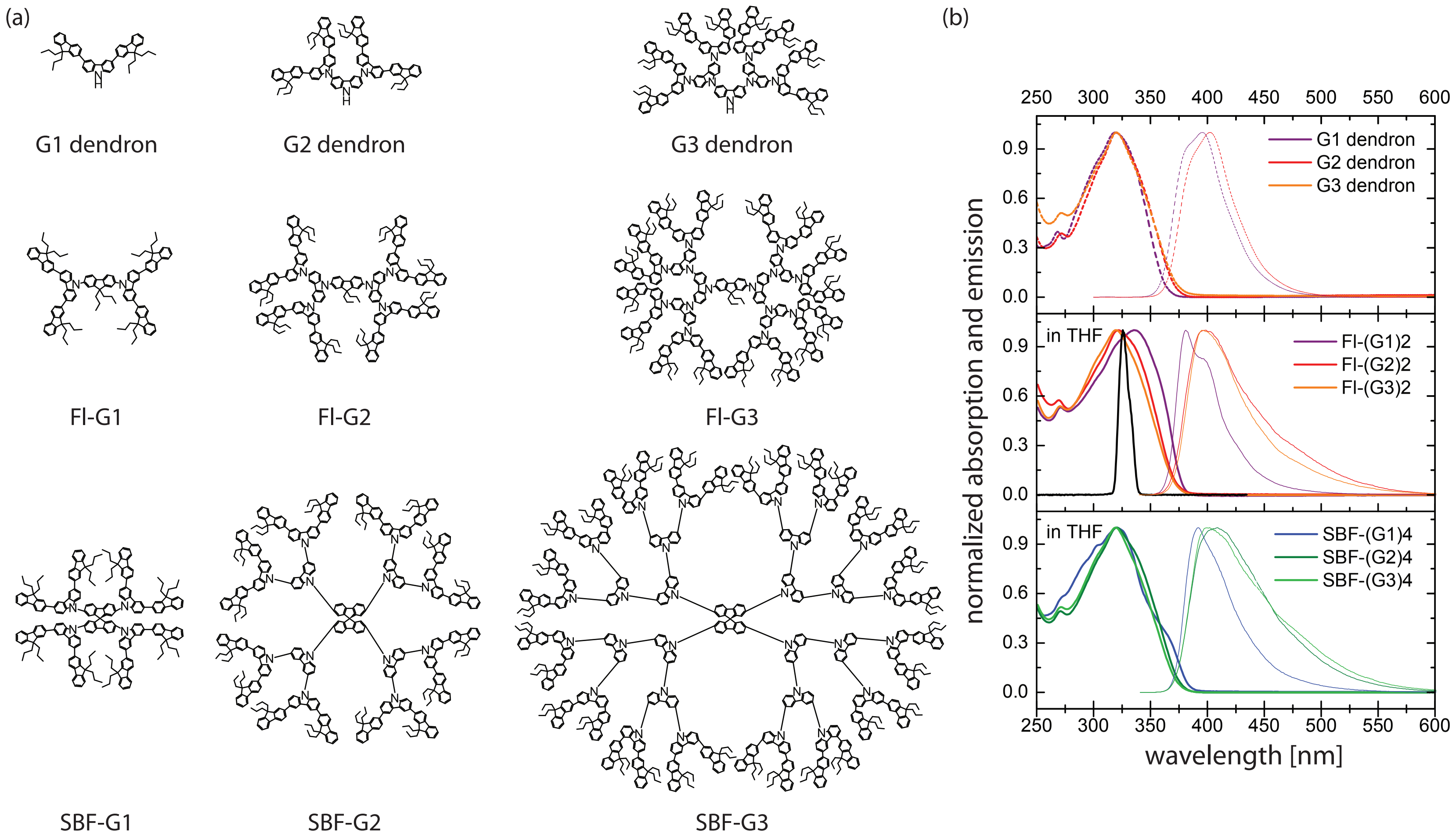

Figure 5.2: Structures (a) and linear absorption and emission spectra (b) of the investigated compounds. The black curve in the middle panel of (b) shows a typical laser spectrum for the time-resolved experiments discussed in the subsequent sections.

Regarding the spatial structure of these macromolecules, we can infer already from the difficulties in drawing the higher generations on a two-dimensional sheet of paper, that they will not be planar. To visualize the compounds semiempirical geometry optimizations with MOPAC (PM6) have been performed for the G1 and G2 dendron, Fl-G1 and Fl-G2 as well as SBF-G1, where the C_3H_7-groups on the fluorene units have been replaced by CH_3 to reduce computational cost. The resulting optimized geometries are displayed in figure 5.3 for two different view angles, and retrieved intramolecular distances and angles are indicated. While these semi-empirical structure should not be over-interpreted [178], the retrieved twisted conformations qualitatively agree with literature: For a molecule similar to the G2 dendron but without the fluorene surface units dihedral angles of 90 deg between the first and second generation carbazoles have been found from DFT/B3LYP/6-311G theoretical modeling [179], and highly twisted conformations have been reported also for a G3 dendron analogue (again without the peripheral fluorenes) [180]. Besides, this latter study [180] has investigated the inductive electron withdrawing effect in (3,6)-substituted carbazole dendrons and finds a significant decrease in electron density at the G1 carbazole with increasing generation, i.e. a (generation-dependent) intramolecular potential gradient. Similarly, we expect a significant outward shift of electron density with increasing generation in our compounds, which is at least qualitatively confirmed in the HOMOs retrieved from semiempirical modelling (cf. figure 5.4). While the discussed twisting of the carbazoles leads to a deviation from a strictly two-dimensional structure in the single dendrons and Fl-Gx compounds, the Fl-Gx compounds can – at least in the first and second generation – still be considered more planar, or disc-shaped, than the SBF-Gx: In the SBF compounds, the orthogonal orientation of the two fluorenes in the spirobifluorene core results in a 3D arrangement already for the G1 molecule.

For all our substances the lowest energy electronic transitions are associated with a broad peak centered at ~ 320 nm in their linear absorption in THF. From the normalized spectra in figure 5.2(b) we recognize a somewhat higher extinction in the red wing of the spectrum for the G2 and G3 dendron compared to the G1 dendron. The Fl-G1 absorption is significantly redshifted with respect to the single dendrons as well as the higher Fl generations. For SBF-G1 a redshifted shoulder at 355 nm is observed in addition to the strongest band at 320 nm, whereas the SBF-G2 and SBF-G3 absorption spectra show little substructure in the main peak and resemble the Fl-G2 and Fl-G3 spectra.

All of the above spectra deviate significantly from a sum over spectra of the isolated fluorene and carbazole subunits (see e.g. figure 2 in [181] and [182]) in that the main absorption peak is significantly redshifted and broader with less substructure and exhibits a much higher extinction than a properly weighted sum over these individual compounds. The origin of these deviations lies in significant ground state interactions on the one hand, i.e. conjugation over neighboring carbazoles and fluorenes, and excited state interactions, more precisely excitonic couplings between the resulting transition dipole moments or transition densities on the other hand.

Comparison of our linear spectra with literature spectra published for substances similar to the G2 dendron (compounds CzG2on and G2ph in [180], spectra in THF, and compound 1A in [179], spectra in THF), G3 dendron (compounds CzG3on and

(a) G1 dendron

(b) G2 dendron

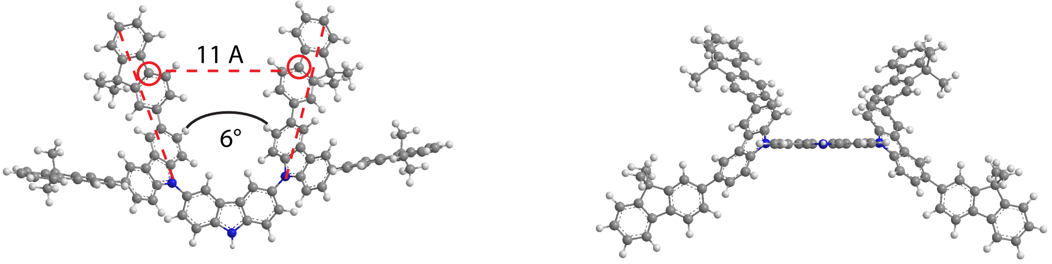

(c) Fl-G1

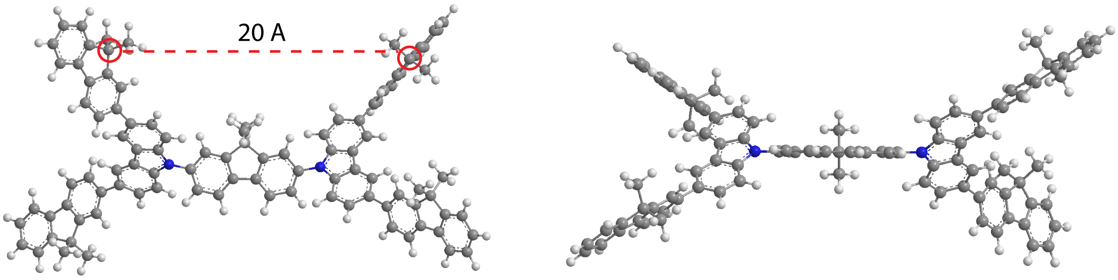

(d) SBF-G1

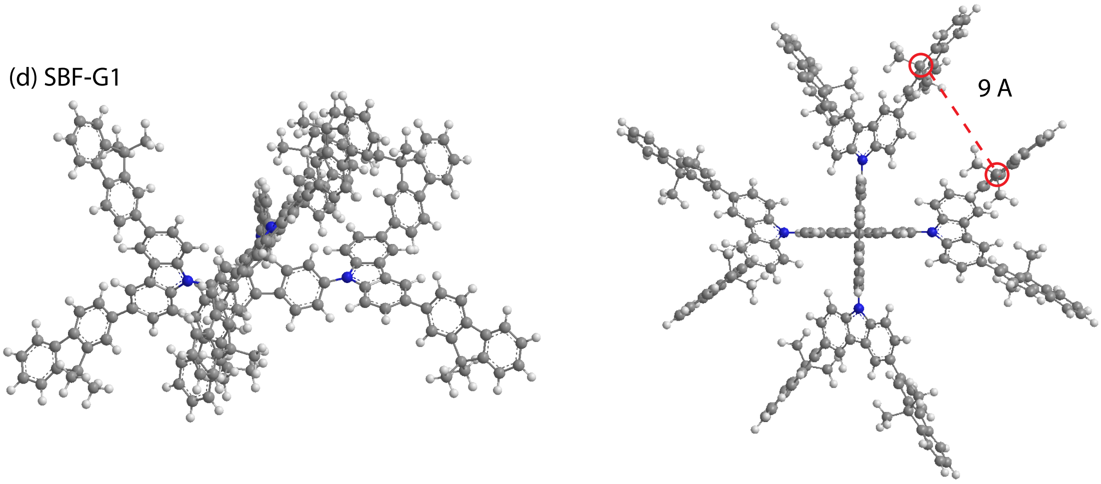

Figure 5.3: MOPAC/PM6-optimized geometries for the G1 dendron (a), G2 dendron (b), Fl-G1(c) and SBF-G1(d) from two different view angles. Retrieved interchromophore distances and angles are indicated.

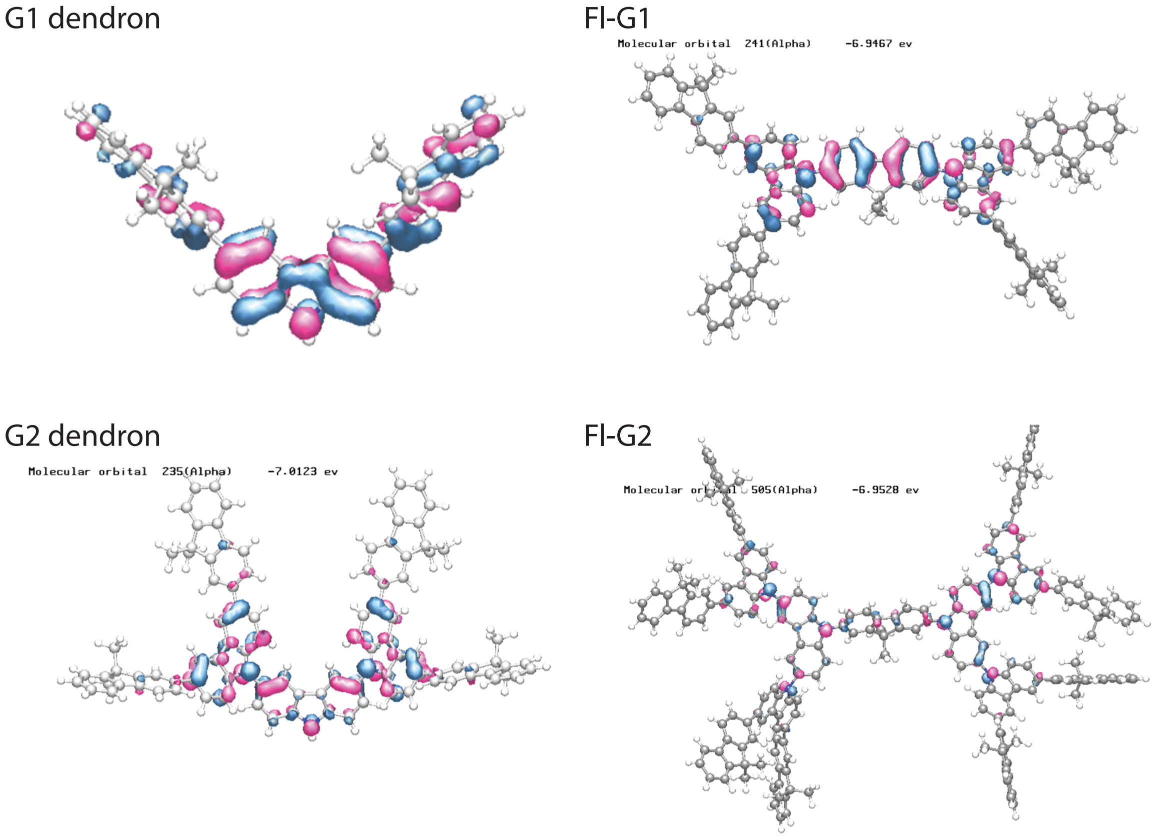
G1 dendron

Fl-G1

G2 dendron

Fl-G2

Figure 5.4: Highest occupied molecular orbitals (HOMOs)

G3ph in [180], spectra in THF), Fl-G1 (compound CF_1 in [183], spectra in $CHCl_3$, and BCZF in [184]) and Fl-G2 (compound G2CF in [185], spectra in $CHCl_3$), that lack the peripheral fluorenes, indicate a strong contribution of these outermost chromophores in our substances to the absorption: The reported extinction coefficient for the G2 dendron analogue of $\epsilon = 1.2 \times 10^4 \, \mathrm{l\,mol^{-1}cm^{-1}}$ for $\lambda = 343$ nm is still ~ 7 times lower than in our compound indicating that the high extinction coefficients in our substances do not predominantly originate from the covalent linkage of carbazoles. Furthermore, the prominent absorption peak at $\lambda \sim 295$ nm reported in [179], [183] as well as [185], and attributed to the local transition of the carbazoles at the terminal ends, is not visible in our spectra.

Therefore, following the line of thought of [186] (even though their focus lies on the delocalization of triplet states) we expect the para-linked fluorene surface groups to result in conjugation over in total at least three p-phenyl rings (blue dashed line in figure 5.5) for all our compounds, leading to a redshifted transition compared to the individual fluorene with high oscillator strength. The absorption of our compounds is still redshifted with respect to PTP suggesting involvement of even larger molecular subunits, possibly the full G1 dendron subunit (blue dotted line in figure 5.5).

The redshifted absorption onset of the G2 dendron and the G3 dendron compared to the G1 dendron is most likely at least partly due to delocalization over neighboring

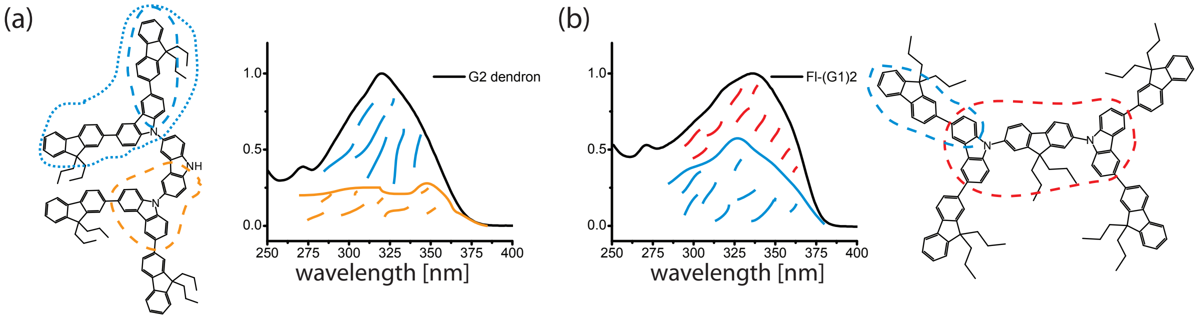

Figure 5.5: Suggested effective chromophores and highly qualitative decomposition of the linear spectra for the G2 dendron (a) and Fl-G1 (b).

carbazoles: The same trend has been observed for compounds similar to our dendrons but without the fluorene surface groups, and saturation of the conjugation length at two to three carbazoles has been suggested [180]. DFT/B3LYP/6-311G/ZINDO calculations on a (3,6)-linked carbazole trimer (=G2 dendron without fluorene) [179] reveal that charge redistribution upon electronic excitation is in fact limited to only one of the second generation carbazole substituents and the neighboring phenyl ring of the first generation carbazole (orange dashed area in figure 5.5 (a)) and the long-wavelength tail in the absorption could be traced back to a partially allowed S_0-S_1 transition in these compounds.

In contrast, the bathochromic shift in the absorption of the Fl-G1 compared to both, the single dendrons and the higher Fl generations results at least partially from conjugation over the core fluorene and neighboring carbazoles (red dashed line in figure 5.5): A pronounced redshift is found when going from CF1 in [183] to G2CF in [185], i.e. in compounds without the peripheral fluorenes. This core related transition will be of minor importance for the higher generation Fl substances not only because the relative number of peripheral fluorenes is increased but also because the aforementioned electron withdrawing effect of the outer layer carbazoles can be expected to significantly reduce conjugation over the central fluorene.

The discussed contributions to the linear absorption in the dendrimers are highly qualitatively visualized in figure 5.5 for the G2 dendron and Fl-G1.

Having roughly identified the effective chromphores in the investigated systems, we will now spend a few words on additional excitonic couplings between the corresponding transition dipoles. If we again use p-terphenyl – with a transition dipole moment of $\mu =$ 7 D as retrieved from its extinction in cyclohexane [187] following the procedure described in the last chapter – as an order of magnitude reference, we see that we are dealing with transition dipoles comparable to the PBI-PMI dimer of the last chapter, comparable or even smaller interchromophore distances (cf figure 5.3) and angles that vary from J-type to H-type arrangement already in the absence of disorder. Consequently, significant excitonic interactions resulting in further initial delocalization of the excitation can be expected.

Regarding the luminescence of our substances (thin lines in figure 5.2(b)), for the Fl-G1 and SBF-G1 compounds we find similar emission spectra exhibiting some substructure

Table 5.1: Spectral properties and fluorecence quantum yield Φ_f in THF

	λ_{abs}	ϵ_{max}	λ_{em}	Φ_f
G1 dendron	319 nm	0.50×10^5 M^{-1}cm^{-1}		-
G2 dendron	320 nm	0.83×10^5 M^{-1}cm^{-1}		-
G3 dendron	320 nm	3.16×10^5 M^{-1}cm^{-1}		-
Fl-(G1)$_2$	336 nm	1.99×10^5 M^{-1}cm^{-1}	–	0.57
Fl-(G2)$_2$	322 nm	3.80×10^5 M^{-1}cm^{-1}	–	0.20
Fl-(G3)$_2$	320 nm	7.76×10^5 M^{-1}cm^{-1}	–	0.20
SBF-(G1)$_4$	320 nm	4.60×10^5 M^{-1}cm^{-1}	–	0.65
SBF-(G2)$_4$	320 nm	7.08×10^5 M^{-1}cm^{-1}	–	0.21
SBF-(G3)$_4$	319 nm	15.8×10^5 M^{-1}cm^{-1}	–	0.16

that can be attributed to vibronic coupling and comparable luminescence quantum yields (table 5.1), suggesting a similar emissive state for these first generation dendrimers. In contrast, the emission spectra of all higher generation compounds show no hints of vibronic progressions, are significantly red-shifted, and exhibit a pronounced long-wavelength tail. This change in emission quality is accompanied by a notable decrease in luminescence quantum yield from $\Phi_{PL} \sim 0.6$ for the first generation dendrimers to $\Phi_{PL} \lesssim 0.2$ for the higher generations. Some differences in the spectral shape can be found between Fl-G2, Fl-G3, SBF-G2 and SBF-G3 but no obvious trend with generation is observed.

5.3 Transient Absorption and Anisotropy Decay

To study the energy redistribution within these systems degenerate transient absorption experiments for different pump pulse polarizations have been carried out for the nine compounds depicted in figure 5.2. To realize spectrally identical pump and probe pulses centered at 325 nm the commercial NOPA TOPAS white (Light Conversion) was tuned to 750 nm and focused with a $f = 50$ cm spherical Ag-mirror on a 65 μm BBO crystal. An exemplary excitation spectrum is shown in figure 5.2 (b) (black line, middle panel). After recollimation with a $f = 35$ cm spherical Al-mirror the second harmonic centered at 325 nm was separated from the fundamental with a pair of dielectric cold mirrors and coupled into the transient absorption setup that has been described in detail in section 3.1. The 85 fs-pump pulse was s-polarized with respect to the laser table surface for all experiments and the probe polarization was set parallel or perpendicular with respect to the pump by rotating a commercial 355 nm zero-order $\lambda/2$-plate. Magic angle transients S_{MA} and anisotropy values r were then calculated from the parallel $S_{\|}$

and perpendicular data sets $S_\perp$ according to

$$S_{\mathrm{MA}} = \frac{S_\parallel + 2S_\perp}{3} \tag{5.1}$$

and

$$r = \frac{S_\parallel - S_\perp}{S_\parallel + 2S_\perp}, \tag{5.2}$$

respectively. The strong solvent signals around time zero have been subtracted from $S_\parallel$ and $S_\perp$ taking into account the wavelength dependence of sample absorbance before further data processing. To average out laser fluctuations ≥ 8 transients have been averaged for each polarization. Furthermore to minimize possible systematic effects, e.g. of solvent evaporation, the measurements were performed in a sandwich type fashion: $N/2$ transients were measured for one polarization setting followed by N transients with orthogonal arrangement followed again by $N/2$ transients in original configuration.

All molecules have been dissolved in spectroscopic grade THF and the concentration was adjusted to yield an optical density of 0.3-0.5 at the pump wavelength of 326 nm in a 200 μm (for the G3 dendron and SBF-G2), or a 500 μm (for all other compounds) path-length flow cell. To avoid photobleaching the sample volumes were constantly exchanged by a micro-angular gear pump. Comparison of linear absorption spectra before and after the TA-experiments showed a slight overall increase in extinction that we attribute to evaporation of THF as well as increased absorption around 275 nm. The latter effect is not related to degradation of the dendrimers as it has also been observed for neat THF solution. Most likely, the THF slowly dissolves the norprene tubing used to attach the cuvette to the micro angular gear pump. To minimize possible data contamination, the sample compartment was thoroughly washed with fresh THF between experiments on different molecules and the measurement time on each molecule was kept as short as possible. In addition, individual transients measured with the same pump polarization were carefully analyzed and no systematic change in the dynamics with increasing measurement time could be identified.

To check the accuracy of the waveplate as well as the sandwich type measurement procedure transient absorption data for both polarization conditions were measured for the laser dye stilbene-3 [188] dissolved in ethanol. For this simple chromophore neither localization effects nor excited state absorptions with transition dipoles including finite angles with respect to the originally pumped transition are expected to influence the anisotropy decay. As can be seen in figure 5.6 (a) the calculated anisotropy values decay from an initial value of $r = 0.4$ to $r = 0$ as the molecules diffusively rotate, proving the applicability of our method.

For systems with high chromophore densities exciton-exciton-annihilation or more generally speaking effects arising from the absorption of two (or even more) photons in a single macromolecule are a concern in spectroscopy experiments already at relatively low pump intensities. Pump photon fluxes F_p employed in the transient absorption experiments described below varied between $F_p = (5-7) \times 10^{13}\ \frac{\mathrm{photons}}{\mathrm{cm}^2}$ as calculated from $F_p = \frac{E_{\mathrm{pulse}}}{E_{\mathrm{photon}}} \frac{1}{\pi r_{pu}^2}$ with the pump pulse energy at the sample, E_{pulse}, the photon energy of a 325 nm photon, E_{photon}, and the pump beam radius at $1/e^2$ intensity level,

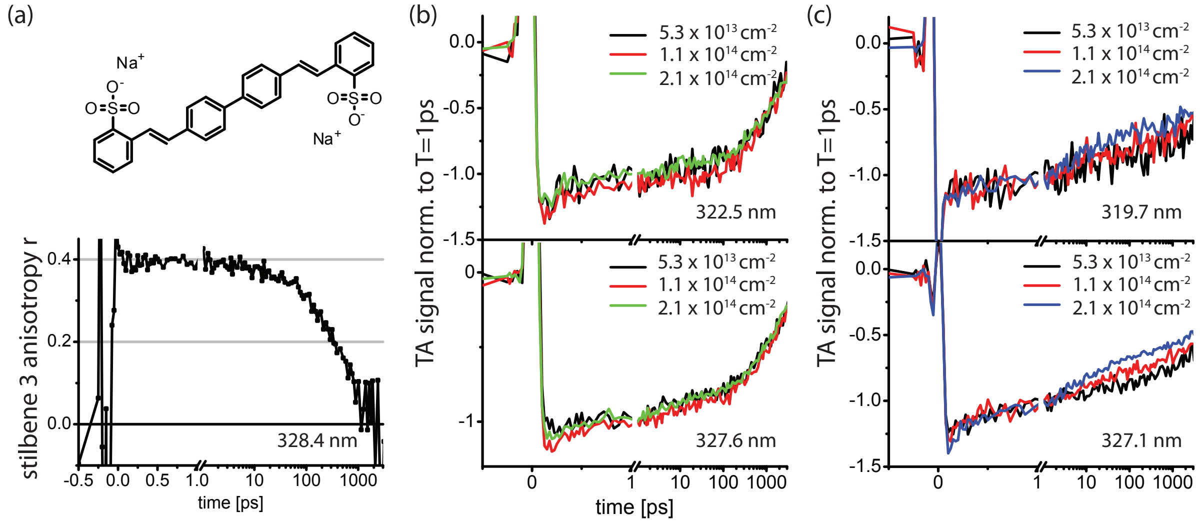

Figure 5.6: Molecular structure and anisotropy decay of the reference molecule stilbene 3 (a). Power dependence of the transient absorption signal for Fl-G1 in toluene (b) and SBF-G3 in THF (c) for different probe wavelength as indicated in the individual graphs.

r_{pu}. While these photon fluxes clearly fall into the regime where the signal depends linearly on the pump power for Fl-G1 (cf. figure 5.6 (b)), the lowest employed photon flux could not be proven to fall into the linear regime for the system with the highest chromophore density, SBF-G3 (cf. figure 5.6 (c)).

5.3.1 Population Relaxation - Magic Angle Results

To analyze the magic angle data sets multi-exponential global fits to wavelength ranges of 318.0 nm to 337.0 nm for all compounds except the G3 dendron and SBF-G2 have been carried with GloTarAn [146]. In the case of the G3 dendron and SBF-G2 only the wavelength range of 327.4 – 329.6 nm has been used for data analysis. The instrument response function of $\tau_{\mathrm{IRF}} = 85$ fs and the probe chirp parameters were kept constant during the fits, while all other parameters, i.e. decay times and amplitudes were free. Following the spartanity principle, fits reproducing the acquired data with the lowest number of time constants are shown in figure 5.7 along with the magic angle transients at 328.4 nm. The corresponding time constants are compiled in table 5.2. Only the Fl-G2 signal is satisfactorily described with a monoexponential decay of $\tau = 4.7$ ns. For all other compounds except Fl-G1 biexponential fit functions were sufficient. In the case of Fl-G1 a third time-constant $\tau_3 = 100$ fs had to be introduced to fit the fast initial decay in particular on the blue side of the covered wavelength range.

A 3–17 ps time constant τ_2 that shows no obvious trend with generation is observed for all compounds except Fl-G2. Given the small wavelength range investigated we can only assign τ_2 to a mixture of processes such as solvent reorganization and energy redistribution in the excited state manifold. A distinction between energy transfer between different electronic states and redistribution of vibrational energy cannot be made. Note that the absence of a decay in the picosecond regime for Fl-G2 in these experi-

Table 5.2: fit results

	magic angle					anisotropy	
	τ_1	τ_2	τ_3	τ_{1r}	τ_{1nr}	τ_1	τ_2
G1 dendron	3.6 ns	5.0 ps	-			180 ps	3.9 ps
G2 dendron	4.5 ns	9.6 ps	-			160 ps	1.5 ps
G3 dendron	8.4 ns	7.3 ps	-			80 ps	1.0 ps
Fl-(G1)$_2$	3.1 ns	6.6 ps	0.1 ps	5.3 ns	7 ns	460 ps	3.0 ps
Fl-(G2)$_2$	4.7 ns	-	-	23.5 ns	5.9 ns		
Fl-(G3)$_2$	4.6 ns	16.7 ps	-	23.0 ns	5.8		
SBF-(G1)$_4$	1.9 ns	9.5 ps	-	2.9 ns	5.4 ns	620 ps	3.0 ps
SBF-(G2)$_4$	7.0 ns	2.5 ps	-	24.1 ns	9.8 ns		
SBF-(G3)$_4$	9.7 ns	10.2 ps	-	60 ns	12 ns		

ments does not necessarily mean that the above-mentioned processes do not occur in this molecule. In fact, it is more likely that the associated amplitudes corresponding to stimulated emission and/or excited state absorptions cancel in the specific narrow wavelength range investigated here.

The longer time constants τ_1 that account for the larger part of the decay amplitudes and fall into the nanosecond regime, on the other hand, increase with generation and correlate with the luminescence quantum yields of the Fl-Gx and SBF-Gx compounds: Molecules with lower luminescence quantum yields exhibit a slower decay in the magic angle transient absorption data, i.e. a slower repopulation of the ground state. The observed bleach-recovery times can be decomposed into radiative (τ_{1r}) and non-radiative (τ_{1nr}) lifetimes using the luminescence quantum yields. Comparing the radiative lifetimes of Fl-G1 and SBF-G1 we find a reduction in τ_{1r} to 70% of the Fl-G1 value for the spirobifluorene-cored compound in reasonable agreement with its 2.3 times higher extinction coefficient. For all higher generation dendrimers, the radiative lifetimes are significantly larger than for the respective first generations despite their much higher extinction coefficients. This finding underlines the qualitatively different emissive state for G2 and G3 dendrimers that we already inferred from the drastic change in the emission spectrum in section 5.2. The retrieved nonradiative constants also differ and decrease with generation within the Fl-Gx series while they increase in SBF-Gx, but the effect is less pronounced.

One possible explanation for decreased quantum yields in combination with a red-shifted emission, in particular the pronounced long-wavelength tail, would be the formation of excimers. Such a formation of local intramolecular dimers after excitation is frequently observed in molecular assemblies with extended π-systems including dendrimers [189]. The primary candidates for such an association would be the peripheral fluorenes within a single dendron. However, the long-wavelength tail is not observed for

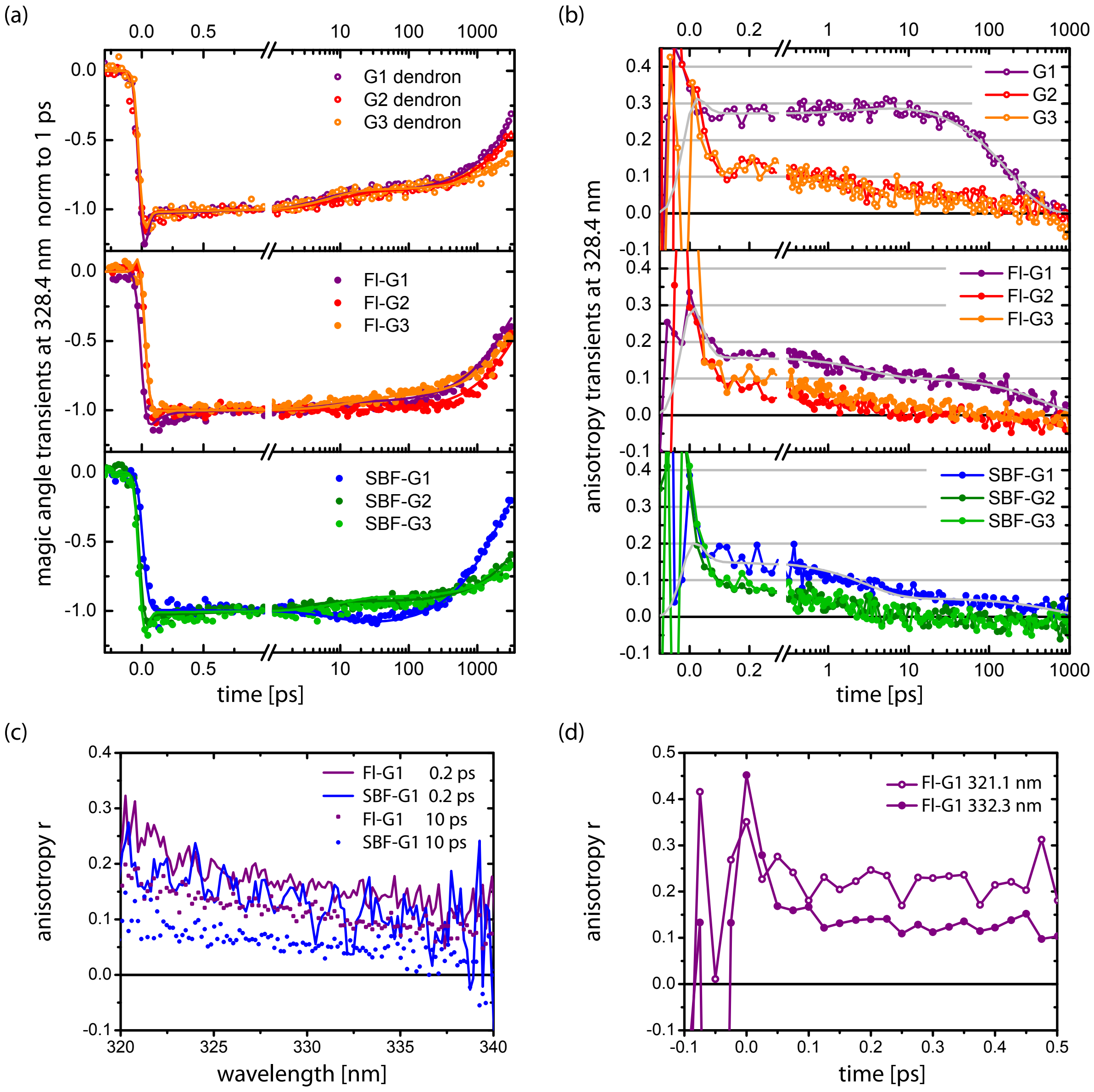

Figure 5.7: Magic angle transients S_{MA} for $\lambda_{pr} = 328.4$ nm normalized to 1 ps as well as monoexponential (Fl-G2), triexpoenential(Fl-G1) and biexponential fits (rest) obtained from GloTarAn (a). Anisotropy decays for $\lambda_{pr} = 328.4$ nm (b). Biexponential fits to the G1 data sets are shown in grey. Note that the solvent signal has not been subtracted for the G3 dendron and SBF-G2 data sets. Anisotropy difference spectra for FL-G1 and SBF-G1 (c), and anisotropy transients for Fl-G1 at the red and the blue edge of the probe spectrum (d).

the G2 and G3 dendron. Therefore one would have to argue that either the presence of the core facilitates the formation of excimers at the molecular periphery or that the two dendrons within the dendrimers get close enough to associate, which seems unlikely in particular for the smaller Fl-G2.

A different possibility lies in the formation of a charge-transfer state after photoexcitation. If so, charge transfer would most likely occur from the electron rich dendrimeric periphery to the fluorene core, as the long-wavelength tail is not observed in the single dendron emission. While the intramolecular potential gradient may support this explanation further studies, including comparably "simple" experiments such as emission spectra in solvents of different polarity, have to be carried out to confirm this hypothesis.

5.3.2 Anisotropy

The magic angle data S_{MA} discussed in the last section is in principle sensitive to population relaxation and solvation. However for the narrow wavelength range examined here it provides little means to distinguish the short time dynamics of our complex dendrimeric systems. The temporally resolved anisotropy $r(t)$ on the other hand describes the evolution of the relative orientation of the transition dipole moments that have originally been excited with the pump pulse and the transition dipole moments that are probed at time t after the pump. As we have learned in Chapter 2.7.7 a disorder-induced localization of an excitation that has initially been delocalized over $n > 1$ non-parallel transition dipoles, leads to a drop in anisotropy. Similarly, in the incohorent limit, hopping-type energy transfer between non-parallel transition dipoles reduces the anisotropy.

In the anisotropy decays depicted in figure 5.7(b) for $\lambda_{pr} = 328.4$ nm, we recognize an ultrafast drop of the initial anisotropy within ~ 150 fs, i.e. on a timescale comparable to our time resolution, followed by further depolarization within a few picoseconds in all investigated compounds. Furthermore, a clear difference is observed between the first generation compounds of all series, single dendrons, Fl-Gx, and SBF-Gx, and the respective higher generations: The anisotropy values after this fast initial decay are significantly larger than for G2 and G3, and an isotropic distribution of transition dipoles (r=0) is reached only after more than 100 ps. The second and third generation anisotropy decay curves are identical for each series within our experimental error limits. For Fl-G1 and SBF-G1 a pronounced wavelength dependence of the anisotropy has been found: The anisotropy is larger for shorter probe wavelengths (cf. figure 5.7(c)). Notably, while the initial anisotropy values at $T = 200$ fs are only slightly smaller in SBF-G1 than in Fl-G1, r reduces to significantly lower values within the first 10 ps.

Before we dive into a more detailed discussion of our results, several remarks on the validity and information content of anisotropy data acquired with a transient absorption setup are indicated. Firstly, as has in detail been shown in chapter 2.7.7, excited state absorption from transitions that include finite angles with the transition dipole moments of the transition that has been excited with the pump pulse will affect the absolute value of r impeding a straight forward interpretation as an ensemble averaged angle between the contributing transitions. The influence of excited state absorptions also complicates conclusions drawn from comparison of anisotropy values for different molecules regarding delocalization and energy transfer: The identification of a lower residual anisotropy value with larger initial delocalization presupposes that the relative amplitudes and angles for the excited state absorptions are the same in both molecules. Secondly, as population relaxation takes place on the excited state surface(s), stimulated emission contributions will redshift and no longer contribute to the signal in our comparably narrowband probe window, while at the same time the amplitude of excited state absorptions may change, i.e. we may measure changes in r that originate from other processes than the interchromophoric energy transfer that we are after. Thirdly, the anisotropy values at delay times comparable to the pump pulse duration will be affected by signal contributions that arise from different time orderings of the interactions with pump and probe pulse (coherent artifact) and signals originating from the solvent. While solvent signals have been subtracted from $S_{\parallel}$ and $S_{\perp}$ for all molecules except the G3 dendron and SBF-G2 before calculation of r, such a signal correction is far from perfect. Furthermore, scattered pump light affects the parallel and perpendicular measurements differently in a degenerate TA-experiment: For parallel polarization of pump and probe pulse, it interferes coherently with the chromophore signal, while it adds incoherently for perpendicular orientation. Therefore the initial anisotropy values do not seem reliable observables. Note that without knowledge on the initial anisotropy, initial excitonic coupling, i.e. delocalization of the excitation cannot be distinguished from very fast incoherent energy transfer. In the following we will nevertheless use the term delocalization as the large transition dipole moments and small intramolecular distances should allow for excitonic interactions.

All the above limitations should be kept in mind in the following discussion of the anisotropy decays in the dendrimers and our experimental findings can be considered compatible or necessary but not sufficient conditions for the presented interpretation.

To quantify the longterm decay in the first generation compounds, anisotropy decay curves have been fitted with a sum over two exponentials convoluted with a Gaussian instrument response function. The retrieved best fits are shown in gray in figure 5.7 (b). We attribute the longterm decay in the G1-molecules to rotational diffusion because assuming a rotating sphere in THF ($\eta = 0.45 \times 10^{-3}$ Pas), the retrieved time constant for the G1 dendron of $\tau_2 = 180$ ps corresponds to a radius ρ

$$\rho = \left(\frac{3kT\tau}{4\pi\eta} \right)^{1/3} = 7 \text{ Å} \tag{5.3}$$

in very good agreement with molecular dimensions predicted from the geometry optimization (cf. figure 5.3). The increase of this time constant to $\tau_2 = 460$ ps for Fl-G1 and $\tau_2 = 620$ ps for SBF-G1, respectively, when going from G1 dendron to Fl-G1 to SBF-G1 is consistent with the increase in molecular dimensions among the first generation compounds. While free fitting yields shorter time constants of $\tau_{1,G2} = 160$ ps and $\tau_{1,G3} = 80$ ps for the G2 and G3 dendron, τ_1 values larger than 200 ps are also compatible with the acquired data . We therefore likewise assign the long term anisotropy decay in these two compounds to rotational diffusion.

Already in the simplest molecule investigated, the G1 dendron, the initial anisotropy value of $r = 0.27$ for $T = 250$ fs deviates significantly from the idealized value of $r = 0.4$ (the value observed for the simple stilbene-3 reference chromophore). An

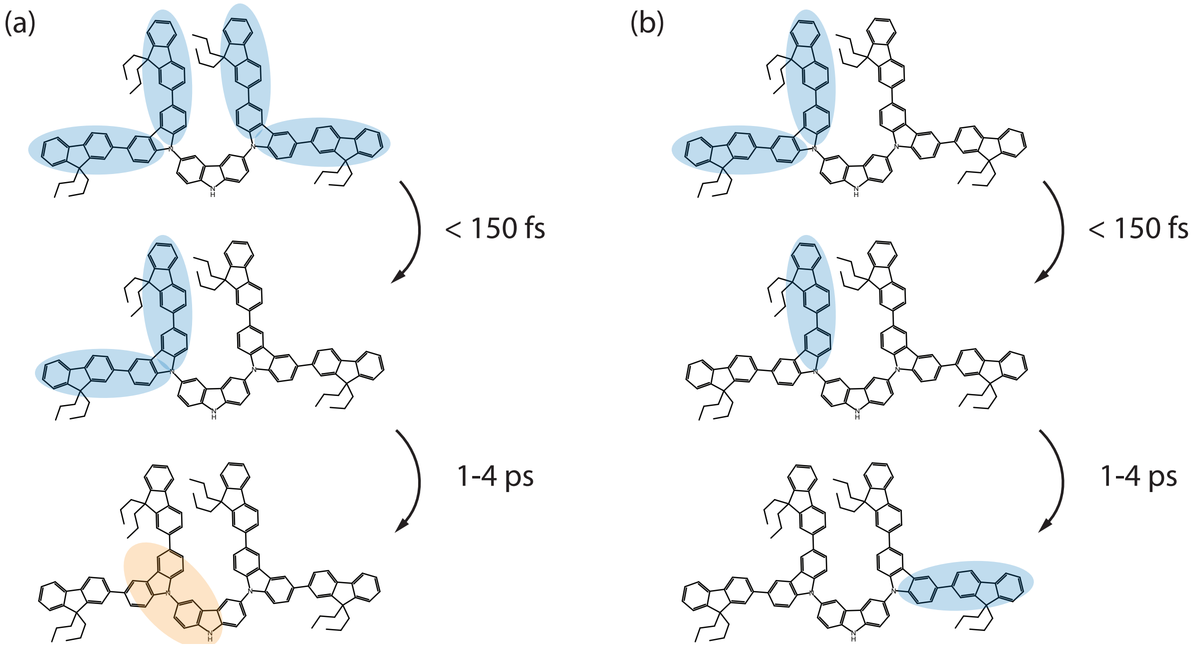

Figure 5.8: Limiting cases for the hypothetical energy redistribution in the G2 dendron: An initially delocalized excitation localizes on the timescale of our instrument response which leads to an ultrafast drop in anisotropy. Subsequent migration of the exciton towards the central carbazole is accompanied by further depolarization (a). If initial delocalization is limited to the G1 subunit, subsequent hopping between terminal fluorenes will lead to depolarization of the signal (b).

ultrafast localization would explain this observation and torsional motion around the fluorene-carbazole linking single bond would be a possible mechanism causing a conjugation break. The fact that the anisotropy reproducibly increases slightly with a time constant of 3.9 ps, however, suggests the presence of a tilted excited state absorption that influences the anisotropy and may account – at least partly – for the deviation from 0.4.

Regarding the G2 dendron, a lower anisotropy value at $T = 250$ fs of $r = 0.13$ compared to the G1 dendron ($r = 0.27$) supports the idea of an initial delocalization of the excitation over a larger number of transition dipoles in this compound. Subsequent energy redistribution is associated with a further depolarization of the transient absorption signal within a few picoseconds. In the limiting case of initial full delocalization over all four terminal fluorenes, incoherent hopping between these terminal branches after localization would not lead to reduced anisotropy values. Therefore we would have to postulate a different underlying process on the ps-timescale such as exciton migration towards the central carbazole unit as depicted in the highly qualitative and speculative sketch in figure 5.8 (a) in this limit.

Interestingly, the G3 dendron anisotropy decay for $T > 100$ fs is virtually identical to its second generation precursor, pointing possibly at a limitation of the initial delocalization and subsequent energy (or charge?) transfer to molecular subunit that does not exceed the G2 dendron.

While the given interpretation is consistent, it is based on the lower anisotropy value at $T = 250$ fs in the G2 and G3 dendron compared to the G1 dendron that indicates an increase in initial delocalization length. If we postulate a tilted excited state absorption in the G2 and G3 dendron as the origin of this lower $T = 250$ fs r-value, the initial delocalization could still be limited to the terminal G1 unit, and subsequent energy hopping between terminal fluorenes could cause the observed further depolarization within a few picoseconds 5.8 (b). While strong transition dipoles of the surface units and small intramolecular distances would support such a mechanism, the higher number of possible energy acceptors in the G3 dendron should result in an increased depolarization rate in this larger molecule, which is not observed.

Emission-based time-resolved techniques such as fluorescence upconversion anisotropy studies that are not influenced by excited state absorptions could resolve this issue.

Note that, if all contributing transition dipoles fall into a plane and sufficient randomization in that plane is already reached after localization of the excitation in G2, the experimental anisotropy will no longer be sensitive to the contribution from additional transition dipoles in G3.

Within the Fl-Gx and SBF-Gx series, we observe the same behavior as in the single dendrons, i.e. the depolarization dynamics of their second and third generation dendrimers are indistinguishable within our experimental uncertainty. Besides, a cross-series comparison between the dendrimers yields very similar values for the early anisotropy, i.e. at $T = 150$ fs, for Fl-G1 and SBF-G1, Fl-G2 and SBF-G2, as well as FL-G3 and SBF-G3, suggesting that the initial delocalization at our pump wavelength is effectively limited to the transition dipole sub-ensemble already present in a single Fl-Gx-branch. In contrast, the significantly lower anisotropy value at longer times, e.g. $T = 10$ ps, when comparing Fl-G1 and SBF-G1 may indicate that the two Fl-G1 subunits within SBF-G1 are indeed coupled, and that energy transfer between these two halves of the molecule occurs.

5.4 Two-Dimensional Spectra of Fluorene-Cored Dendrimers

Two-dimensional spectroscopy experiments on the dendrimers of the Fl-Gx series have been carried out with the all-reflective box-geometry setup described in detail in section 3.4. Excitation pulses spectrally identical to the ones employed in the transient absorption studies, i.e. centered at 325 nm, have been generated with the same optical setup. Pulse duration at the sample position was 30 fs (corresponding to 2× their transform limit) as determined from heterodyne detected transient grating of a 1 mm fused silica plate. Photon fluxes were $1.2 \times 10^{13}\ \frac{\text{photons}}{\text{cm}^2}$ in each of the three excitation pulses. The molecules have again been dissolved in THF and optical densities were 0.6 for Fl-G2 (in 200 μm) and FL-G3 (in 500 μm), and 0.78 for FL-G1 (in 500 μm). Note that reabsorption effects cannot be neglected for such optically dense samples.

The data was analyzed following the procedure described in section 3.3.2 and the absolute values of the retrieved two-dimensional spectra are depicted in figure 5.9 along with 2D spectra of neat THF. As the $T = 0$ fs signals are strongly affected by solvent

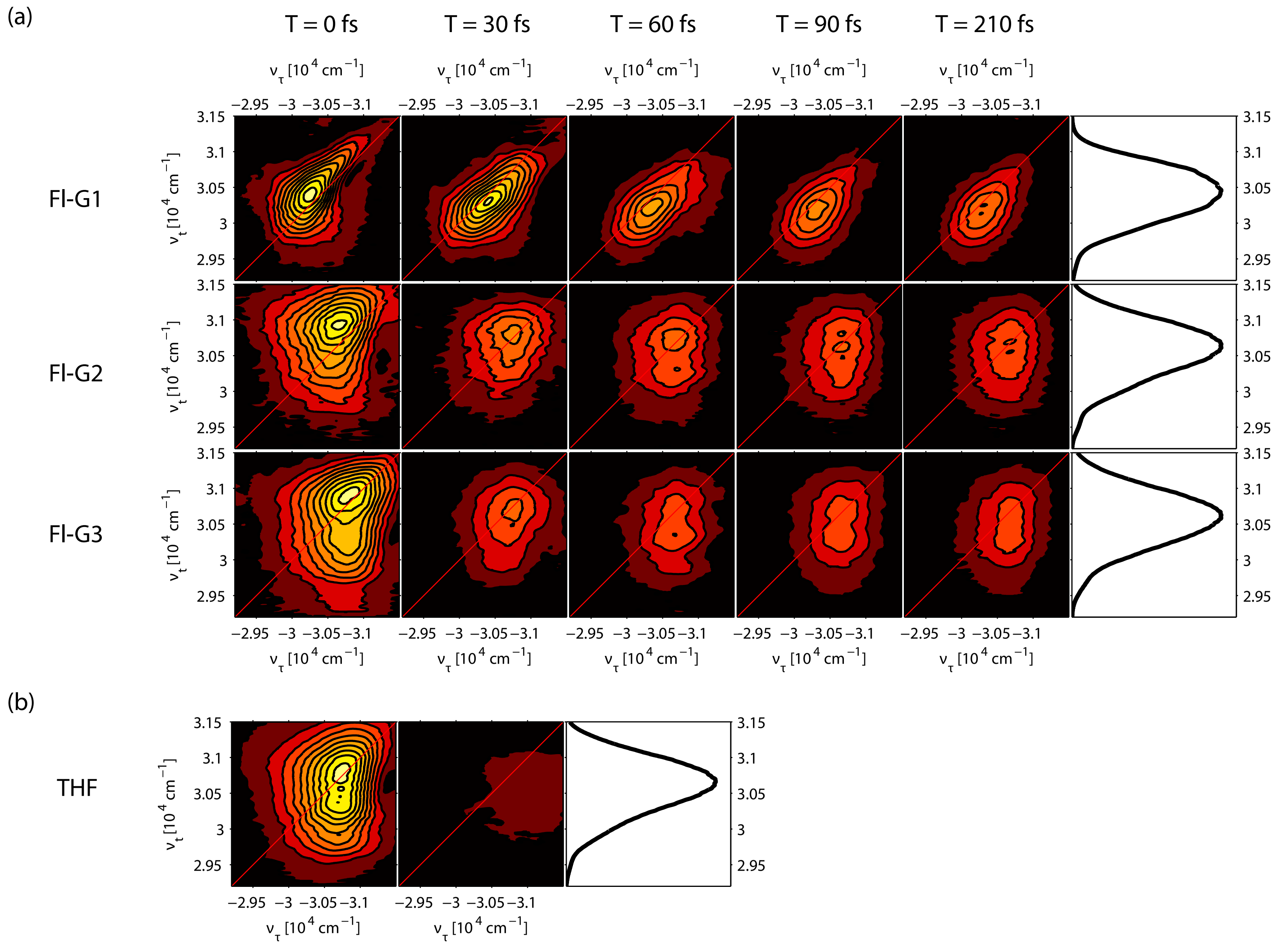

Figure 5.9: Absolute values of the 2D spectra of Fl-G1 (a,top), Fl-G2 (a, middle) and Fl-G3 (a, bottom) and neat THF (b) for various population times. Spectra have been normalized to the maximum value at $T = 0$ fs and contourlines are drawn in steps of 10% stating at 95% of the $T = 0$ fs spectrum. The black curve on the right shows the LO-spectrum after the sample.

contributions, they should be treated with care and will not be included in the following discussion.

Strong qualitative differences can be found in the absolute value of the 2D spectra of Fl-G1 and Fl-G2: For Fl-G1 we observe an overall diagonal elongation that persists up to 210 fs as well as shape changes in particular below the diagonal that occur within the first 100 fs. In contrast, Fl-G2 exhibits a larger antidiagonal width pointing at a larger number of coupled transitions than in Fl-G1. Literally no pump-wavelength dependence is resolved for $T \geq 30$ fs in Fl-G2 and we find only a slight decrease in the overall amplitude between 30 fs and 210 fs. The absolute values of the two-dimensional spectra of Fl-G2 and Fl-G3 for $T > 0$ fs are identical within our noise limit in agreement with our discussion of the anisotropy decays for these compounds, that the maximum number of coupled chromophores for optical excitation is reached in Fl-G2.

For a more quantitative analysis of the Fl-G1 spectra, the absolute value on the diagonal has been integrated over the 180 cm^{-1}-wide squares depicted in figure 5.10(a) and the time dependence of the resulting amplitudes (figure 5.10 (b)) for 30 fs $\leq T \leq$ 210 fs has individually been fitted with a mono-exponential decay, $I(t) = a\ \mathrm{e}^{-T/\tau} + I_0$. The retrieved ultrafast diagonal decay times vary between $\tau = 16$ fs and $\tau = 25$ fs and are plotted in figure (c) as a function of the pump wavenumber, ν_τ.

For $\nu_\tau \leq 30500\ \text{cm}^{-1}$ we observe a faster decay with increasing pump energy which meets simple-minded straight-forward expectations: For population in a higher lying level, a larger number of lower lying levels opens up more decay channels leading thus to a faster depopulation than at lower pump energies. In addition, the net depopulation of the lower lying levels is slowed down as they act as energy acceptors for the higher lying ones. Remarkably, we find a deviation from this trend for $\nu_\tau \geq 30500\ \text{cm}^{-1}$, that is accompanied by peculiar dynamics below the diagonal which becomes most obvious in the transients for the grey and the black off-diagonal square depicted in figure 5.10(d). To understand the origin of these dynamics, we have to take into account the relative polarizations of the excitation beams and local oscillator in our setup: Even though the box geometry introduces small angles between the four beams, they will still mainly be polarized parallel. Given the pronounced anisotropy dynamics reported earlier, the detected 2D amplitudes will therefore not only reflect population (and coherence) dynamics but will also be sensitive to reorientation of transition dipoles. Knowing this and taking into account that the anisotropy initially decays faster on the red edge of the probe spectrum in Fl-G1 (cf. figure 5.7(d)) corresponding to a faster drop of the parallel signal $S_\parallel$ at lower probe wavenumbers (gray square) we can conclude that we are actually resolving the fast initial depolarization here. The faster initial drop in anisotropy at low probe frequencies seems to originate mainly from processes initiated from the blue part of our pump spectrum. Besides, the cross-peak amplitude loss due to depolarization initially counterbalances the increase in off-diagonal intensity as a consequence of energy transfer, that takes over at $T \sim 75$ fs when the intensity in the gray square increases again. The presence of an additional ultrafast energy transfer within Fl-G1 agrees with the necessity to include a ~ 100 fs time constant in the fits for the magic angle transient absorption decays. Though it is tempting to relate this ultrafast process to energy transfer from the peripheral fluorenes to the core, we have no unambiguous proof for such an assignment: Ultrafast solvation for example could provoke similar dynamics.

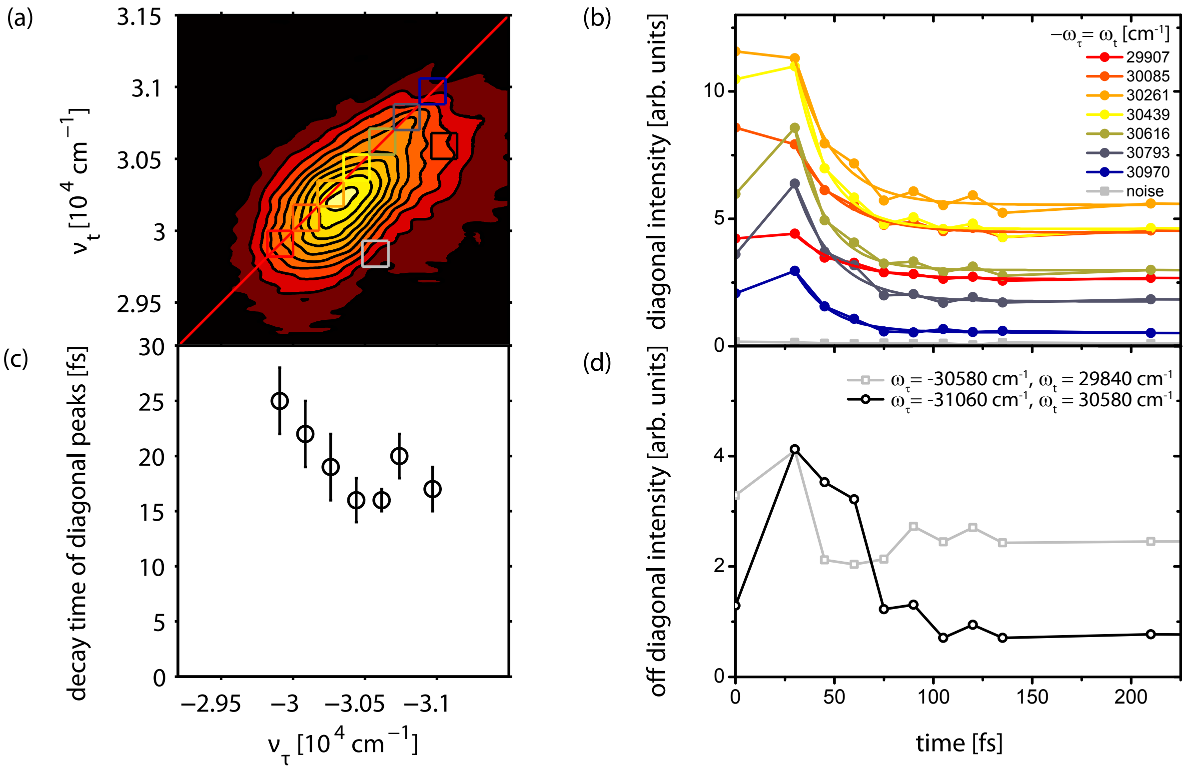

Figure 5.10: Fl-G1 2D analysis. (a) Absolute value of the Fl-G1 2D spectrum for $T = 60$ fs with contour lines drawn in steps of 10% starting from 95% of the maximum value. The signal amplitude in the indicated 180 cm^{-1} wide squares has been integrated for the further analysis depicted in (b)-(d). (b) Intensity of the diagonal squares as a function of the population time T and monoexponential fits, $I(t) = a\ \mathrm{e}^{-T/\tau} + I_0$, to the $T = 30 - 210$ fs data subsets. The retrieved time constant τ are depicted in (c) as a function of the pump wavenumber with error bars corresponding to the fit errors. (d) T-dependent intensity of the two off-diagonal squares.

5.5 Summary and Outlook

In summary, thorough analysis of linear spectra, transient absorption data and two-dimensional spectroscopy have led to the following preliminary photophysical picture of the investigated fluorene-carbazole dendrimers and single dendrons: Linear absorption in all compounds except the first generation dendrimers, Fl-G1 and SBF-G1, is dominated by strong transitions involving the peripheral fluorene units. Possibly, the effective chromophore is conjugated over the full G1 dendron molecular subunit in these compounds. Conjugation within the carbazole backbone is limited to two neighboring carbazoles and the associated electronic transitions are comparably weak. With increasing generation we expect the electron-density to shift towards the periphery as a result of the electron-withdrawing effect of the outerlayer carbazoles. The first generation dendrimers take on a special position in that within these compounds conjugation over the fluorene cores occurs, leading to a strong and redshifted transition.

Magic angle data retrieved from transient absorption data acquired for different mutual polarization of pump and probe with degenerate narrowband UV pulses could be reproduced with a biexponential fit function for all compounds except Fl-G1 and Fl-G2. The faster of the two retrieved time constants falls into the low picosecond regime and shows no clear trend with generation. It has been attributed to a mixture of solvation and intramolecular energy redistribution. The increase of the slower, ns-time-constant with generation could be traced back to a pronounced, 4–20 fold increase in the radiative lifetime when comparing first generation and higher generation compounds. As a consequence of this slower radiative depopulation of the excited state, non-radiative deactivation mechanisms with comparatively weakly generation-dependent time-constants become more competitive resulting in the lower luminescence quantum yields for the G2 and G3 dendrimers. Intramolecular charge transfer from the periphery to the core in the higher generation dendrimers has been suggested as the underlying mechanism, because it would explain the broadened and bathochromically shifted emission spectra of these compounds. To confirm this reasonable hypothesis several continuative experiments could be carried out: Besides emission spectra in different solvents, that should show strong polarity dependence as the charge seperated state is differently stabilized, transient absorption experiments with a UV-VIS continuum probe would be particularly interesting, as they could map the formation of the emissive state along with the (non)radiative backreactions to the ground state.

In the anisotropy decays, an ultrafast initial depolarization on the time scales of our instrument response has been observed for all nine compounds. Within each series, single dendrons, Fl-Gx, and SBF-Gx, we found a significant reduction in anisotropy values when going from G1 to G2, that has been interpreted as an increased delocalization of the initial excitation within the G2 molecule that localizes within < 100 fs. For all three series the second and third generation depolarization dynamics are undistinguishable within our experimental uncertainty pointing at a saturation of the initial delocalization length with G2. Furthermore, the early anisotropy values at $T \sim 250$ fs are almost identical for Fl-Gi and SBF-Gi suggesting that the initial exciton is confined to a transition dipole subensemble already present in a single Fl-Gx-branch. In SBF-G1 the anisotropy drops to a significantly lower value at $T = 10$ ps than in Fl-G1 possibly indicating inter-Fl-branch energy transfer in this compound. Anisotropy dynamics retrieved from emission-based techniques such as fluorescence upconversion that avoid the disambiguity arising from excited-state absorptions in transient absorption measurements could verify the above interpretations.

The results of our 2D measurements, virtually identical spectra for Fl-G2 and Fl-G3 that qualitatively differ strongly from Fl-G1, confirm our observations from the anisotropy experiments. The larger anti-diagonal width of the higher generations compared to the diagonally elongated spectrum of Fl-G1 would be compatible with the idea of a larger number of coupled chromophores contributing to the G2 and G3 signals. More detailed analysis of the Fl-G1 spectra revealed pump wavelength dependent sub 30 fs decay constants for the diagonal intensity. As 2D experiments have been carried out for mainly parallelly polarized excitation beams, we are sensitive to reorientation of dipole moments in addition to energy relaxation. Most likely, we are resolving the ultrafast depolarization dynamics in our 2D spectra.

6 Exciton Delocalization and Energy Transfer in Artificial Light-harvesting Antennae

Nature has produced two highly efficient light-harvesting (LH) concepts in photosynthetic organisms: In plants and algae, sunlight-absorbing chromophores are embedded in protein scaffolds, that hold their transition dipole moments at fixed relative angles and distances to ensure optimal coupling and energy transfer, e.g. in photo system I and II. In contrast, the antenna systems of green sulfur bacteria are self-assembled aggregates of bacteriochlorophylls, i.e. their supramolecular architecture is solely based on pigment-pigment interactions of the absorbing chromophores themselves. The light-harvesting organelles of these latter species, the chlorosomes, exhibit the highest chromophore density of all LH systems and largest exciton diffusion lengths known for dye aggregates [190].

Within a chlorosome (figure 6.1), photons are absorbed by up to 400-600 nm long BChl aggegates and excitation energy is efficiently transferred to the so-called baseplate from where it migrates via FMO complexes to the reaction center to eventually induce charge separation [191].

To close the experimental section of this thesis, preliminary results on tubular zinc chlorin (ZnChl) aggregates, semi-synthetic analogues of the chlorosomal light-harvesting antennae, will be presented. Such synthetic systems are potential candidates for supramolecular photonic and electronic devices, in particular when combined with other chromophores [190, 192–194], and can help unravel the architectural details of natural systems, because – in contrast to natural chlorosomes – some of them can be crystallized [191]. At the same time these synthetic systems enable us to study the couplings and energy transfer properties of the neat antenna systems without the influences of the baseplate. Moreover, synthetic ZnChl aggregates with their comparably well defined geometry open up the possibility to separate intra-aggregate disorder, from disorder of the super-supramolecular structure, i.e. the simultaneous presence of different aggregates in a chlorosome. Hence, in principle, different contributions to inhomogenous broadening can be determined.

The results discussed in the following are again the result of a cooperation with the group Prof. Dr. Frank Würthner, University of Würzburg, where the investigated compounds have been synthesized.

We will begin this chapter with an introduction to the structural and excited state properties of bacteriochlorophyll monomers and aggregates before turning to the closely related ZnChl systems we investigated. Transient absorption data will then reveal exciton annihilation effects already at very low pump photon densities, pointing at signifi-

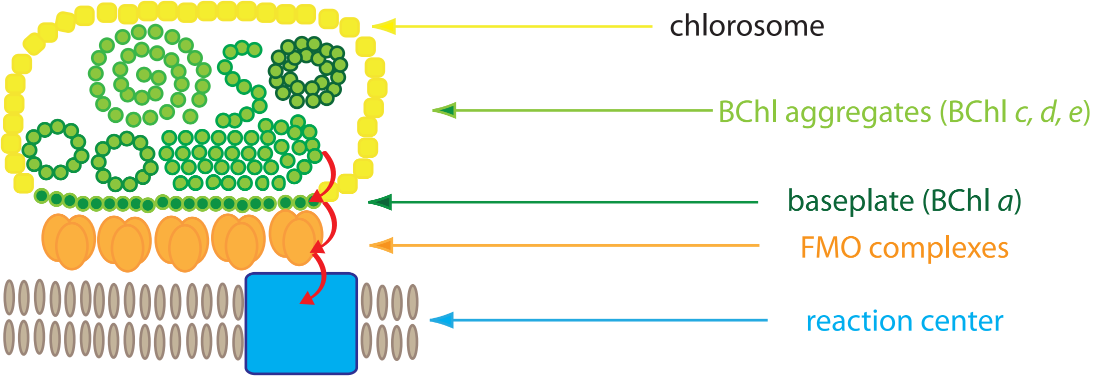

Figure 6.1: Schematic view of a chlorosome, attached via FMO complexes to the cytoplasmatic membrane that contains the reaction centers. Different architectures, lamellar, single- and multi-walled cylinders and spirals have been discussed for the light harvesting BChl aggregates within chlorsomes (Modified after [191]).

cant delocalization and efficient exciton diffusion in the investigated synthetic antenna systems. From two simplified models we will derive an estimate for the effective delocalization length L_d of the excited state wavefunctions that is a measure for the ratio of interchromophoric coupling and local disorder. Finally, preliminary two-dimensional spectra will unravel ultrafast incoherent energy transfer between different coherently coupled agregate segments as one of the mechanisms underlying the tremendous efficiency of photosynthetic processes.

6.1 The Zinc Chlorin Chromophore

The basic building block of the light-harvesting antenna in natural chlorosomes is the monomeric bacteriochlorophyll (BChl) chromophore depicted on the right in figure 6.2. It belongs to the family of tetrapyrroles, and its structure can be described as a bacteriochlorin with an additional 5-membered ring (ring E in figure 6.2) [191]. Different bacteriochlorophylls differ in the side chains attached to this macrocycle. BChl c, BChl d, and BChl e are referred to as bacteriochlorophylls for historical reasons (they were found in bacteria), strictly speaking they are based on chlorin, not on bacteriochlorin, and would have to be called Chlorophylls, Chl.

The spectroscopic properties of *monomeric* (B)Chls in the visible and near-UV spectral range are largely associated with $\pi - \pi^*$ electronic transitions, polarized along the x- and y-axis of the macrocycle and connecting the two highest occupied and the two lowest unoccupied molecular orbitals [195]. In contrast to the structurally related porphyrin, due to the lower symmetry of the (B)Chls these transitions are not degenerate and split into four bands, the Q-bands in the visible spectral range, Q_y $(600 - 800$ nm), Q_x $(500 - 600$ nm), and the so-called Soret bands, B_y and B_x, associated with a near-UV absorption $(350 - 420$ nm). The subscript denotes the polarization of the respective transition.

The fluorescence spectra of monomeric chlorin-type (B)Chls typically exhibit a small

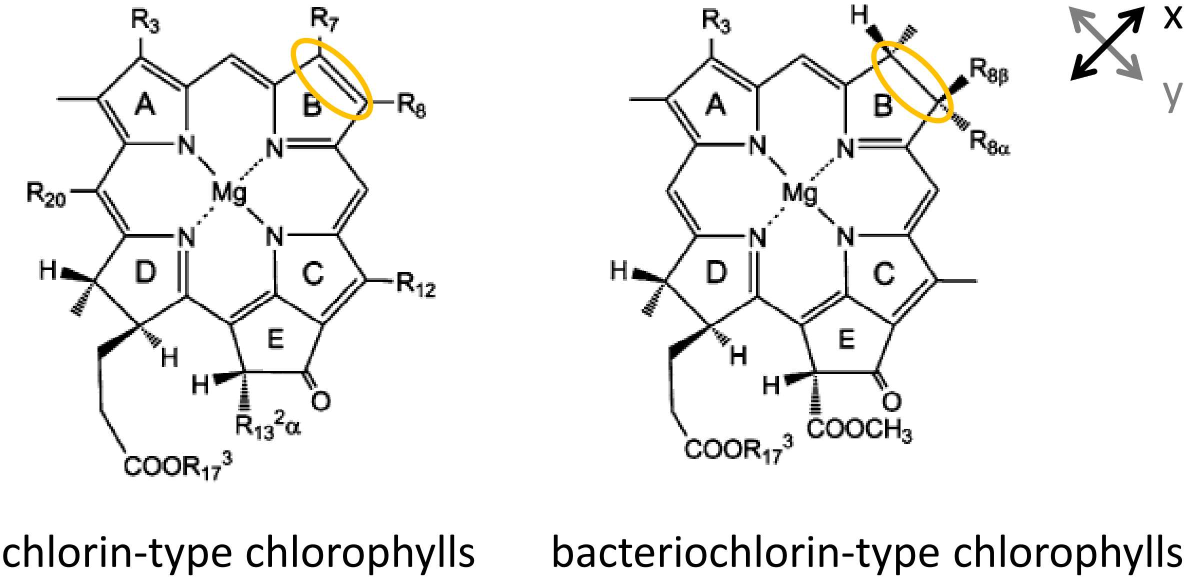

Figure 6.2: Macrocycles of chlorin-type (left) and bacteriochlorin-type (right) natural chlorophylls. They differ in the degree of macrocycle-saturation (cf. orange circles). Polarization axis of the optical transitions, x and y, are indicated in the upper right corner.

Stokes shift of $\leq 160\ \mathrm{cm}^{-1}$ and fluorescence lifetimes (in deoxygenated samples) fall into the low nanosecond regime ($\tau_f = 3 - 6$ ns). The population of triplet states competes with radiative deactivation of the excited singlet-states and stretching motions of the keto-group in ring E have been suggested as the dominant coupling mode.

Self-assembly of BChls into large aggregates is mediated by three non-covalent intermolecular interactions [191], the strongest of which is metal ligation of the central Magnesium atom. Secondly, different carbonyl side groups can act as acceptors for hydrogen bonding and their cooperative interplay leads to tight and directional binding. And finally, π-π interactions between the extended π-systems of the conjugated macrocycles contribute to aggregate formation.

Regarding the supramolecular structures of bacteriochlorophyllic antennae realized in the light-harvesting organelles, the chlorosomes, double- and single-walled cylinders, spirals and lamellar sheets have been discussed [196], and the simultaneous presence of lamellar and cylindrical arrangements seems to be the case [197] in some organisms. Regarding the short range organization, several models have been proposed [20,198–201].

The linear absorption spectra of chlorosomes are strongly red-shifted with respect to the monomer, indicating the presence of J-type alignment of the electronic transition dipoles. With respect to fluorescence lifetimes, multi-exponential decays occuring significantly faster than those of monomeric BChls are frequently reported. Measured decay rates (e.g. [192, 202–208]) vary widely which can be traced back to three major issues in the spectroscopy of chlorosomes: First of all, natural chlorosomes consist of mixtures of different BChls with the actual composition depending on the sample source, i.e. the specific bacteria or plants. Here, the relative number of baseplate BChl a molecules, that act as acceptors for the energy harvested by the (mostly BChl c) antenna systems

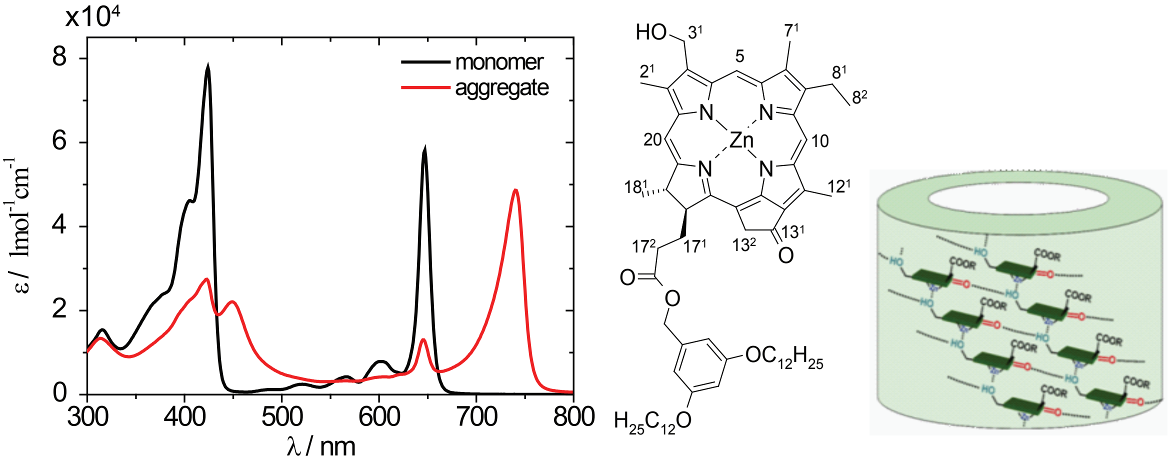

Figure 6.3: Room-temperature extinction coefficients of the monomeric ZnChl (black) in THF and the aggregate in n-heptane/THF (100:1), $c = 1.6\times10^{-5}$ M (red). Structure of the monomer and schematic of the proposed assembly into tubular rod-aggregates [modified after [209]].

is a decisive quantity [197]. Furthermore, heterogeneity in the supramolecular structure as well as differences in the local geometry, i.e. the microscopic disorder, will influence the lifetimes.

Besides, oxidized chlorin acts as an efficient fluorescence quencher already at very small concentrations [192, 202], thus leading to a strong dependence of the measured decay times on the sample preparation method. In fact, if these oxidized sites are considered deactivating defects that can be reached during exciton diffusion along the aggregate, population dynamics will include additional time-dependent rates.

Last but not least, the dense packing of chromophores in chlorosomal aggregates, the resulting delocalization of the excitons and their high mobility along the chlorosome leads to exciton-exciton-annihilation effects already at very low excitation energy densities. All these issues limit the validity of exciton delocalization length estimates from a comparison of radiative lifetimes between monomer and aggregate, and as oxidation and annihilation lead to reduction in aggregate lifetime, length estimates derived from formula (2.22) can only be considered upper bounds.

The artificial chlorosomal antenna systems investigated in our experiments are based on semi-synthetic ZnChlorin derived from natural Chlorophyll a [209–211]. They have been synthesized by Sanchita Sengupta in the group of Prof. Frank Würthner. Figure 6.3 shows their monomeric structure as well as a schematic aggregate architecture. The major differences to its natural precursor lie in the replacement of the central Mg-atom in the natural chromophore by a Zn-atom and the introduction of hydrophobic side chains leading to a reversible self-assembly process in non-polar organic solvents rather than aequous media. The formation of tubular (rod-like) structures with (300±97) nm lengths and (5.8 ± 0.4) nm heights has been evidenced by atomic force microscopy studies after spin-coating aggregate-solution onto highly ordered pyrolytic graphite surfaces [211]. When comparing the linear absorption spectra of monomer and aggregate (figure 6.3) a pronounced red-shift is observed, similar to natural chlorsomes. Yet, in our antenna systems, the J-band is significantly more asymmetric, exhibiting a steep onset on the low-frequency side, typical for linear and tubular J-aggregates. This is an immediate result of the missing BChl a baseplate that acts as an energy acceptor in natural systems.

6.2 Transient Absorption

To study the exciton diffusion dynamics within these systems degenerate spectrally resolved pump-probe experiments were performed, i.e. the same 35 fs pulses centered at 730 nm and covering the full spectral width of the J band generated in the TOPAS white non-collinear optical parametric amplifier served as pump and probe. A pair of glass wedges was introduced into the TA setup described in section 3.1 to split off a small fraction of the beam to be used as probe. The relative polarization axis of pump and probe were set to the magic angle and a polarizer aligned along the probe polarization axis was inserted behind the sample to reduce scattered pump light.

Samples of aggregated ZnChl in heptane/THF solution with a peak optical density of OD ~ 0.5 in 1 mm path length were provided by our collaboration partner. The ZnChl aggregates showed extremely high affinity to glass, such that the commonly used glass filters that protect the micro-angular gear pump in our flow-cell sample setup had to be omitted. In addition, a passivating surface treatment was applied to the 1 mm path length cuvette to avoid sticking of the molecules to the cuvette windows [212]. Sample integrity was checked by comparison of linear spectra before and after the experiment. Small amounts of precipitation accompanied by an up to 20% decrease in maximum absorbance with little effect on the overall peak shape in the J-band were frequently observed over the course of $12-48$ hours. In the time-resolved measurements, however, no change in dynamics could be detected, merely a decrease in the overall signal amplitude. Preferential alignment of the rod-like aggregates along the flow-direction in the cuvette as reported e.g. in [213] was checked by comparison of experiments with different cuvette arrangements relative to the pump polarization and could not be observed.

The transient maps acquired for 7 different pump energy densities spanning almost 2 orders of magnitude are shown in figure 6.4. All data sets have been normalized to the maximum bleach signal at $T = 30$ fs. They exhibit a strong bleach as well as a weaker, blue-shifted excited state absorption that can be attributed to transitions to the two-exciton manifold. This blue shift is an immediate result of the Pauli exclusion of a double excitation of a single monomer in the aggregate [17].

Only the $2-3$ lowest employed pump photon fluxes fall into the linear regime, as can be verified from a comparison of their difference spectra (figure 6.5(a)) and transients (figure 6.5(c)). As will be discussed in detail in the next section, the fact that deviations from a linear pump power dependence occur already at very low energy densities indicates significant delocalization of the excited state wave functions. Furthermore, the much faster signal decrease as a result of exciton-exciton annihilation within the first picosecond points at a remarkable exciton mobility along the aggregate, i.e. efficient exciton diffusion.

Neglecting the presence of oxidized trap sites that would require a model with time

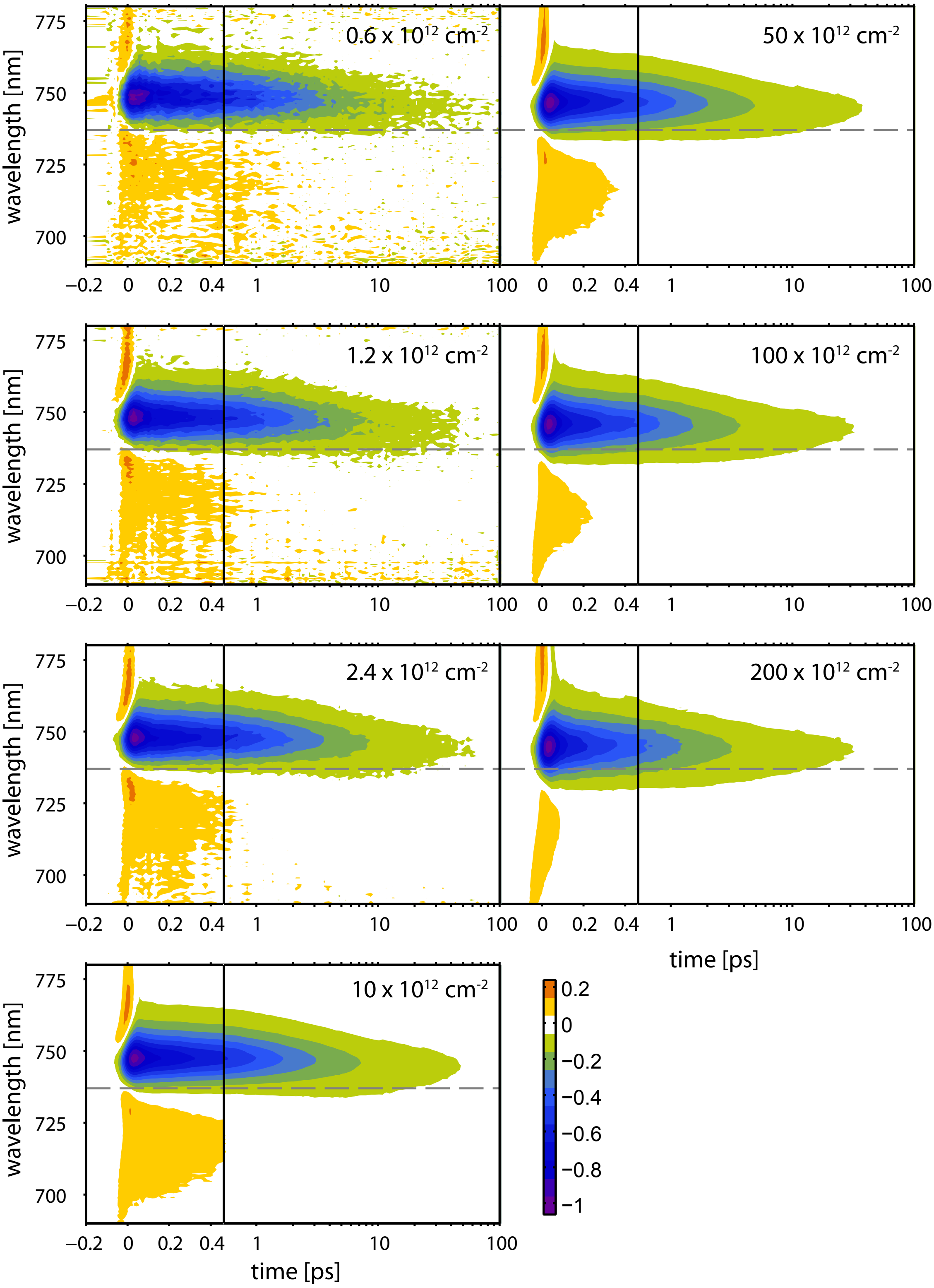

Figure 6.4: Transient maps acquired for different pump photon fluxes, indicated in the upper right corner of each graph. Each data set has been normalized to the maximum bleach signal at $T = 30$ fs.

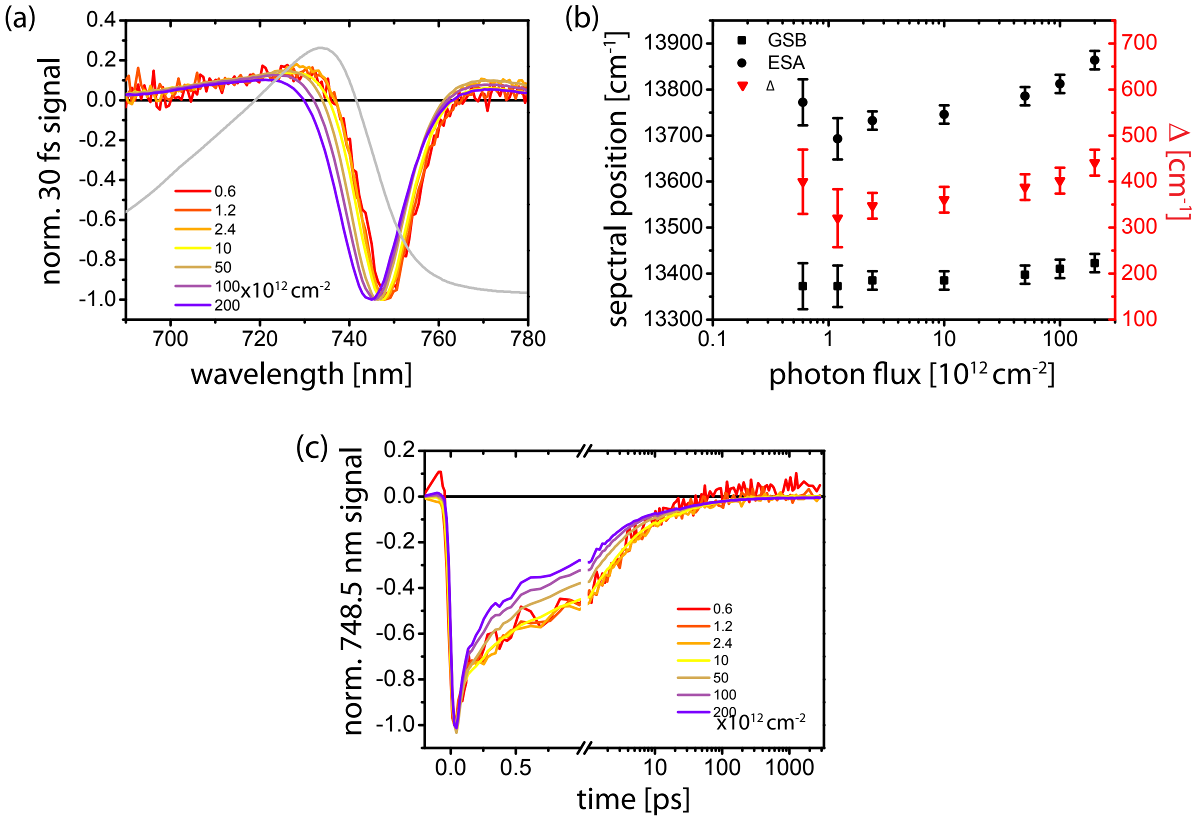

Figure 6.5: Normalized $T = 30$ fs difference spectra for different photon fluxes (a). Spectral position of the maximum bleach, ν_{GSB} and maximum ESA signal, ν_{ESA} as a function of the photon flux (black) and $\Delta = \nu_{\mathrm{ESA}} - \nu_{\mathrm{GSB}}$ (red)(b). Normalized 748.5 nm transients for different photon fluxes (c).

dependent rates, the low power data sets can be fitted with a sum over three exponentials convoluted with a fixed instrument response function of $\tau = 35$ fs. Decay times of $\tau_1 = 180$ fs, $\tau_2 = 2.6$ ps, and $\tau_3 = 70$ ps have been retrieved for the $1.2 \times 10^{12}\ \frac{1}{\mathrm{cm}^2}$ data set. The fastest time constant τ_1 is comparable to a $200-300$ fs decay observed in TA-studies on natural chlorsomes of *Chloroflexus aurantiacus* under anaerobic conditions [208]. If we neglect the influence of quenching mechanisms in our samples this might question either their assignment to an energy transfer between neighboring rod-shaped BChl-aggregates – as our inter-tubular distances should be considerably larger than their assumed $1 - 2$ nm – or the presence of individual ZnChl tubes in our solution. The latter seems less likely given the observation of isolated tubes in the AFM studies paired with the fact that the shape of the J-band showed little dependence on the concentration.

With increasing pump power, we immediately recognize a faster initial signal decrease in the TA data along with a spectral broadening of the bleach feature accompanied by a significant blue shift of the nodal line between bleach and excited state absorption. The latter becomes more evident from a look a the normalized $T = 30$ fs difference spectra in figure 6.5 (a). It is an immediate consequence of multiple excitations with increasing pump power, and occurs in similar fashion also in linear J-aggregates, in which case it has also been studied theoretically [17]. Extracting the spectral positions of the maximum bleach and maximum ESA signal from figure 6.5 we realize that while both quantities blue shift with increasing power, ν_{ESA} shifts more strongly, resulting in a net increase in the energy gap between both features.

For linear J-aggregates, the effective delocalization length L_d is related to the spectral shift between monomer and aggregate absorption $2J$ and the separation $\Delta = \nu_{\mathrm{ESA}} - \nu_{\mathrm{GSB}}$ between maximum GSB and ESA at early times,

$$L_d = \sqrt{3\pi^2 \frac{J}{\Delta}}. \tag{6.1}$$

Approximating our tubular ZnChl aggregate as linear and using $\Delta(\Phi = 1.2\times10^{12}\mathrm{cm}^{-2}) = 320\ \mathrm{cm}^{-1}$ as well as $J = 916\ \mathrm{cm}^{-1}$, the excitation would be delocalized over $L_d = 9$ monomeric units. Even for linear aggregates, equation 6.1 holds only in the limit $L_d \gg 1$ and L_d significantly smaller than $\sqrt{3\pi^2 \frac{J}{\gamma}}$, where γ is a measure for the homogenous width, which is roughly fulfilled in our case [214]. Furthermore, the derived value for L_d must be considered an upper limit, because the difference spectra are only sensitive to the delocalization until a saturation length is reached.

6.2.1 Exciton Delocalization Length

By applying a very simple model, we will derive an estimate for the exciton delocalization length from the power dependence of the initial transient absorption signal. The key idea of this model is the following: If we assume a monomeric solution with N_{mono} molecules in the probed sample volume and if we know the number of pump photons that have interacted with the molecular ensemble contained in that volume, P_{int}, then we can predict the fraction of monomers that will have interacted with one pump photon n_{1ex}, two pump photons $n_{2ex}, \ldots, m$ pump photons n_{mex} for each value of the pump photons per monomer $P_{\mathrm{int/mono}} = \frac{P_{\mathrm{int}}}{N_{mono}}$ from simple statistics.

The initial TA-signal as a function of $P_{\mathrm{int/mono}}$ should then be a weighted sum over contributions from these singly excited n_{1ex}, doubly excited n_{2ex}, ..., m-fold n_{mex} excited monomers.

$$S_{TA}(T = 0, P_{\mathrm{int/mono}}) = \sum_i a_i n_{iex}(P_{\mathrm{int/mono}}). \tag{6.2}$$

The weighting factors a_i reflect the difference in oscillator strength of the final state that has been populated after interaction with i photons and the ground state. For example, if two-fold excitation of the same monomer exclusively leads to deactivation of the excited state back to the ground state, then $a_2 = 0$.

As we will see below, both, the number of interacting pump photons and the number of monomers in the probed sample volume, are accessible quantities at least in the limit of two-level systems.

Now consider an aggregate with delocalized excitonic states, i.e. the situation where the absorption of a single photon leads to the excitation of more than one monomer.

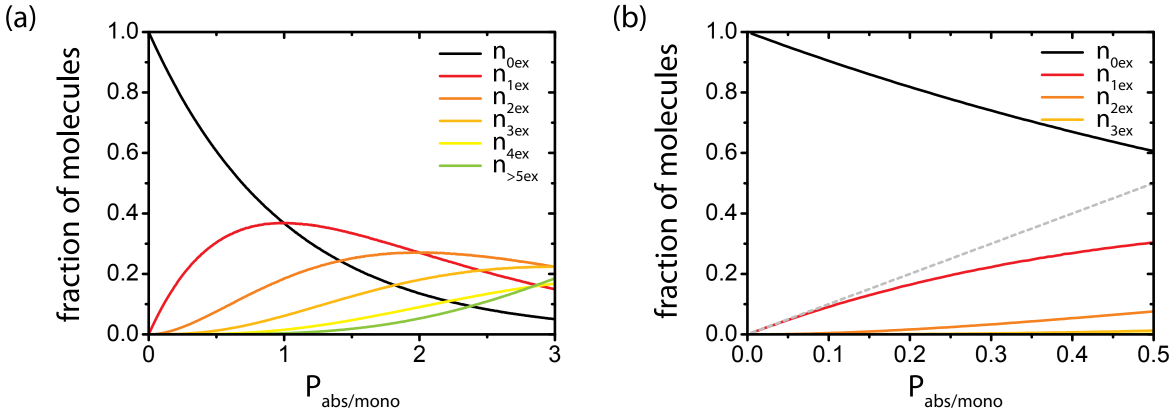

Figure 6.6: Fraction of molecules that absorbs 1 (n_{1ex}), 2 (n_{1ex}), ...> 5($n_{>\mathrm{5ex}}$), photons as a function of the total number of photons absorbed by the ensemble divided by the number of molecules, $P_{\mathrm{abs/mono}}$(a). A zoom to low power excitation conditions is shown in (b). When the red curve can be approximated by the gray dashed line, one works in the linear regime.

In this case the decisive quantity for the power dependence of the TA signal will be the number of interacting photons per exciton $P_{int/exc}$. For an effective delocalization length L_d (measured in monomeric units, i.e. $L_d = 3$ corresponds to delocalization over 3 monomers in the aggregate) the relation between $P_{int/exc}$ and the $P_{\mathrm{int/mono}}$ can be written as

$$P_{int/exc} = \frac{P_{\mathrm{int}}}{N_{exc}} = \frac{P_{\mathrm{int}}}{\frac{N_{mono}}{L_d}} = L_d P_{\mathrm{int/mono}}. \tag{6.3}$$

Thus, if we rescale the x-axis in equation 6.2 with the exciton delocalization length L_d, the power dependence of the TA signal should follow the functional form of this equation, providing a way to determine L_d from a simple fitting routine.

To obtain the functional form of n_{1ex}-, n_{2ex}-, ..., n_{mex}-curves, numerical simulations have been performed. $P = 0 - 1000$ photons were randomly distributed over $N = 200$ molecules, assuming equal absorption probability for all molecules, and the number of molecules receiving 0, 1, 2, ... m photons was counted for a total of 5000 realizations for each value of P.

The resulting n_{1ex}-, n_{2ex}-, ..., n_{mex}-curves as a function of $\frac{P}{N} = \frac{P_{\mathrm{int}}}{N_{mono}}$ are shown in figure 6.6. They deserve the reader's attention, as they are not only relevant for the specific application discussed above, but should be kept in mind for all spectroscopic experiments: The fraction of molecules that interact with two photons becomes significant already at counterintuitively small photon densities of ~ 0.1 photons per molecule. Thus, if more than 10% of the molecules are excited, e.g. in a TA experiment, one is no longer working in the linear regime (gray dashed curve in figure 6.6 (b)) and measured system dynamics will be influenced by higher order effects.

To calculate the number of photons that interact with an individual monomer in the probed volume, we will follow the derivation given in [19], but the width of our excitation spectrum compared to the absorption line shape requires taking into account the wavelength dependence of both, the pump spectrum and the sample absorbance, explicitly. In our case the number of interacting photons, P_{int}, is given by the integral

$$P_{\text{int}} = \int_{-\infty}^{\infty} N_{pu}(\lambda)(1 - 10^{-OD(\lambda)})\,\mathrm{d}\lambda. \tag{6.4}$$

Here, $OD(\lambda)$ is the optical density of the sample and $N_{pu}(\lambda)$ is the total number of pump photons per wavelength intervall impinging on the probe area. The latter can be calculated from the pump pulse energy $E_{pu}(\lambda)$ as well as the pump and probe beam radii, r_{pu} and r_{pr} (both defined at $1/e^2$ intensity level)

$$N_{pu}(\lambda) = \frac{E_{pu}(\lambda)\lambda}{hc} \frac{\int_0^{r_{pr}} r\mathrm{e}^{-2r^2/r_{pu}^2}\mathrm{d}r}{\int_0^{\infty} r\mathrm{e}^{-2r^2/r_{pu}^2}\mathrm{d}r} \tag{6.5}$$

where we have used that the energy of a single photon $E_{ph} = \frac{hc}{\lambda}$ can be calculated from its wavelength, Planck's constant h, and the speed of light c.

We approximate the wavelength-dependence of the pump pulse energy from a wavelength integrated power measurement yielding $\tilde{E}_{pu}$ and a separately measured spectrum $I_{pu}(\lambda)$ as

$$E_{pu}(\lambda) = \frac{\tilde{E}_{pu}}{\int_{-\infty}^{\infty} I_{pu}(\lambda)\mathrm{d}\lambda} I_{pu}(\lambda) \tag{6.6}$$

The number of monomers N_{mono} in the probed volume are calculated from the extinction coefficient, the sample OD, the cuvette path length, the probe radius and Avogadro's constant

$$N_{mono} = \frac{OD}{\epsilon d} \pi r_{pr}^2 d N_A. \tag{6.7}$$

A major experimental error source may lay in the assumption of an ideal Gaussian beam. Hence, to check the accuracy we reach in the determination of $P_{\text{int/mono}}$ from experimental parameters, power dependent TA-measurements on a monomeric reference system, the laser dye HITCI in ethanol, were carried out. In this particular chromophore, no hints of excited state absorptions in the wavelength range covered in our experiments are observed, justifying the assumption that stimulated emission back to the ground state is the only mechanism present for double excitation, i.e. $a_2 \sim 0$.

We take the integrated absolute value of the transient absorption signal at $T = 30$ fs, S_{int},

$$S_{\text{int}} = \int \mathrm{d}\lambda\, |S_{\text{TA}}(\lambda, T = 30 \text{ fs})| \tag{6.8}$$

as a measure for the generated excitons. $P_{\text{int/mono}}$ can be calculated from equations (6.4) and (6.7) with $r_{pu} = 97\ \mu$m, $r_{pr} = 57\ \mu$m, $d = 1$ mm, $\epsilon = 21.5 \times 10^4$ lmol^{-1}cm^{-1} [188], and $OD = 0.54$ as well as an experimental laser spectrum and the employed pump pulse energies $\tilde{E}_{pu}$.

S_{int} as a function of the calculated $P_{\text{int/mono}}$-values for the HITCI measurement is shown in figure 6.7 (a) together with the n_{1ex}-curve retrieved from numerical simulations. Error bars in all graphs in this section correspond to standard deviations retrieved

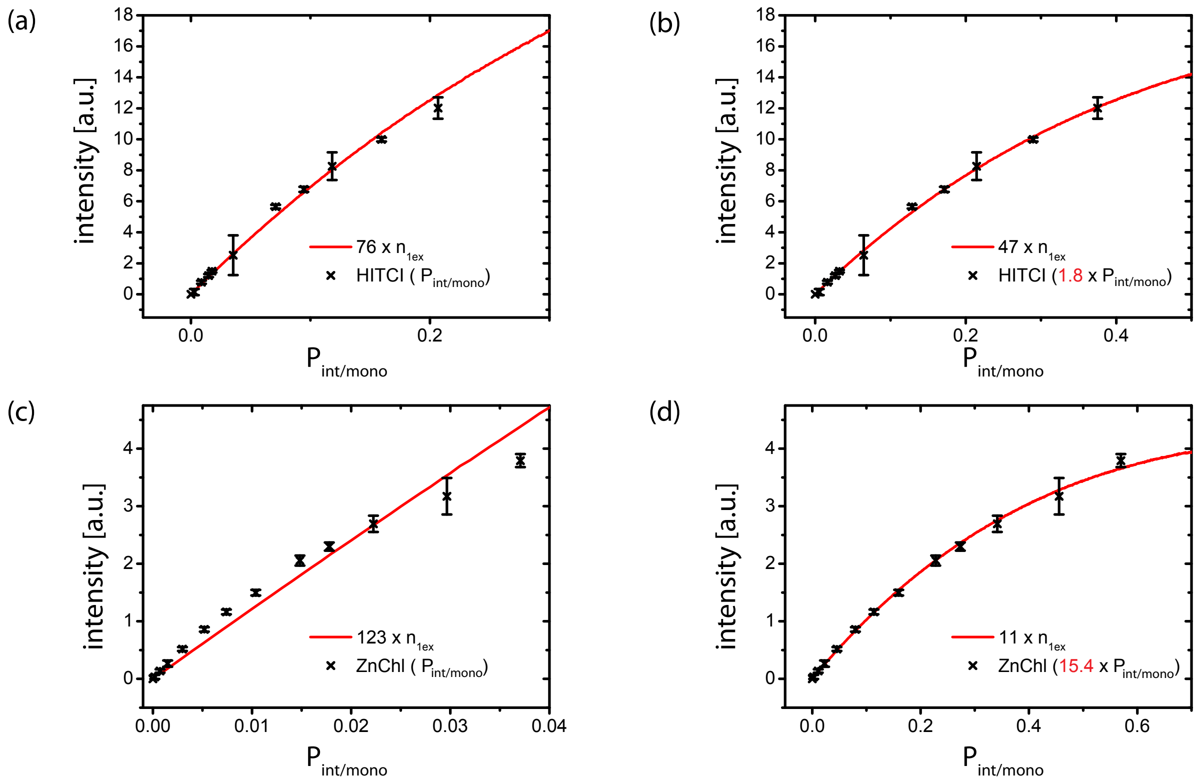

Figure 6.7: Comparison between the fraction of singly excited molecules, n_{1ex} (amplitude rescaled as indicated in the graphs) and the integrated signal S_int as a function of the absorbed photons per monomer $P_\mathrm{int/mono}$ for HITCI ((a) and (b)) and the ZnChl aggregates ((c) and (d)). In (a) and (c) x-values are as calculated from the experimental parameters, while $P_\mathrm{int/mono}$ has been rescaled with a delocalization length $\tilde{L}_d$ of $\tilde{L}_d = 1.8$ and $\tilde{L}_d = 15.4$ as retrieved from a fitting routine to yield the optimal overlap presented in (b) and (d), respectively.

from averaging over several difference spectra for each power. While the overlap between the acquired data points and the n_{1ex}-curve (rescaled with an overall amplitude prefactor of $a_1 = 76$) is not too bad, a much better match is found when rescaling the calculated experimental $P_\mathrm{int/mono}$-values with a factor of 1.8 (cf. figure 6.7(b)). As this corresponds to a feigned delocalization over 1.8 molecules which is impossible in the monomeric HITCI solution, we deduce a calibration factor for L_d of $L_\mathrm{d} = \frac{\tilde{L}_\mathrm{d}}{1.8}$ from this reference measurement, where $\tilde{L}_\mathrm{d}$ is the delocalization length retrieved from the parameters described in the last paragraph.

Applying the same procedure to the $T = 30$ fs-data retrieved for the ZnChl aggregates, yields the curves displayed in figure 6.7(c) and (d): When the x-axis is not rescaled (figure 6.7(c)), overlap between experimental data and simulation is extremely poor, indicating significant delocalization of the excited state wavefunctions in our light-harvesting antennae. In contrast, when introducing a delocalization length $\tilde{L}_\mathrm{d} = 15.4$ (figure 6.7(d)), excellent overlap with the simulated n_{1ex}-curve is achieved. Taking into account our calibration factor yields $L_d = 8.5$, i.e. effective delocalization over approximately 9 monomeric units.

Even if involvement of higher lying exciton bands cannot be neglected for these aggregates, the processes occuring between these higher levels should be similar to those occuring from the first excited state at early times except for small spectral shifts. If we further assume that after absorption of the first photon, stimulated emission back to the ground state and promotion to the two exciton band occur with comparable probability, then $a_2 \sim 0.5 \times a_1$ and error margins of $L_d = 5 - 20$ seems a reasonable assumption for the retrieved value. The excellent agreement with the $L_d = 9$ value derived from an approximation as a linear aggregate in the last section, however, should be considered coincidence.

6.3 Two-dimensional Spectra

Two-dimensional spectra of the ZnChl aggregates have been obtained with the setup described in detail in section 3.3. Excitation pulse durations were comparable to the TA experiments and again the complete J-band was spectrally covered. An exemplary spectrum is shown in the upper panel of figure 6.8 (b) along with the sample absorption. The same sample preparation method was used.

For each population time, the coherence time was varied between $\tau = \pm 122.914$ fs in steps of $\Delta\tau = 5.587$ fs for the data presented in figure 6.8 and $\tau = \pm 120.69$ fs in steps of $\Delta\tau = 4.47$ fs for the data in figure 6.9, respectively. The real and imaginary parts of $3-5$ individual spectra were averaged before phasing all population times with transient absorption data obtained within the same experimental setup using beam 3 as probe.

The photon flux of all three excitation pulses combined was $18 \times 10^{12}\ \frac{1}{\mathrm{cm}^2}$, which could not be confirmed to fall into the linear regime: Figure 6.8 shows the real part of the $T = 30$ fs 2D spectra measured at total photon fluxes of $18 \times 10^{12}\ \frac{1}{\mathrm{cm}^2}$, $39 \times 10^{12}\ \frac{1}{\mathrm{cm}^2}$, and $78 \times 10^{12}\ \frac{1}{\mathrm{cm}^2}$, respectively, normalized to their individual maxima in the left column. The deviation between the higher power data and the $18 \times 10^{12}\ \frac{1}{\mathrm{cm}^2}$-experiment is depicted in the right column. The real part of the 2D spectrum is comprised of a strong positive contribution originating from ground state bleach and stimulated emission (red), and a weaker negative excited state absorption (blue). With increasing power, a broadening of the features is observed along with a decrease in the relative amplitude of the ESA-feature in agreement with the power-dependent TA data. As one would expect the deviations are largest at pump frequencies ν_τ that correspond to the maximum of the linear absorption. This excludes the possibility of drastically larger exciton delocalization lengths on the blue edge of the J-band.

While in 2D experiments on natural chlorsomes [214] total photon fluxes of $15 \times 10^{12}\ \frac{1}{\mathrm{cm}^2}$ were assumed to correspond to annihilation free conditions, from the data presented in figure 6.8 and our transient absorption results we must conclude that the preliminary 2D spectra discussed in the following are somewhat distorted from annihilation effects.

Nevertheless, we will now have a closer look at spectra retrieved for the lowest photon flux. The absolute value and the real part for population times up to $T = 540$ fs are depicted in figure 6.9(a) and (b), respectively. Note that the real parts have been normalized to their individual maxima to emphasize the changes in the line shapes.

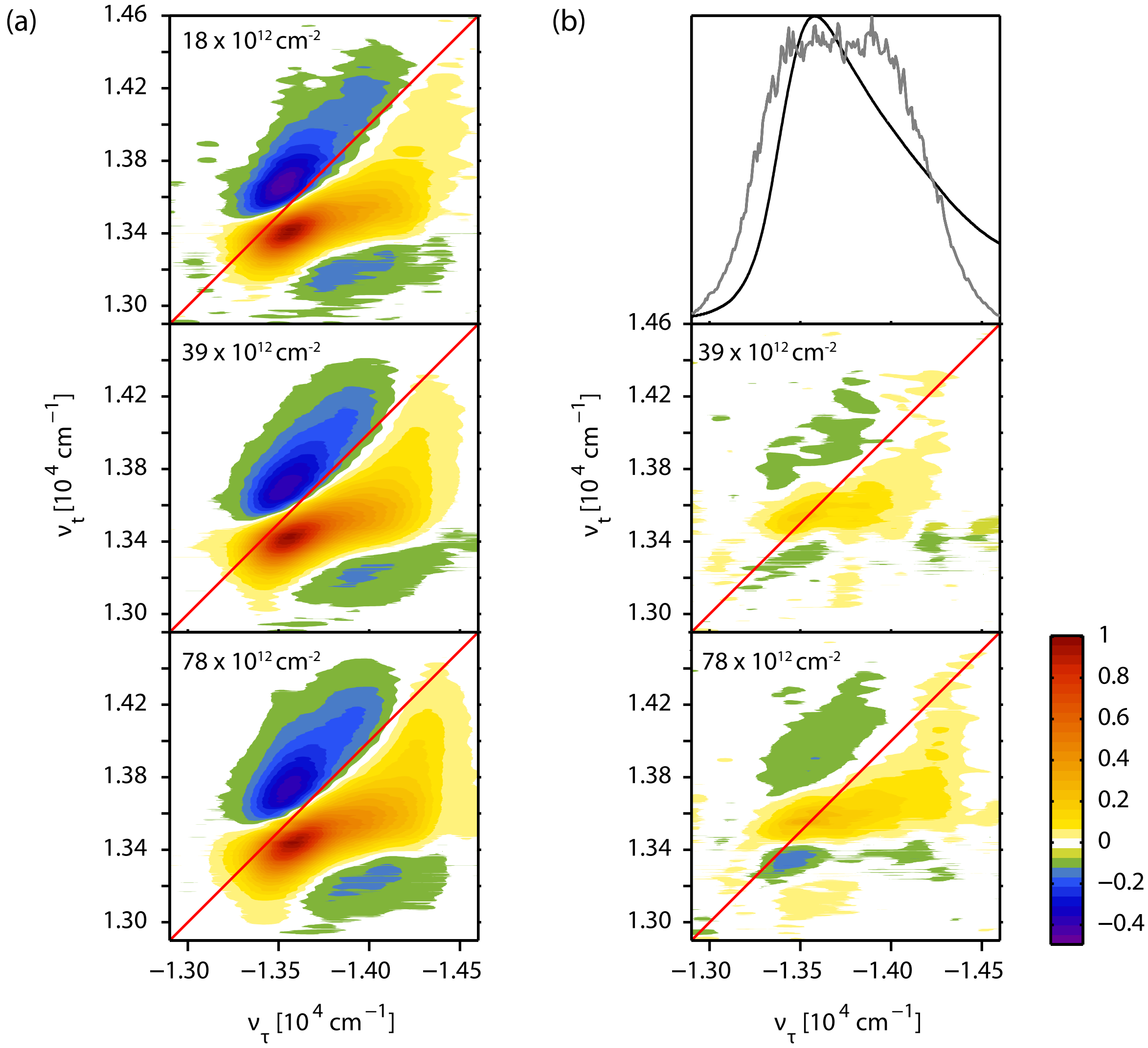

Figure 6.8: Real part of $T = 30$ fs 2D spectra retrieved for different photon fluxes as indicated in the graphs (a). Each spectrum has been normalized to each individual maximum. Contour lines are drawn in steps of 5% starting at 0.95. Deviations between the higher power and lowest power spectrum, i.e. Re(high power)-Re(lowest power), are shown in (b) along with the sample absorption (black) and an exemplary laser spectrum (gray) in the top panel.

The $T = 0$ fs spectrum is strongly elongated along the diagonal, i.e. excitation and emission frequencies are highly correlated. While some increase in the anti-diagonal width with increasing pump frequency is observed, the overall dominant diagonal elongation indicates that coherent coupling is *not* present over the whole frequency range: In the hypothetical case of a giant coherently coupled antenna, all transitions contributing to the linear absorption would share a common ground state resulting in significant off-diagonal intensity (cross peaks) in the $T = 0$ fs correlation spectrum. Instead, in the investigated ZnChl aggregates the delocalization of excited state wave functions is limited to segments of the total aggregates, for which the ratio of local (diagonal and off-diagonal) disorder and pigment-pigment interaction is comparably small. This finding

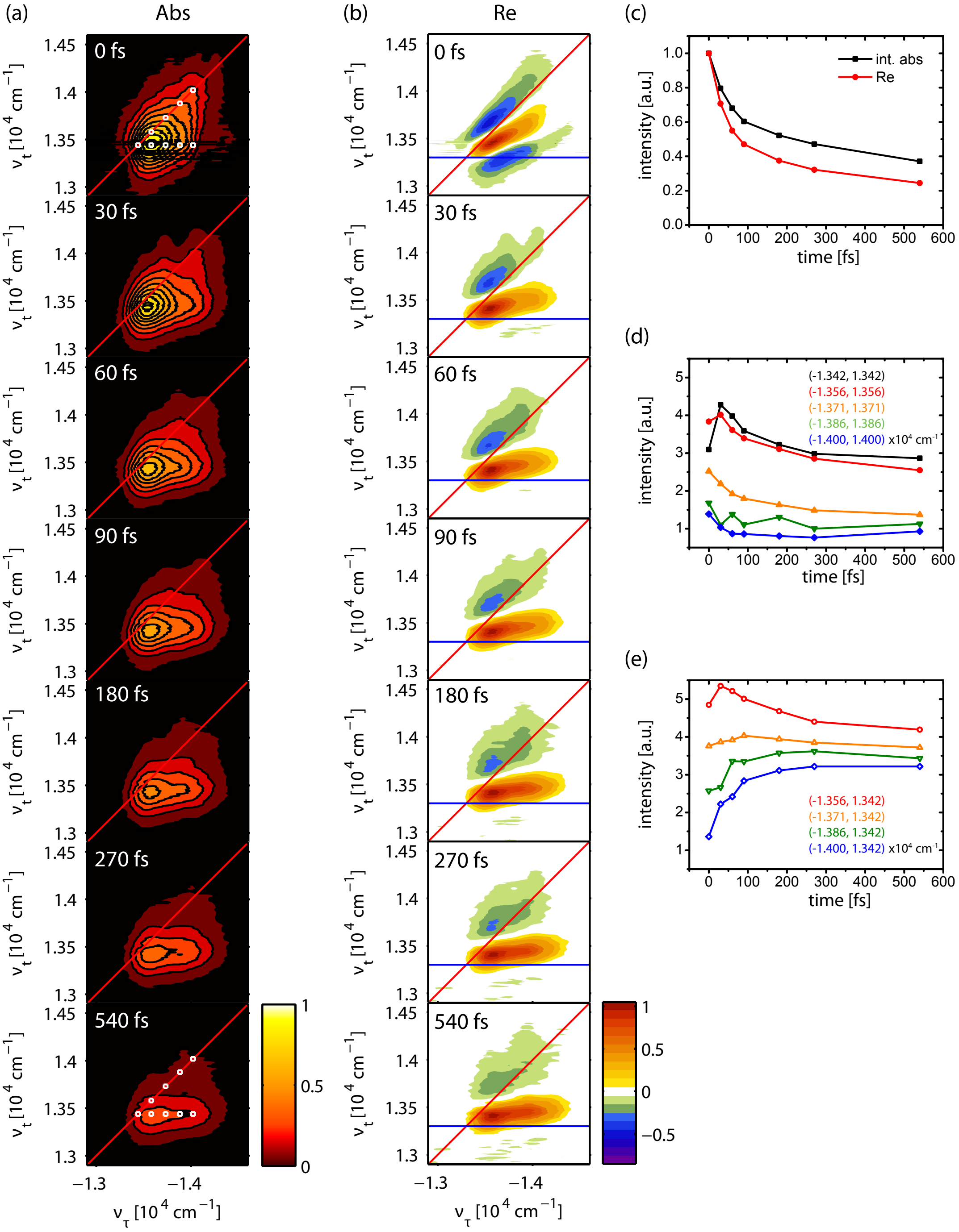

Figure 6.9: Absolute value (a, contour lines from 95% of the first spectrum, steps of 10%) and real part (b, normalized to individual maxima) of 2D spectra for T-values as indicated in the upper right corner. Decay of the integrated absolute value (black) and the point of maximum amplitude in the real part at $T = 0$ s (red) (c). Dynamics of the diagonal (d) and off-diagonal (e) intensity relative to the integrated amplitude for spectral positions marked with white boxes in (a).

is consistent with an inhomogeneously broadened absorption in natural chlorosomes deduced from photon echo experiments [215] and in line with the coherence-domain picture deduced for chlorosomes of *Chlorobaculum tepidum* from 2D measurements [214].

The subsequent dynamics within the first 540 fs (cf. figures 6.9 (a)-(c)) is governed by an ultrafast component that is associated with drastic changes in the 2D lineshape: The overall intensity completely loses its diagonal shape within the first $\sim$ 100 fs, and becomes elongated along the ν_τ-axis as energy is efficiently transferred to high oscillator strength excited states at the low frequency edge of the J-band. Transfer times are pump frequency dependent (cf. figures 6.9 (d), (e))), and the majority of transfer processes is completed after $\sim$ 200 fs. Homogeneous lineshape dynamics of individual excitonic transitions can be excluded as the origin for these early shape changes, as their spectral width would be significantly smaller than the diagonal line width of the 2D spectrum [214]. In the real part, we observe a significant broadening that is more pronounced on the high probe frequency side as a result of the asymmetric absorption lineshape, along with a decrease in the relative amplitude of the excited state absorption feature. In addition, the slope of the nodal line separating positive and negative amplitude levels off as the dynamics become progressively independent of the initial excitation conditions.

Thus, while disorder impedes coherent coupling of neighboring domains, they are still in very close proximity allowing for ultrafast incoherent energy transfer, i.e. highly efficient exciton diffusion.

A peculiar modulation in the lineshape within the first 100 fs around $\nu_\tau = 13800$ cm^{-1} that manifests itself also as modulation in the dynamics of the corresponding diagonal and anti-diagonal peaks (green curves in figures (d) and (e)) deserves the attention of future experiments and theoretical modeling. Approximating BChl aggregates as idealized cylinders, the transitions underlying the blue part of the absorption spectrum are the ones polarized along an axis perpendicular to the long axis of the cylinder. After the discussion of the dendrimeric 2D spectra in the last chapter, one can speculate on an ultrafast depolarization contribution to these features.

6.4 Conclusion and Outlook

In summary the following photophysical picture of the investigated semisynthetic light-harvesting systems has emerged: A pronounced redshift of $J \sim 900$ cm^{-1} in the linear spectra upon going from the monomer to cylindrical aggregates suggests significant interchromophoric coupling in the latter. The delocalization length of the excited state wave functions L_{d} as a result of these strong pigment-pigment interactions has been estimated from a simplified statistical model describing the power dependence of the early time bleach signal and an independent approximation as a linear aggregate applied to the difference spectra retrieved from transient absorption experiments. Both methods yielded consistent results and the retrieved value of $L_{\mathrm{d}} = 5 - 20$ is comparable to values published for natural chlorosomes of $2 - 12$ monomers [205,215] and other semisynthetic ZnChl aggregates [192].

Two-dimensional spectra suggest that the origin of highly efficient energy transfer in natural antenna systems originates from ultrafast $\tau < 100$ fs *incoherent* energy transfer between neighboring coherence domains: while disorder limits coherent coupling of neighboring molecules to L_d, the emerging oscillators are in very close proximity within the aggregate allowing for ultrafast exciton diffusion via Förster type mechanisms.

For future experiments different, water-soluble zinc chlorin aggregates would be advantageous, as in such samples a reducing agent, dithionate, can be added. Hence, influences of oxidation on measured dynamics can be prevented and better comparability to natural systems, typically investigated under anaerobic conditions in water, can be achieved.

The presented 2D results have to be confirmed in these future experiments under completely annihilation free conditions. As stated above, the origin of a lineshape modulation observed on the high-frequency side of the J-band deserves the attention of such future investigations, and a theoretical model including the cylindrical shape of the aggregates is called for. As depolarization as a result of energy transfer between differently polarized transition dipole moments has been suggested as an underlying mechanism, a comparison of tubular and linear ZnChl aggregates [210] would be particularly instructive: In the latter systems that can be obtained when substituting the 3^1 hydroxy with a methoxy group which impedes hydrogen bonding to the 13-keto groups, such dynamics should be absent. Furthermore, the lower dimensionality of linear aggregates should affect exciton diffusion processes, as the number of potential acceptor sites is significantly reduced.

7 Conclusions and Outlook

Time-resolved spectroscopic studies of energy transfer between molecules in solution form a basis for both, our understanding of fundamental natural processes like photosynthesis as well as directed synthetic approaches to optimize organic opto-electronic devices. Here, coherent two-dimensional (2D) spectroscopy opens up new possibilities, as it reveals the correlation between absorption and emission frequency and hence the full cause-and-effect chain.

On the technological side, it was the objective of this thesis to design and implement an optical setup for fully noncollinear coherent two-dimensional (2D) spectroscopy that addresses the specific challenges of ultraviolet excitation wavelengths. To this end, the concept of pairwise beam manipulation (PBM) already successfully realized in a setup for visible excitation during my Diploma thesis was first investigated in more detail: When steering the four beams of a 2D experiment only in pairs that enter the measured phase with opposite sign, the detected signal modulation is governed by the difference between system and laser frequency $\Delta\omega = \omega_{eg} - \omega_0$, rather than the much faster oscillation of the transition frequency ω_{eg}. In other words, the rotating frame is inherent in a PBM scanning scheme. Hence, the full benefits of a noncollinear beam geometry – higher sensitivity, separation of non-rephasing and rephasing Liouville pathways as well as measurement of absorptive and dispersive 2D spectra – can be retrieved under timing precision and mechanical stability requirements that are significantly reduced to fractions of the pulse duration. This has been theoretically derived for the more illustrative case of a linear polarization and experimentally demonstrated in measurements where mistimings were deliberately introduced.

Based on these considerations an all-reflective, miniaturized setup for 2D-UV spectroscopy that specifically suits the low dispersion needs of ultraviolet excitations has been developed. The feasibility of fully non-collinear 2D spectroscopy in the UV was demonstrated in a proof-of-principle experiment on *para*-terphenyl, and phase stability values comparable to the best values reported for the visible have been obtained.

In the second part of this thesis, transient absorption (TA) and 2D spectroscopy have been applied to reveal the couplings and energy transfer dynamics associated with electronic transitions of multichromophoric assemblies of increasing complexity in the visible and ultraviolet regime: Perylene bisimide-perylene monoimide dyads in cooperation with Prof. Dr. Frank Würthner and Prof. Dr. Bernd Engels, both at the University of Würzburg, a series of fluorene-carbazole dendrimers in cooperation with Prof. Dr. Gregory Scholes (University of Toronto, Canada) and Prof. Dr. Paul Burn (University of Queensland, Australia), and tubular zinc chlorin aggregates, again in cooperation with Prof. Dr. Frank Würthner.

The linear absorption of all systems studied showed evidence of excitonic coupling, i.e. coherent interaction between the constituing chromophores that leads to delocalization of the excited state wave functions.

With a decoupled ground state and synthetically fixed interchromophoric distances and angles, the perylene bisimide-perylene monoimide dyads represented an ideal exitonic model system to study the couplings and energy transfer resulting from Coulombic interactions of two transition densities. The clear deviation of the bichromophoric linear absorption spectra from a sum over the extinction of the two composing monomers could be attributed to the redistribution of oscillator strength in a geometrically confined J-type-dimer arrangement. While a point dipole model could only qualitatively explain the observed absorption, quantitative agreement with *ab initio* calculations performed in the group of Prof. Dr. Bernd Engels was found. In transient absorption experiments, ultrafast energy transfer with time constants of $\sim 70 - 160$ fs could be resolved. The retrieved transfer times fall into the order of magnitude predicted by Förster theory, but are significantly shorter than the calculated values of $\tau = 340 - 450$ fs, thus pointing at the limitations of this widely used theory at donor-acceptor distances comparable to the size of the chromophores.

Regarding these dimeric systems, future studies could focus on this inter-chromophore charge transfer, that within the scope of this work has only been postulated as the most likely explanation for a non-radiative decay mechanism evident from the fluorescence quantum yields and the TA data. Extending the probe wavelengths further to the NIR in transient absorption experiments, where the spectral signature of the PBI-anion is expected, could prove our hypothesis and disentangle the time scales of charge transfer – including potential back electron transfer rates – from conformational dynamics.

In going from the bichromophores to dendrimeric compounds, the complexity increased drastically: As covalent bonding results in conjugation over neighboring moieties in these systems, the assumption of a decoupled ground state had to be dropped. At the same time, the number of almost degenerate electronic states increased drastically, and semi-empirical calculations as well as extensive literature review had to be employed to identify the effective chromophores and postulate an intramolecular potential gradient. Results of TA experiments under magic angle conditions and broadened red-shifted emission spectra suggested an intramolecular charge transfer in the higher generation compounds. Ultrafast localization of an initially delocalized excited state on the timescales of our instrument response could be deduced from anisotropy data followed by energy migration via incoherent hopping processes. Saturation of the initial delocalization with the second generation has been suggested as second and third generation anisotropy dynamics were indistinguishable in the investigated wavelength range. Two-dimensional spectra of the fluorene-cored compounds confirmed these observations and were consistent with a higher number of coupled transitions in the higher generations compared to G1. In addition, ultrafast depolarization dynamics with time constants of ~ 30 fs could be resolved in the first generation compound, FL-G1.

Even though the zinc chlorin aggregates studied in the last chapter comprised by far the largest number of chromophores of all systems studied, the comparably defined transition dipole orientation realized in their tubular geometry leads to a reduction in complexity, as oscillator strength is concentrated into few electronic transitions. In contrast to the other systems investigated, interaction energies in these aggregates are so large compared to fluctuations in site energies and couplings that even at room temperature coherence domains – comprising $5 - 20$ monomers according to our results – prevail.

Two-dimensional spectra suggested that the origin of highly efficient energy transfer in natural antenna systems originates from ultrafast ($\tau < 100$ fs) *incoherent* energy transfer between these coherence domains: while disorder limits coherent coupling of neighboring molecules to L_{d}, the emerging oscillators are in very close proximity within the aggregate allowing for ultrafast exciton diffusion.

Having successfully identified sample preparation methods and excitation conditions for these highly delicate systems and developed a general understanding of its dynamics, future experiments in combination with theoretical modeling can focus on more detailed questions, such as the origin of a distinct lineshape modulation observed on the high frequency side of the spectrum. Besides, a comparison of tubular and linear ZnChl aggregates could shed further light on the dimensionality of the exciton diffusion process.

With regard to technological advancements, ambiguities in the discussion of the dendrimer data revealed the necessity to complement the employed methods with emission based techniques, i.e. time-resolved fluorescence studies. Such a disentanglement of excited state and ground state dynamics would also be beneficial for other coupled multichromophore systems. As energy migration is associated with depolarization, i.e. anisotropy values that can be linked to the molecular geometry via symmetry arguments, full exploitation of the polarizations of the involved fields will provide further insights. In fluorescence anisotropy studies, the challenge lies in maintaining and improving the time resolution. To this end, a combination of excitation via two-photon absorption and Kerr-gating based detection to reduce phasematching constraints could be implemented. Furthermore, two-dimensional anisotropy maps could unravel the pump wavelength dependence of depolarization dynamics.

Bibliography

[1] Wikipedia contributors.
Dampfmaschine (August 2012).
Page Version ID: 106159090.

[2] Wikipedia contributors.
Elektrizität (July 2012).
Page Version ID: 105783924.

[3] *BP Statistical Review of World Energy June 2012* (June 2012).

[4] C. J. Brabec, N. S. Sariciftci, and J. C. Hummelen.
Plastic Solar Cells.
Advanced Functional Materials **11**, 1526 (2001).

[5] V. Sundström.
Light in elementary biological reactions.
Progress in Quantum Electronics **24**, 187–238 (September 2000).

[6] B. H. Bransden and C. J. Joachain.
Physics of Atoms and Molecules.
Second edition. Prentice Hall (April 2003).

[7] J. D. Jackson.
Classical Electrodynamics.
Third edition. John Wiley & Sons (December 1998).

[8] M. Kasha.
Paths of molecular excitation.
Radiation Research Supplement **2** (1960).

[9] M. Kasha.
Energy Transfer Mechanisms and Molecular Exciton Model for Molecular Aggregates.
Radiation Research **20**, 55 (1963).

[10] E. G. McRae and M. Kasha.
The molecular exciton model (1964).

[11] E. O. Potma and D. A. Wiersma.
Exciton superradiance in aggregates: The effect of disorder, higher order exciton-phonon coupling and dimensionality.
Journal of Chemical Physics **108**, 4894–4903 (March 1998).

[12] F. C. Spano.
Excitons in Conjugated Oligomer Aggregates, Films, and Crystals.
Annual Review of Physical Chemistry **57**, 217–243 (2006).

[13] F. C. Spano.
The Spectral Signatures of Frenkel Polarons in H- and J-Aggregates.
Accounts of Chemical Research **43**, 429–439 (March 2010).

[14] F. C. Spano.
Multiple-photon absorption and saturation in Frenkel-exciton chains.
Physical Review B **46**, 13017–13034 (November 1992).

[15] V. Baleviius Jr., A. Gelzinis, D. Abramavicius, T. Manal, and L. Valkunas.
Excitation dynamics and relaxation in a molecular heterodimer.
Chemical Physics **404**, 94–102 (August 2012).

[16] F. C. Spano.
Fermion excited states in one-dimensional molecular aggregates with site disorder: Nonlinear optical response.
Physical Review Letters **67**, 3424–3427 (December 1991).

[17] T. Kobayashi.
J-Aggregates.
World Scientific (1996).

[18] J. Knoester.
Modeling the optical properties of excitons in linear and tubular J-aggregates.
International Journal of Photoenergy **2006**, 1–10 (2006).

[19] H. Marciniak, X. Li, F. Würthner, and S. Lochbrunner.
One-Dimensional Exciton Diffusion in Perylene Bisimide Aggregates.
The Journal of Physical Chemistry A **115**, 648–654 (February 2011).

[20] V. Prokhorenko, D. Steensgaard, and A. Holzwarth.
Exciton Theory for Supramolecular Chlorosomal Aggregates: 1. Aggregate Size Dependence of the Linear Spectra.
Biophysical Journal **85**, 3173–3186 (November 2003).

[21] C. Didraga and J. Knoester.
Chiral exciton wave functions in cylindrical J aggregates.
The Journal of Chemical Physics **121**, 946 (2004).

[22] C. Didraga and J. Knoester.
Optical spectra and localization of excitons in inhomogeneous helical cylindrical aggregates.
The Journal of Chemical Physics **121**, 10687–10698 (December 2004).

[23] T. Förster.
Energiewanderung Und Fluoreszenz.
Naturwissenschaften **33**, 166–175 (1946).

[24] T. Förster.
Zwischenmolekulare Energiewanderung und Fluoreszenz.
Annalen Der Physik **2**, 55–75 (1948).

[25] T. Förster.
Experimentelle und theoretische Untersuchung des Zwischenmolekularen Übergangs von Elektronenanregungsenergie.
Zeitschrift Für Naturforschung **4**, 321–327 (1949).

[26] T. Förster.
10th Spiers Memorial Lecture - Transfer Mechanisms of Electronic Excitation.
Discussions of the Faraday Society pp. 7–17 (1959).

[27] S. E. Braslavsky, E. Fron, H. B. Rodríguez, E. S. Román, G. D. Scholes, G. Schweitzer, B. Valeur, and J. Wirz.
Pitfalls and limitations in the practical use of Förster's theory of resonance energy transfer.
Photochemical & Photobiological Sciences **7**, 1444 (2008).

[28] D. L. Andrews and A. A. Demidov.
Resonance Energy Transfer.
First edition. John Wiley & Sons (March 1999).

[29] D. Beljonne, C. Curutchet, G. D. Scholes, and R. J. Silbey.
Beyond Forster Resonance Energy Transfer in Biological and Nanoscale Systems.
The Journal of Physical Chemistry B **113**, 6583–6599 (2009).

[30] A. Olaya-Castro and G. D. Scholes.
Energy transfer from Förster-Dexter theory to quantum coherent light-harvesting.
International Reviews in Physical Chemistry **30**, 49–77 (2011).

[31] P. J. Walla, P. A. Linden, C.-P. Hsu, G. D. Scholes, and G. R. Fleming.
Femtosecond dynamics of the forbidden carotenoid S1 state in light-harvesting complexes of purple bacteria observed after two-photon excitation.
Proceedings of the National Academy of Sciences **97**, 10808–10813 (September 2000).

[32] J. R. Higgins.
Sampling Theory in Fourier and Signal Analysis: Volume 1: Foundations.
Oxford University Press (May 1996).

[33] L. Lepetit, G. Chériaux, and M. Joffre.
Linear techniques of phase measurement by femtosecond spectral interferometry for applications in spectroscopy.
Journal of the Optical Society of America B **12**, 2467–2474 (December 1995).

[34] S. Mukamel.
Principles of Nonlinear Optical Spectroscopy.
Oxford University Press, USA (April 1999).

[35] T. Brixner, T. Mancal, I. V. Stiopkin, and G. R. Fleming.
Phase-stabilized two-dimensional electronic spectroscopy.
The Journal of Chemical Physics **121**, 4221 (2004).

[36] D. M. Jonas.
Two-dimensional femtosecond spectroscopy.
Annual Review of Physical Chemistry **54**, 425–463 (2003).

[37] G. R. Fleming.
Chemical Applications of Ultrafast Spectroscopy, volume 13 of *International Series of Monographs on Chemistry.*
Oxford University Press, USA (May 1986).

[38] K. Wynne and R. Hochstrasser.
Coherence effects in the anisotropy of optical experiments.
Chemical Physics **171**, 179–188 (April 1993).

[39] K. Wynne and R. M. Hochstrasser.
Anisotropy as an ultrafast probe of electronic coherence in degenerate systems exhibiting Raman scattering, fluorescence, transient absorption and chemical reactions.
Journal of Raman Spectroscopy **26**, 561–569 (1995).

[40] D. M. Jonas, M. J. Lang, Y. Nagasawa, T. Joo, and G. R. Fleming.
PumpProbe Polarization Anisotropy Study of Femtosecond Energy Transfer within the Photosynthetic Reaction Center of Rhodobacter sphaeroides R26.
The Journal of Physical Chemistry **100**, 12660–12673 (1996).

[41] M. Förster.
Design and implementation of four-wave-mixing setups in the ultraviolet regime.
Master's thesis, Universität Würzburg (2011).

[42] S. Mukamel.
Multidimensional femtosecond correlation spectroscopies of electronic and vibrational excitations.
Annual Review of Physical Chemistry **51**, 691–729 (2000).

[43] M. Cho.
Coherent two-dimensional optical spectroscopy.
Chemical Reviews **108**, 1331–1418 (April 2008).

[44] J. D. Hybl, A. W. Albrecht, S. M. G. Faeder, and D. M. Jonas.
Two-dimensional electronic spectroscopy.
Chemical Physics Letters **297**, 307–313 (November 1998).

[45] P. Hamm, M. Lim, and R. M. Hochstrasser.
Structure of the amide I band of peptides measured by femtosecond nonlinear-infrared spectroscopy.
The Journal of Physical Chemistry B **102**, 6123–6138 (July 1998).

[46] S. Woutersen and P. Hamm.
Structure determination of trialanine in water using polarization sensitive two-dimensional vibrational spectroscopy.
The Journal of Physical Chemistry B **104**, 11316–11320 (November 2000).

[47] O. Golonzka, M. Khalil, N. Demirdöven, and A. Tokmakoff.
Vibrational anharmonicities revealed by coherent two-dimensional infrared spectroscopy.
Physical Review Letters **86**, 2154–2157 (March 2001).

[48] M. L. Cowan, J. P. Ogilvie, and R. J. D. Miller.
Two-dimensional spectroscopy using diffractive optics based phased-locked photon echoes.
Chemical Physics Letters **386**, 184–189 (March 2004).

[49] T. Brixner, I. V. Stiopkin, and G. R. Fleming.
Tunable two-dimensional femtosecond spectroscopy.
Optics Letters **29**, 884–886 (April 2004).

[50] J. D. Hybl, Y. Christophe, and D. M. Jonas.
Peak shapes in femtosecond 2D correlation spectroscopy.
Chemical Physics **266**, 295–309 (May 2001).

[51] T. Brixner, J. Stenger, H. M. Vaswani, M. Cho, R. E. Blankenship, and G. R. Fleming.
Two-dimensional spectroscopy of electronic couplings in photosynthesis.
Nature **434**, 625–628 (March 2005).

[52] G. S. Engel, T. R. Calhoun, E. L. Read, T. Ahn, T. Mancal, Y. Cheng, R. E. Blankenship, and G. R. Fleming.
Evidence for wavelike energy transfer through quantum coherence in photosynthetic systems.
Nature **446**, 782–786 (April 2007).

[53] E. Collini, C. Y. Wong, K. E. Wilk, P. M. G. Curmi, P. Brumer, and G. D. Scholes.
Coherently wired light-harvesting in photosynthetic marine algae at ambient temperature.
Nature **463**, 644–647 (February 2010).

[54] G. S. Schlau-Cohen, A. Ishizaki, T. R. Calhoun, N. S. Ginsberg, M. Ballottari, R. Bassi, and G. R. Fleming.
Elucidation of the timescales and origins of quantum electronic coherence in LHCII.
Nature Chemistry **4**, 389–395 (2012).

[55] F. Milota, J. Sperling, A. Nemeth, and H. Kauffmann.
Two-dimensional electronic photon echoes of a double band J-aggregate: Quantum oscillatory motion versus exciton relaxation.
Chemical Physics **357**, 45–53 (2009).

[56] E. Collini and G. D. Scholes.
Coherent Intrachain Energy Migration in a Conjugated Polymer at Room Temperature.
Science **323**, 369–373 (January 2009).

[57] M. Aeschlimann, T. Brixner, A. Fischer, C. Kramer, P. Melchior, W. Pfeiffer, C. Schneider, C. Ströber, P. Tuchscherer, and D. V. Voronine.
Coherent Two-Dimensional Nanoscopy.
Science **333**, 1723–1726 (September 2011).

[58] X. Li, T. Zhang, C. N. Borca, and S. T. Cundiff.
Many-body interactions in semiconductors probed by optical two-dimensional Fourier transform spectroscopy.
Physical Review Letters **96**, 057406 (February 2006).

[59] K. Stone, K. Gundogdu, D. Turner, X. Li, S. Cundiff, and K. Nelson.
Two-Quantum 2D FT Electronic Spectroscopy of Biexcitons in GaAs Quantum Wells.
Science **324**, 1169–1173 (May 2009).

[60] D. B. Turner and K. A. Nelson.
Coherent measurements of high-order electronic correlations in quantum wells.
Nature **466**, 1089–1092 (August 2010).

[61] M. Kira, S. W. Koch, R. P. Smith, A. E. Hunter, and S. T. Cundiff.
Quantum spectroscopy with Schrodinger-cat states.
Nature Physics **7**, 799–804 (2011).

[62] D. B. Turner, Y. Hassan, and G. D. Scholes.
Exciton Superposition States in CdSe Nanocrystals Measured Using Broadband Two-Dimensional Electronic Spectroscopy.
Nano Lett. **12**, 880–886 (2011).

[63] J. A. Myers, K. L. Lewis, P. F. Tekavec, and J. P. Ogilvie.
Two-color two-dimensional Fourier transform electronic spectroscopy with a pulse-shaper.
Optics Express **16**, 17420–17428 (October 2008).

[64] P. F. Tekavec, J. A. Myers, K. L. M. Lewis, and J. P. Ogilvie.
Two-dimensional electronic spectroscopy with a continuum probe.
Optics Letters **34**, 1390–1392 (May 2009).

[65] P. Tekavec, K. Lewis, F. Fuller, J. Myers, and J. Ogilvie.
Toward Broad Bandwidth 2-D Electronic Spectroscopy: Correction of Chirp From a Continuum Probe.
Selected Topics in Quantum Electronics, IEEE Journal of **18**, 210 –217 (February 2012).

[66] E. L. Read, G. S. Engel, T. R. Calhoun, T. Mancal, T. K. Ahn, R. E. Blankenship, and G. R. Fleming.
Multidimensional Ultrafast Spectroscopy Special Feature: Cross-peak-specific two-dimensional electronic spectroscopy.
Proceedings of the National Academy of Sciences **104**, 14203–14208 (2007).

[67] J. Kim, S. Mukamel, and G. D. Scholes.
Two-Dimensional Electronic Double-Quantum Coherence Spectroscopy.
Accounts of Chemical Research **42**, 1375–1384 (2009).

[68] A. Nemeth, J. Sperling, J. Hauer, H. F. Kauffmann, and F. Milota.
Compact phase-stable design for single- and double-quantum two-dimensional electronic spectroscopy.
Optics Letters **34**, 3301–3303 (November 2009).

[69] P. F. Tekavec, G. A. Lott, and A. H. Marcus.
Fluorescence-detected two-dimensional electronic coherence spectroscopy by acousto-optic phase modulation.
The Journal of Chemical Physics **127**, 214307 (2007).

[70] P. Tian, D. Keusters, Y. Suzaki, and W. S. Warren.
Femtosecond phase-coherent two-dimensional spectroscopy.
Science **300**, 1553–1555 (June 2003).

[71] E. M. Grumstrup, S. Shim, M. A. Montgomery, N. H. Damrauer, and M. T. Zanni.
Facile collection of two-dimensional electronic spectra using femtosecond pulse-shaping technology.
Optics Express **15**, 16681–16689 (December 2007).

[72] S. Yan and H. Tan.
Phase cycling schemes for two-dimensional optical spectroscopy with a pumpprobe beam geometry.
Chemical Physics **360**, 110–115 (June 2009).

[73] A. Nemeth, F. Milota, T. Mancal, V. Lukes, J. Hauer, H. F. Kauffmann, and J. Sperling.
Vibrational wave packet induced oscillations in two-dimensional electronic spectra. I. Experiments.
The Journal of Chemical Physics **132**, 184514 (2010).

[74] Y. Cheng and G. R. Fleming.
Coherence Quantum Beats in Two-Dimensional Electronic Spectroscopy.
The Journal of Physical Chemistry A **112**, 4254–4260 (May 2008).

[75] J. Köhler, M. Wollenhaupt, T. Bayer, C. Sarpe, and T. Baumert.
Zeptosecond precision pulse shaping.
Optics Express **19**, 11638–11653 (June 2011).

[76] T. Zhang, C. Borca, X. Li, and S. Cundiff.
Optical two-dimensional Fourier transform spectroscopy with active interferometric stabilization.
Optics Express **13**, 7432–7441 (2005).

[77] V. Volkov, R. Schanz, and P. Hamm.
Active phase stabilization in Fourier-transform two-dimensional infrared spectroscopy.
Optics Letters **30**, 2010–2012 (2005).

[78] U. Selig, F. Langhojer, F. Dimler, T. Löhrig, C. Schwarz, B. Gieseking, and T. Brixner.
Inherently phase-stable coherent two-dimensional spectroscopy using only conventional optics.
Optics Letters **33**, 2851—2853 (2008).

[79] R. Trebino, K. W. DeLong, D. N. Fittinghoff, J. N. Sweetser, M. A. Krumbügel, B. A. Richman, and D. J. Kane.
Measuring ultrashort laser pulses in the time-frequency domain using frequency-resolved optical gating.
Review of Scientific Instruments **68**, 3277–3295 (1997).

[80] B. Gieseking.
Kohärente 2D-Spektroskopie bei tiefen Temperaturen.
Diplomarbeit, Universität Würzburg (2009).

[81] F. Langhojer.
New techniques in liquid-phase ultrafast spectroscopy.
Dissertation, Universität Würzburg (2009).

[82] K. Hyeon-Deuk, Y. Tanimura, and M. Cho.
Ultrafast exciton transfers in DNA and its nonlinear optical spectroscopy.
The Journal of Chemical Physics **128**, 135102 (2008).

[83] J. Jiang, D. Abramavicius, C. Falvo, B. M. Bulheller, J. D. Hirst, and S. Mukamel.
Simulation of Two-Dimensional Ultraviolet Spectroscopy of Amyloid Fibrils.
The Journal of Physical Chemistry B **114**, 12150–12156 (2010).

[84] A. R. Lam, J. Jiang, and S. Mukamel.
Distinguishing Amyloid Fibril Structures in Alzheimers Disease (AD) by Two-Dimensional Ultraviolet (2DUV) Spectroscopy.
Biochemistry **50**, 9809–9816 (2011).

[85] J. Jiang and S. Mukamel.
Probing Amyloid Fibril Growth by Two-Dimensional Near-Ultraviolet Spectroscopy.
The Journal of Physical Chemistry B **115**, 6321–6328 (2011).

[86] J. Jiang and S. Mukamel.
Two-dimensional near-ultraviolet spectroscopy of aromatic residues in amyloid fibrils: a first principles study.
Physical Chemistry Chemical Physics **13**, 2394 (2011).

[87] P. Baum, S. Lochbrunner, and E. Riedle.
Tunable sub-10-fs ultraviolet pulses generated by achromatic frequencydoubling.
Optics Letters **29**, 1686–1688 (July 2004).

[88] M. Beutler, M. Ghotbi, F. Noack, D. Brida, C. Manzoni, and G. Cerullo.
Generation of high-energy sub-20 fs pulses tunable in the 250-310 nm region by frequency doubling of a high-power noncollinear optical parametric amplifier.
Optics Letters **34**, 710–712 (March 2009).

[89] U. Selig, C.-F. Schleussner, M. Foerster, F. Langhojer, P. Nuernberger, and T. Brixner.
Coherent two-dimensional ultraviolet spectroscopy in fully noncollinear geometry.
Optics Letters **35**, 4178–4180 (December 2010).

[90] N. Christensson, Y. Avlasevich, A. Yartsev, K. Müllen, T. Pascher, and T. Pullerits.
Weakly chirped pulses in frequency resolved coherent spectroscopy.
The Journal of Chemical Physics **132**, 174508 (2010).

[91] D. Zimdars, R. S. Francis, C. Ferrante, and M. D. Fayer.
Electronic dephasing in nonpolar room temperature liquids: UV photon echo pulse duration dependent measurements.
The Journal of Chemical Physics **106**, 7498 (1997).

[92] Q. Xu, Y. Ma, I. V. Stiopkin, and G. R. Fleming.
Wavelength-dependent resonant homodyne and heterodyne transient grating spectroscopy with a diffractive optics method: Solvent effect on the third-order signal.
The Journal of Chemical Physics **116**, 9333 (2002).

[93] A. M. Moran, R. A. Nome, and N. F. Scherer.
Resolving the emission times of solute and solvent four-wave mixing signals by spectral interferometry.
The Journal of Chemical Physics **125**, 031101–4 (July 2006).

[94] C. hung Tseng, S. Matsika, and T. C. Weinacht.
Two-dimensional ultrafast Fourier transform spectroscopy in the deep ultraviolet.
Optics Express **17**, 18788–18793 (October 2009).

[95] C.-h. Tseng, P. Sndor, M. Kotur, T. C. Weinacht, and S. Matsika.
Two-Dimensional Fourier Transform Spectroscopy of Adenine and Uracil Using Shaped Ultrafast Laser Pulses in the Deep UV.
The Journal of Physical Chemistry A **116**, 2654–2661 (2011).

[96] B. A. West, J. M. Womick, and A. M. Moran.
Probing Ultrafast Dynamics in Adenine With Mid-UV Four-Wave Mixing Spectroscopies.
The Journal of Physical Chemistry A **115**, 8630–8637 (2011).

[97] B. A. West, J. M. Womick, and A. M. Moran.
Influence of temperature on thymine-to-solvent vibrational energy transfer.
The Journal of Chemical Physics **135**, 114505–114505–9 (September 2011).

[98] G. Auböck, C. Consani, F. van Mourik, and M. Chergui.
Ultrabroadband femtosecond two-dimensional ultraviolet transient absorption.
Optics Letters **37**, 2337–2339 (June 2012).

[99] H. Cailleau, J. Baudour, J. Meinnel, A. Dworkin, F. Moussa, and C. M. E. Zeyen.
Double-well potentials and structural phase transitions in polyphenyls.
Faraday Discussions of the Chemical Society **69**, 7–18 (1980).

[100] G. Heimel, M. Daghofer, J. Gierschner, E. J. W. List, A. C. Grimsdale, K. Müllen, D. Beljonne, J. Bredas, and E. Zojer.
Breakdown of the mirror image symmetry in the optical absorption/emission spectra of oligo(paraphenylene)s.
The Journal of Chemical Physics **122**, 054501 (2005).

[101] A. A. Oskouei, O. Bräm, A. Cannizzo, F. van Mourik, A. Tortschanoff, and M. Chergui.
Photon echo peak shift experiments in the UV: p-terphenyl in different solvents.
Journal of Molecular Liquids **141**, 118–123 (June 2008).

[102] A. A. Oskouei, O. Bräm, A. Cannizzo, F. van Mourik, A. Tortschanoff, and M. Chergui.
Ultrafast UV photon echo peak shift and fluorescence up conversion studies of non-polar solvation dynamics.
Chemical Physics **350**, 104–110 (June 2008).

[103] V. I. Prokhorenko, A. Halpin, and R. D. Miller.
Coherently-controlled two-dimensional photon echo electronic spectroscopy.
Optics Express **17**, 9764–9779 (June 2009).

[104] F. Würthner.
Perylene bisimide dyes as versatile building blocks for functional supramolecular architectures.
Chemical Communications p. 1564 (2004).

[105] B. A. Jones, A. Facchetti, M. R. Wasielewski, and T. J. Marks.
Tuning Orbital Energetics in Arylene Diimide Semiconductors. Materials Design for Ambient Stability of n-Type Charge Transport.
Journal of the American Chemical Society **129**, 15259–15278 (2007).

[106] T. Weil, T. Vosch, J. Hofkens, K. Peneva, and K. Müllen.
The Rylene Colorant Family-Tailored Nanoemitters for Photonics Research and Applications.
Angewandte Chemie International Edition **49**, 9068–9093 (2010).

[107] F. Würthner, S. Ahmed, C. Thalacker, and T. Debaerdemaeker.
Core-Substituted Naphthalene Bisimides: New Fluorophors with Tunable Emission Wavelength for FRET Studies.
Chemistry - A European Journal **8**, 4742–4750 (2002).

[108] H. Langhals, S. Demmig, and H. Huber.
Rotational barriers in perylene fluorescent dyes.
Spectrochimica Acta Part A: Molecular and Biomolecular Spectroscopy **44**, 1189–1193 (April 1988).

[109] P. Osswald, D. Leusser, D. Stalke, and F. Würthner.
Perylene Bisimide Based Macrocycles: Effective Probes for the Assessment of Conformational Effects on Optical Properties.
Angewandte Chemie International Edition **44**, 250–253 (2005).

[110] P. Osswald and F. Würthner.
Conformational Effects of Bay Substituents on Optical, Electrochemical and Dynamic Properties of Perylene Bisimides: Macrocyclic Derivatives as Effective Probes.
Chemistry - A European Journal **13**, 7395–7409 (2007).

[111] E. Fron, R. Pilot, G. Schweitzer, J. Qu, A. Herrmann, K. Müllen, J. Hofkens, M. V. der Auweraer, and F. C. De Schryver.
Photoinduced electron-transfer in perylenediimide triphenylamine-based dendrimers: single photon timing and femtosecond transient absorption spectroscopy.
Photochemical & Photobiological Sciences **7**, 597–604 (2008).

[112] C. Hippius, I. H. M. van Stokkum, M. Gsanger, M. M. Groeneveld, R. M. Williams, and F. Würthner.
Sequential FRET Processes in Calix[4]arene-Linked Orange-Red-Green Perylene Bisimide Dye Zigzag Arrays.
The Journal of Physical Chemistry C **112**, 2476–2486 (February 2008).

[113] M. Hennessy, Z. Soos, R. Pascal Jr., and A. Girlando.
Vibronic structure of PTCDA stacks: the excitonphonon-charge-transfer dimer.
Chemical Physics **245**, 199–212 (July 1999).

[114] X. Li, X. Zhang, S. Ghosh, and F. Würthner.
Highly Fluorescent Lyotropic Mesophases and Organogels Based on J-Aggregates of Core-Twisted Perylene Bisimide Dyes.
Chemistry - A European Journal **14**, 8074–8078 (2008).

[115] J. M. Giaimo, A. V. Gusev, and M. R. Wasielewski.
Excited-State Symmetry Breaking in Cofacial and Linear Dimers of a Green Perylenediimide Chlorophyll Analogue Leading to Ultrafast Charge Separation.
Journal of the American Chemical Society **124**, 8530–8531 (March 2002).

[116] M. W. Holman, R. Liu, L. Zang, P. Yan, S. A. DiBenedetto, R. D. Bowers, and D. M. Adams.
Studying and Switching Electron Transfer: From the Ensemble to the Single Molecule.
Journal of the American Chemical Society **126**, 16126–16133 (December 2004).

[117] M. W. Holman, P. Yan, D. M. Adams, S. Westenhoff, and C. Silva.
Ultrafast Spectroscopy of the Solvent Dependence of Electron Transfer in a Perylenebisimide Dimer.
The Journal of Physical Chemistry A **109**, 8548–8552 (2005).

[118] M. J. Fuller, L. E. Sinks, B. Rybtchinski, J. M. Giaimo, X. Li, and M. R. Wasielewski.
Ultrafast Photoinduced Charge Separation Resulting from Self-assembly of a Green Perylene-based Dye into π-Stacked Arrays.
The Journal of Physical Chemistry A **109**, 970–975 (February 2005).

[119] D. Veldman, S. M. A. Chopin, S. C. J. Meskers, M. M. Groeneveld, R. M. Williams, and R. A. J. Janssen.
Triplet Formation Involving a Polar Transition State in a Well-Defined Intramolecular Perylenediimide Dimeric Aggregate.
The Journal of Physical Chemistry A **112**, 5846–5857 (July 2008).

[120] C. Hippius, I. H. M. van Stokkum, E. Zangrando, R. M. Williams, M. Wykes, D. Beljonne, and F. Würthner.
Ground- and Excited-State Pinched Cone Equilibria in Calix[4]arenes Bearing Two Perylene Bisimide Dyes.
The Journal of Physical Chemistry C **112**, 14626–14638 (2008).

[121] J. M. Giaimo, J. V. Lockard, L. E. Sinks, A. M. Scott, T. M. Wilson, and M. R. Wasielewski.
Excited Singlet States of Covalently Bound, Cofacial Dimers and Trimers of Perylene-3,4:9,10-bis(dicarboximide)s.
The Journal of Physical Chemistry A **112**, 2322–2330 (2008).

[122] D. Ernst, R. Hildner, C. Hippius, F. Würthner, and J. Köhler.
Photoblinking dynamics in single calix[4]arene-linked perylene bisimide dimers.
Chemical Physics Letters **482**, 93 – 98 (2009).

[123] A. S. Lukas, Y. Zhao, S. E. Miller, and M. R. Wasielewski.
Biomimetic Electron Transfer Using Low Energy Excited States: A Green Perylene-Based Analogue of Chlorophyll a.
The Journal of Physical Chemistry B **106**, 1299–1306 (February 2002).

[124] D. Veldman, S. M. A. Chopin, S. C. J. Meskers, and R. A. J. Janssen.
Enhanced Intersystem Crossing via a High Energy Charge Transfer State in a Perylenediimide-Perylenemonoimide Dyad.
The Journal of Physical Chemistry A **112**, 8617–8632 (2008).

[125] G. D. Belder, S. Jordens, M. Lor, G. Schweitzer, R. De, T. Weil, A. Herrmann, U. Wiesler, K. Müllen, and F. De Schryver.
Femtosecond fluorescence upconversion study of rigid dendrimers containing peryleneimide chromophores at the rim.
Journal of Photochemistry and Photobiology A: Chemistry **145**, 61–70 (November 2001).

[126] G. Schweitzer, R. Gronheid, S. Jordens, M. Lor, G. D. Belder, T. Weil, E. Reuther, K. Müllen, and F. C. De Schryver.
Intramolecular Directional Energy Transfer Processes in Dendrimers Containing Perylene and Terrylene Chromophores.
The Journal of Physical Chemistry A **107**, 3199–3207 (March 2003).

[127] B. K. Kaletas, R. Dobrawa, A. Sautter, F. Würthner, M. Zimine, L. D. Cola, and R. M. Williams.
Photoinduced Electron and Energy Transfer Processes in a Bichromophoric Pyrene-Perylene Bisimide System.
The Journal of Physical Chemistry A **108**, 1900–1909 (March 2004).

[128] A. Sautter, B. K. Kaletas, D. G. Schmid, R. Dobrawa, M. Zimine, G. Jung, I. H. M. van Stokkum, L. D. Cola, R. M. Williams, and F. Würthner.
Ultrafast Energy-Electron Transfer Cascade in a Multichromophoric Light-Harvesting Molecular Square.
Journal of the American Chemical Society **127**, 6719–6729 (May 2005).

[129] C. Scharf, K. Peter, P. Bauer, C. Jung, M. Thelakkat, and J. Köhler.
Towards the characterization of energy-transfer processes in organic donor–acceptor dyads based on triphenyldiamine and perylenebisimides.
Chemical Physics **328**, 403–409 (2006).

[130] Y. Shibano, T. Umeyama, Y. Matano, N. V. Tkachenko, H. Lemmetyinen, and H. Imahori.
Synthesis and Photophysical Properties of Electron-Rich Perylenediimide-Fullerene Dyad.
Organic Letters **8**, 4425–4428 (March 2006).

[131] C. Hippius, I. H. M. van Stokkum, E. Zangrando, R. M. Williams, and F. Würthner.
Excited State Interactions in Calix[4]arene-Perylene Bisimide Dye Conjugates: Global and Target Analysis of Supramolecular Building Blocks.
The Journal of Physical Chemistry C **111**, 13988–13996 (2007).

[132] W. Xu, H. Chen, Y. Wang, C. Zhao, X. Li, S. Wang, and Y. Weng.
Photoinduced Electron and Energy Transfer in Dyads of Porphyrin Dimer and Perylene Tetracarboxylic Diimide.
ChemPhysChem **9**, 1409–1415 (2008).

[133] M. Berberich, A. Krause, M. Orlandi, F. Scandola, and F. Würthner.
Toward Fluorescent Memories with Nondestructive Readout: Photoswitching of Fluorescence by Intramolecular Electron Transfer in a Diaryl Ethene-Perylene Bisimide Photochromic System13.
Angewandte Chemie International Edition **47**, 6616–6619 (2008).

[134] A. I. Oliva, B. Ventura, F. Würthner, A. Camara-Campos, C. A. Hunter, P. Ballester, and L. Flamigni.
Self-assembly of double-decker cages induced by coordination of perylene bisimide with a trimeric Zn porphyrin: study of the electron transfer dynamics between the two photoactive components.
Dalton Transactions p. 4023 (2009).

[135] C. C. Hofmann, P. Bauer, S. A. Haque, M. Thelakkat, and J. Köhler.
Energy- and charge-transfer processes in flexible organic donor-acceptor dyads.
The Journal of Chemical Physics **131**, 144512–10 (October 2009).

[136] N. V. Anh, F. Schlosser, M. M. Groeneveld, I. H. M. van Stokkum, F. Würthner, and R. M. Williams.
Photoinduced Interactions in a Pyrene-Calix[4]arene-Perylene Bisimide Dye System: Probing Ground-State Conformations with Excited-State Dynamics of Charge Separation and Recombination.
The Journal of Physical Chemistry C **113**, 18358–18368 (October 2009).

[137] A. Prodi, C. Chiorboli, F. Scandola, E. Iengo, E. Alessio, R. Dobrawa, and F. Würthner.
Wavelength-Dependent Electron and Energy Transfer Pathways in a Side-to-Face Ruthenium Porphyrin/Perylene Bisimide Assembly.
Journal of the American Chemical Society **127**, 1454–1462 (February 2005).

[138] M. Ghirotti, C. Chiorboli, C. You, F. Würthner, and F. Scandola.
Photoinduced Energy and Electron-Transfer Processes in Porphyrin-Perylene Bisimide Symmetric Triads.

The Journal of Physical Chemistry A **112**, 3376–3385 (March 2008).

[139] J. Feng, Y. Zhang, C. Zhao, R. Li, W. Xu, X. Li, and J. Jiang.
Cyclophanes of Perylene Tetracarboxylic Diimide with Different Substituents at Bay Positions.
Chemistry - A European Journal **14**, 7000–7010 (2008).

[140] I. Pugliesi, A. Walter, H. Langhals, and E. Riedle.
Highly efficient energy transfer in a dyad with orthogonally arranged transition dipole moments: Beyond the Limits of Förster?
In *Ultrafast Phenomena XVII*, Proceedings of the 17th International Conference, pp. 343–345. Oxford University Press, New York (2011).

[141] C. Curutchet, F. A. Feist, B. V. Averbeke, B. Mennucci, J. Jacob, K. Müllen, T. Basch, and D. Beljonne.
Superexchange-mediated electronic energy transfer in a model dyad.
Physical Chemistry Chemical Physics **12**, 7378–7385 (2010).

[142] J. Hernando, E. M. H. P. van Dijk, J. P. Hoogenboom, J. García-López, D. N. Reinhoudt, M. Crego-Calama, M. F. García-Parajó, and N. F. van Hulst.
Effect of Disorder on Ultrafast Exciton Dynamics Probed by Single Molecule Spectroscopy.
Physical Review Letters **97**, 216403 (November 2006).

[143] J. Hernando, J. Hoogenboom, E. van Dijk, M. Garcia-Parajo, and N. F. van Hulst.
Ultrafast single-molecule photonics: Excited state dynamics in coherently coupled complexes.
Journal of Luminescence **128**, 1050 – 1052 (2008).

[144] W. Liu, V. Settels, P. H. P. Harbach, A. Dreuw, R. F. Fink, and B. Engels.
Assessment of TDDFT and TDHF based approaches for the prediction of exciton coupling parameters, potential energy curves, and electronic characters of electronically excited aggregates.
Journal of Computational Chemistry **32**, 1971–1981 (July 2011).

[145] E. Fron, G. Schweitzer, P. Osswald, F. Würthner, P. Marsal, D. Beljonne, K. Müllen, F. C. De Schryver, and M. V. der Auweraer.
Photophysical study of bay substituted perylenediimides.
Photochemical & Photobiological Sciences **7**, 1509–1521 (2008).

[146] J. J. Snellenburg, S. P. Laptenok, R. Seger, K. M. Mullen, and I. H. M. van Stokkum.
Glotaran: A Java-Based Graphical User Interface for the R Package TIMP.
Journal of Statistical Software **49**, 1–22 (June 2012).

[147] J. Guthmuller, F. Zutterman, and B. Champagne.
Multimode simulation of dimer absorption spectra from first principles calculations: Application to the 3,4,9,10-perylenetetracarboxylic diimide dimer.
The Journal of Chemical Physics **131**, 154302 (2009).

[148] J. Hunger, A. Stoppa, A. Thoman, M. Walther, and R. Buchner.
Broadband dielectric response of dichloromethane.
Chemical Physics Letters **471**, 85–91 (March 2009).

[149] J.-Y. Bigot, M. T. Portella, R. W. Schoenlein, C. J. Bardeen, A. Migus, and C. V. Shank.
Non-Markovian dephasing of molecules in solution measured with three-pulse femtosecond photon echoes.
Physical Review Letters **66**, 1138–1141 (March 1991).

[150] A. Deshpande, A. Beidoun, A. Penzkofer, and G. Wagenblast.
Absorption and emission spectroscopic investigation of cyanovinyldiethylaniline dye vapors.
Chemical Physics **142**, 123–131 (March 1990).

[151] E. Lang, R. Hildner, H. Engelke, P. Osswald, F. Würthner, and J. Köhler.
Comparison of the Photophysical Parameters for Three Perylene Bisimide Derivatives by Single-Molecule Spectroscopy.
ChemPhysChem **8**, 1487–1496 (2007).

[152] G. Oster and Y. Nishijima.
Fluorescence and Internal Rotation: Their Dependence on Viscosity of the Medium1.
Journal of the American Chemical Society **78**, 1581–1584 (February 1955).

[153] O. A. Matthews, A. N. Shipway, and J. Stoddart.
DendrimersBranching out from curiosities into new technologies.
Progress in Polymer Science **23**, 1–56 (1998).

[154] A. W. Bosman, H. M. Janssen, and E. W. Meijer.
About Dendrimers: Structure, Physical Properties, and Applications.
Chemical Reviews **99**, 1665–1688 (1999).

[155] M. Fischer and F. Vögtle.
Dendrimers: From Design to Application-A Progress Report.
Angewandte Chemie International Edition **38, 38**, 884–905 (April 1999).

[156] D. Astruc and F. Chardac.
Dendritic Catalysts and Dendrimers in Catalysis.
Chemical Reviews **101**, 2991–3024 (2001).

[157] T. G. Goodson.
Optical Excitations in Organic Dendrimers Investigated by Time-Resolved and Nonlinear Optical Spectroscopy.
Accounts of Chemical Research **38**, 99–107 (2004).

[158] S. Lo and P. L. Burn.
Development of Dendrimers: Macromolecules for Use in Organic Light-Emitting Diodes and Solar Cells.
Chemical Reviews **107**, 1097–1116 (2007).

[159] P. L. Burn, S. Lo, and I. D. W. Samuel.
The Development of Light-Emitting Dendrimers for Displays.
Advanced Materials **19**, 1675–1688 (2007).

[160] M. R. Shortreed, S. F. Swallen, Z. Shi, W. Tan, Z. Xu, C. Devadoss, J. S. Moore, and R. Kopelman.
Directed Energy Transfer Funnels in Dendrimeric Antenna Supermolecules.
The Journal of Physical Chemistry B **101**, 6318–6322 (1997).

[161] T. Minami, S. Tretiak, V. Chernyak, and S. Mukamel.
Frenkel-exciton Hamiltonian for dendrimeric nanostar.
Journal of Luminescence **8789**, 115–118 (May 2000).

[162] J. C. Kirkwood, C. Scheurer, V. Chernyak, and S. Mukamel.
Simulations of energy funneling and time- and frequency-gated fluorescence in dendrimers.
The Journal of Chemical Physics **114**, 2419 (2001).

[163] R. Kishi, M. Nakano, T. Minami, H. Fukui, H. Nagai, K. Yoneda, and H. Takahashi.
Theoretical Study on Exciton Recurrence Motion in Anthracene Dimer Using the Ab Initio MO-CI Based Quantum Master Equation Approach.
The Journal of Physical Chemistry A **113**, 5455–5462 (2009).

[164] M. Nakano, R. Kishi, T. Minami, and K. Yoneda.
Theoretical Study on Exciton Dynamics in Dendritic Systems: Exciton Recurrence and Migration.
Molecules **14**, 3700–3718 (2009).

[165] V. D. Kleiman, J. S. Melinger, and D. McMorrow.
Ultrafast Dynamics of Electronic Excitations in a Light-Harvesting Phenylacetylene Dendrimer.
The Journal of Physical Chemistry B **105**, 5595–5598 (2001).

[166] O. Varnavski, T. Goodson, L. Sukhomlinova, and R. Twieg.
Ultrafast Exciton Dynamics in a Branched Molecule Investigated by Time-Resolved Fluorescence, Transient Absorption, and Three-Pulse Photon Echo Peak Shift Measurements.
The Journal of Physical Chemistry B **108**, 10484–10492 (March 2004).

[167] S. A. Lahankar, R. West, O. Varnavski, X. Xie, T. Goodson, L. Sukhomlinova, and R. Twieg.
Electronic interactions in a branched chromophore investigated by nonlinear optical and time-resolved spectroscopy.
The Journal of Chemical Physics **120**, 337 (2004).

[168] T. S. Ahn, A. L. Thompson, P. Bharathi, A. Müller, and C. J. Bardeen.
Light-Harvesting in Carbonyl-Terminated Phenylacetylene Dendrimers: The Role of Delocalized Excited States and the Scaling of Light-Harvesting Efficiency with Dendrimer Size.
The Journal of Physical Chemistry B **110**, 19810–19819 (2006).

[169] O. Varnavski, X. Yan, O. Mongin, M. Blanchard-Desce, and T. Goodson.
Strongly Interacting Organic Conjugated Dendrimers with Enhanced Two-Photon Absorption.
The Journal of Physical Chemistry C **111**, 149–162 (January 2007).

[170] M. Maus, R. De, M. Lor, T. Weil, S. Mitra, U.-M. Wiesler, A. Herrmann, J. Hofkens, T. Vosch, K. Müllen, and F. C. De Schryver.
Intramolecular Energy Hopping and Energy Trapping in Polyphenylene Dendrimers with Multiple Peryleneimide Donor Chromophores and a Terryleneimide Acceptor Trap Chromophore.
Journal of the American Chemical Society **123**, 7668–7676 (August 2001).

[171] O. Varnavski, I. D. W. Samuel, L. Pålsson, R. Beavington, P. L. Burn, and T. Goodson.
Investigations of excitation energy transfer and intramolecular interactions in a nitrogen corded distrylbenzene dendrimer system.
The Journal of Chemical Physics **116**, 8893 (2002).

[172] O. P. Varnavski, J. C. Ostrowski, L. Sukhomlinova, R. J. Twieg, G. C. Bazan, and T. Goodson.
Coherent Effects in Energy Transport in Model Dendritic Structures Investigated by Ultrafast Fluorescence Anisotropy Spectroscopy.
Journal of the American Chemical Society **124**, 1736–1743 (February 2002).

[173] M. Lor, R. De, S. Jordens, G. D. Belder, G. Schweitzer, M. Cotlet, J. Hofkens, T. Weil, A. Herrmann, K. Müllen, M. V. D. Auweraer, and F. C. De Schryver.
Generation-Dependent Energy Dissipation in Rigid Dendrimers Studied by Femtosecond to Nanosecond Time-Resolved Fluorescence Spectroscopy.
The Journal of Physical Chemistry A **106**, 2083–2090 (March 2002).

[174] E. Badaeva, M. R. Harpham, R. Guda, O. Suzer, C. Ma, P. Bäuerle, T. Goodson, and S. Tretiak.
Excited-State Structure of Oligothiophene Dendrimers: Computational and Experimental Study.
The Journal of Physical Chemistry B **114**, 15808–15817 (2010).

[175] M. Guo, O. Varnavski, A. Narayanan, O. Mongin, J.-P. Majoral, M. Blanchard-Desce, and T. Goodson.
Investigations of Energy Migration in an Organic Dendrimer Macromolecule for Sensory Signal Amplification.
The Journal of Physical Chemistry A **113**, 4763–4771 (April 2009).

[176] M. E. K. Ase, P. Graf, N. Kopidakis, S. E. Shaheen, K. Kim, and G. Rumbles.
Exciton Migration in Conjugated Dendrimers: A Joint Experimental and Theoretical Study.
ChemPhysChem **10**, 3285–3294 (2009).

[177] G. Tang, S. S. Y. Chen, P. E. Shaw, K. Hegedus, X. Wang, P. L. Burn, and P. Meredith.
Fluorescent carbazole dendrimers for the detection of explosives.
Polymer Chemistry **2**, 2360 (2011).

[178] M. E. Köse, W. J. Mitchell, N. Kopidakis, C. H. Chang, S. E. Shaheen, K. Kim, and G. Rumbles.
Theoretical Studies on Conjugated Phenyl-Cored Thiophene Dendrimers for Photovoltaic Applications.
Journal of the American Chemical Society **129**, 14257–14270 (March 2007).

[179] A. Tomkeviciene, J. V. Grazulevicius, K. Kazlauskas, A. Gruodis, S. Jursenas, T. Ke, and C. Wu.
Impact of Linking Topology on the Properties of Carbazole Trimers and Dimers.
The Journal of Physical Chemistry C **115**, 4887–4897 (2011).

[180] K. Albrecht and K. Yamamoto.
Dendritic Structure Having a Potential Gradient: New Synthesis and Properties of Carbazole Dendrimers.
Journal of the American Chemical Society **131**, 2244–2251 (2009).

[181] K. Wong, Y. Chen, Y. Lin, H. Su, and C.-c. Wu.
Nonconjugated Hybrid of Carbazole and Fluorene: A Novel Host Material for Highly Efficient Green and Red Phosphorescent OLEDs.
Organic Letters **7**, 5361–5364 (2005).

[182] *NIST Chemistry WebBook.*
Number 69 in NIST Standard Reference Database. Gaithersburg MD.

[183] V. Promarak, S. Saengsuwan, S. Jungsuttiwong, T. Sudyoadsuk, and T. Keawin.
Synthesis and characterization of N-carbazole end-capped oligofluorenes.
Tetrahedron Letters **48**, 89–93 (January 2007).

[184] W. Ma, Y. Wu, J. Han, D. Gu, and F. Gan.
Large three-photon absorption cross-section in a novel class of bis-(N-carbazolyl) fluorene derivatives.
Chemical Physics Letters **403**, 405–409 (February 2005).

[185] V. Promarak, M. Ichikawa, T. Sudyoadsuk, S. Saengsuwan, S. Jungsuttiwong, and T. Keawin.
Synthesis of electrochemically and thermally stable amorphous hole-transporting carbazole dendronized fluorene.
Synthetic Metals **157**, 17–22 (January 2007).

[186] K. Brunner, A. van Dijken, H. Brner, J. J. A. M. Bastiaansen, N. M. M. Kiggen, and B. M. W. Langeveld.
Carbazole Compounds as Host Materials for Triplet Emitters in Organic Light-Emitting Diodes: Tuning the HOMO Level without Influencing the Triplet Energy in Small Molecules.
Journal of the American Chemical Society **126**, 6035–6042 (2004).

[187] *p-Terphenyl.*
http://omlc.ogi.edu/spectra/PhotochemCAD/html/003.html.

[188] U. Brackmann.
Lambdachrome Laser Dyes.
Third edition. Lambda Physik AG, Goettingen (2000).

[189] S. Swallen, R. Kopelman, J. Moore, and C. Devadoss.
Dendrimer photoantenna supermolecules: energetic funnels, exciton hopping and correlated excimer formation.
Journal of Molecular Structure **485–486**, 585–597 (August 1999).

[190] C. Röger, M. G. Müller, M. Lysetska, Y. Miloslavina, A. R. Holzwarth, and F. Würthner.
Efficient Energy Transfer from Peripheral Chromophores to the Self-Assembled Zinc Chlorin Rod Antenna: A Bioinspired Light-Harvesting System to Bridge the “Green Gap”.
Journal of the American Chemical Society **128**, 6542–6543 (March 2006).

[191] T. Balaban, H. Tamiaki, and A. Holzwarth.
Chlorins Programmed for Self-Assembly.
In F. Würthner (Ed.), *Supermolecular Dye Chemistry*, volume 258 of *Topics in Current Chemistry*, pp. 585–585. Springer Berlin / Heidelberg (2005).

[192] V. I. Prokhorenko, A. R. Holzwarth, M. G. Müller, K. Schaffner, T. Miyatake, and H. Tamiaki.
Energy Transfer in Supramolecular Artificial Antennae Units of Synthetic Zinc Chlorins and Co-aggregated Energy Traps. A Time-Resolved Fluorescence Study.
The Journal of Physical Chemistry B **106**, 5761–5768 (June 2002).

[193] M. Katterle, V. I. Prokhorenko, A. R. Holzwarth, and A. Jesorka.
An artificial supramolecular photosynthetic unit.
Chemical Physics Letters **447**, 284–288 (October 2007).

[194] C. Röger, Y. Miloslavina, D. Brunner, A. R. Holzwarth, and F. Würthner.
Self-Assembled Zinc Chlorin Rod Antennae Powered by Peripheral Light-Harvesting Chromophores.
Journal of the American Chemical Society **130**, 5929–5939 (March 2008).

[195] D. M. Niedzwiedzki and R. E. Blankenship.
Singlet and triplet excited state properties of natural chlorophylls and bacteriochlorophylls.
Photosynthesis Research **106**, 227–238 (2010).

[196] J. M. Linnanto and J. E. I. Korppi-Tommola.
Investigation on chlorosomal antenna geometries: tube, lamella and spiral-type self-aggregates.
Photosynthesis Research **96**, 227–245 (2008).

[197] G. T. Oostergetel, H. Amerongen, and E. J. Boekema.
The chlorosome: a prototype for efficient light harvesting in photosynthesis.
Photosynthesis Research **104**, 245–255 (2010).

[198] T. Nozawa, K. Ohtomo, M. Suzuki, H. Nakagawa, Y. Shikama, H. Konami, and Z.-Y. Wang.
Structures of chlorosomes and aggregated BChl c in Chlorobium tepidum from solid state high resolution CP/MAS^{13}*C NMR.*
Photosynthesis Research **41**, 211–223 (1994).

[199] A. Holzwarth and K. Schaffner.
On the structure of bacteriochlorophyll molecular aggregates in the chlorosomes of green bacteria. A molecular modelling study.
Photosynthesis Research **41**, 225–233 (1994).

[200] T. Jochum, C. M. Reddy, A. Eichhfer, G. Buth, J. Szmytkowski, H. Kalt, D. Moss, and T. S. Balaban.
The supramolecular organization of self-assembling chlorosomal bacteriochlorophyll c, d, or e mimics.
Proceedings of the National Academy of Sciences **105**, 12736–12741 (February 2008).

[201] S. Ganapathy, G. T. Oostergetel, P. K. Wawrzyniak, M. Reus, A. G. M. Chew, F. Buda, E. J. Boekema, D. A. Bryant, A. R. Holzwarth, and H. J. M. d. Groot.
Alternating syn-anti bacteriochlorophylls form concentric helical nanotubes in chlorosomes.
Proceedings of the National Academy of Sciences **106**, 8525–8530 (May 2009).

[202] T. P. Causgrove, D. C. Brune, J. Wang, B. P. Wittmershaus, and R. E. Blankenship.
Energy transfer kinetics in whole cells and isolated chlorosomes of green photosynthetic bacteria.
Photosynthesis Research **26**, 39–48 (1990).

[203] M. Mimuro, M. Hirota, Y. Nishimura, T. Moriyama, I. Yamazaki, K. Shimada, and K. Matsuura.
Molecular organization of bacteriochlorophyll in chlorosomes of the green photosynthetic bacterium Chloroflexus aurantiacus: Studies of fluorescence depolarization accompanied by energy transfer processes.
Photosynthesis Research **41**, 181–191 (1994).

[204] Z. Fetisova, A. Freiberg, K. Mauring, V. Novoderezhkin, A. Taisova, and K. Timpmann.
Excitation energy transfer in chlorosomes of green bacteria: theoretical and experimental studies.
Biophysical Journal **71**, 995–1010 (August 1996).

[205] S. Savikhin, D. R. Buck, W. S. Struve, R. E. Blankenship, A. S. Taisova, V. I. Novoderezhkin, and Z. G. Fetisova.
Excitation delocalization in the bacteriochlorophyll c antenna of the green bacterium Chloroflexus aurantiacus as revealed by ultrafast pump-probe spectroscopy.
FEBS Letters **430**, 323–326 (July 1998).

[206] A. Yakovlev, V. Novoderezhkin, A. Taisova, and Z. Fetisova.
Exciton dynamics in the chlorosomal antenna of the green bacterium Chloroflexus aurantiacus: experimental and theoretical studies of femtosecond pump-probe spectra.
Photosynthesis Research **71**, 19–32 (2002).

[207] J. Psencík, Y. Ma, J. B. Arellano, J. Hála, and T. Gillbro.
Excitation Energy Transfer Dynamics and Excited-State Structure in Chlorosomes of Chlorobium phaeobacteroides.
Biophysical Journal **84**, 1161–1179 (February 2003).

[208] J. Martiskainen, J. Linnanto, R. Kananavičius, V. Lehtovuori, and J. Korppi-Tommola.
Excitation energy transfer in isolated chlorosomes from Chloroflexus aurantiacus.
Chemical Physics Letters **477**, 216–220 (July 2009).

[209] S. Sengupta.
Bio-inspired Zinc Chlorin Dye Assemblies for Supramolecular electronics.
Dissertation, Universität Würzburg (2011).

[210] V. Huber, M. Lysetska, and F. Würthner.
Self-Assembled Single- and Double-Stack π-Aggregates of Chlorophyll Derivatives on Highly Ordered Pyrolytic Graphite.
Small **3**, 1007–1014 (2007).

[211] V. Huber, S. Sengupta, and F. Würthner.
Structure-Property Relationships for Self-Assembled Zinc Chlorin Light-Harvesting Dye Aggregates.
Chemistry - A European Journal **14**, 7791–7807 (2008).

[212] G. A. Olah, S. C. Narang, B. G. B. Gupta, and R. Malhotra.
Synthetic methods and reactions. Transformations with chlorotrimethylsilane/sodium iodide, a convenient in situ iodotrimethylsilane reagent.
The Journal of Organic Chemistry **44**, 1247–1251 (April 1979).

[213] J. Sperling, A. Nemeth, J. Hauer, D. Abramavicius, S. Mukamel, H. F. Kauffmann, and F. Milota.
Excitons and Disorder in Molecular Nanotubes: A 2D Electronic Spectroscopy Study and First Comparison to a Microscopic Model.
The Journal of Physical Chemistry A **114**, 8179–8189 (August 2010).

[214] J. Dostl, T. Manal, R.-n. Augulis, F. Vcha, J. Penk, and D. Zigmantas.
Two-Dimensional Electronic Spectroscopy Reveals Ultrafast Energy Diffusion in Chlorosomes.
Journal of the American Chemical Society **134**, 11611–11617 (July 2012).

[215] V. Prokhorenko, D. Steensgaard, and A. Holzwarth.
Exciton Dynamics in the Chlorosomal Antennae of the Green Bacteria Chloroflexus aurantiacus and Chlorobium tepidum.
Biophysical Journal **79**, 2105–2120 (October 2000).

Acknowledgements

- First of all, I would like to thank my supervisor, **Prof. Dr. Tobias Brixner**, for giving me the opportunity to work in this field of research, for his trust in my abilities, and for encouraging me to visit many national and international conferences. Tobias, I benefited a lot from your perfectionism in my academic work and beyond, and truely appreciate the fairness and rationality that governed your group-leadership.

- **Dr. Patrick Nürnberger** for his unique combination of an enjoyable and helpful personality, remarkable intellect, and inexhaustible knowledge. Patrick, you are one of the most competent scientists I've met, and I wish you the very best for your journey through the academic jungle.

- **Dr. Johannes Buback**, for excellently maintaining and advancing our data acquisition framework, ParameterScan, for his implementation of a kHz-readout for our CCD-cameras that served as the basis for the presented transient absorption measurements, for always sharing his expertise, for many lab-hours somewhere between fun, desperation and insanity, when we were still struggling with the old laser system. Last but not least I thank you, Johannes, for your friendship, that I appreciate more than words can say.

- **Dr. Florian Langhojer** and **Frank Dimler** for everything they have taught me and, of course, for their contributions to the 2D VIS and 2D UV setups. You guys have been great fun to work with and I am glad to have shared some of the most frustrating as well as some of the most rewarding moments of this thesis with you!

- **Michael Förster** for his valuable contributions to the 2D UV stability measurements and for installing the transient absorption setup during his Master's thesis, for his curiosity, endurance and intellectual grasp. Michael, I have rarely seen so much wisdom in such a young mind, and your calming personality has helped me through many of the darkest hours in the lab.

- **Carl-Friedrich Schleussner**, for his dedication to the design and implementation of the 2D UV setup during his Master's thesis as well as for numerous interesting discussions about Physics and beyond.

- **Björn Gieseking, Nadja Bertleff** and **Philipp Terberger**, for participating in the 2D VIS projects during their Diploma theses. Guys (and Gals) your sweat and nerves are at the bottom of the presented results, and I hope you feel some satisfaction in seeing that our night and weekend shifts finally paid off!

- **Andreas Steinbacher** for being such a straight-forward man of action, always ready to lend a hand (beamsplitter, power meter, or car) or give advice.

- **Prof. Dr. Bernd Engels** for creating the GRK 1221, for his genuine commitment to create a high quality education for its student members in an open-minded, cooperative and motivating research environment. For listening to my ideas and his interest in my work, for initiating Volker's *ab initio* calculations, for discussions that truly deserve the term "fruitful", because they not only deepened my understanding of the matter but also encouraged me to carry on.

- **Volker Settels** for the *ab initio* calculations presented in the dimer chapter, for proof-reading the respective part of this work as well as many helpful discussions.

- **Prof. Dr. Frank Würthner** for always fitting our meetings into his tight schedule, for his steady interest in present and future collaborations, for initialising and overseeing the synthesis of the PBI-PMI dyads and zinc chlorin compounds, for fruitful discussions and many helpful remarks.

- **Dr. Volker Dehm** for the synthesis of the dimers and for providing the linear spectra and quantum yields, for introducing me to the secrets of organic synthesis, for being absolutely reliable and always open for discussions throughout our cooperation, and for his incomparable Franconian sense of humor.

- **Marcel Gsänger** for the synthesis of the reference compound, MG086, and providing the linear spectra and quantum yields.

- **Dr. Sanchita Sengupta** for the synthesis of the Zinc Chlorin aggregates and providing the linear spectra.

- **Markus Steeger** for passivating the glass surface of our cuvettes for the zinc chlorin measurements. Thanks a bunch, really!

- **Dr. Matthias Stolte** for his cooperative, patient, and friendly attitude in many helpful discussions on various to a greater or lesser extent Chemistry-related issues and for careful proof-reading of the "Chemistry sections" in this thesis.

- **Prof. Dr. Gregory Scholes** for initiating the dendrimer project, **Prof. Dr. Paul Burn** for providing the samples, and **Dr. Inchan Hwang** for his contributions to the experiments and data analysis.

- **Federico Koch, Arthur Hipke, Thomas Keitzl, Philip Tuchscherer, and Jochen Aulbach** who have been tremendous office colleagues as well as the rest of the PC1/EP1 bunch **Fabian Ebert, Dr. Stefan Eyring, Dr. Susanne Fechner, Nico Franke, Ole Hüter, Sebastian Jung, Florian Kanal, Stephanie Karg, Sabine Keiber, Christian Kern, Christian Kramer, Anja Krischke, Martin Kullmann, Jan Lohbreier, Tatjana Quast, Andreas Reiserer, Andreas Reuss, Christian Rewitz, Alexander Rodenberg, Philipp Rudolf, Stefan Rützel, Marco Schade, Sebastian Schott, Christoph Schwarz, Dr.**

Reimer Selle, Robert Spitzenpfeil, Christoph Stolzenberger, Dr. Philip Tuchscherer, Dr. Dmitri Voronine, and **Dr. Daniel Wolpert** for creating such a unique working atmosphere.

- The machine shop team around **Wolfgang Liebler**, who with their expertise and flexibility have enabled many of the experiments and saved me various times when spontaneously fixing broken parts and modifying others.
- The administrative and technical staff, **Andrea Gehring**, **Sabine Fuchs**, and **Belinda Böhm** for keeping the place running.
- **All members of the GRK 1221**, students and professors, for numerous instructive lectures, fruitful discussions, enjoyable seminars and funny get-togethers. In particular, I want to thank **Uschi Rüppel**, the GRK's secretary, for her excellent organisational skills and commitment.
- The **Deutsche Forschungsgemeinschaft (DFG)** for financial support of my PhD work, various lab equipment, and many conference attendances within the framework of the GRK 1221.
- The **Daimler-Benz-Stiftung** for financially supporting my stay at the University of Texas at Austin, a wonderful experience that shaped both, my professional and personal development.
- **Professor Paul F. Barbara** and **his group at UT Austin** for a great time and memorable moments – both, inside and outside the lab!
- Last, but not least, I want to thank the most important people in my life, **my parents, Marie-Luise** and **Manfred**, **my brother, Tilman,** as well as **my husband, Christian**, for their unconditional love and support.

List of Publications

U. Selig, F. Langhojer, F. Dimler, T. Löhrig, C. Schwarz, B. Gieseking, and T. Brixner,
Inherently phase-stable coherent two-dimensional spectroscopy using only conventional optics,
Optics Letters **33**, 2851–2853 (2008).

U. Selig, F. Langhojer, F. Dimler, and T. Brixner,
Vorrichtung und Verfahren zur kohärenten mehr-dimensionalen optischen Spektroskopie,
German patent granted, DE 10 2008 025 170 (2008), international patent pending, PCT/EP2009/003274 (2009).

T. Brixner, F. Langhojer, U. Selig, and C.-F. Schleussner,
Optical assembly, apparatus and method for coherent two- or more-dimensional optical spectroscopy,
European patent pending 09178542.8-2217 (2009).

U. Selig, C.-F. Schleussner, M. Foerster, F. Langhojer, P. Nuernberger, and T. Brixner,
Coherent two-dimensional ultraviolet spectroscopy in fully noncollinear geometry,
Optics Letters **35**, 4178–4180 (2010).

F. Koch, M. Kullmann, U. Selig, P. Nuernberger, D. C. G. Götz, G. Bringmann, and T. Brixner,
Coherent 2D electronic spectroscopy in the Soret band of a chiral porphyrin dimer,
submitted to New Journal of Physics (2012).

The contents of Chapter 4 of this work a currently being prepared for publication.